
THE HERSCHEL PERSPECTIVE ON NEARBY GALAXIES

by

Matthew W. L. Smith

A THESIS SUBMITTED TO CARDIFF UNIVERSITY
FOR THE DEGREE OF DOCTOR OF PHILOSOPHY

SEPTEMBER 2012

Author: Matthew W. L. Smith

Title: The Herschel Perspective on Nearby Galaxies

Date of submission: September 2012

Permission is granted to Cardiff University to circulate and to have copied for non-commercial purposes, at its discretion, the above title upon the request of individuals or institutions. The author reserves other publication rights, and neither the thesis nor extensive extracts from it may be printed or otherwise reproduced without the author's written permission.

Copyright © 2017 by Matthew W. L. Smith

Declaration

This work has not been submitted in substance for any other degree or award at this or any other university or place of learning, nor is being submitted concurrently in candidature for any degree or other award.

Signed: _____ (candidate) **Date:** _____

Statement 1

This thesis is being submitted in the partial fulfillment of the requirements for the degree of PhD.

Signed: _____ (candidate) **Date:** _____

Statement 2

This thesis is the result of my own independant work/investigation, except where otherwise stated. Other sources are acknowledged giving explicit references. The views expressed are my own.

Signed: _____ (candidate) **Date:** _____

Statement 3

I hereby give consent for my thesis, if accepted, to be available for photocopying and for inter-library loan, and for the title and summary to be available to outside organisations.

Signed: _____ (candidate) **Date:** _____

Statement 4: Previously Approved Bar on Access

I hearby give consent for my thesis, if accepted, to be available for photocopying and for inter-library loans **after expiry of a bar on access previously approved by the Academic Standards & Quality Committee**

Signed: _____ (candidate) **Date:** _____

*“It is not knowledge, but the act of learning,
not possession but the act of getting there,
which grants the greatest enjoyment.”*

Carl Friedrich Gauss

ACKNOWLEDGEMENTS

When driving down the M4 to Cardiff for my PhD interview I knew very little about the city or university. Four years on I am very glad I made the choice to move to Wales and continue studying. I would first like to thank my supervisors Steve and Jon, as well as Haley for all their help, support, and time spent correcting my terrible English. While they might have questionable taste in rugby teams or in the final year ask “Matt, who’s your supervisor, is it me?”, it is due to them that I have been involved with some great projects and visited some amazing places.

As a new postgraduate I was fortunate to be warmly welcomed into the ‘galaxy lads’ office. I owe a lot to Luca, Tom and Rhys who were always very helpful with all my very basic questions, and taught me a huge amount. I can only hope that I repay them by offering my help with future PhD students. The galaxy office has never been (and I hope never will be) a ‘dull’ place to work and I kept my sanity during the write-up due to all the office banter/games with Andreas, Chris, Chris, Elisabeta, Ezzy, George, Mat and Robbie. The regular coffee, cake, pub and ‘random adventurous activities’ with all the postgrads/postdocs¹, as well as my brilliant housemates Jess, Maria, Mat and Mark, has made my time in Cardiff a great one.

Most of this thesis would not exist without the great work of the SPIRE team and ESA for building a superb instrument and telescope. I am also indebted to Richard and Rodney for keeping my computer running and putting up with my many visits for help.

Finally, I have to say a massive thank you to my parents, who have always supported me in my undertakings and dreams for the last 27 years.

¹Tom Adams, Mat Allen, Robbie Auld, Scott Balfour, Pete Barry, Tom Brien, Sara Carver, Chris Clark, James Clark, Luca Cortese, Dave Cunnah, Ali Darioush, Tom Dent, Mark Doost, Simon Dye, Vanessa Evans, Steve Flynn, George Ford, Chris Fuller, Ed Gomez, Mark Hampton, Ian Harrison, Ian Harry, Sarah Harry, Tom Hughes, Matt Hutchings, Gareth Jones (1), Gareth Jones (2), Ioannis Kamaretsos, Jason Kirk, Sebastian Khan, Fraser Lewis, Oliver Lomax, Stuart Lowe, Duncan Macleod, Erin Macdonald, David McKechnie, Andrew McLeod, Chris Messenger, Lorenzo Moncelsi, Chris North, Laura Nuttal, Dave Nutter, Frank Ohme, Andreas Papageorgiou, Ezzy Pearson, Ellis Pires, Michael Pohlen, Geraint Pratten, Valeriu Predoi, Michael Pürer, Ciara Quinn, Gwen Raymond, Tom Rayner, Vikki Roloff, Sam Rowe, Patricia Schmidt, Sam Shutts, Rob Simpson, Rory Smith, Dimitris Stamatellos, Adam Strang, Rhys Taylor, Elisabetta Valiante, John Veitch, Steffi Walch, Lucy Wilcock, Andrew Williamson, Jo Woodward.

ABSTRACT

This thesis presents an investigation of local galaxies using new data from the *Herschel Space Observatory*. *Herschel* observes the entire far-infrared peak of galaxies, at higher sensitivities and angular resolution than previously possible, and can observe large samples of galaxies or areas of sky. I developed data reduction routines to optimise the data processing of SPIRE extragalactic fields, and found the best methods of flux extraction for galaxies and for fitting of spectral energy distributions. For all the objects I investigated, a single-temperature modified blackbody was a good fit to the global fluxes between 100–500 μm . Within an individual galaxy (i.e., M 31, NGC 4501 and NGC 4567/8) the dust temperature varies between 15–30 K. In M 31 the dust emissivity index varies between 1.2–2.5 suggesting a change in the physical properties of the grains. The dust and gas are highly correlated in M 31, with the gas-to-dust ratio varying from \sim 20 in the centre to \sim 200 at 18 kpc as expected from the metallicity gradient of the galaxy. By averaging the radial profiles of the late-type objects in the Herschel Reference Survey (HRS), I have shown that dust emission can be traced to at least twice the optical radius (R_{25}) of the galaxy. Within the HRS, dust is detected in 24% of Ellipticals and 62% of S0s and has a mean temperature of 23.9 ± 0.8 K for early-type galaxies, warmer than that found for other *Herschel* studies of late-type galaxies. The mean dust mass for the entire detected early-type sample is $\log M_d = 6.1 \pm 0.1 M_\odot$ with a mean dust-to-stellar-mass ratio of $\log(M_d/M_*) = -4.3 \pm 0.1$, a factor of \sim 50 lower dust-to-stellar-mass ratio than for the spiral galaxies in the HRS. The wide range in the dust-to-stellar-mass ratio for ETGs and the lack of a correlation between dust mass and optical luminosity suggest that much of the dust in the ETGs detected by *Herschel* has been acquired as the result of interactions, although these are unlikely to have had a major effect on the stellar masses of the ETGs.

PUBLICATIONS

FIRST AUTHOR PUBLICATIONS

Smith, M. W. L., Vlahakis, C., Baes, M., et al. 2010, *The Herschel Virgo Cluster Survey. IV. Resolved dust analysis of spiral galaxies*, A&A, 518, L51+

Smith, M. W. L., Gomez, H. L., Eales, S. A., et al. 2012, *The Herschel Reference Survey: Dust in Early-type Galaxies and across the Hubble Sequence*, ApJ, 748, 123

Smith, M. W. L., Eales, S. A., Gomez, H. L., et al. 2012, *The Herschel Exploitation of Local Galaxy Andromeda (HELGA). II. Dust and Gas in Andromeda*, ApJ, 756, 40

SECOND AUTHOR PUBLICATIONS

Eales, S. A., Smith, M. W. L., Wilson, C. D., et al. 2010, *Mapping the interstellar medium in galaxies with Herschel/SPIRE*, A&A, 518, L62+

Auld, R., Smith, M. W. L., Bendo, G., et al. 2012, *Herschel observations of Cen A: stellar heating of two extragalactic dust clouds*, MNRAS, 420, 1882

Eales, S. A., Smith, M. W. L., Auld, R., et al. 2012, *Can Dust Emission be Used to Estimate the Mass of the Interstellar Medium in Galaxies—A Pilot Project with the Herschel Reference Survey*, ApJ, 761, 168

A full list of publications can be found at <http://www.mwlsmith.co.uk/Publication.php>

CONTENTS

Acknowledgements	vii
Abstract	ix
Publications	xi
List of Tables	xviii
List of Figures	xx
1 Introduction	1
1.1 ‘Island Universes’	1
1.1.1 Galaxy Evolution	2
1.1.2 Morphology	4
1.1.3 The Interstellar Medium	6
1.2 Dust	7
1.2.1 Dust Composition, Growth and Destruction	10
1.2.2 Why Study Dust?	12
1.3 Far Infrared and Sub-millimetre Observatories	14
1.4 The Herschel Space Observatory	16
1.4.1 The Spectral and Photometric Imaging Receiver (SPIRE) . . .	18
1.4.2 The Photodetector Array Camera and Spectrometer (PACS) .	20
1.4.3 The Herschel-Heterodyne Instrument for the Far-Infrared (HIFI)	21
1.5 The Herschel Surveys	22
1.5.1 The Herschel Reference Survey (HRS)	22
1.5.2 The Herschel Virgo Cluster Survey (HeViCS)	24
1.5.3 The Herschel Fornax Cluster Survey (HeFoCS)	26
1.5.4 The Herschel Exploitation of Local Galaxy Andromeda (HELGA)	26

1.5.5	Other Connected Herschel Surveys	28
1.6	Thesis Outline	28
2	SPIRE Data Reduction	31
2.1	Introduction to Herschel Processing	31
2.2	SPIRE Photometer Observing Modes	32
2.2.1	HRS Observing Strategy	33
2.2.2	HeViCS and HeFoCS Observing Strategy	34
2.2.3	HELGA Observing Strategy	34
2.3	The Standard Pipeline	34
2.3.1	Raw Level-0 Creation	35
2.3.2	Engineering Conversion from Level-0 to Level-0.5	35
2.3.3	Timeline Processing: Level-0.5 to Level-1	35
2.3.4	Final Products: Level-1 to Level-2 Pipeline	40
2.4	BRight Galaxy Adaption Element (BRIGADE)	41
2.4.1	Combining Building Blocks	41
2.4.2	‘Jump’ Correction	42
2.4.3	Thermal Drift Correction	44
2.4.4	High Pass Filtering?	47
2.4.5	De-Striper	50
2.4.6	Map Making	50
2.4.7	Post Map-Making Checks	51
2.5	Comparison with Other Reduction Pipelines	53
2.5.1	SPIRE Extragalactic Science Team Review, July 2010	53
2.5.2	Present Day Comparison	58
2.6	Second Order Deglitching	58
2.7	WCS Alignment	59
2.7.1	Cross-Correlation Method	59
2.7.2	Point Source Method	62
2.8	Andromeda: A special Case	62
2.9	Relative Gain Corrections	65
2.10	Summary	66

3 SPIRE Flux Extraction and SED Fitting	67
3.1 Introduction to SPIRE Source Extraction and SED Fitting	67
3.2 Point Source Flux Extraction	67
3.2.1 Calculating Point Source Uncertainties	69
3.3 Extended Sources	71
3.3.1 Extended Source Uncertainties	72
3.3.2 Mathematical Expressions for Uncertainties	73
3.3.3 Extended Correction Factors	76
3.3.4 Extended or Point Source?	77
3.3.5 HRS Photometry	79
3.4 Spectral Energy Distribution Fitting	80
3.4.1 Modified Blackbody Model	82
3.4.2 Input/Output Modes	82
3.4.3 Choices	84
3.4.4 Color-Correction	84
3.4.5 Correlated Uncertainties	85
3.4.6 Bootstrapping for Uncertainties	85
3.4.7 Speeding Up the Code	85
3.5 Summary	87
4 Resolved Dust Analysis of Spiral Galaxies	89
4.1 Introduction	89
4.2 Observations and data reduction	90
4.3 Analysis	92
4.4 Results	93
4.5 Conclusions	97
5 Dust and Gas in Andromeda	99
5.1 Introduction	99
5.2 The Data	102
5.2.1 Far-infrared Observations	102
5.2.2 Gas Measurements	103
5.3 The FIR–Submillimeter Spectral Energy Distribution	103
5.3.1 SED Fitting	106

5.3.2	Results of the Fits	107
5.3.3	Simulations	109
5.3.4	Spatial Distribution of Dust Mass, Temperature, and Emissivity Index	111
5.4	Results	112
5.4.1	Radial Distribution of Gas and Dust	115
5.4.2	$500\mu\text{m}$ Excess	116
5.5	Discussion	118
5.5.1	Heating Mechanisms and Dust Distribution	118
5.5.2	Dust Emissivity and Temperature Relation	123
5.5.3	Why a Transition at 3.1 kpc?	128
5.5.4	Dark Gas and X factor	129
5.6	Conclusions	133
6	Dust in Early-Type Galaxies	135
6.1	Introduction	135
6.2	The Sample	138
6.2.1	Data Reduction and Flux Extraction	142
6.2.2	Data at other wavelengths	148
6.3	Results	150
6.3.1	Detection Rates	150
6.3.2	Residual Star Formation?	155
6.3.3	Dust Masses and Temperatures	157
6.4	Dust, Stars and Gas	162
6.4.1	Dust and stellar mass along the Hubble Sequence	166
6.4.2	The origin of dust in ETGs	169
6.4.3	A cool interstellar medium in early-type galaxies?	172
6.5	Discussion	175
6.5.1	Evidence for dust-depleted disks in S0s	175
6.5.2	Ellipticals and S0s or slow rotators and fast rotators?	177
6.5.3	Galaxy evolution	180
6.6	Conclusions	180

7 Extended Dust in the Full HRS	183
7.1 Introduction	183
7.2 Stacked Radial Profiles	184
7.3 The Extent of Dust in Galaxies	185
7.4 Comparison with HI-Deficiency	189
7.5 Dependence on Morphology?	189
7.6 Conclusions	192
8 Discussion & Conclusion	195
8.1 Thesis Overview	195
8.2 Key Results	196
8.2.1 Dust in Late-Type Galaxies	197
8.2.2 Dust in Early-Type Galaxies	198
8.3 Future Work	199
8.4 Concluding Remarks	202
A Images of Galaxies in the HRS	203
B Bar Graphs Comparing Object Fluxes for Tested Pipelines	249
C Proof of Modified Blackbody Dust Emission Model	253
D Notes on Ellipticals Detected by Herschel	257
E FIR emission versus optical and X-ray for Early-Type Galaxies	261
Bibliography	264

LIST OF TABLES

1.1	Point Spread Function FWHM for SPIRE and PACS Photometers	20
2.1	SPIRE Mask Values	36
2.2	Comparison of Sky Noise Values	56
2.3	Point Source Fitting Results	57
3.1	Multiplicative SPIRE Color Corrections	70
3.2	K_4 Values for Point and Extended Sources	77
5.1	Spearman Correlation Coefficients for Properties of M 31	119
6.1	The Sample	139
6.2	<i>IRAS</i> Fluxes and <i>Herschel</i> PACS for Detected Galaxies.	149
6.3	The Number of Early-type and Elliptical Galaxies Detected with <i>Herschel</i>	152
6.4	SED Parameters and Gas Masses	165
6.5	Mean Parameters for the Sample	168
6.6	Results of the Two-sample Tests	170

LIST OF FIGURES

1.1	Luminosity Function of Galaxies	3
1.2	Evolution of star formation rate density with redshift	4
1.3	Galaxy Color-Magnitude Diagram	5
1.4	Kennicutt-Schmidt Law	8
1.5	Extinction curves of the Milky Way, SMC and LMC	9
1.6	The Witch Head reflection nebula	10
1.7	MIR and FIR spectrum	11
1.8	The extragalactic background from UV to millimetre wavelengths . .	13
1.9	HIFI Spectrum of Orion	22
1.10	The Herschel Reference Survey	25
1.11	The Herschel Virgo Cluster Survey	27
1.12	The Herschel Exploitation of Local Galaxy Andromeda Survey	29
2.1	Level-0.5 to level-1 flowchart	37
2.2	An example thermistor ‘jump’	42
2.3	Example bolometer ‘jumps’ in SPIRE maps	43
2.4	Example of ‘jump’ correction procedure	44
2.5	Effect of source masking on baseline subtraction	48
2.6	Example of gaussian fit to source in the timeline	48
2.7	Example of thermal drift correction on a timeline	49
2.8	Example of the de-striper improving observations with heavy cirrus .	51
2.9	Example glitch tails in SPIRE maps	52
2.10	Example of a glitch tail in the timeline.	52
2.11	Map-making review sample	55
2.12	Present day pipeline comparison	59
2.13	Example of cross-correlation method	61

2.14	HeViCS V3 offsets from point source extraction	63
2.15	Image of the HELGA Mapping Strategy	64
2.16	Effective of relative gain corrections on SPIRE ‘Error’ Map in M 31 . .	66
3.1	The SPIRE relative spectral response function	69
3.2	Example methods to measure the background uncertainty	76
3.3	Subtracting timeline Gaussian fits to test for extended emission . . .	78
3.4	Results from adding artificial sources and extracting global fluxes . .	81
3.5	Example galaxy SEDs showing each models available in the SED fitter	83
3.6	Automatic plot of the results of the bootstrap analysis when SED fitting	86
4.1	Global and example single pixel one component SED fits.	91
4.2	Images and SED fitting results for NGC 4501	95
4.3	Images and SED fitting results for NGC 4567/8	96
5.1	<i>Herschel</i> images of M 31	104
5.2	Ancillary images for M 31	105
5.3	Distribution of χ^2 values	108
5.4	Examples of SED fits for pixels in different regions	109
5.5	Simulations of the SED fitting performance	110
5.6	Correlated uncertainties between β and temperature	112
5.7	Distribution of dust surface density, temperature, and β in M 31 . .	113
5.8	Results from the SED fits for each pixel plotted vs. radius	114
5.9	Distribution of atomic, molecular and gas-to-dust ratio versus radius	114
5.10	The distribution of the $500 \mu\text{m}$ excess	117
5.11	Correlations between dust properties and $3.6 \mu\text{m}$ flux or SFR	120
5.12	$\log(3.6 \mu\text{m})$ flux vs. $\log(\text{Temperature})$ for the inner 3.1kpc	122
5.13	Comparison of SFR map and dust temperature map	123
5.14	Variation of the dust temperature with emissivity index in M 31 . . .	126
5.15	Simulated relation between dust temperature with emissivity index .	127
5.16	Radially corrected Σ_{dust} vs. total column density of gas	131
5.17	Radially corrected Σ_{dust} vs. N_H^{Tot} where H ₂ fraction is >20%	131
5.18	Map of $\Sigma_{\text{dust}}/N_H^{\text{Tot}}$ ratio in M 31	132
6.1	SDSS and $250 \mu\text{m}$ SPIRE maps of the 24 detected HRS S0+S0a galaxies	144

6.2	SDSS and 250 μm SPIRE maps of the 23 HRS elliptical galaxies	146
6.3	Comparison of the ETG sample with B -band, X-ray and gas data	156
6.4	The NUV– r color vs. the stellar mass of the HRS sample	158
6.5	Spectral energy distributions of the 24 detected S0+S0a galaxies	160
6.6	Spectral energy distribution of the seven detected ellipticals	161
6.7	Histograms of dust temperature, M_{dust} and M_* for the ETG sample .	163
6.8	Dust-to-stellar-mass ratio vs. stellar mass for the ETG sample	167
6.9	Dust-to-stellar-mass ratio vs. morphological type	170
6.10	FIR luminosity and dust mass vs. B -band and X-ray luminosity	173
6.11	Ratio of the submm and optical sizes for the HRS sample	176
6.12	The dust-to-stellar-mass ratio vs. the optical kinematics	179
7.1	Average radial profiles of HRS late-type galaxies	186
7.2	The 250 μm /500 μm surface brightness ratio	188
7.3	Average radial profiles of HRS galaxies split by HI_{Def}	190
7.4	Average Profiles of HRS galaxies split by morphology	191
7.5	The Herschel Astrophysical Terahertz Large Area Survey	193
8.1	A CO($J = 1 - 0$) map of NGC 1097 created by Mopra	200
8.2	The Environment of the HRS	201
A.1	Images of Galaxies in the Herschel Reference Survey	203
B.1	Difference in M 100 Flux for repeated observations split by pipeline .	250
B.2	Percentage difference in M 100 flux between pipelines (obs:0x5000273A)	250
B.3	Percentage difference in M 100 Flux between pipelines (obs:0x50002CE3)	251
B.4	Percentage difference in M 82 flux between pipelines	251
B.5	Percentage difference in M 91 flux between pipelines	252
B.6	Percentage difference in NGC 6822 flux between pipelines	252

CHAPTER 1

INTRODUCTION

“I have looked further into space than any human being did before me.”
William Herschel

1.1 ‘ISLAND UNIVERSES’

It was only in 1923 that Edwin Hubble made the observation which proved that the universe consisted of more than just the Milky Way. Speculation that objects like the Milky Way could exist in the universe has been found in publications as early as the 18th century (e.g., Swedenborg, 1734), although these suggestions lacked corroborating evidence from observations. Thomas Wright in 1750 speculated that the Milky Way consisted of a flat layer of stars and proceeded to write:

“..the many cloudy spots, just perceptible by us, as far without our Starry regions, in which tho’ visibly luminous spaces, no one star or particular constituent body can possibly be distinguished; those in all likelihood may be external creation, bordering upon the known one, too remote for even our telescopes to reach.”

Wright (1750)

which implies that the universe contained more than just our own galaxy, the Milky Way. Immanuel Kant expanded on the ideas presented by Wright in 1755 and was the first to coin the phrase ‘island universes’. Unfortunately the observational data were unable to distinguish between galaxies and nebulae in the Milky Way. The debate whether the Milky Way constituted the whole universe continued on to the beginning of the 20th century and catalogues made by both Messier and Herschel contain a mixture of galactic and extra-galactic objects. In the early 20th century evidence began to accumulate that these objects were outside the Milky Way; the

final proof was published in Hubble (1925) who measured Cepheid variable stars in M31 and M33 and calculated them to be at a distance of 285 kpc, far outside any estimate of the size of the Milky Way.

1.1.1 GALAXY EVOLUTION

The current paradigm of the cosmic history of galaxies is based on the Λ -CDM model. In this model the matter in the universe is dominated by cold dark matter (CDM) with dark energy which is represented by the cosmological constant (Λ) driving an accelerated expansion of the universe. Primordial fluctuations in the density of the early universe are created due to quantum fluctuations. These slight over-densities grow by attracting gas and dark matter leading to the formation of dark matter halos. The gas that collects in these halos cools and condenses leading to the birth of the first galaxies and stars. These first galaxies initially are small but grow over time by collecting more gas and by merging with other galaxies leading to the large galaxy systems we see today. This process is commonly referred to as the ‘hierarchical model’ of galaxy formation.

Simulations of Λ -CDM lead to a luminosity function of galaxies as shown in Figure 1.1. In this figure it can be seen that the theoretical luminosity function at low and high galaxy luminosities is an overestimate compared with the observations. To resolve the discrepancy different forms of feedback can be added to the model. At low luminosities supernova feedback is believed to be able to explain the difference between the observations and simulations. The dark matter halo in low luminosity galaxies would be low mass, therefore supernovae are capable of expelling gas from the halo, leading to a reduction in the star formation rate (SFR). At high luminosities feedback from active-galactic nuclei is seen as a likely mechanism in suppressing star formation in the host galaxy by either preventing the cooling of gas or by ejecting gas out the galaxy (Fabian, 2012). Evidence for this can be seen in the tight relations found between the black hole mass and the mass and/or velocity dispersion in galaxy bulges (e.g., Kormendy & Gebhardt, 2001).

There are some potential problems with Λ -CDM and the ‘hierarchical’ model of galaxy formation. One issue is that the highest mass galaxies in the local universe normally have old stellar populations and higher metallicities, which suggests that their stars formed a lot earlier than expected from the ‘hierarchical’ model. This process is often referred to ‘downsizing’, as the most massive galaxies appear to have formed earlier in the universe rather than by mergers of small galaxies at later times.

The history of star formation in the universe is keenly studied as the birth

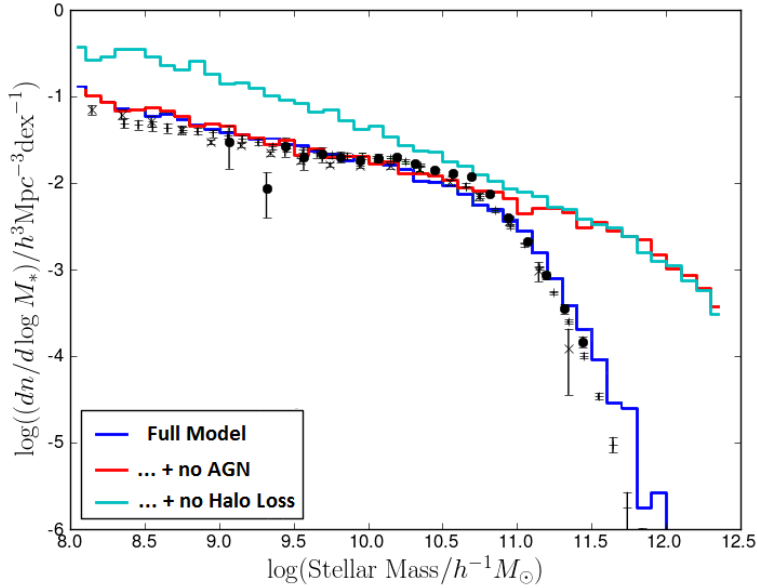


Figure 1.1. The luminosity function of galaxies, taken from Figure 1 (with slight modifications) of Bower et al. (2012). The black data points are the observed luminosity function of galaxies and the blue line shows the full Bower et al. (2012) model. The red line is a model with no AGN feedback and the cyan line is a model with no AGN or gas loss from the halo (e.g, from supernovae).

and death of stars has produced all the stars, galaxies and heavy elements found in the universe today. To study the history of star formation either an archaeological approach in local galaxies or direct observation of high redshift galaxies is required. The ‘fossil record’ approach involves observing nearby galaxies with spectroscopy and multi-band photometry to identify the stellar populations present today and then trying to reconstruct the star formation history within that galaxy. This is often likened to archaeology as the history of the galaxy is reconstructed based on the current emission from the galaxy. This technique has the advantage that nearby galaxies are relatively easy to observe and large area surveys like the Sloan Digital Sky Survey (SDSS; York et al., 2000) are available. The disadvantage is that reconstructing the history of a galaxy is very difficult; a unique solution may not exist and several assumptions may have to be made. The alternative is to attempt to directly observe galaxies at higher redshift, i.e., actually looking back in time. From optical, UV and near-infrared measurements the star formation, stellar mass and the metal abundance can potentially be found. By measuring many objects at different redshifts a history of star formation in the universe can be found. This method can be affected by observation biases, dust absorption/reddening and the technical challenges of observing such faint objects.

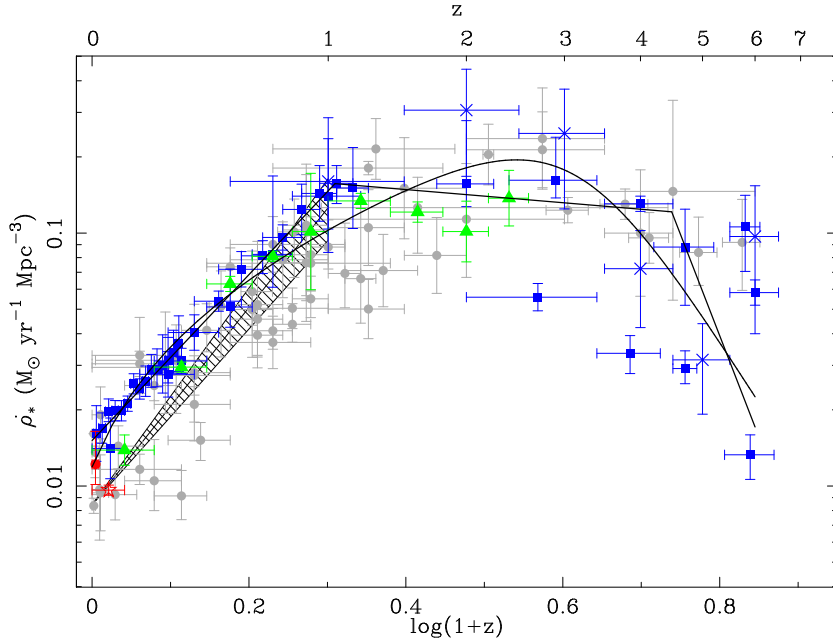


Figure 1.2. The evolution of SFR density ($\dot{\rho}_*$) with redshift (z) is taken from Hopkins (2007) (Figure 1). The figure includes data from Bouwens et al. (2003a,b, 2006); Wolf et al. (2003); Bunker et al. (2004); Hopkins (2004); Ouchi et al. (2004); Arnouts et al. (2005); Baldry et al. (2005); Le Floc'h et al. (2005); Mauch (2005); Pérez-González et al. (2005); Hanish et al. (2006); Thompson et al. (2006).

By using a combination of methods the star formation history of the universe has been fairly well defined. Figure 1.2 is a figure taken from Hopkins (2007) which shows the standard curve showing the star formation history of the universe. From this curve it can be seen that the peak of star formation occurs between a redshift of two and three with over an order of magnitude increase on the current star formation activity of the universe.

1.1.2 MORPHOLOGY

Soon after the first galaxies were identified as being outside the Milky Way it became apparent that galaxies seemed to fit into two classes of object: spirals and ellipticals. While more complicated classification systems now exist with the addition of many more classes of galaxy (e.g., irregular, dwarfs, lenticular, barred), a plot of the UV-optical colors versus optical magnitude of galaxies still produces a bivariate distribution. An example of this is a plot taken from Wyder et al. (2007) and shown in Figure 1.3. The two clouds are often referred to as the ‘blue cloud’ and the ‘red sequence’. This bimodal distribution is found to exist at least to a redshift of one (Bell et al., 2004).

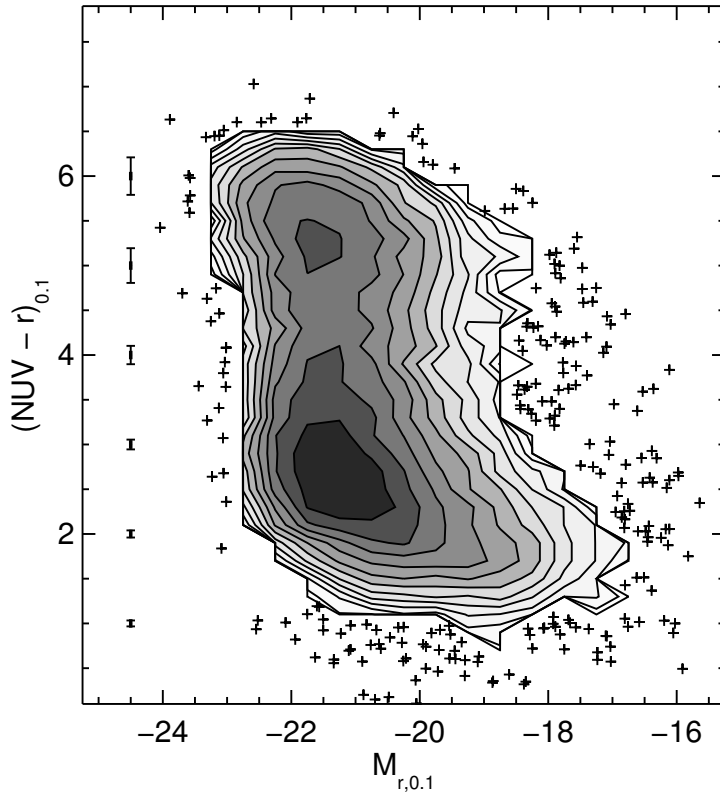


Figure 1.3. The galaxy color-magnitude diagram taken from Wyder et al. (2007) (Figure 7). M_r is the absolute r-band magnitude and the y-axis is the NUV–r color (for full details see Wyder et al., 2007).

The ‘blue cloud’ is primarily composed of spiral galaxies, which have blue colors due to their ongoing star formation. The red sequence comprises ellipticals and lenticular galaxies which are dominated by their old stellar population (lenticular and ellipticals are often collectively referred to as early-type galaxies). Older stellar populations are redder in color as they consist of longer-lived low-mass massive stars. Early-type galaxies are believed to contain little ISM (this is discussed more in Chapter 6) and have little or no star formation. Lenticular galaxies differ from ellipticals as they contain a definite disk structure but no spiral arms, while ellipticals do not contain any disk structure.

The cause of the bi-modality in the color-magnitude diagram is not known. A possible explanation is that galaxies form their stars in the blue cloud, but then a process occurs to quench the star formation leading to a migration of the galaxy to the red sequence. Quenching of the star-formation could occur from either AGN feedback or from some external mechanism. This does not explain how disk galaxies can become elliptical in shape. Observationally it has been known for a long time that early-type galaxies are preferentially found in dense environments like galaxy

clusters (Zwicky, 1942; Dressler, 1980). This suggests that some effect of the surrounding environment of the galaxy like ram pressure stripping or harassment (these are explained in more detail in Section 1.1.3) could be a significant influence on galaxy evolution.

1.1.3 THE INTERSTELLAR MEDIUM

The interstellar medium (ISM) comprises of all the material found between stars in galaxies. The ISM typically has a very low density with an average value of $\sim 10^6$ atoms m^{-3} (Whittet, 2003) i.e., 1 atom per cubic centimetre, a factor of 10^{19} less than the density of the atmosphere at sea level. Despite its low density the ISM constitutes approximately 15–20% of the mass of the disk in the Milky Way (Yin et al., 2009). The ISM is overwhelmingly made of hydrogen in either atomic, molecular or ionised form. Helium is the next biggest component followed by metals (e.g., carbon, oxygen, silicon) and dust. The hydrogen and helium are mostly the primordial matter created after the big bang while most of the heavier elements must have been formed by stars.

The ISM is a key component of a galaxy as it provides the fuel to create new stars. Several processes can occur to quench star formation, including ones which expel or heat the gas. Internal mechanisms to prevent star formation in the disk of galaxies are thought to include AGN feedback or bars. Bars can reduce star formation in the disk by channelling gas out of the disk towards the centre of the galaxy where either rapid star formation occurs or the gas is accreted onto an AGN. External interactions can either remove or heat the gas leading to a quenching of star formation. This can include tidal interactions (e.g., harassment, Moore et al., 1999), mergers with other galaxies, direct interaction with the hot cluster gas through ram-pressure stripping (Gunn & Gott, 1972) or thermal evaporation, and starvation/strangulation (Larson et al., 1980; Bekki et al., 2002) due to the loss of the hot halo preventing further gas replenishment in the disk. All these environmental effects are discussed in much more detail in Boselli & Gavazzi (2006). Enhancements in star formation can also be caused by galaxy mergers, interactions or supernova shocks (e.g., Krebs & Hillebrandt, 1983; Chapman et al., 2004; Engel et al., 2010). Mergers and interactions can trigger large bursts of star formation within a galaxy and can significantly affect the amount of stars in a galaxy

Evidence that environmental effects can affect the ISM in galaxies is that cluster members tend to be HI deficient (e.g., Giovanelli & Haynes, 1985). HI deficiency is a measure of how much HI gas is missing compared to a field galaxy with similar mass

and morphological type (see Haynes & Giovanelli, 1984). The dominant mechanism which causes this effect by the cluster environment is not known and investigations of how the dust and molecular gas are affected are ongoing (e.g., Cortese et al., 2010b).

The surface density of star formation is related to the surface density of gas in a galaxy. Schmidt (1963) first suggested that the relation between the volume densities of gas and star formation could be linked by a power law. As the observable quantities are the projected surface densities the Schmidt law is often written as

$$\Sigma_{\text{SFR}} = A \Sigma_{\text{gas}}^N, \quad (1.1)$$

where Σ_{SFR} and Σ_{gas} are the surface densities of SFR and cold gas (atomic and molecular hydrogen), respectively, and A and N are constants. In a series of papers Kennicutt has investigated the law in samples of galaxies, from 15 galaxies in Kennicutt (1989) to 97 galaxies in Kennicutt (1998b), where the Schmidt index was found to be $N = 1.4 \pm 0.15$; this became known as the Kennicutt-Schmidt Law (a plot of the relationship is shown in Figure 1.4). When looking on sub-kpc scales Bigiel et al. (2008) find a strong correlation between surface density of molecular gas and the surface density of SFR with an index of 1.0 ± 0.2 . They interpret this as evidence that stars are forming in giant molecular clouds with uniform properties (i.e., each GMC has the same molecular gas mass so a measurement of the molecular gas density in a galaxy effectively counts the number of GMCs present). A few other studies have found higher indexes on sub-kpc scales (see Kennicutt & Evans, 2012, and references therein), but this could be due to differences in how the diffuse background is subtracted or different methods used to calculate the star formation rate (Kennicutt & Evans, 2012). Further work in this area is needed to address if there is a universal star formation law and a minimum gas threshold for star formation to occur.

In this section, I have tried to show that the ISM is intimately linked with the evolution of a galaxy and is a key area of investigation.

1.2 DUST

The existence of dust in the ISM was first suggested in 1847 by Wilhelm Struve to explain measurements that the density of stars decreased as a function of distance from the solar system (Struve, 1847). The presence of inter-stellar dust was not universally believed until the early part of the 20th century (see Whittet, 2003, and references therein). Dust was (and often still is) considered a nuisance to astronomers as it causes extinction of optical and UV light from stars and can make

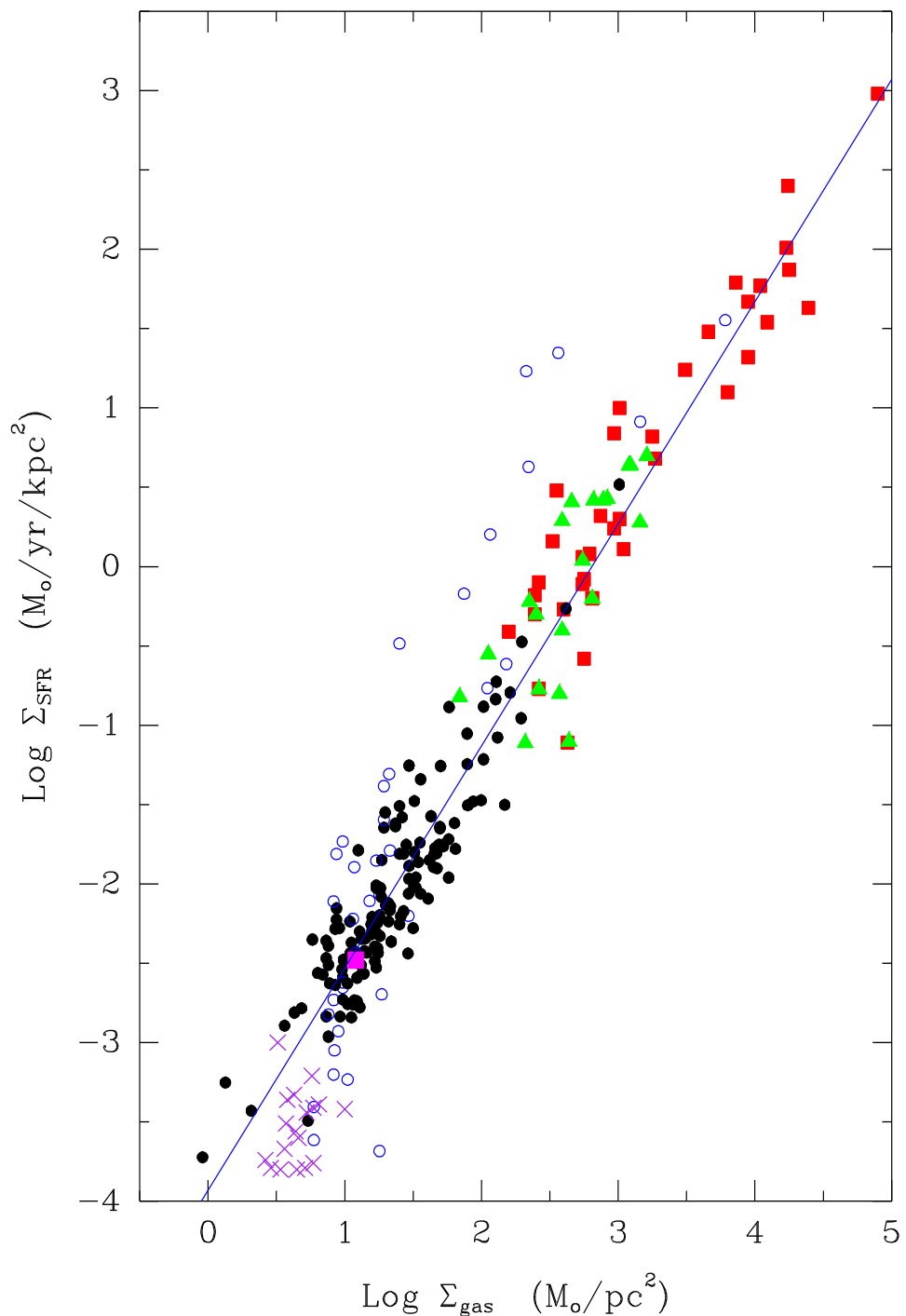


Figure 1.4. This figure is taken from Kennicutt & Evans (2012). The plot shows the surface density of star formation versus the surface density of gas for a sample of galaxies. The straight line represents the Kennicutt-Schmidt law with an index of 1.4.

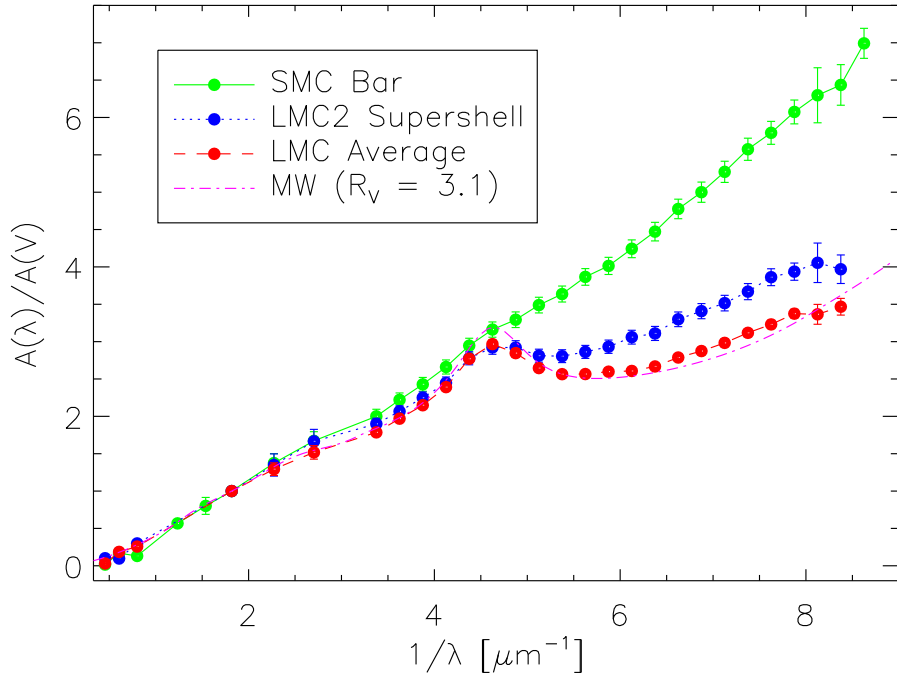


Figure 1.5. Average extinction curves for the Milky Way, SMC and LMC taken from Gordon et al. (2003) (Figure 10). $A(\lambda)$ is the total extinction for a particular wavelength and $A(V)$ is the extinction in the V-band.

objects appear redder than their real emission (due to more efficient absorption at shorter wavelengths, see Figure 1.5). Extinction by dust is caused by two effects: scattering and absorption.

Scattering is the dominant source of continuum extinction at wavelengths below $1\,\mu\text{m}$ (Li, 2005). Evidence for this process can easily be seen from reflection nebulae, which are clouds of dust which reflect the light of nearby stars. These are often blue as the scattering is more efficient for shorter wavelengths; an image of a reflection nebula is shown in Figure 1.6.

The other source of extinction is from absorption of light, which heats the dust grains, which then radiate the absorbed energy in the far infrared (FIR). For large grains an equilibrium temperature is reached, which occurs when the energy absorbed by the grain from the optical/UV photons equals that emitted by the grain. For a typical interstellar radiation field (ISRF) and grain size the dust temperature typically ranges between 15–30 K (e.g., Smith et al., 2012b; Davies et al., 2012; Dunne et al., 2011) with the peak of the FIR emission at approximately $160\,\mu\text{m}$ (more extreme temperatures are found in star formation regions).



Figure 1.6. The Witch Head reflection nebula which glows blue due to the scattered light from the nearby bright star, Rigel (Image credit: NASA).

1.2.1 DUST COMPOSITION, GROWTH AND DESTRUCTION

From early studies of dust the extinction curve (illustrated in Figure 1.5) has been found to be roughly described by $A_\lambda \propto \lambda^{-1}$ which suggests dust grains have sizes comparable to the wavelength of visible light. The composition of dust is still uncertain and has been found to vary between galaxies (e.g., the different extinction curves in Figure 1.5). The 2175 Å feature clearly seen in Figure 1.5 is widely believed to originate from small graphite grains ($\text{radius} < 0.02 \mu\text{m}$) as the feature matches that predicted from theoretical models, and graphite grains could survive for long periods in the ISM. Larger grains ($\sim 0.1 \mu\text{m}$) are required to explain the extinction in the UV and the cold dust emission. These large grains are believed to either be made of silicates or amorphous carbon. Figure 1.7 shows a near to far-infrared dust model (see Draine & Li, 2007a) that has been fitted to fluxes from a galaxy. One feature that is evident in this fit is a bump in the spectrum around $10 \mu\text{m}$ which suggests the presence of very hot grains around $\sim 1000 \text{ K}$. This can be explained by a population of small grains ($\text{radius} \approx 0.001 \mu\text{m}$) which are not in thermal equilibrium. Instead when absorbing a photon the grain exhibits a large spike in temperature and then cools. This is often referred to as stochastic heating or transiently heated dust.

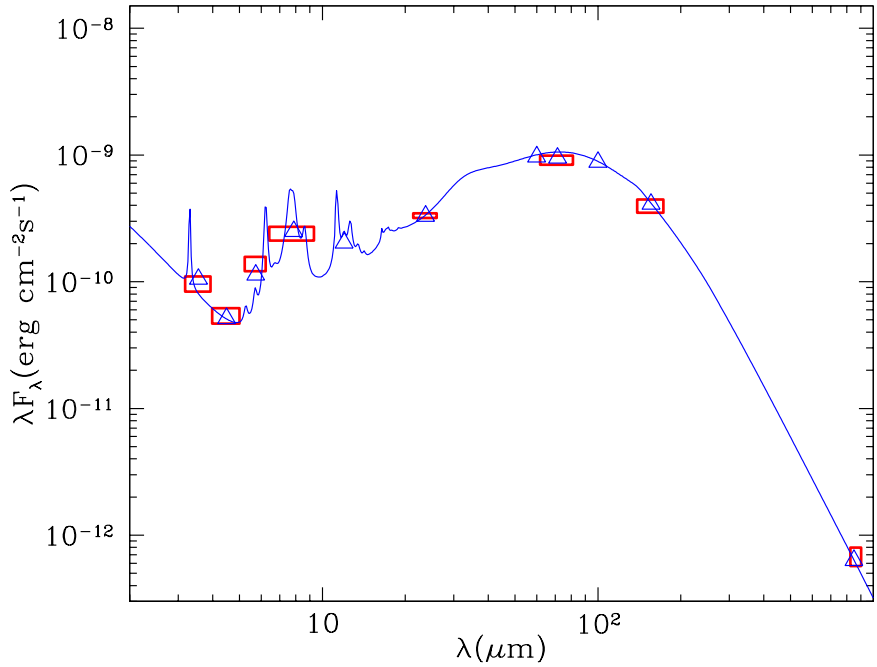


Figure 1.7. An example mid-infrared to far-infrared spectrum for NGC 2798. The image is adapted from Figure 3 in Draine et al. (2007). The blue line is a model dust SED which has been fitted to the data. The triangles show the model convolved with the *Spitzer*, *IRAS*, and SCUBA bands and the best fit model is shown by the solid blue line.

The other features clearly visible are some sharp emission lines at 3.3, 6.2, 7.7 and 11.3 μm . These represent poly-aromatic hydrocarbons (PAHs), which are molecules made out of a number of benzene rings. The PAHs are estimated to contain 3–15% of the carbon in the ISM (Allamandola et al., 1989).

The cold dust emission in the FIR can also provide insights into the composition of the dust. By using the Mie solution (Mie, 1908) of Maxwell’s equations the dust absorption efficiency can be calculated. From Kirchhoff’s law this has to be equal to the dust emission efficiency, and as the dust emits at far-infrared wavelengths the small grain approximation is valid. The general solution is then obtained that

$$Q_{FIR} \propto \lambda^{-\beta} \quad (1.2)$$

where Q_{FIR} is the dust emission efficiency. The spectral index β depends on the composition of the dust emitting the radiation. For dielectric materials like metals and crystalline substances a β closer to two is expected. Low values of β towards one would be consistent with small amorphous carbon (Seki & Yamamoto, 1980). The constant of proportionality normally used to convert between the dust emission and dust mass is still highly uncertain.

Dust can be created in the atmospheres of post-main sequence stars, which include giants, supergiants and asymptotic giant branch (AGB) stars. Dust is expected to form in a shell around the stars where the temperature has fallen below ~ 2000 K (Salpeter, 1974) but where the number-density of particles is still high enough to allow grain growth. This region is expected to contain a large variety and abundance of atoms and molecules for absorption into grains. The other main source of dust is supernovae. In these spectacular events many heavy elements are produced, which can condense into dust grains after the initial shock-wave (Gomez et al., 2012). While dust has been observed around AGB stars (Sargent et al., 2010) and in supernovae (Matsuura et al., 2011), the quantities and composition of dust formed in each is still uncertain.

Grains can grow in the interstellar medium through two processes, either coagulation or mantle growth. Coagulation can occur when two dust grains hit each other at a low velocity resulting in a larger dust grain. The amount of coagulation therefore depends on the number density of dust grains with higher densities leading to more collisions. Mantle growth is the process where atoms and molecules in the gas bind with the surface of the dust grain. Mantles are thought to be largely composed of C, N and O due to their abundance in the ISM. The surface of the grain is an excellent place for chemical reactions to occur, including the creation of H₂O. The importance of the grain as catalyst can be illustrated as one of the most common dust mantles are ‘icy mantles’ despite the only source of H₂O being from reactions on the grain surface.

There are two main processes which are believed to contribute to dust destruction. The first process is high velocity grain-grain collisions. High velocity interactions (>50 km/s) are likely to occur when a shock wave created by a supernova passes through low density gas. The second method is sputtering, in which atoms or ions bombarding the grain result in particles or atoms on the surface of the dust grain being ejected (e.g., Barlow, 1978).

1.2.2 WHY STUDY DUST?

Dust comprises approximately 1% of the mass of the ISM (Whittet, 2003) which in total only comprises 15–20% of the mass in the disk of the Milky Way (Yin et al., 2009). However, the emission of dust is a vital component in many areas of astronomy. Measurements of the Cosmic Infrared Background (CIB) reveal that half of the energy emitted by stars throughout the history of the universe has been absorbed and re-emitted by dust. This is shown in Figure 1.8 where the peaks in

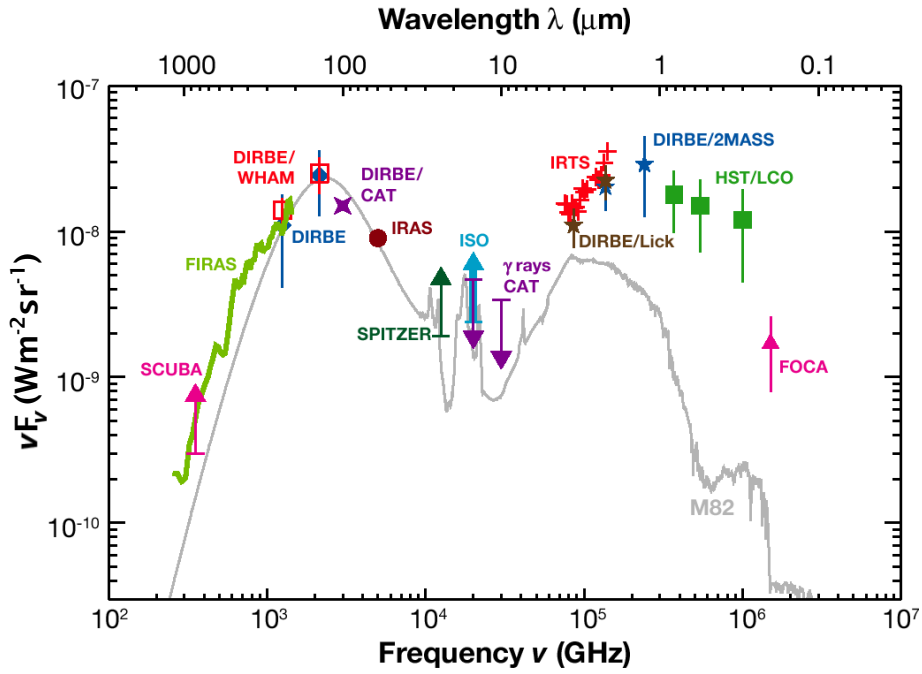


Figure 1.8. The extragalactic background from UV to millimetre taken from Lagache et al. (2005) (Figure 2). The grey line is a spectral energy distribution of M82 (Chantal, 2003), a starburst galaxy but normalised to the CIB at $140\text{ }\mu\text{m}$. The plot uses data from Armand et al. (1994); Hauser et al. (1998); Elbaz et al. (1999); Gorjian et al. (2000); Lagache et al. (2000); Renault et al. (2001); Wright (2001); Bernstein et al. (2002); Miville-Deschénes et al. (2002); Smail et al. (2002); Mattila (2003); Matsumoto et al. (2005); Papovich et al. (2004)

the optical ($\sim 10^5\text{ GHz}$) and in the far-infrared ($\sim 10^3\text{ GHz}$) have approximately the same area. To fully trace the emission of galaxies the FIR band therefore has to be studied. Studies of the local universe find the FIR emission to correspond to about a third of the total energy emitted by galaxies showing there has been evolution of the FIR emission with redshift.

In the late 1960s and 1970s a small number of objects were discovered using mid-infrared measurements that had the same luminosity in the infrared as in the optical (Low & Kleinmann, 1968; Rieke & Low, 1972). The *InfraRed Astronomical Satellite* (IRAS; Neugebauer et al., 1984) was the first telescope capable of detecting large numbers of galaxies in the mid and far-infrared and identified many objects that had much higher far-infrared luminosities (e.g., Soifer et al., 1984; Aaronson & Olszewski, 1984). These are referred to as Luminous Infrared Galaxies (LIRG) with $10^{11} < L_{\text{FIR}} < 10^{12} L_{\odot}$, Ultra-Luminous Infrared Galaxies (ULIRGS) with $10^{12} < L_{\text{FIR}} < 10^{13} L_{\odot}$ and Hyper-Luminous Infrared Galaxies (HLIRGS) with $L_{\text{FIR}} > 10^{13} L_{\odot}$. These objects are often found to be the result of a major merger

event which leads to a starburst or an increase in AGN activity. These objects are important to studies of the universe as they can form a large amount of stars on a short timescale and could be similar to the progenitors of elliptical galaxies in the local universe. While these objects do form a significant population of star forming galaxies at a $z \sim 2$ they only make up $\sim 10\%$ of the total star formation in the universe at those times (Maiolino et al., 2008, 2010).

Dust has an important role in many chemical processes that occur in the ISM (astro-chemistry). One of its most important is that dust acts as a catalyst for the conversion of atomic hydrogen to molecular hydrogen in the ISM. This process can then lead to the formation of dense molecular clouds where stars are formed. The surface of dust grains is also thought to catalyse many reactions in the ISM which otherwise would not occur. Dust has many absorption and emission features, which provide clues to its composition, and to the abundances of elements in different regions of a galaxy.

Hildebrand (1983) suggested that dust might be a good tracer of the total mass of the ISM, including phases hidden from traditional gas tracers. Dust has the advantage that the emission is almost always optically thin except in extreme objects (Rangwala et al., 2011), and therefore measurements are sampling the entire galaxy through the line of sight. HI is a good tracer of the atomic hydrogen, but it can become optically thick above a column density of 10^{21} cm^{-2} for normal disk conditions (Davies, 2012). In practice this should not be an issue as the atomic gas converts to molecular gas at lower densities (e.g., Bigiel et al., 2008). Molecular hydrogen gas in the cold ISM is far harder to trace as it cannot be observed directly due to its lack of a permanent dipole moment (Davies, 2012). The CO molecule is often used to trace the gas but the conversion from the CO line flux to molecular gas column-density is highly uncertain. Dust therefore can potentially be a good tracer of the total ISM density but there are many complications, for example varying dust-to-gas ratios and metallicity (see Chapter 4 and 5).

1.3 FAR INFRARED AND SUB-MILLIMETRE OBSERVATORIES

Far infrared and Sub-millimetre astronomy is a relatively young field due to the major technical challenges that these wavebands present. In the far infrared observations can only be made in space due to the absorption of the atmosphere. Some sub-millimetre observations can be made from the ground through narrow observing windows, but even in these windows there is still considerable absorption and

background emission from the atmosphere. Space observatories still face considerable challenges; one challenge is the instruments and telescope must be cooled to prevent masking of the astronomical signal. This often requires cryogenic cooling, which limits the lifetime of the satellite and the heavy cryostat significantly increases the weight to be lifted to space. Another challenge is the resolution which is significantly poorer than both optical telescopes at shorter wavelengths and interferometers in the radio bands. A summary of the technical challenges in the far infrared can be found in Swinyard & Wild (2010). The following paragraphs provide a brief description of the most influential observatories/instruments in the wavelength range 100–850 μm .

The first major observations in the far-infrared were made in 1983 with the launch of the *InfraRed Astronomical Satellite* (*IRAS*; Neugebauer et al., 1984). *IRAS* observed the whole sky (96% of the entire sky) at 12, 25, 60, and 100 μm with resolutions between 30'' to 2'. *IRAS* was a major leap forward, detecting \sim 350,000 sources in the infrared. One of the first studies by de Jong et al. (1984) showed that for a sample of galaxies with $B < 13$ mag most spiral galaxies are detected but no elliptical galaxies. With only measurements at 60 and 100 μm in the FIR, *IRAS* was not sensitive to dust colder than 30 K and so could potentially miss up to 90% of the dust in galaxies (Devereux & Young, 1990).

In 1995 the *Infrared Space Observatory* (*ISO*; Kessler et al., 1996) was launched by the European Space Agency and was designed to follow up *IRAS* sources at wavelengths 2.4–240 μm with both cameras and spectroscopy. *ISO* had a highly elliptical orbit to avoid emission from the Sun, Earth and Moon. However, this resulted in it passing through the van Allen radiation belt and loss of seven hours of observing a day and poor object visibility. *ISO* had an improved sensitivity and resolution compared to *IRAS*, despite a similar size mirror of 60 cm. *ISO* made several important discoveries including the detection of water vapour and proto-planetary disks. Davies et al. (1999) found that *ISO* observations of NGC 6946 showed 200 μm dust emission out to the optical diameter and a suggestion that dust emission extends further. *ISO* like *IRAS* was not sensitive to very cold dust due to its wavelength coverage.

The *Spitzer Space Telescope* (Werner et al., 2004) was a NASA satellite launched in 2003. *Spitzer* included the next generation of instruments, and observed between 3–160 μm , with its far-infrared camera, the Multiband Imaging Photometer for Spitzer (MIPS, Rieke et al., 2004), operating at 24, 70 and 160 μm . *Spitzer* made the first direct detection of extra-solar planets (Deming et al., 2005) and detected young star forming regions. One of the largest nearby galaxy studies conducted with *Spitzer* was the *Spitzer* Nearby Galaxy Survey (SINGS) which observed a sample of 75 nearby

galaxies with photometry and spectroscopy in the 3–160 μm range. Kennicutt et al. (2009) found that the best measure of star formation from photometry is obtained by using a combination of H α and total IR luminosity in SINGS galaxies. However, the 8 or 24 μm band can be substituted for total IR luminosity and work nearly as well. As many 24 μm observations have been obtained with *Spitzer*, the 24 μm band has become a very common measure of obscured star formation in galaxies. *Spitzer*, like *ISO* and *IRAS* was not sensitive to the dust colder than 20 K (Bendo et al., 2003) and did not significantly improve on the resolution of *ISO* at FIR wavelengths.

The Sub-millimetre Common-User Bolometer Array (SCUBA; Holland et al., 1998) was a sub-millimetre camera which was installed on the James Clark Maxwell Telescope (JCMT) in 1996 and observed at 450 and 850 μm . SCUBA had 91 and 37 pixels operating in its short and long wavelength range respectively, and its increased field of view (2.3') and sensitivity made it a factor of 10000 faster at mapping than its single-pixel predecessor. SCUBA was good at detecting high-redshift objects as at high-redshift the peak of the dust SED is shifted into the SCUBA bands, and the SCUBA surveys were responsible for the discovery of the first high redshift ULIRGs (e.g., Hughes et al., 1998). In the Milky Way SCUBA made possible the detection of the very coldest pre-stellar cores. The SCUBA Local Universe Galaxy Survey (SLUGS) surveyed 104 galaxies from the *IRAS* bright galaxy sample and 81 optically selected galaxies. In a series of three papers (Dunne et al., 2000; Dunne & Eales, 2001; Vlahakis et al., 2005) they found that, when fitting flux measurements at 60, 100, 450 and 850 μm , that two dust components were required. The colder dust component had temperatures of \sim 20 K which leads to gas-to-dust ratios in agreement with those measured in the Milky Way. While SCUBA did provide long wavelength coverage of the dust SED of galaxies, it had limited sensitivity especially for observing low-redshift galaxies where emission peaks at a much shorter wavelength than the SCUBA bands.

1.4 THE HERSCHEL SPACE OBSERVATORY

The *Herschel Space Observatory* (Pilbratt et al., 2010) was launched on the 19th May 2009 at 13:12 UT and represented a major leap forward for the far infrared/sub-millimetre field. *Herschel* has a 3.5 m primary dish which is the largest mirror currently in space. The high sensitivity, resolution and large wavelength coverage make it invaluable for many studies of the ISM across many different areas of astronomy. On the 14th June 2009 the cryostat cover was opened providing first light for the instruments. The Science Demonstration Phase started in September 2009 and routine

observations began in the following December.

Herschel was first proposed in 1982 and was originally called the ‘Far Infrared and Sub-millimetre Telescope’ (FIRST) and was eventually accepted as an European Space Agency (ESA) cornerstone mission. The name was changed to *Herschel* in 2000 to recognise the 200th anniversary of the discovery of infrared radiation by William Herschel. The satellite has a modular design with two modules: the Extended Payload Module (EPLM) which houses the scientific payload (cryostat, optical bench, dish and sun shade), and the Service Module (SVM) which contains the warm electronics, power and attitude/orbital control. The mirror was the largest one that could fit within the limits of the Ariane 5 rocket used to launch the satellite (without using a folding mechanism which can lead to additional complications). The mirror is a significant improvement over the next largest FIR space mirror of *Spitzer* (0.85 m). The large mirror was possible as it is passively cooled, therefore it does not require large amounts of coolant. During the design phase many changes were made including lessons learnt from the *ISO* mission. One such change was the decision to operate *Herschel* at the second Lagrangian point (L2) approximately 1,500,000 km, from Earth. This ensures the Sun and the Earth are always close together on the sky ($< 40^\circ$) from the telescopes perspective. This makes it possible for the sunshade to shield the telescope from the emission of the Sun and Earth without large restrictions on the visibility of targets. Two disadvantages of using L2 are the long distance for communications and that no servicing of the observatory is possible. To allow for sufficient communication with the observatory the *Herschel* observing day consists of a 21-hour observing period and a three hour communication slot during which the data from the observations are downloaded and the programme for the new observing day is uploaded. The telescope itself remains at ~ 80 K and was designed with a low emissivity to prevent its own heat affecting observations.

To achieve a high sensitivity the detectors in the PACS and SPIRE instruments are cooled using a ^3He coolant down to 0.3 K. All three instruments have enclosures maintained at 1.7 K which contain the detector modules and final optics by direct connection to the ^4He tank (the HIFI detectors operate at 1.7 K). The boil-off gas from the helium tank cools the instrument cold focal place enclosures to ~ 4.5 K. When the coolant leaves the instruments it is used to cool the sun-shields surrounding the cryostat. The cryostat originally contained 2160 litres of coolant and burns-off He at a rate of 2 mg s^{-1} , about half that of ISO. The dependence on liquid He limits the life of the observatory. The minimum design requirements were for three years of scientific observations and the latest measurements suggest that the helium will run out after ~ 3.5 years. Unlike *Spitzer*, *Herschel* will have no warm phase as all three

of the instruments require temperatures $\leq 1.7\text{ K}$ to operate and the instruments are expected to reach 50 K temperatures within a few hours.

Herschel covers the entire wavelength range between $60\text{--}680\,\mu\text{m}$ at diffraction limited resolution. While wavelengths less than $200\,\mu\text{m}$ have been covered by other space instruments, the high resolution and sensitivity of *Herschel* make possible much more detailed studies. The wavelength range between $200\text{--}680\,\mu\text{m}$ is only visible through certain atmospheric windows from the ground (e.g., SCUBA at $450\,\mu\text{m}$), but these ground-based observations had very poor sensitivities. ALMA will observe at both 350 and $450\,\mu\text{m}$ with high resolution but has a small field of view and will struggle to map large areas of sky. While balloon experiments can observe in this window (e.g., BLAST) they are limited to small observing slots and are still affected by the atmosphere (for example during the 2006 flight only six nearby galaxies were observed; Wiebe et al., 2009).

The pointing of the observatory is performed using a combination of gyroscopes and star-tracker cameras (*Herschel* Observer’s Manual, 2012). The gyroscopes provide very accurate measures of the telescopes’ angular rate of movement but only on short timescales. The two star-tracker cameras (one is only ever used at a time to reduce coolant consumption) each have a $16.4^\circ \times 16.4^\circ$ field of view and provides an absolute pointing reference. Combining the information from the gyroscopes and star-trackers provide the information required to perform observations. The design specification was to reach an absolute pointing accuracy of $3.7''$ and a relative pointing accuracy of $0.3''$. Since launch the absolute accuracy has been found to be $2''$ (Pilbratt et al., 2010).

Herschel has three instruments which are a mixture of broadband photometers and spectrometers. A description of each instrument and an outline of their science objectives is given below.

1.4.1 THE SPECTRAL AND PHOTOMETRIC IMAGING RECEIVER (SPIRE)

The Spectral and Photometric Imaging Receiver (SPIRE, Griffin et al., 2010) was specifically designed to investigate the poorly explored $200\text{--}700\,\mu\text{m}$ range and make full use of the potential capabilities of *Herschel*. SPIRE consists of an imaging photometer and medium resolution spectrometer. The instrument is kept at 4.5 K while the detectors are cooled to 0.3 K .

The photometer observes simultaneously in three bands centred at 250 , 350 and $500\,\mu\text{m}$ (each band with a $\lambda/\Delta\lambda \sim 3$). The detectors are feedhorn-coupled

bolometers arrays (for full information see Turner et al., 2001) with 139, 88, 43 spider-web bolometers in the 250, 350 and 500 μm arrays, respectively. In the *Herschel* data reduction pipeline and in this thesis the 250, 350 and 500 μm arrays are often referred to by PSW, PMW and PLW which stand for Photometer Short/Medium/Long Wavelength. The photometer has an $8' \times 4'$ field of view but a fixed pointing is not instantaneously fully sampled. To create a fully sampled map the instrument is scanned across the target area and continuous measurements taken (for more information see Section 2.2).

The photometer arrays reached the design sensitivity in the 250 and 500 μm band, and exceeded predictions for the 350 μm band by a factor of 1.5–2.0. The high sensitivity of SPIRE means that observations very quickly reach the confusion limit (where the instrumental noise is equal to the noise created by the overlapping signal of background galaxies) which has been estimated by Nguyen et al. (2010) as 5.8, 6.3 and 6.8 mJy/beam for the PSW, PMW and PLW band, respectively.

The ‘glitch’ (usually a single high-energy photon hit on the detectors) rate matches expectations for L2 at a solar minimum with a rate of 0.6, 0.7 and 1.5 glitches/detector/minute for the PSW, PMW and PLW arrays, respectively, leading to less than 1% loss in data. The SPIRE photometer modes are described in detail in Section 2.2, but the vast majority of observations use scan-maps where the array is scanned over the sky at either 30''/s or 60''/s. The scanning angle is chosen to give full spatial sampling and uniform coverage of the area observed. The SPIRE beams are diffraction limited and well fitted by a 2D-Gaussian to 15 dB; the full-width half maximum (FWHM) of the beams are given in Table 1.1.

The SPIRE spectrometer is a medium resolution ($\lambda/\Delta\lambda \sim 1300$ at 200 μm and ~ 370 at 670 μm) imaging Fourier transform spectrometer (FTS) which works in the range 194–671 μm . Two overlapping bolometer arrays cover the wavelength range with a 2.6' field of view and can reach a 5σ sensitivity of $\sim 1.5 \times 10^{-17} \text{ W m}^{-2}$ in a one hour observation. The observing modes for the spectrometer allow three different spectral resolutions (1.2, 7.2 and 25 GHz) and sparse, intermediate or fully sampled mapping (see SPIRE Observers’ Manual, 2011, for full details).

There are many science goals for SPIRE, especially as the 200–700 μm waveband is the least explored by previous instruments. The long wavelength coverage allows measurements of the coldest pre-stellar cores, the measurement of accurate dust masses in the local universe, as well as many other applications. FTS observations will expand our understanding of the chemical make up of the ISM with observations of a multitude of chemical lines including carbon monoxide and water lines.

Table 1.1
Point Spread Function FWHM for SPIRE and PACS Photometers

Instrument	Wavelength (μm)	Scan Rate (''/s)	Major Axis FWHM (''')	Minor Axis FWHM (''')	Ellipticity (%)
SPIRE	500	30/60	37.0	33.4	10.1
	350	30/60	24.7	23.2	6.6
	250	30/60	18.3	17.0	8.1
PACS	160	10	12.1	10.5	14.2
	160	20	12.1	10.7	12.3
	160	60	13.3	11.3	16.3
	160	60 (parallel)	15.7	11.6	30.0
	100	10	6.8	6.6	3.0
	100	20	6.9	6.7	2.9
	100	60	9.7	6.9	33.7
	100	60 (parallel)	12.7	7.0	57.9
	70	10	5.6	5.3	5.5
	70	20	5.8	5.5	5.3
	70	60	9.0	5.8	43.2
	70	60 (parallel)	12.2	5.9	69.6

Notes. The SPIRE values quoted are taken from SPIRE Observers’ Manual (2011) and are calculated on 1'' maps. The FWHM for larger pixel scales will be slightly larger (by approximately 5%). The PACS values are taken from PACS Observers’ Manual (2011) and more detailed information can be found in PACS Photometer Point Spread Function Document (2012).

1.4.2 THE PHOTODETECTOR ARRAY CAMERA AND SPECTROMETER (PACS)

The Photodetector Array Camera and Spectrometer (PACS, Poglitsch et al., 2010) is a photometer and medium resolution spectrometer covering the 60–210 μm regime. The photometer has three bands centred at 70, 100 and 160 μm (with $\lambda/\Delta\lambda \sim 2$), and can observe either the 70 or 100 μm band (blue channel) simultaneously with the 160 μm band (red channel). The field of view of the photometer is 3.5' \times 1.75' with 32 \times 16 pixels in the red array and 64 \times 32 pixels in the blue array. Each array is made up of 16 \times 16 pixel sub-arrays which are fully filled except for small gaps between sub-arrays. Each pixel corresponds to 3.2'' and 6.4'' on the sky for the blue and red band, respectively. The whole instrument is cooled to 3–5 K except for the detectors which are cooled to 0.3 K.

The photometer is diffraction limited and the beam widths for each band are given in Table 1.1. The detectors are read out at 40 Hz, but due to data-rate limitations of *Herschel*, four read-outs (frames) are averaged on board before the results are sent to Earth. For parallel mode the averaging is increased to eight frames (simultaneous SPIRE and PACS observations), which leads to beam smearing in the

scan-direction for fast scanning speeds. The photometer can be used in point-source chop-nod mode but is predominately used in scan-map mode, where $20''/\text{s}$ is the optimum scanning speed but 10 and $60''/\text{s}$ is also possible. The sensitivity of the photometer depends on the scanning strategy and target type but for a mini-map a 5σ instrumental noise of 4.7 , 5.5 and 10.5 mJy can be reached in one hour for point sources (see PACS Observers' Manual, 2011).

The spectrometer is a medium resolution spectrometer (with $\lambda/\Delta\lambda \sim 1000$ – 4000) and was particularly designed with extragalactic sources in mind. It is an imaging spectrometer with 5×5 spatial pixels, which covers an area of $47'' \times 47''$. The typical line sensitivity for the spectrometer is approximately $2.0 \times 10^{-18} \text{ W m}^{-2}$ (5σ / 1 h), and a variety of observing modes, including chop-nodding and raster mapping, are available.

PACS provides photometric observations of the peak of dust emission of galaxies in the nearby universe at high spatial resolution. The science case for PACS also includes the goal of mapping spectral lines in the FIR, including important C[II] and oxygen lines, in the Milky Way and local galaxies.

1.4.3 THE HERSCHEL-HETERODYNE INSTRUMENT FOR THE FAR-INFRARED (HIFI)

The *Herschel*-Heterodyne Instrument for the Far-Infrared (HIFI) is the high resolution spectrograph on board *Herschel* (de Graauw et al., 2010). The main aim when building HIFI was to have a spectrograph which had a high resolution but could observe over a large frequency range. HIFI has a frequency coverage between 480 – 1250 GHz (only $2 \times 4 \text{ GHz}$ instantaneously) with a resolving power of up to 10^7 (0.3 – 300 km/s) and a sensitivity close to the quantum-noise limit. HIFI, unlike PACS and SPIRE, has only a single spatial pixel, but maps can be made using either a series of pointings or on-the-fly mapping (for more information see HIFI Observers' Manual, 2011).

The main science objective of HIFI is to understand the interaction between stars and the ISM in galaxies (i.e., stars form from the ISM but also over their lifetimes enrich the ISM). HIFI makes possible the observation of many molecular rotational lines (including water) and fine-structure transition lines of atoms and ions in star-forming regions, proto-planetary disks, stellar winds and AGN toroids. The wealth of molecular lines is illustrated in Figure 1.9, a spectrum of the Orion nebula.

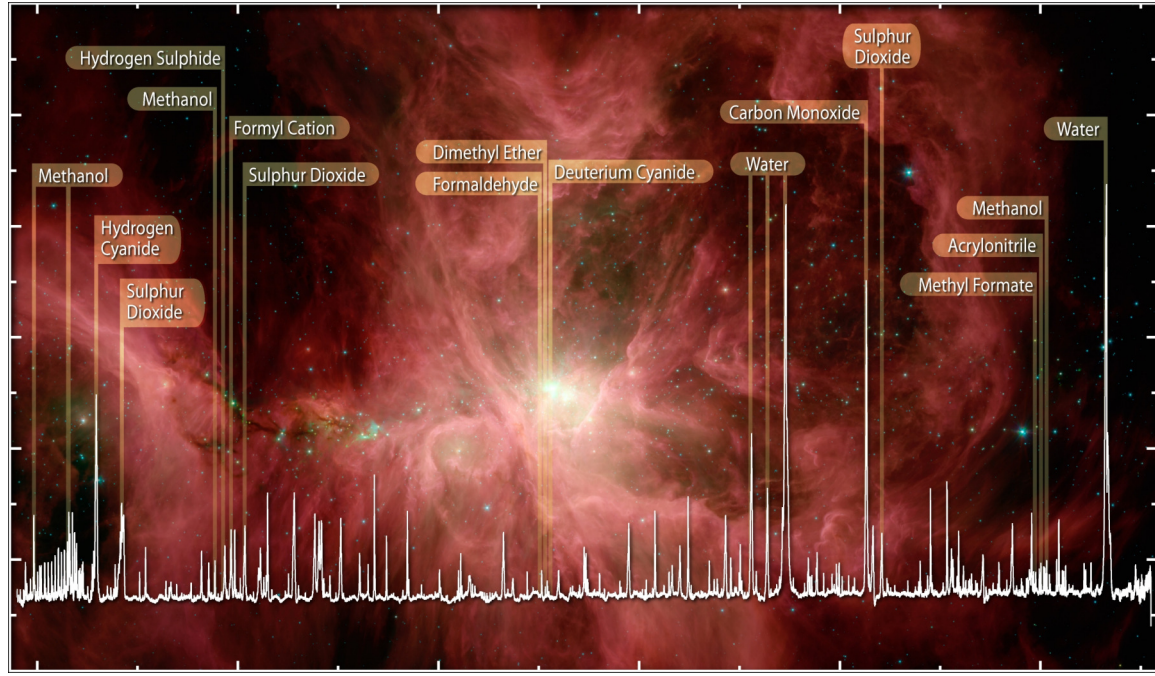


Figure 1.9. This image is a modified version of an ESA press release and shows a HIFI spectrum of water and organic molecules in the Orion Nebula. The background image is a colour composite of the region using *Spitzer* IRAC and MIPS images (Credit NASA). The HIFI data were obtained for the HEXOS and HIFI consortia.

1.5 THE HERSCHEL SURVEYS

In this section I describe the observing strategy and science goals of the main *Herschel* surveys that I have used during my PhD. The surveys are a mix of guaranteed time (for institutions contributing towards the instruments) and open time. All the surveys make use of the BRIGADE pipeline (see Section 2.4) that I developed.

1.5.1 THE HERSCHEL REFERENCE SURVEY (HRS)

The Herschel Reference Survey (HRS) is a guaranteed time program to observe a statistically complete sample of 323 galaxies with SPIRE at 250, 350 and 500 μm . The sample of galaxies has two criteria. First, the galaxy must fall within the chosen volume: $15 < D < 25 \text{ Mpc}$; $|b| > 55^\circ$ (Boselli et al., 2010b). Second, the galaxy must be brighter than a limit in the near-IR K-band, for late-type spirals and irregulars $K_{Tot} \leq 12$ while for ellipticals and lenticulars $K_{Tot} \leq 8.7$. For detailed selection criteria see Boselli et al. (2010b).

The volume was chosen to cover a range of galactic environments (i.e., field and cluster) and to be at high galactic latitude to avoid galactic cirrus contaminating the observations. The K-band magnitude limit means the HRS is effectively limited

to galaxies with high stellar masses. The limit is more stringent for early-type galaxies as they contain a significantly lower amount of dust. The images are confusion limited and cover an area of the optical diameter of the galaxy for early-types and $1.5 \times$ the optical diameter for late-types. An example of a selection of observations spanning a range of morphological type is shown in Figure 1.10. Full details of the observing strategy are given in Subsection 2.2.1 and Appendix A shows the optical image and SPIRE images for every galaxy in the sample.

The main science goal of the HRS was to provide a statistical survey of dust in galaxies at zero redshift which could be used as a reference for higher redshift *Herschel* surveys. The aims of the survey were defined as follows:

- Trace the cold dust present in galaxies. Little is known about the mass, distribution or temperature of the cold dust in galaxies (<20 K). The SPIRE coverage of the HRS maps the cold dust for a diverse range of galaxies.
- Study the relation between dust and gas in galaxies. Dust has been suggested as a good tracer of the total gas content in galaxies (see Subsection 1.2.2). This can be tested and calibrated with the HRS by comparing gas measurements with our dust observations.
- Study the connection between dust emission and star-formation. Previous studies have created laws which relate the FIR luminosity with star-formation rates without having data at wavelengths larger than $160 \mu\text{m}$. The HRS can confirm and refine these relations.
- Study the relation between dust extinction and emission. *Herschel* observations tell us about the emission from dust; optical and UV images exist which allow us to compare the absorption and emission properties of dust.
- Study dust in elliptical galaxies. Very little is known about the dust in ellipticals, how much is present, where it forms and how long it survives.
- Estimate the local FIR/sub-millimetre luminosity function.
- Study the role of the environment on the evolution of galaxies. It is well known that the gas in galaxies can be affected by the cluster environment with many cluster galaxies containing less atomic gas than counterparts in the field. Whether the dust is affected as well as the gas is unknown, but can be answered with the HRS.

The HRS covers a large range of luminosities, environments and morphologies in a statistically complete sample. It is therefore a useful reference for any studies of nearby galaxies. The survey is complementary to that of the Very Nearby Galaxy Survey and KINGFISH (Kennicutt et al., 2011) which target closer or interesting objects but which are not part of a statistically complete sample.

1.5.2 THE HERSCHEL VIRGO CLUSTER SURVEY (HeViCS)

The Herschel Virgo Cluster Survey (HeViCS) is a project to map approximately 80 square degrees of the Virgo cluster. The observations are run in parallel mode (see Section 2.2) producing data at 100, 160, 250, 350 and 500 μm with a sensitivity dominated by the confusion noise in the SPIRE bands. The Virgo region was chosen as it is the nearest large cluster, making it an ideal target to investigate how the dust properties of galaxies change in a high density environment. Being a nearby cluster ($\sim 17 \text{ Mpc}$) it is also the subject of multiple observing campaigns at other wavelengths. For full details of the HeViCS observing strategy see Subsection 2.2.2.

The large number of local galaxies in the Virgo cluster means HeViCS has many similar science goals to the HRS (Section 1.5.1). However, unlike the HRS, HeViCS is a far-IR/sub-mm survey of the whole cluster and is not targeting galaxies selected in another band. The main science goals of HeViCS are:

- Investigate the intra-cluster medium (ICM). The ICM has long been known to be enriched with metals, which can only be formed from stars (Sanders & Fabian, 2006; Werner et al., 2006) and indicates that outflows, tidal stripping and ram-pressure stripping can transport material out of a galaxy. Stickel et al. (2002) have previously detected intracluster dust in the Coma cluster using ISO measurements. HeViCS aims to measure the amount of dust present in the ICM.
- Search for the cold dust in the outskirts of galaxies.
- Estimate the FIR/sub-millimetre luminosity function in a cluster.
- Model the UV to sub-millimetre spectral energy distribution (SED) of galaxies.
- Search for dust in dE and low surface brightness galaxies. Historically low surface brightness galaxies (LSBG) and dwarf galaxies with low star-formation rates and metallicites were believed to contain little or no dust. However, recent

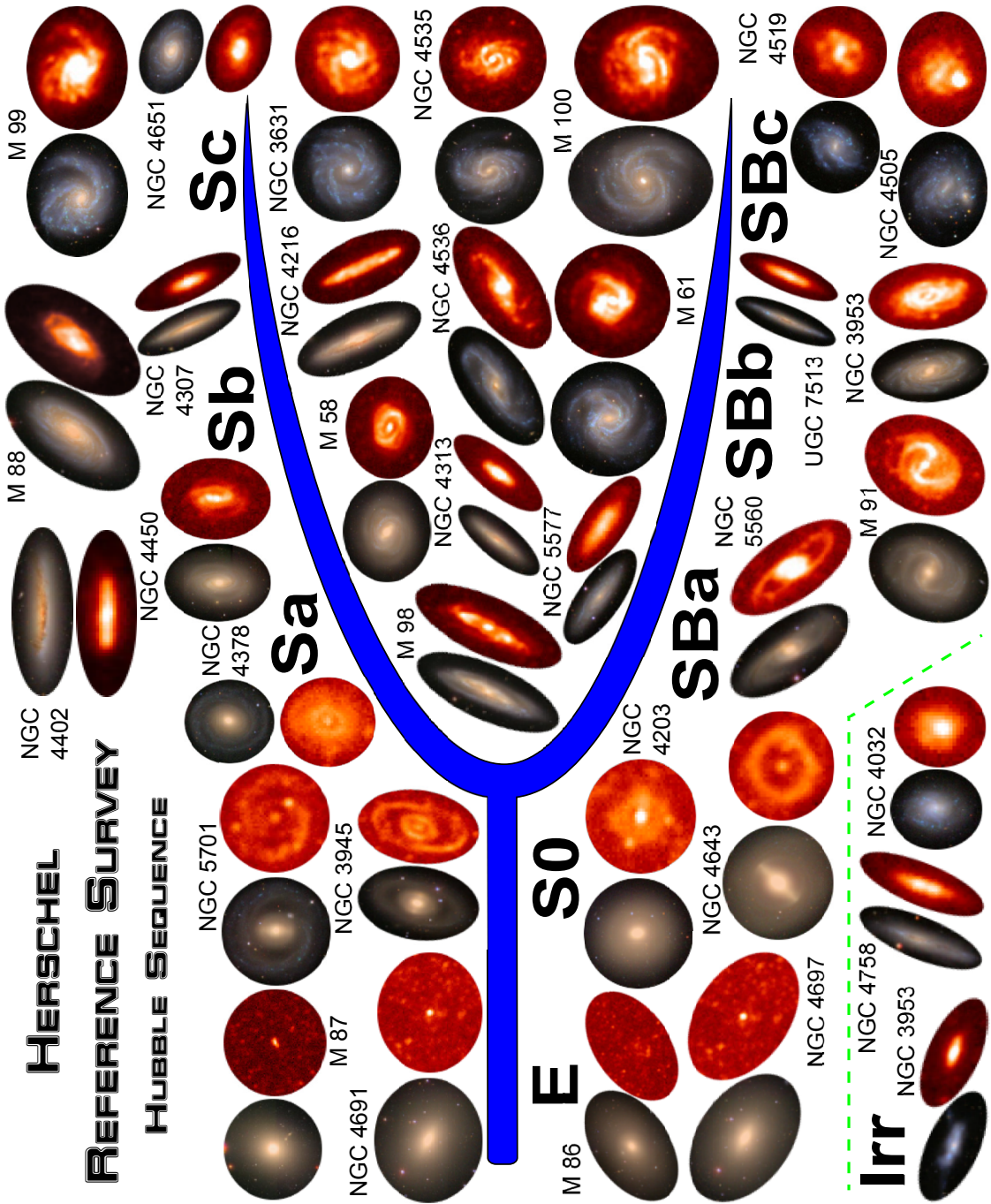


Figure 1.10. An image showing a selection of objects from the Herschel Reference Survey split by morphology. For each galaxy an optical SDSS image (left or top) and a 250 μm SPIRE image (right or bottom) are shown. The full HRS sample contains 323 galaxies.

Spitzer results (Hinz et al., 2007) have shown that some of these objects can contain modest amounts of dust.

- Investigate dust in cluster irregular galaxies. Most studies of cold dust have concentrated on spiral galaxies. Irregular galaxies tend to be more gas-rich and have a lower metallicity. They therefore provide an interesting environment to investigate relationships between gas, dust and star-formation, an environment which may more closely resemble the conditions in the early Universe.
- Investigate the dust in cluster elliptical galaxies. While this is a shared goal with the HRS, HeViCS can extend the study to lower stellar masses as HeViCS is a blind survey and not K-band limited.

As the HRS covers the HeViCS region a data agreement was reached between the surveys to share the data for the HRS objects within the HeViCS fields. Due to the extra time made available the HeViCS team has also made $70\,\mu\text{m}$ observations with PACS of all the bright galaxies and made measurements of the $158\,\mu\text{m}$ C[II] and the $51.8\,\mu\text{m}$ O[III] line in Virgo dwarf galaxies.

1.5.3 THE HERSCHEL FORNAX CLUSTER SURVEY (HEFOCS)

The Herschel Fornax Cluster Survey (HeFoCS) is an extension of the HeViCS survey and shares the same science goals. The advantage of observing Fornax is the the cluster is much more dynamically evolved than Virgo. It is therefore likely that the processes that affect galaxies in the cluster environment will be even more prominent. With additional data from the Coma cluster (observed as part of H-ATLAS, see Sub-Section 1.5.5), how galaxies are affected by differences in the size and age of the cluster can begin to be probed.

1.5.4 THE HERSCHEL EXPLOITATION OF LOCAL GALAXY ANDROMEDA (HELGA)

The Herschel Exploitation of Local Galaxy Andromeda (HELGA) survey is a guaranteed time survey to map the entire region of M 31 in the range $100\text{--}500\,\mu\text{m}$. The field is chosen to cover a region of $5.5^\circ \times 2.5^\circ$, which is approximately a factor of five times larger than previous *Spitzer* surveys (Barmby et al., 2006; Gordon et al., 2006) and completes the missing spectral range between 160 and $500\,\mu\text{m}$ (see Subsection 2.2.3 for more details). This area encompasses the whole HI disk allowing us to trace

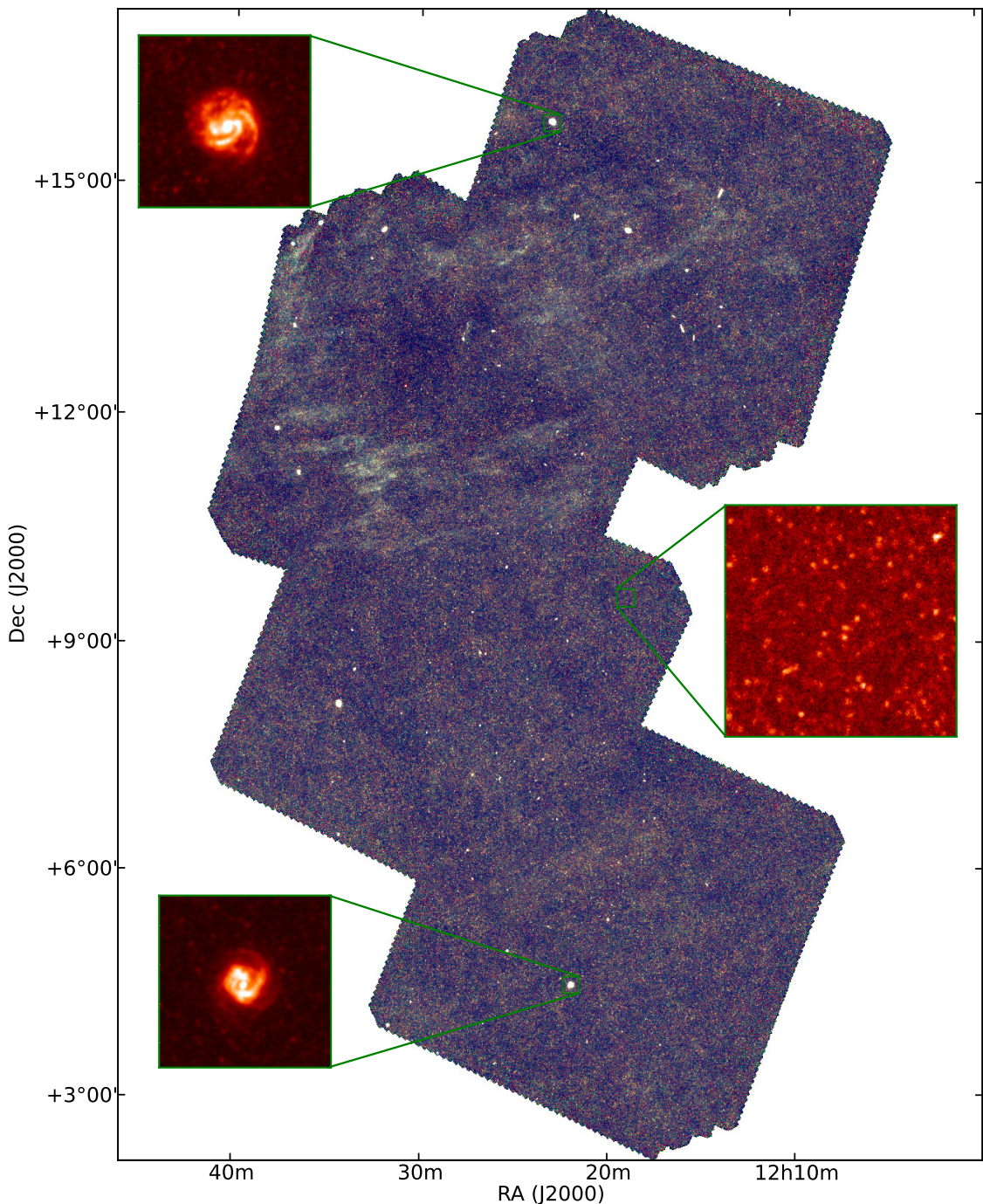


Figure 1.11. An image showing the The Herschel Virgo Cluster Survey (HeViCS). The color image is a SPIRE 3-color image with the 250, 350 and 500 μm band represented by blue, green and red, respectively. The zoom regions are taken from the 250 μm image. The survey covers an area ~ 84 square degrees. The image is orientated with North upwards and East to the left.

dust to the very outskirts of the galaxy (see Figure 1.12). The $250\,\mu\text{m}$ image from the HELGA survey is shown in Figure 1.12.

Andromeda is the closest spiral galaxy to the Milky Way; it has a disk approximately twice the scalelength of the Milky Way but is forming stars at a lower rate (Yin et al., 2009). At a distance of 785 kpc (McConnachie et al., 2005) at $100\,\mu\text{m}$ a spatial resolution of 48 pc is attained (this increases to 140 pc at $500\,\mu\text{m}$). Some images from the HELGA survey are shown in Figure 1.12 including some ancillary images from other observatories.

The *Spitzer* surveys lacked long wavelength coverage ($>160\,\mu\text{m}$) and resolution at FIR wavelengths. The HELGA survey makes it possible to trace the cold dust to large radii and provide high-resolution images of star-forming clumps at shorter wavelengths. *Planck* has produced dust images of the whole Milky Way with high-spatial resolution at $350\,\mu\text{m}$ to 3 mm. HELGA is the equivalent survey for Andromeda allowing in depth comparisons of the two galaxies. As well as the science goals the HELGA survey has been very successfully used for outreach and press-release images including a first live showing on BBC television.

1.5.5 OTHER CONNECTED HERSCHEL SURVEYS

In addition to the surveys listed above BRIGADE (Section 2.4) has been used to reduce all the SPIRE extra-galactic guaranteed time surveys which includes the Very Nearby Galaxy Survey (VNGS) and the Dwarf Galaxy Survey (DGS) as well as the Herschel Edge-On Galaxy Survey (HEROES).

1.6 THESIS OUTLINE

The main goal of this thesis is to exploit the new *Herschel* data to investigate dust in nearby galaxies. The new data allow us to investigate the cold dust in large samples of objects with higher sensitivity and greater resolution than ever before. The organisation of this thesis is as follows:

- Chapter 2 describes the standard SPIRE data pipeline and a custom SPIRE pipeline that I developed called BRIGADE.
- Chapter 3 discusses the optimal method for SPIRE photometry of galaxies and its application to the HRS. The second half of the chapter describes a fitting routine which provides the optimal method for fitting a dust model to the photometry for *Herschel* and other FIR instruments.

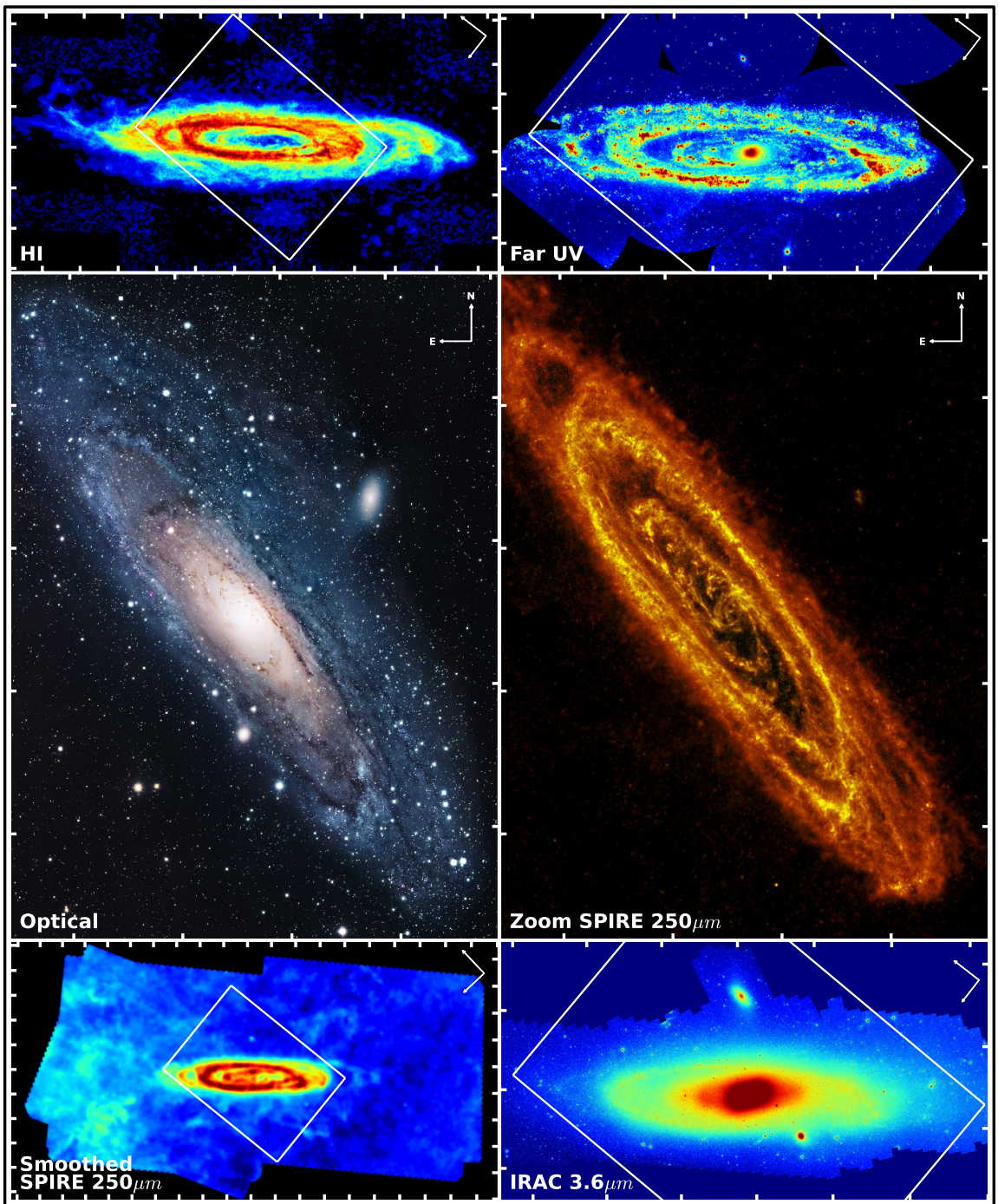


Figure 1.12. The Herschel Exploitation of Local Galaxy Andromeda Survey and ancillary images. The white rectangle in the top and bottom images show the area covered by the images in the middle row. The IRAC, HI and UV data are taken from Barmby et al. (2006); Braun et al. (2009); Martin & GALEX Team (2005), respectively.

- Chapter 4 presents the first dust analysis performed on *Herschel* which fits spectral energy distributions to every pixel of extended galaxies. This analysis was performed during the science demonstration period on three galaxies from the HeViCS survey.
- Chapter 5 describes the results of a dust analysis of Andromeda with \sim 140 kpc spatial resolution using data from the HELGA survey. The chapter discusses the properties and heating of the dust as well as a search for “dark gas”.
- Chapter 6 presents a study of the early-type galaxies in the HRS. The investigation includes a comparison of the dust with gas and the stellar properties of the object.
- Chapter 7 describes an investigation to try and detect the emission of dust outside the optical disk of a galaxy. This analysis uses data from the whole HRS sample rather than using individual objects.
- Chapter 8 summarises the main results from the entire thesis and describes some possible future investigations.

Parts of the work in this thesis have been used in three refereed astronomy journal articles; see Smith et al. (2010), Smith et al. (2012a) and Smith et al. (2012b).

CHAPTER 2

SPIRE DATA REDUCTION

“Where should we be if nobody tried to find out what lies beyond? Have you never wanted to look beyond the clouds and stars, to know what causes trees to bud and what changes darkness into light? But if you talk like that people call you crazy...”

Henry Frankenstein - “Frankenstein”

In this chapter I describe the method I developed to reduce extra-galactic SPIRE data called BRIGADE (see Section 2.4). Section 2.1 describes the *Herschel* data structures and Section 2.2 introduces the different types of SPIRE observing modes. The processing steps of the standard pipeline are described in Section 2.3 and Section 2.5 compares the standard pipeline and BRIGADE reduction methods. Sections 2.7–2.9 describes some additional processing steps.

2.1 INTRODUCTION TO HERSCHEL PROCESSING

The *Herschel* science centre automatically processes all *Herschel* observations with the standard pipeline when the data enters the archive. Many user scripts are provided by the Instrument Control Centres (ICCs) to optimise the pipelines for the observation mode, source type and latest developments. All *Herschel* data products are split into four levels which are:

- Level-0: This consists of the ‘raw’ data products with minimal processing.
- Level-1: At this level the data products have been processed so the instrument read-outs have been fully calibrated with minimal user interaction. For example at level-1 the SPIRE timelines have been converted from voltage to Jy/beam, with most of the instrument systematic effects removed.

- Level-2: The level-2 products are the normal output of the pipeline, on which scientific analysis of the data can be performed. Example products include images and data cubes.
- Level-3: These are publishable science products, usually provided by science users, where an analysis has been performed on the level-2 products. This could include catalogues, spectral line properties or line identifications.

More information on *Herschel* data products and the science archive can be found in the *Herschel* Observer’s Manual (2012). All data processing is performed within the *Herschel* Interactive Processing Environment (HIPE, Ott, 2010) which uses a combination of Java and Jython.

2.2 SPIRE PHOTOMETER OBSERVING MODES

The SPIRE photometer has three main observing templates. All of these templates are for all three bands (250, 350 and 500 μm) simultaneously. The three modes are large scan-map, small scan-map, and point-source jiggle mode. In addition to the SPIRE-only modes, the *Herschel Space Observatory* offers parallel mode where both PACS and SPIRE instruments observe simultaneously. A brief description of each observing mode is outlined below (a full description is available in the SPIRE Observers’ Manual, 2011) :

- **Point Source Mode:** The point source mode is designed to provide the most accurate flux measurement of bright isolated point sources (in the range 0.2–4.0 Jy). This mode uses a seven point jiggle pattern with a chop and nod throw. The lower limit of 0.2 Jy for the point source flux was chosen due to the likelihood of chopping or nodding onto a background source (likely as SPIRE observations tend to be confusion limited) which would dominate the uncertainties. For sources brighter than 4 Jy the uncertainty will be dominated by the pointing jitter.
- **Small Scan-Map:** This mode is used if the observer wants a map with a size of $4' \times 4'$ or less with uniform coverage over the observed area. The instrument is scanned across the designated area at $30''/\text{s}$ and is immediately followed by a cross scan. One cross-linked scan in SPIRE prime mode ($30''/\text{s}$) reaches an instrumental noise of 9.0, 7.5 and 10.8 mJy/beam (SPIRE Observers’ Manual, 2011) and can be observed in six minutes. This is repeated until the desired sensitivity is reached.

- **Large Scan-Map:** The large scan-map mode is used for SPIRE maps which have a width greater than $5'$. In this mode the telescope scans over the target (at either 30 or $60''/\text{s}$) with the length and number of adjacent scan-legs set by the desired area of the map. The default option includes a cross scan to help correct for $1/f$ noise, and the scanning pattern is repeated until the desired sensitivity is reached.
- **Parallel Mode:** In parallel mode observations are taken with PACS and SPIRE simultaneously providing measurements at 70 or $100, 160, 250, 350$ and $500\,\mu\text{m}$, scanning at either 20 or $60''/\text{s}$. Due to the different locations of the detectors in the focal plane there is approximately a $22'$ offset between the areas observed with PACS and SPIRE. Parallel mode is therefore most often used for large-area surveys, although it can be used for smaller areas. To account for the extra data load a lower sample rate is used for SPIRE; instead of the default $18.2\,\text{Hz}$ the sample rate is reduced to $10\,\text{Hz}$. This has a minimal effect on the quality of the SPIRE data. For PACS due to the on-board averaging there is a slight degradation of the PSF in the scan direction (worst for the fast scanning rate), often referred to as ‘beam smearing’.

The following subsections describe the observing strategies used by the *Herschel* surveys utilised in this thesis.

2.2.1 HRS OBSERVING STRATEGY

For each target in the HRS, apart from the early-type galaxies, the observing area is at least $1.5 \times D_{25}$ (where D_{25} is defined as the optical isophotal diameter corresponding to a brightness magnitude in the B-band of $25\,\text{mag}\,\text{arcsec}^{-2}$) with a minimum observing area of $\sim 4'$ set by the size of the small scan-map mode. For each galaxy three cross-scans are performed giving an instrumental 1σ sensitivity of $5.6, 5.7, 6.6\,\text{mJy}/\text{beam}$ ($0.57, 0.32$ and $0.18\,\text{MJy}/\text{sr}$) for the $250, 350$ and $500\,\mu\text{m}$ band, respectively. As early-type galaxies have significantly less dust, they were observed for longer with eight cross-scans giving a 1σ sensitivity of $3.5, 3.5$ and $4.1\,\text{mJy}/\text{beam}$ ($0.35, 0.20$ and $0.11\,\text{MJy}/\text{sr}$) for the $250, 350$ and $500\,\mu\text{m}$ band, respectively. To save observing time for the deeper early-type targets the observations are designed to map an area of $1.0 \times D_{25}$ as early-types are not expected to have dust outside the optical radii. Due to the sensitivity of SPIRE exceeding design specifications sensitivities for both sets of observations were lower than the confusion noise, which is $5.8, 6.3$ and $6.8\,\text{mJy}/\text{beam}$ for the $250, 350$ and $500\,\mu\text{m}$ band, respectively (Nguyen et al., 2010).

2.2.2 HEViCS AND HEFoCS OBSERVING STRATEGY

As HeViCS is a large-area survey, it uses parallel mode to obtain data at 100, 160, 250, 250 and 500 μm over a \sim 55 square degrees area. Due to rotation between observations a much larger area is observed (\sim 84 square degrees) but not at full sensitivity. The area was chosen to maximise the number of Virgo galaxies observed (750 Virgo galaxies lie within the HeViCS area) in a reasonable observing time. The total area is split into four tiles (as seen in Figure 1.11) each approximately $4^\circ \times 4^\circ$ in area. Each tile is observed by 8 separate scans at fast scanning rate (or 4 cross-scans) which results in an instrumental 1σ sensitivity of 23, 21, 4.9, 4.9 and 5.6 mJy/beam (11, 4.7, 0.50, 0.28 and 0.15 MJy/sr) at 100, 160, 250, 350 and 500 μm . The area covered by the observations can be seen in Figure 1.11. The HeFoCS survey uses a similar strategy to HeViCS except that only 4 scans were used on a single $4^\circ \times 4^\circ$ tile.

2.2.3 HELGA OBSERVING STRATEGY

The HELGA survey was designed to observe a large area around M31 and consists of two $3^\circ \times 2.5^\circ$ tiles each observed with one fast ($60''/\text{s}$) cross-scan in parallel mode. Each observation reaches a sensitivity of 120, 160, 9.7, 9.6, 11 mJy/beam (58, 35, 0.97, 0.54 and 0.30 MJy/sr) for the 100, 160, 250, 350 and 500 μm band, respectively. The observed area is shown in Figure 1.12.

2.3 THE STANDARD PIPELINE

This section aims to provide a brief overview of the standard pipeline for SPIRE scan-map mode and the main processing steps involved. A full description of all the processing modules can be found in the SPIRE Pipeline Description Document (2009) and The SPIRE Analogue Signal Chain and Photometer Detector Data Processing Pipeline (2009).

The *Herschel* pipeline uses two types of data structures: contexts and products. A context is a form of container that can hold other contexts or products and provides methods of accessing its contents. The most general context is the “observation context” which contains all the available data (science, calibration, etc) for a given observation. A product is a data structure that contains scientific data, for example a scan-leg timeline or calibration values.

2.3.1 RAW LEVEL-0 CREATION

The observing context which enters the start of the pipeline contains the raw level-0 data as well as a calibration context and an auxiliary context. The calibration context contains all the calibration data required based on the observing mode, although in most cases the calibration data can be substituted for the latest calibration contained within HIPE. The auxiliary context contains all the pointing information of the telescope needed to calculate the on-sky position of the SPIRE instrument.

2.3.2 ENGINEERING CONVERSION FROM LEVEL-0 TO LEVEL-0.5

At this stage in the pipeline the format of the raw level-0 data is converted into the standard SPIRE data products (the SPIRE ICC has termed this level-0.5). In the level-0.5 product a mask table is created to hold a mask for every sample in each channel (bolometer, thermistor, dark pixel, etc.), where each element is a 32-bit integer value. To allow several masks to be set simultaneously, each mask is associated with a different bit of the 32-bit integer. Whole channel masks are set at this stage for channels which should not be used, i.e., dead, noisy or slow bolometers (a full list of mask values are given in Table 2.1). Mask values are set at this stage if a cosmic ray hit is found on the Analogue-Digital Converter, or a truncation in the timeline is detected.

An exact time is then assigned to each sample and the samples re-ordered into chronological order. Currently no correction is made for delays between the readout of successive channels as this is believed to be small. The last few steps of level-0 to level-0.5 involve converting the channel read-out values to voltage and calculating the bolometer bath temperature.

2.3.3 TIMELINE PROCESSING: LEVEL-0.5 TO LEVEL-1

At level-0.5 the timelines now exist with the appropriate engineering conversions applied and are ready to be converted into scientifically useful data. A modified flow chart from SPIRE Pipeline Description Document (2009) is shown in Figure 2.1. The stages are:

- **Electrical Crosstalk:**

Electrical crosstalk can arise either from capacitive or inductive coupling between channels, or a strong signal on multiple bolometers causing a reduction in the array bolometer bias voltage. These affect the timelines as a signal

Table 2.1
SPIRE Mask Values

Bit	Value	Name	Description
0	1	MASTER	Indicates data should not be used.
1	2	INVALID_TIME	The sample time calculated is invalid
2	4	ADC_LATCH	Problem with the channel Analogue to Digital Converter.
3	8	TRUNCATED	The conversion has resulted in data being truncated (appears in channel timeline as flat line).
4	16	TRUNCATED_UNCORR	The truncation in the data (see previous mask) is unable to be corrected.
5	32	GLITCH	A glitch was detected in the sample.
6	64	GLITCH_UNCORR	A detected glitch has not been corrected.
7	128	ISDEAD	The channel is ‘dead’.
8	256	ISNOISY	The channel is ‘noisy’.
9	512	ISNOCHOPSKY	Indicates that the channel is not chopped to sky.
10	1024	VOLTAGE_OOL	The channel voltage is outside the fitted portion of the responsivity curve.
11	2048	GLITCH_FIRST_LEVEL	A glitch was detected in the sample during first level deglitching.
12	4096	GLITCH_FIRST_LEVEL_UNCORR	A first level glitch was detected ad not corrected.
13	8192	GLITCH_SECOND_LEVEL	A glitch was detected in the sample during second level deglitching.
14	16384	GLITCH_SECOND_LEVEL_UNCORR	A second level glitch was detected ad not corrected.
15	32768	ISSLOW	The sample is in a channel which has been identified as ‘slow’ (i.e., delay in responding).
16	65536	VOLTAGE_BELOW_K3	Voltage is lower than the ‘K3’ calibration factor.
17	131072	NO_RESP_DATA	No flux conversion is possible.
18	262144	TSIGNAL_HDV	Either the thermistor or dark pixels has a larger range of values than those excepted from thermal drift.

Notes. If either the MASTER, ISDEAD, ISNOISY, TRUNCATED, GLITCH_FIRST_LEVEL is set the sample is not used by the mapper.

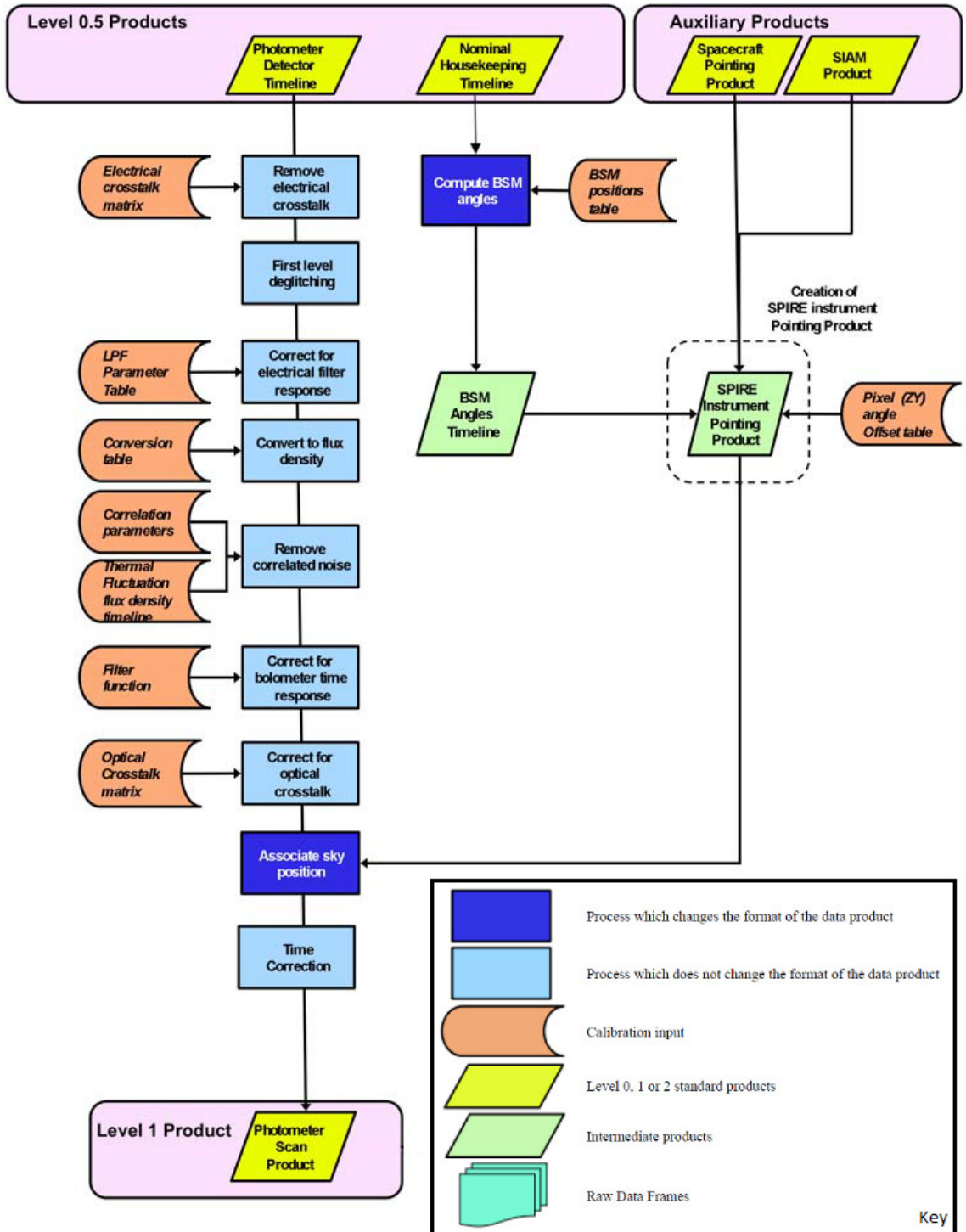


Figure 2.1. A flow chart showing the processing stages from Level-0.5 to Level-1 for a SPIRE scan-map. This figure is an adapted image of Figure 5 in SPIRE Pipeline Description Document (2009).

measured in one bolometer creates a ‘ghost’ signal in other channels. Currently no significant electrical cross talk has been measured between bolometers, but some crosstalk has been measured between bolometers and the array thermistors. For images of compact bright sources (e.g., Neptune) significant deviations in the background can be seen. To correct for this effect the channel voltages are multiplied by an electrical crosstalk matrix (which is close to the identity matrix as off diagonal terms are small) which removes this affect.

- **First Level Deglitching:**

The timelines of the channels can have artefacts which are usually caused by cosmic ray hits on the detectors. The first step is to run the ‘concurrent-GlitchDeglitcher’ module which searches for and removes glitches which affect all bolometers (in all arrays) simultaneously. To identify and remove glitches which affect a single bolometer there are two options, either the wavelet deglitcher (default) or the sigma-kappa deglitcher.

The wavelet deglitcher performs a complex analysis to identify glitches, by using a continuous wavelet transform with a Mexican Hat wavelet and a local regulatory analysis (assuming the glitch appears as a delta function). Full details on the wavelet method can be found in Ordénovic et al. (2008). An alternative to the wavelet deglitcher is the sigma-Kappa deglitcher which searches for a glitch by looking for samples above a specified threshold, which depends on the noise level. Both deglitching methods attempt to remove the glitch by linearly interpolating from the identified start to end of the glitch (these samples are recorded in the mask table).

While the wavelet deglitcher is recommended as the default deglitcher for SPIRE scan-map modes, recent tests I performed with HeViCS and tests carried out by the H-ATLAS team have shown that for parallel mode the sigma-kappa deglitcher currently performs better than the wavelet deglitcher.

- **Electrical Low Pass Filter Response Correction:**

The electronics of each array creates a delay which has to be corrected for to ensure the bolometer timelines and the pointing product match up. The correction accounts for the amplitude and phase effects and is the same for all bolometers.

- **Flux Conversion:**

At this stage the timelines are converted from voltage into units of Jy/beam. The calibration is constructed to provide correct monochromatic fluxes at 250, 350 and 500 μm if the source is a point source and has an SED satisfying $\nu F_\nu = \text{constant}$ (where ν is the frequency and F_ν is the flux density). The module checks that the input voltages are within the valid range of the values in the calibration table. If the voltage is not within the range a flag is raised inside the mask table.

- **Thermal Drift Correction:**

During the *Herschel* observing phase a module was developed to remove the influence of the ^3He fridge temperature variations on the timelines. As the bolometers essentially measure the changes in temperature caused by an incident astronomical signal, any fluctuations in the fridge temperature can affect the final maps by producing large scale gradients across the map. To correct for the thermal drifts, the module subtracts from the bolometer timeline a scaled thermistor timeline (scaling parameters are given in the calibration context) or dark pixel timeline if both thermistors are saturated. The thermistor/dark pixel timeline has the high frequency noise removed to ensure that extra noise is not added into the bolometer timelines from the subtraction.

- **Bolometer Time Response:**

The SPIRE photometer bolometers have been shown to have a response to astronomical signals with a time constant of ~ 6 ms. This effect is corrected by dividing the timeline with the bolometer transfer function in Fourier space. Even though evidence of an additional “slow-time” constant has been observed in glitch data, it is not clear if this is an optical effect (i.e., how the bolometers respond to an astronomical signal) or specifically related to how cosmic ray hits affect the detectors. The current pipeline, therefore, does not include a correction for a “slow-time” constant.

- **Optical Crosstalk Correction:**

Optical crosstalk occurs when a fraction of an astronomical signal falls on a bolometer other than its intended one. This is corrected in a similar manner to the electrical crosstalk, although in this case the diagonal elements of the correction matrix are non-unity as optical crosstalk results in loss of power from the primary bolometer. To date no optical crosstalk has been observed to occur within SPIRE.

- **Associate Sky Position:**

The associate sky position task assigns an absolute right-ascension (RA) and declination (DEC) to every sample in all the timelines. This correction is calculated from the beam steering mechanism (an adjustable mirror which adjusts the optical path allowing for chopping and “jiggling”), the array detector offset (i.e., separation of the bolometer from the reference position), the spacecraft pointing product and the time the sample was taken.

- **Time Correction:**

Due to some drifts of the on-board clock since launch a small correction is made to change the sample times to match International Atomic Time. This is done by comparing the time stamp on the transmitted data compared to the time the signal was received, corrected for the time taken for the transmission to travel from the spacecraft to earth.

2.3.4 FINAL PRODUCTS: LEVEL-1 TO LEVEL-2 PIPELINE

The default action for the pipeline is to perform a median baseline subtraction for each scan-leg on every bolometer. The subtraction results in all timelines having an approximate zero background (the SPIRE calibration is a relative not absolute value so the zero level could be set to any value). Options are also available in HIPE to remove a polynomial baseline rather than just a median and to define a region-of-interest which can be masked from these baseline subtraction methods.

At this stage the timelines are fully processed and ready for a map to be created. HIPE has two in-built mappers available to create maps of SPIRE data, the naïve mapper and MADmap (Cantalupo et al., 2010). The naïve map maker is the default for the SPIRE pipeline. The algorithm works by creating a pixel grid and then placing samples into the nearest pixels. The final pixel values are calculated by averaging the samples in each pixel. An error extension to the FITS file is created by calculating the uncertainty on the mean from the standard deviation of the samples assigned to that pixel. A coverage extension is also included to store the number of samples used for each pixel. If a particular pixel size or World Coordinate System (WCS) are required these can be passed to the mapper.

MADmap was originally designed to create maps of the CMB and is based on a maximum likelihood method. This has the advantage that all Fourier modes that are suppressed in the naïve mapper (i.e., in directions orthogonal to the scan direction) are included. There are two problems when applying MADmap as a default. First

MADmap requires an accurate understanding of the noise properties of the bolometers (although preliminary ones are available). Second, MADmap applies a high-pass filter to the data which requires bright or extended sources to be removed from the timeline before processing and then added back onto the map. Due to these complications the naïve mapper is used as the default in all observations.

2.4 BRIGHT GALAXY ADAPTION ELEMENT (BRIGADE)

The BRIGADE is a custom pipeline that I wrote to reduce level-1 data to the level-2 map product. BRIGADE was created as an optimal method to reduce extra-galactic observations and its main advantage is improved thermal drift correction and artefact removal (a complete comparison between the pipelines is performed in Section 2.5). In particular BRIGADE has the ability to deal with cooler ‘burps’, which is a rapid change in the array temperature and occurs every two days (an example is shown in Figure 2.7). Subsections 2.4.1–2.4.7 provide a description of the various stages in this pipeline.

2.4.1 COMBINING BUILDING BLOCKS

A building block is a single logical operation, such as configuring the instrument or science data collecting. Building blocks are combined to map an area of sky or repeated to give higher signal-to-noise. The first stage of the BRIGADE processing is to take all the building blocks (usually one scan-leg) which are initially kept separate by the initial pipeline processing and combine them into one continuous timeline for the whole observation. The point of this is that it makes it possible to produce a much better model of the thermal drifts affecting the arrays. For the subsequent processing steps an entire continuous timeline is used, and therefore data taken during the turn-around period (i.e., at the end of a scan leg the satellite slows and changes direction) is included in the processing and the final map. Tests by the SPIRE ICC and the H-ATLAS team have verified that there are no issues arising from using data taken during this period. Actually in some turn-around regions very deep data can be attained as the telescope is moving at a far slower rate than the scan rate requested.

At this stage the information on when the start and end of the nominal scan rate occurred is extracted from the level-1 meta-data for potential use in later stages. During the science demonstration phase (SDP) the observations can include Photometer-Calibration (P-CAL) measurements. In these periods no samples are measured from the bolometers, so when viewing the bolometer signal versus sample

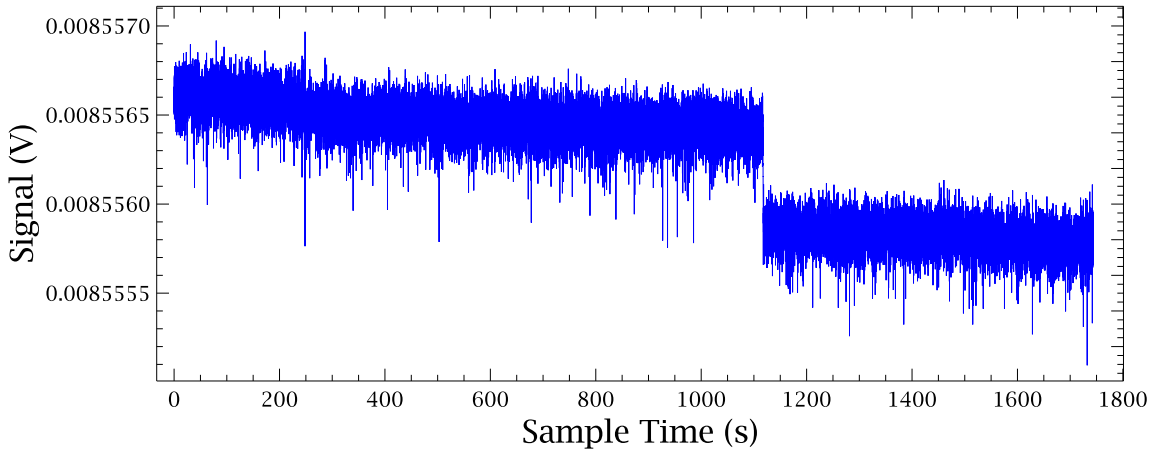


Figure 2.2. An example ‘jump’ from thermistor PSWT1 during an observation of M 100.

index an artificial step is observed. As the following steps require a continuous timeline, the BRIGADE script adds in the appropriate number of samples using a linear interpolation and artificial noise (these extra samples are removed before the maps are made).

2.4.2 ‘JUMP’ CORRECTION

The first stage of the process is to correct the thermistor (or dark pixel) timelines for ‘jumps’. These are instantaneous DC offsets which occur randomly in the timelines and have an unknown origin. An example is shown in Figure 2.2 although most are much less obvious. These have to be corrected because otherwise the thermal drift correction will create artefacts in the bolometer timelines. To find ‘jumps’ in the timelines for a large-area observation or a small set of observations I manually search through the timelines by exporting the data in binary format to a timeline viewer called Kst¹. Searching manually through large sets of observations would be far too time-consuming. Therefore to reduce the time required I wrote a program to output an image file of all the thermistor timelines. As large sets of images tend to be made up of short observations an image should reveal if a jump is present. Recently (2011) the SPIRE ICC have released an automatic thermistor ‘jump’ finder, although we still choose to look manually as the automatic method can miss small ‘jumps’ and does not correct the timeline. On average 19 thermistor ‘jumps’ are found per eight hour HeViCS observation.

¹Kst is a data visualising tool created by Barth Netterfield, for more information see <http://kstplot.kde.org/>.

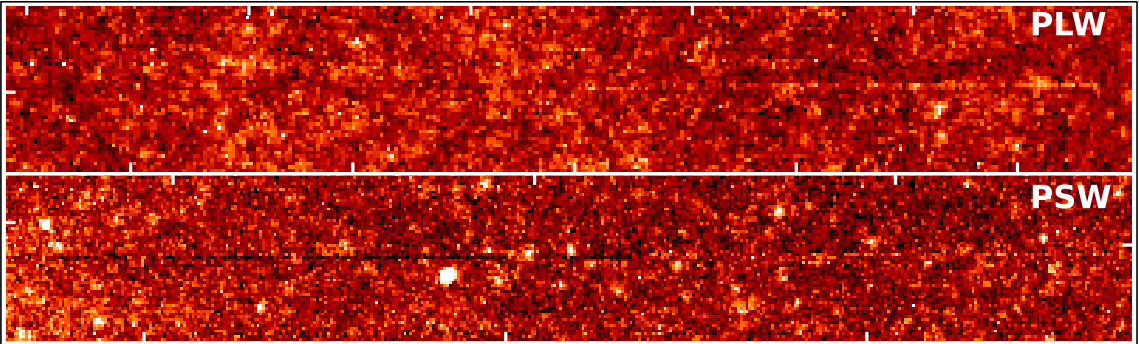


Figure 2.3. Two bolometer ‘jumps’ found in HeViCS observation ‘0x50088BC’ in the PSW and PLW array. The characteristic light or dark line can be seen in both panels. The tick spacing are in $6'$ intervals.

‘Jumps’ are not limited to just the thermistor timelines. They also occur in the bolometer timelines, luckily at a significantly lower rate than for the thermistors (~ 4 per eight hour HeViCS observation). Locating a bolometer ‘jump’ however is more challenging due to both the large number of bolometers and the real astronomical signal present in the timelines. To detect the bolometer ‘jumps’ we have to use the resultant maps and check for their presence on a map. As baseline subtraction methods aim to create a flat timeline, the ‘jump’ tends to create a negative and positive artefact on either side of the ‘jump’ (an example is shown in Figure 2.3). The bolometer ‘jumps’ are located using the procedure described in Subsection 2.4.7, and corrected using the same method as for the thermistor jumps.

Initially the ‘jumps’ were corrected in BRIGADE by calculating the average of 100 samples before and after the region identified as the ‘jump’. The difference between the averages was then subtracted from all samples following the ‘jump’. This method had the disadvantage that if the ‘jump’ occurred on a strong gradient then the correction could over-correct the ‘jump’. To solve this problem the offset in the sky is now calculated by fitting a linear model to 500 samples before the ‘jump’, and then extrapolating the linear fit to the 500 samples after the ‘jump’. The offset is then calculated as the average difference between the predicted model value and the sample value. The choice of 500 samples was found as a compromise between local variations and the larger scale gradients, but can be adjusted if necessary. As a ‘jump’ is not always instantaneous and can affect a number of samples, the region affected is replaced with artificial data. To achieve this the script uses the linear fit and adds a random value to each sample drawn from a normal distribution with mean of zero and standard deviation equivalent to timeline noise (estimated in the 500 preceding samples). To ensure our random noise is not used in either the thermal

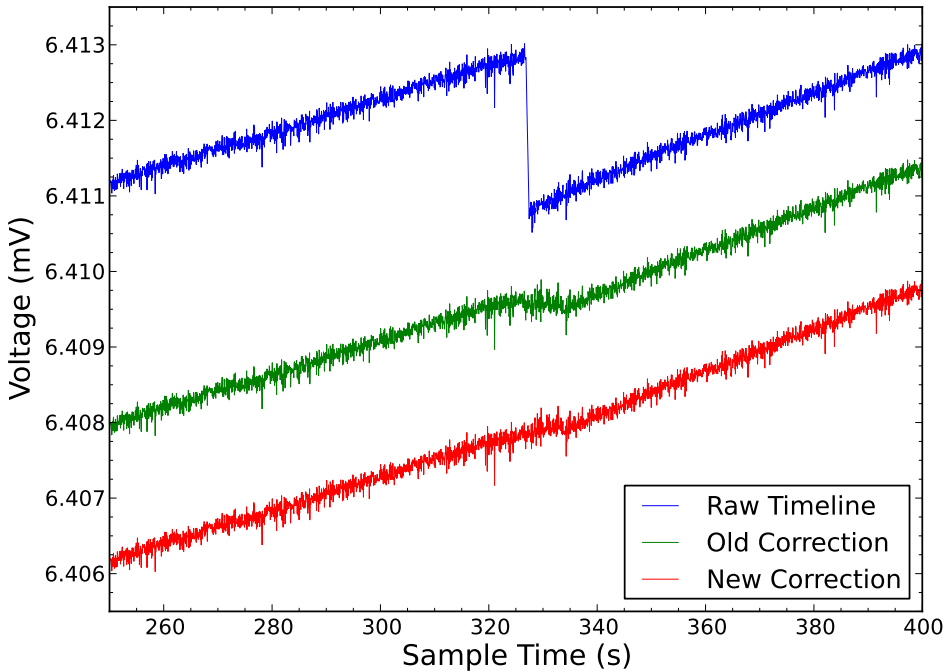


Figure 2.4. An example of ‘jump’ and the resulting timeline after correction. The blue shows the raw timeline, the green is the old correction method and the red shows the linear fitting correction. The old method illustrates that even with a mild gradient an offset remains. Each timeline was given an offset to prevent them overlapping.

drift correction or included in the final map we create a mask array to store these locations. An example jump and the old and new correction is shown in Figure 2.4

2.4.3 THERMAL DRIFT CORRECTION

At this stage most bolometer timelines are affected by the thermal drift of the ^3He fridge temperature, as bolometers essentially operate by measuring small changes in temperature. For example if the ^3He fridge slightly lowers in temperature, the resistance of the bolometer decreases which causes an increase in the output voltage (which is converted to Jy/beam). To correct for the thermal drift BRIGADE uses the information from the thermistors or dark pixels. Each array contains two thermistors which track the temperature of the array, and two dark pixels which are bolometers in the array but are not exposed to any astronomical signal. BRIGADE can use any combination of one or two thermistor/dark pixels to correct for the thermal drift. As a default, both thermistors are used. However thermistor-2 in the PMW² array has not been operational since launch, so instead for the PMW array as a default

²PSW, PMW and PLW are abbreviations for the Photometer Short/Medium/Long Wavelength array which observe at 250, 350 and 500 μm , respectively.

we use thermistor-1 and dark pixel-1. A choice of two thermistors/dark pixels is preferable as the channel that most closely matches the bolometer is used. This has the advantage that if any ‘jumps’ or other artefacts are missed in the thermistor/dark pixel timelines then the other channel will automatically be used. For observations with extreme ‘jumps’ or where the thermistor/dark pixel saturates we choose the best combination available.

To correct the thermal drift the following steps are taken:

1. Initial check

An initial check is performed to make sure our choice of thermistor and/or dark pixel is viable. On rare occasions a thermistor or dark pixel can saturate which will trigger the pipeline to set a mask value for the entire timeline. BRIGADE will alter your input choice to working thermistors/dark pixels and print a message to the screen.

2. Thermistor/Dark Pixel Glitch Interpolation

To ensure that no artefacts are added to the timelines during either low-pass or high-pass filtering stages we ensure that no ‘jumps’ or glitches are present in the thermistor/dark pixel timelines. While the standard pipeline does reconstruct glitches (as discussed in Subsection 2.3.3), the default glitch mask may be too small or other artefacts may need to be removed. To do this we fit a straight line to 250 samples before and after the masked area and replace the data with the linear fit with added noise (similar to Subsection 2.4.2).

3. Low-Pass Filtering of Thermistor/Dark Pixel Timeline

To stop introducing additional noise into the bolometer timelines when subtracting the baseline, a low-pass filter is applied to the thermistor/dark pixels. Before the filter is applied BRIGADE fits a fifth-order polynomial to the thermistor/dark pixel timeline and then subtracts this polynomial fit from the timeline, as gradients are not well represented in Fourier space. A 20 mHz low-pass filter is then applied and subsequently the fitted polynomial is added back to the timeline (both the baseline fitting and fast-Fourier transforms are executed with internal HIPE tasks).

4. Bolometer Check

Once the thermistor/dark pixel processing is completed the script loops over all bolometers in the current array. An initial check of the mask is carried out to ensure the bolometer is not ‘dead’ (certain bolometers have not been

functional since launch), ‘truncated’ or set by the pipeline as unusable. To avoid having to check the mask of each sample for the entire timeline, BRIGADE uses the same technique as the HIPE naïve mapper where just the first element of the timeline is checked. This is possible as the pipeline sets the masks for every element in the timeline if the bolometer is identified as being unusable. In addition we create a new mask array that controls which samples are used to calculate the thermal drift baseline to be removed (for convenience this is referred to as thermoMask). This mask is initially set to include all samples except for samples where a glitch has been identified, the channel is truncated or that are in a region that has been reconstructed (i.e., the centre of ‘jumps’).

5. Emission Masking

Before we apply the thermistor fitting we need to identify the regions of the timeline that have significant emission from sources. If we do not mask these regions from the timeline it can significantly bias the baseline removed, which can lead to significant artefacts on the map. This occurs as a bolometer in one location on the array may pass through a bright source leading to a higher fit while another bolometer may not. Figure 2.5 illustrates the difference on the calculated baseline that will be subtracted for the case when the source masking is not applied and when it is applied.

The first step to identifying the sources of the emission is to attempt a rough baseline subtraction. To do this we split the timeline into 5000 sample sections but with a 2000 sample overlap between sections to reduce boundary issues. A linear baseline is then subtracted from each region to create a rough baseline subtracted timeline. The noise in each bolometer is estimated from the standard deviation of the first and last 100 samples of the timeline. We then locate all peaks that are greater than 5σ , but limiting the list to one peak per 100 samples to avoid identifying multiple points of the same peak. A rough estimate of the position, amplitude and the standard deviation for each peak is recorded.

For each identified peak, a Gaussian is fitted to the data within ± 500 samples centred at the position of the initial guess. A check is performed to ensure the fitting produce has not returned a standard deviation that is too high (i.e., fitting temperature drift and not astronomical signal). The thermoMask is set so any sample within $\pm 10\sigma$ of the peak is not used in the thermistor fitting. An example of an identified peak and the region masked out is shown in Figure 2.6.

6. Thermistor/Dark Pixel Fitting

To fit the thermistor/dark pixel timeline to the bolometer timelines the script initially removes any samples that have been flagged (i.e., astronomical signal, glitches). The bolometer signal is then assumed to be a linear scaling of the thermistor/dark pixel signal. The scaling parameters between the bolometer and thermistor/dark pixel signal are found by minimising the χ^2 value. The default option for BRIGADE is to try two thermistors/dark pixels and use the thermistor/dark pixel which results in the lowest χ^2 value to create the baseline.

To remove the thermal drift there are two options (i): to fit the entire thermistor/dark pixel timeline to the bolometer timeline; (ii) to perform a separate fit for each scan. Both options are available as the linear correlation between the thermistor/dark pixel timelines breaks down for a long observation (e.g., large area parallel observations like HeViCS or H-ATLAS). For short observations, typical of most SAG2 surveys, the whole timeline is used, while for large area parallel-scan observations we perform the analysis scan-by-scan. For specific cases the exact length was adjusted to fit the observation, although the boundary between fitted regions is always kept in the middle of a turn around region (i.e., at end of a scan leg).

7. Baseline Subtraction

The baseline to be subtracted from the bolometer timelines is calculated by using the fitted coefficients calculated in Point 6 to appropriately scale the thermistor/dark pixel timeline. If the thermistor/dark pixel fitting is performed on a scan-by-scan basis the baseline is built up from each individual section. The baseline is then subtracted from the bolometer timeline to complete the thermal drift correction.

An example of the thermal drift correction for a timeline with large thermal drift correction is shown in Figure 2.7. Unlike the standard pipeline, after the BRIGADE thermal drift correction no further baseline subtraction is required.

2.4.4 HIGH PASS FILTERING?

BRIGADE as a default does not use any high-pass filtering, which surveys like H-ATLAS apply on a scale of 4° . The main reason for this is that instead of applying filtering, BRIGADE can apply the thermistor fitting on a scan-by-scan basis. Both methods effectively produce the same result as features on scales larger than scan-leg are suppressed. The choice of not applying filtering has the benefits that bright

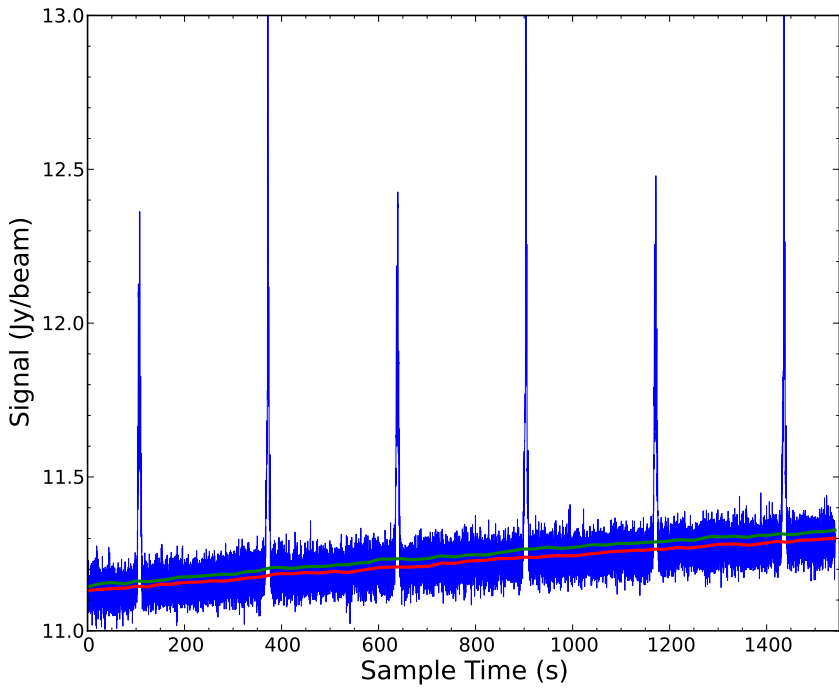


Figure 2.5. An example timeline of an observation with a bright central galaxy. The green line represents the baseline that would have been subtracted if the source was not masked. The red line shows the baseline to be removed with source masking, which is significantly offset from the green line and would be noticeable on the resultant map.

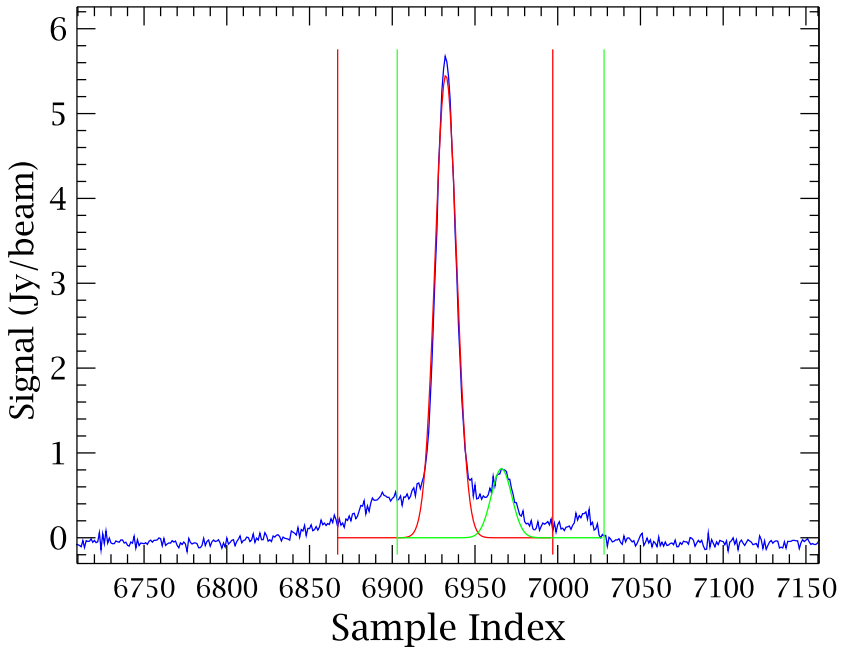


Figure 2.6. Example of a Gaussian fit to a peak found in the timeline, and the region automatically masked from the thermistor fitting (vertical lines). The best fit Gaussian is shown in red and green, and the bolometer timeline is shown in blue.

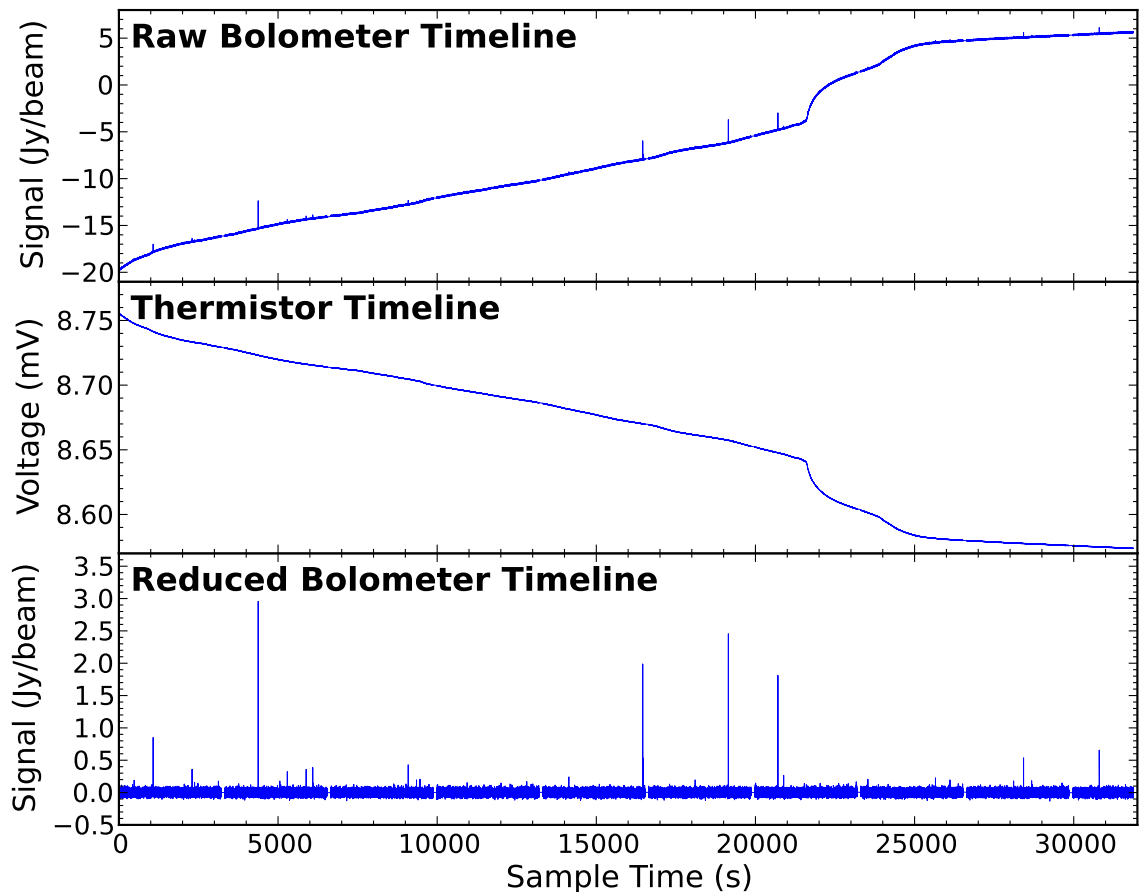


Figure 2.7. An example of a thermal drift correction on an large observation. The raw bolometer timeline (top) has had the thermal drift removed using the thermistor timeline (middle) to give the flat corrected timeline (bottom). The observation contains a cooler ‘burp’ with its characteristic change in temperature occurring at a Sample Time of ~ 21500 s.

sources do not have to be identified and removed from the timeline to prevent ‘ringing’ from the Fourier transform. This is less of an issue for H-ATLAS as the number of large extended galaxies is lower than, for example the HeViCS survey. In addition, by not filtering, no correction needs to be applied for any flux attenuation. BRIGADE does contain the ability to high-pass filter using the masks created in thermal drift correction (Subsection 2.4.3), but this is mainly used for trials of removing large-scale cirrus structures.

2.4.5 DE-STRIPER

An optional addition to the standard processing is the ICC de-striper. The de-striper is an algorithm which aims to reduce the residual offsets between bolometers and improve the map. The de-striper works by creating a preliminary map and for each bolometer creating an expected timeline for a bolometer from the pixel values in the map. The difference between the actual bolometer timeline and the expected timeline is found and an offset function (the user specifies the degree of polynomial) is fitted. This offset function is then subtracted from the actual bolometer timeline and a new map created and the whole process repeated for multiple iterations until the defined χ^2 threshold is reached. More information can be found at the de-striper website³.

The de-striper is in the vast majority of cases not used with BRIGADE for two reasons; first in most cases this additional step is not required, and the memory and processing time required for large surveys is prohibitory (making its use for surveys like HeViCS impossible). For a couple of Dwarf Galaxy Survey observations the de-striper is used in conjunction with BRIGADE to optimise the data reduction where there are very large and uneven cirrus clouds present in the image. In these cases the cirrus clouds can induce issues with the thermistor fitting, which the de-striper can correct for. An example of such an observation before and after the correction is shown in 2.8.

2.4.6 MAP MAKING

As mentioned in Subsection 2.3.4, there are two mapping modules available in HIPE, the naïve mapper and MADmap. As BRIGADE is mainly used for nearby galaxy surveys which contain bright and extended structures, the use of MADmap is difficult due to artefacts created when its inbuilt high-pass filtering applied. Work is

³De-striper Website: <https://nhscsci.ipac.caltech.edu/sc/index.php/Spire/PhotScanMapDestriper>

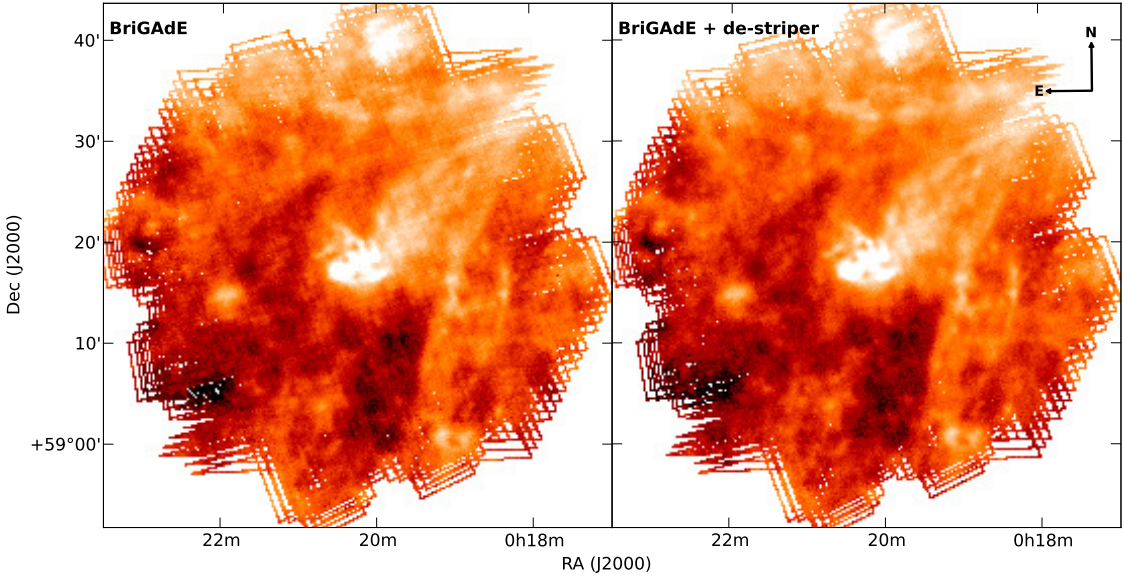


Figure 2.8. An observation of dwarf galaxy IC 0010 which is surrounded by heavy cirrus structure. The left hand image is a SPIRE 500 μm map reduced with the BRIGAdE pipeline which still exhibits some residual striping. The right hand image is the same image but with the de-striper added to the processing, in this image the striping is significantly reduced.

on-going as part of the H-ATLAS survey in checking the MADmap calibrations and applying MADmap to SPIRE data. Mosaics of several observations can be made by loading each observation into HIPE and passing all the data to the mapping function (for very large maps HIPE pools can be used to reduce memory usage).

The default pixel sizes for the SPIRE pipeline are 6, 10 and 14'' for the 250, 350 and 500 μm respectively. When I investigated the map-making methods for galaxies for the SPIRE Extragalactic Science team I also looked at the issue of pixel size. It was found that for virtually all observations a pixel scale of 6, 8, 12'' could be used without creating ‘NaN’ pixels (‘NaN’ pixels in SPIRE observations correspond to pixels where no sample falls in that region). I used this for making the maps of the HRS, HeViCS, HeFoCS, HELGA, Very Nearby Galaxy Survey, Dwarf Galaxy Survey and HEROES as for each band the pixel size is roughly equivalent to a third of the full-width half maximum (FWHM).

2.4.7 POST MAP-MAKING CHECKS

Once an observation has been processed, a check is made to look for two artefacts which are often present in large observations. This check is carried out before a mosaic of several observations is created, as artefacts in a single observation will

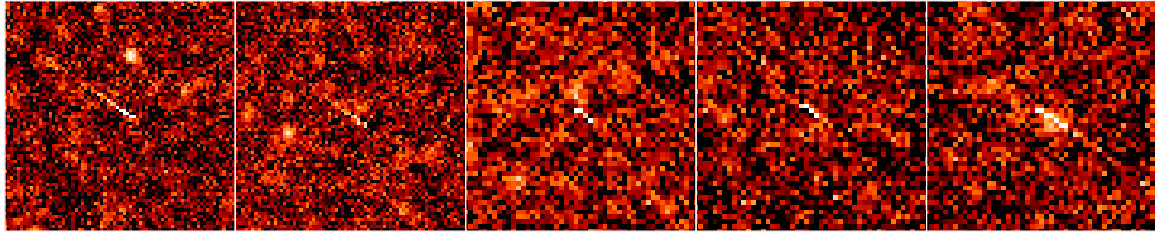


Figure 2.9. Five examples of glitch tails from an observation of the Fornax cluster (obsid:1342240276). The two left hand images are from the $350\mu\text{m}$ map and the three right hand images are from the $500\mu\text{m}$ map. Each image covers an area of $9.6'\times 9.6'$.

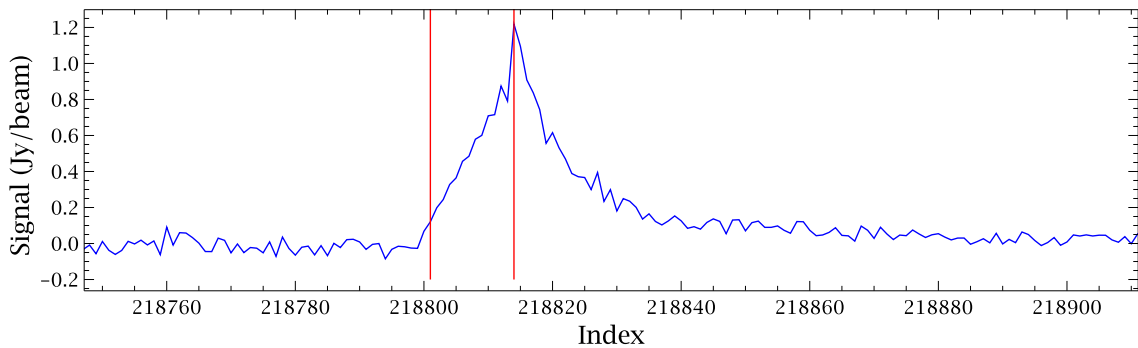


Figure 2.10. An example of a glitch tail in the timeline (left example in Figure 2.9). The region between the two red lines illustrate the region masked as a glitch and the pipelines reconstruction in that region. The tail visible on the map in Figure 2.9 results from the samples to the right of the second red line.

be less obvious when multiple observations are added together. Bolometer ‘jumps’, which have been mentioned in Subsection 2.4.2 can create artefacts seen in the map as shown by Figure 2.3. The second kind of artefact is referred to as a ‘glitch tail’. These originate from glitches that have been identified by the deglitcher but where all the samples affected by the glitch have not been corrected or masked. This occurs as the deglitcher corrects a fixed number of samples (early versions were limited to only seven samples) whereas a glitch can affect up to ~ 100 samples. Figure 2.9 shows how these tails appear in the map and Figure 2.10 illustrates the appearance in the bolometer timeline. Figure 2.10 clearly illustrates an initial region where the linear correction has been applied before the end of the glitch and then a ‘tail’ region where the bolometer signal gradually returns to the normal baseline level. To search for either of these artefacts before processing would be impossible to do manually due to the large number of bolometers and is difficult to automate due to confusion with real astronomical signal.

I wrote a script to find the positions of the glitch tails in the timelines. The script searches the whole observation for any bolometer which crosses a given map

pixel and plots a cut out of the resultant timelines.

For bolometer ‘jumps’ the correction is the same as for the thermistor ‘jumps’ as outlined in Subsection 2.4.2. The only difference is that for the centre of the ‘jumps’ the master mask value is set to stop the reconstructed area being used in the new map. To correct for the glitch ‘tails’ the GLITCH_FIRST_LEVEL mask is set in the region manually identified as resulting from the glitch; this also prevents those samples being used in the map-making. After this check the full processing is repeated as the artefacts could bias the thermal drift correction, although this affect is probably small.

2.5 COMPARISON WITH OTHER REDUCTION PIPELINES

2.5.1 SPIRE EXTRAGALACTIC SCIENCE TEAM REVIEW, JULY 2010

In July 2010, I took part in a review by the SPIRE Extragalactic Science Team to decide the best way of mapping galaxies. The observations carried out by the HRS, Very Nearby Galaxy Survey and Dwarf Galaxy Survey are predominantly relatively small SPIRE maps, covering only a single galaxy. The targets can vary from low-surface brightness extended galaxies to very bright point sources.

Map-Making Methods

For the map-making review all potential methods that existed at the time were compared on a ‘test’ sample of objects (Note, at the time of this review the standard pipeline did not include a thermal drift correction. A current comparison including this module is described in Subsection 2.5.2). The following map-making methods were examined:

- **HIPE based methods:**

- **BriGAdE**, as described in Section 2.4.
- **bc1**, standard pipeline with a scan-by-scan linear baseline removal using first and last 100 samples of each scan leg.
- **bd**, standard pipeline including subtracting a median value of the entire timeline.
- **bx(Y)**, standard pipeline including a polynomial baseline removal to the entire timeline, where the polynomial Y can vary from 0 to 5.

- **Non-HIPE based methods:**

- **SANEPIC**, method developed for BLAST (Patanchon et al., 2008). For this comparison maps were provided by Alexandre Beelen.
- **Scanamorphos**, method to build maps from bolometer arrays (Roussel, 2011). Hélène Roussel provided maps for this analysis.

In addition in this review, the effect of changing to a 6, 8, 12'' pixel size for the 250, 350 and 500 μm band, respectively, the use of a prototype de-striper and the choice of Naïve versus MADmap was investigated.

Test Observations

To compare the various map-making methods a sample of six observations were chosen that cover a wide variety of source emission and instrumental artefacts. The sources included are:

- **M 100**

M 100 is a typical galaxy from the HRS and was especially chosen for this comparison as by accident it was observed twice which makes it possible to test whether the map-making algorithm produces repeatable results.

- **M 82**

M 82 is a starburst galaxy from the Very Nearby Galaxy Survey and was included as it is the brightest galaxy observed in the science programme of the SPIRE Extragalactic Science Team.

- **M 91**

M 91 is an extended galaxy from the HRS and was chosen as it has a large extended structure but also contains a bright central source.

- **NGC 4565**

NGC 4565 is an edge on spiral from the HRS and is chosen as the observation was conducted during a cooler ‘burp’.

- **NGC 6822**

NGC 6822 is from the Dwarf Galaxy Survey and is included as the image contained large-scale structures.

These test objects are shown in Figure 2.11.

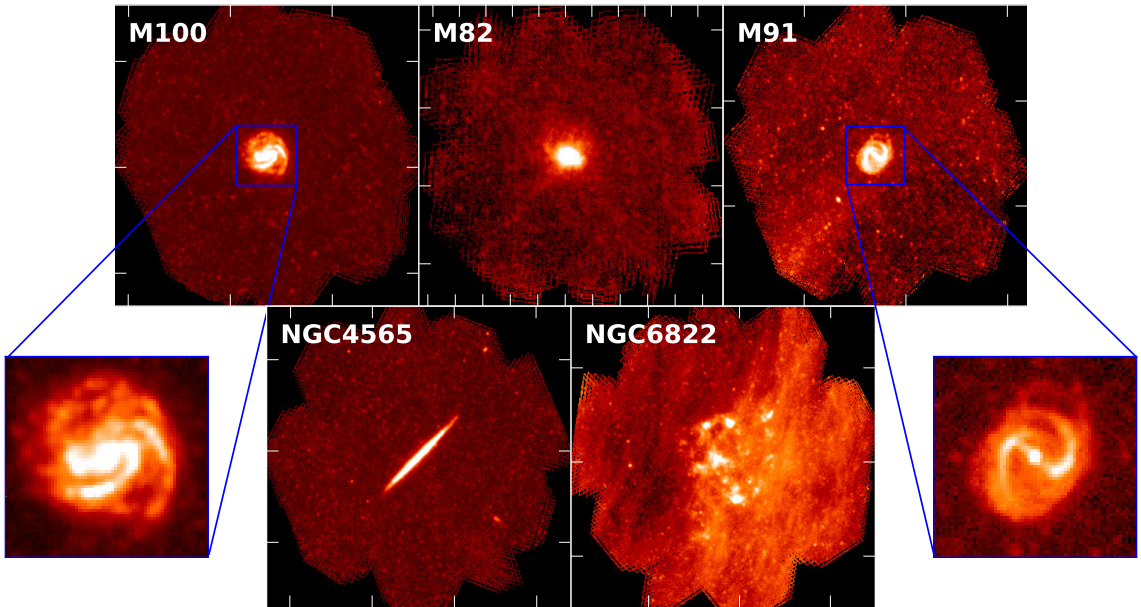


Figure 2.11. The galaxies used to compare different map-making methods available. The images shown have been reduced using the BRIGADE pipeline. The tick markings are at $12'$ intervals and are orientated with North upwards and East to the left.

Results

Overall most map-making methods produced good quality maps and often extreme examples were needed to highlight issues between the methods. The proposed pixel size of 6, 8, 12'' (see Subsection 2.5.1) was found to perform well in all the maps with no increase in NaN pixels.

When comparing MADmap maps with those made from the Naïve mapper it was found that MADmap did help reduce striping for methods which have artefacts in their equivalent naïve map. However as mentioned in Subsection 2.5.1, it was found that the high-pass filter MADmap applies creates significant artefacts on fields with bright galaxies. It was also found at the time that certain flags set by the mask were not being used by MADmap creating small stripes or dark artefacts in the map. Due to these issues it was decided to use the Naïve mapper as standard for SPIRE galaxy observations.

Similar to MADmap, the SANEPIC maps were found to contain artefacts from the strong sources in M 91 and M 100. For the brightest galaxy, M 82, a map could not be created with SANEPIC. Several HIPE methods produced background striping artefacts caused by known issues in Level-1 data, but the cooler ‘burp’ seemed to cause most difficulty. This is to be expected as polynomial or median baseline removal methods make the assumption that the thermal drift can be explained by a simple

Table 2.2
Comparison of Sky Noise Values

Galaxy	Method	Noise (mJy/Beam)		
		PSW	PMW	PLW
M 82	bc1-ds	10.5	9.9	10.9
	BRIGADE	11.1	10.0	10.9
	Scanamorphos	8.9	7.5	8.3
M 91	bc1-ds	8.8	8.8	10.8
	BRIGADE	9.0	7.5	11.0
	Scanamorphos	7.7	9.0	8.8
M 100	bc1-ds	13.3	9.8	14.0
	BRIGADE	13.1	9.4	13.4
	Scanamorphos	9.9	7.5	9.4
NGC 4565	bc1-ds	12.5	9.6	9.1
	BRIGADE	8.2	7.1	10.6
	Scanamorphos	7.3	7.1	7.7

function when the real fluctuations are more complicated. Due to the large artefacts, the bd, bx(0), bx(3) and bx(5) (with or without the de-striper) were rejected. The bc1 method with the de-striper applied, Scanamorphos and BRIGADE worked well for all observations.

Flux and Noise Values

For all maps tested, the global fluxes tend to vary between the various methods by ~ 0.5 , 1 and 3% for the PSW, PMW and PLW band, respectively (excluding extreme cases where the subtraction is bad). Bar graphs showing the difference in flux levels relative to BRIGADE flux are shown in Appendix B. These figures are hard to interpret as the ‘true’ flux is unknown. A potentially more informative test is to compare the returned fluxes from the two independent observations of M 100 and see which method is most consistent (see Figure B.1).

The fluxes were corrected for the background level and the noise was estimated from the standard deviation of the pixels in the background regions. Table 2.2 shows the noise values for the BRIGADE, Scanamorphos and bc1-ds methods using observations without excessive cirrus contamination. Both bc1-ds and BRIGADE methods give similar values while the Scanamorphos maps have a lower noise.

Table 2.3
Point Source Fitting Results

Band	Method	FWHM (")	Peak Fit (Jy/Beam)	Peak Pixel (Jy/Beam)
PSW	bc1-ds	26.428	1.794	1.951
	BRIGADE	26.409	1.793	1.943
	Scanamorphos	26.898	1.739	1.910
PMW	bc1-ds	32.645	1.047	1.076
	BRIGADE	32.713	1.048	1.073
	Scanamorphos	32.874	1.021	1.067
PLW	bc1-ds	44.161	0.600	0.633
	BRIGADE	44.149	0.600	0.619
	Scanamorphos	45.248	0.562	0.604

Point Source Fitting

To investigate the effect of the different map makers on point sources, we fitted a Gaussian to the brightest point source in NGC 6822 (the results are shown in Table 2.3). This shows that Scanamorphos maps have a $\sim 2\%$ larger PSF than the HIPE based methods and a $\sim 4\%$ lower peak flux (both fitted and peak pixel value). If a local background subtraction is included, the difference in the peak fluxes for the HIPE and Scanamorphos images increases to approximately 5% for the PSW and PMW, but differs by up to 16% for the PLW. The differences between the methods is most likely due to the difference in how Scanamorphos and the naïve mapper assign sample values to the map. The naïve mapper assigns the sample information to the nearest pixel, whereas Scanamorphos uses a ‘drizzle’ method. The ‘drizzling’ technique applies a weighted fraction of each sample to the pixels around the sample. This larger FWHM and lower peak value accounts for the lower background noise found in the Scanmorphos maps.

Final Choice

Three map-making methods were found to work well across all our test objects, BRIGADE, bc1-ds and Scanamorphos. Scanamorphos was not chosen as the ‘drizzling’ algorithm may not be appropriate for a feed horn array and the calibration of the SPIRE pipeline is based on the instantaneous position of the samples. In addition,

to reduce the data for the large sample of galaxies in the HRS, Very Nearby Galaxy Survey and the Dwarf Galaxy Survey, it was clear that a HIPE-based method would be easier to process. The bc1-ds method and BRIGADE were found to be very similar in most respects, the only appreciable difference found was for the NGC 6822 PLW image where some minor baseline subtraction artefacts were found in the bc1-ds map. A practical issue with the bc1-ds pipeline is at the time of this review the de-striper software took apparently \sim 1 hour per observation to process compared to \sim 3 minutes per observation for BRIGADE. In addition BRIGADE was the only technique with an existing way to deal with level-1 artefacts such as ‘jumps’. For these reasons, I used BRIGADE to produce the final maps for the HRS, Very Nearby Galaxy Survey, Dwarf Galaxy Survey, HELGA, HeViCS, HeFoCS and HEROES.

2.5.2 PRESENT DAY COMPARISON

Since this map-making review the standard pipeline has been updated to include a correction for thermal drift (as described in Subsection 2.3.3). The largest advantage of BRIGADE over the standard pipeline is in dealing with slow temperature variations which tend to affect long/large-area observations much more significantly than short observations. The advantage of BRIGADE over the current pipeline is still apparent. In Figure 2.12, there are significant artefacts on the image of the Fornax Cluster created with the standard pipeline compared with the BRIGADE map. Recent work by the SPIRE ICC has found the scaling constants used in the standard pipeline for the subtraction of the thermal drifts are different for regions affected by a ‘cooler burp’.⁴ As BRIGADE fits these constants for each observation or scan leg, rather than assuming the scaling values are fixed, it accounts for any potential changes.

2.6 SECOND ORDER DEGLITCHING

While the normal deglitcher picks up most glitches, a subset of glitches appear to exist which have a small amplitude and only exist for a very small number of samples (i.e., 1–3). These present themselves in a map as bright single pixels. Several codes are being developed that are based on the concept that by examining all the samples that go into an individual pixel, certain samples can be automatically flagged as outliers. This would reduce the impact of both these small glitches and the glitch

⁴Since submission a ‘cooler burp’ correction module has been implemented by the ICC. This in most cases (but not all) removes the most prominent artefact as seen in Figure 2.12. The slight striping toward the south-east of Figure 2.12 however is still present.

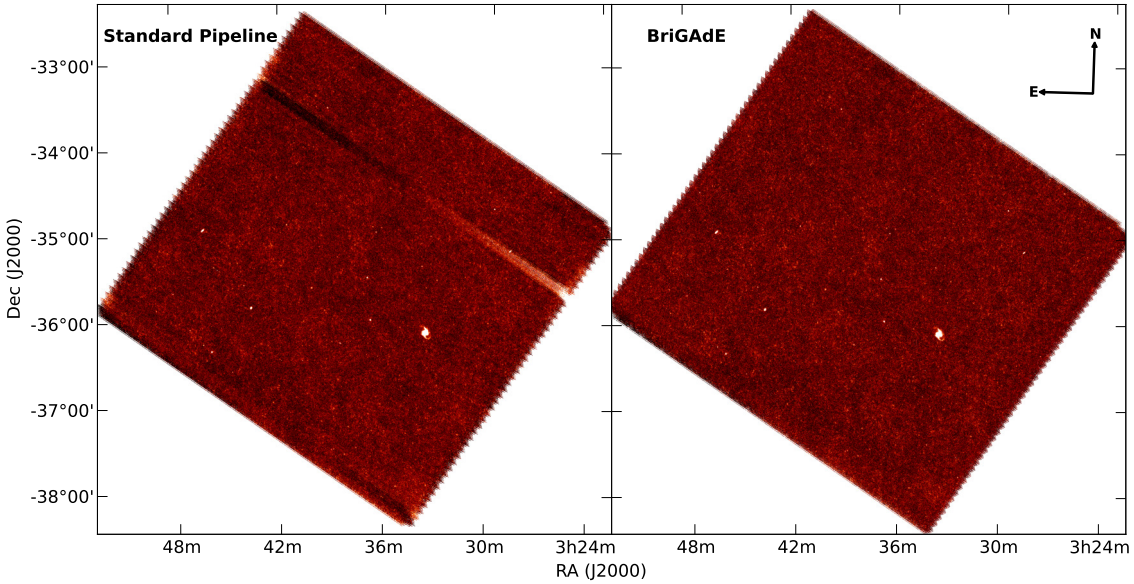


Figure 2.12. The left hand image shows an image created with the standard pipeline (HIPE developers build v8.0), while the right hand panel is the same observation reduced using the BriGAdE method. The standard pipeline reduction includes a large artefact from the cooler ‘burp’ and other artefacts towards the end of the observation. The observation is from the HeFoCS survey.

‘tails’. Observations that have greater depth (i.e., with more samples per pixel), would benefit most from this technique as it is easier to locate the outliers produced by glitches. The SPIRE ICC is intending to include this type of analysis within the de-striper module (see Subsection 2.4.5).

2.7 WCS ALIGNMENT

The *Herschel Space Observatory* has an absolute pointing error of $1.9''$ in pointing mode or $2.3''$ in scanning mode. However, significant fixed offsets between observations have been found to occur. These deviations are usually of the order of a few arcseconds and can lead to blurring of sources and larger uncertainties in the error map. I have developed two techniques which have been employed to correct for these offsets.

2.7.1 CROSS-CORRELATION METHOD

The cross-correlation method involves taking two $250\mu\text{m}$ maps which have the same co-ordinate system and shifting one map relative to the reference map by a whole number of pixels in each direction. For each shift the corresponding pixels in

each map are multiplied together and the sum of all pixels calculated. If there was no alignment between the maps and both maps have a mean of zero you would expect the output value to be zero. When all the features on the map are correctly aligned a maximum value of the function is returned. If the map is dominated by point sources then creating an image of the returned values should produce an image with a Gaussian peak. The offset between the images is therefore the distance between the centre of the fitted Gaussian relative to the original position before shifting. As a Gaussian is fitted to the data it allows for sub-pixel scale accuracy in the offset.

The first HIPE implementation of this method was written by SPIRE ICC member A. Papageorgiou, but I modified this to allow for a slope in the correlation image (which might occur due to large scale structure) and included the ability to split large-area observations into regions. Splitting into regions is also important to look for offsets that vary with position in the image. The advantage of this method is it is very easy and quick to apply; rotations are easily found and it uses all the information in the image. The disadvantages with this method are that, it is only a relative correction (i.e., it does not fix WCS to an external catalogue) and it does not work well when there is large-scale structures like cirrus clouds.

The main advantage of this method was realised for an H-ATLAS observation where the star-tracker (STR) was switched mid-observation. *Herschel* has two STRs; STR1 is the primary STR and is used for all observations. STR2 is only used if an error occurs with STR1, in which case the telescope automatically switches to STR2. A fixed offset in the WCS is known to exist between STRs which has to be corrected before two observations are combined. An additional problem is that STR2 is not cooled until it is switched on and in the cooling phase the returned pointing is incorrect. As the error depends on the temperature of the instrument, it is impossible to predict the size of this effect. In the H-ATLAS observation (obsid:1342211317) STR1 developed a fault during the observation and switched to STR2 which was initially warm. The corresponding cross-scan observation was then carried out with STR2 that had reached its operating temperature. I used my algorithm to measure the correlation between the first observation, during which STR1 developed the fault and the cross-scan. My method showed that the offset between STRs varied as STR2 was cooling down and Figure 2.13 illustrates the results. The northern part of the observation, made before the switch, has a fixed offset when compared to the cross-scan taken with STR2. When the switch occurs approximately two thirds into the observation, it can be seen initially there is a large discrepancy which gradually reduces as STR2 cools. As a result of my analysis, the H-ATLAS team carried out a repeat observation of the bottom third of the first scan.

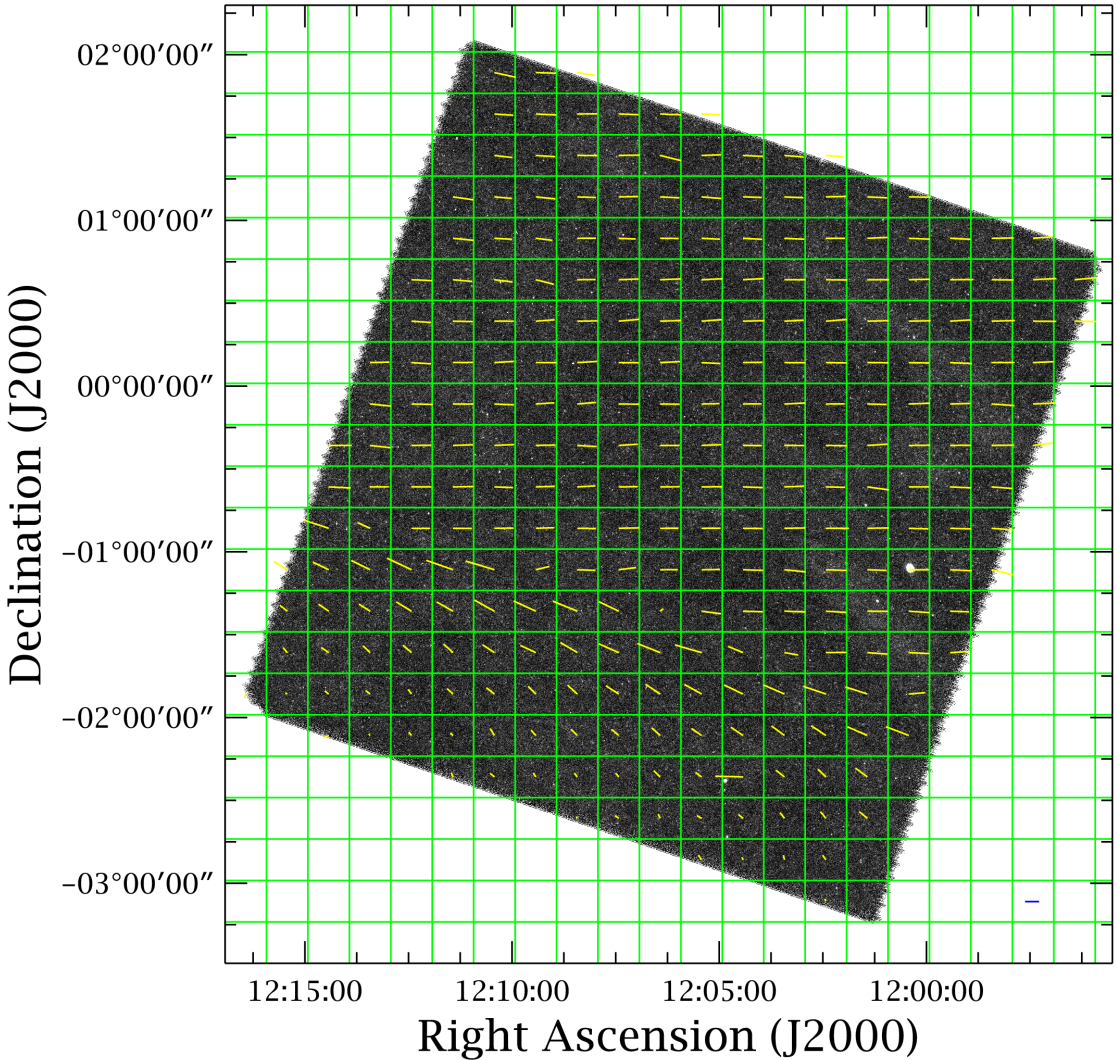


Figure 2.13. An example of the results produced by the cross-correlation method. The cross-correlation was performed separately within each green square. I have used the method to measure the offsets between the two cross-scan observations making an H-ATLAS image. During the first observation the default star tracker (STR1) failed and for the rest of the observation and the next observation, the back-up star tracker (STR2) was used. The direction and magnitude of the offset is represented by the yellow lines. For scale the blue bar in the bottom right corner represents an offset of $10''$. For the northern two thirds of the image the expected constant offset is found (from the known shift between the star trackers). When the STR switches the magnitude of the offset gradually decreases as the new STR cools until the end of the observation where no significant offset is found.

2.7.2 POINT SOURCE METHOD

The point source method requires you to select a population of bright point sources in the map, which have positions known from an external catalogue. For observations in the northern hemisphere, this external catalogue is often the SDSS. A disadvantage of this method is that the large sub-mm beam can result in several objects in the external catalogue being potentially associated with a single sub-mm source. For the HeViCS survey this problem is slightly reduced as the the bright point sources usually correspond to obvious Virgo galaxies. Chris Fuller and I wrote a script which compares the HeViCS point source catalogue for each observation and checks which sources are in common. A check is then made to find the SDSS source and then the offsets between the two observations are calculated and a histogram created for all the offsets.

The main advantage of this method is it allows a very precise measure of a fixed offset to be calculated and it determines the absolute pointing of the observation. As well as the identification problem mentioned, another downside is it requires more time and a few complicated steps. An example of the offset calculation between the eight scans making up one HeViCS image is shown in Figure 2.14.

2.8 ANDROMEDA: A SPECIAL CASE

In December 2010/January 2011 the HELGA team observed M 31 in parallel mode covering an area of $\sim 5.5^\circ \times 2.5^\circ$ centred on M 31. This presented a challenge in the data reduction due to the large size of the galaxy and the observing strategy used. To avoid any issues with the thermal drift correction in BRIGADE, I selected an elliptical region to cover the galaxy for a rough reduction of the data. Any samples which lie inside this region are automatically flagged and not used in the thermal drift correction. However, this leads to the problem due to the scanning strategy used. Figure 2.15 shows an IRAS 100 μm image with the Astronomical Observation Request (AOR) over-plotted (using HSpot⁵) showing the area covered and the scan directions. To observe the large area, the observing strategy was to split the observation into two halves, with each half covered by a cross-scan. For the scans which are parallel to the major axis, there is a problem as some of the scan-legs start or terminate inside the galaxy. If the thermal drift correction is then performed scan-by-scan a large fraction of the correction is being extrapolated. To avoid this BRIGADE was

⁵The *Herschel* Observing Planning Tool (HSpot) is an observation planning and visualising tool created by the *Herschel* Science Centre. For more information see <http://herschel.esac.esa.int/Docs/HSPOT/html/hspot-help.html>.

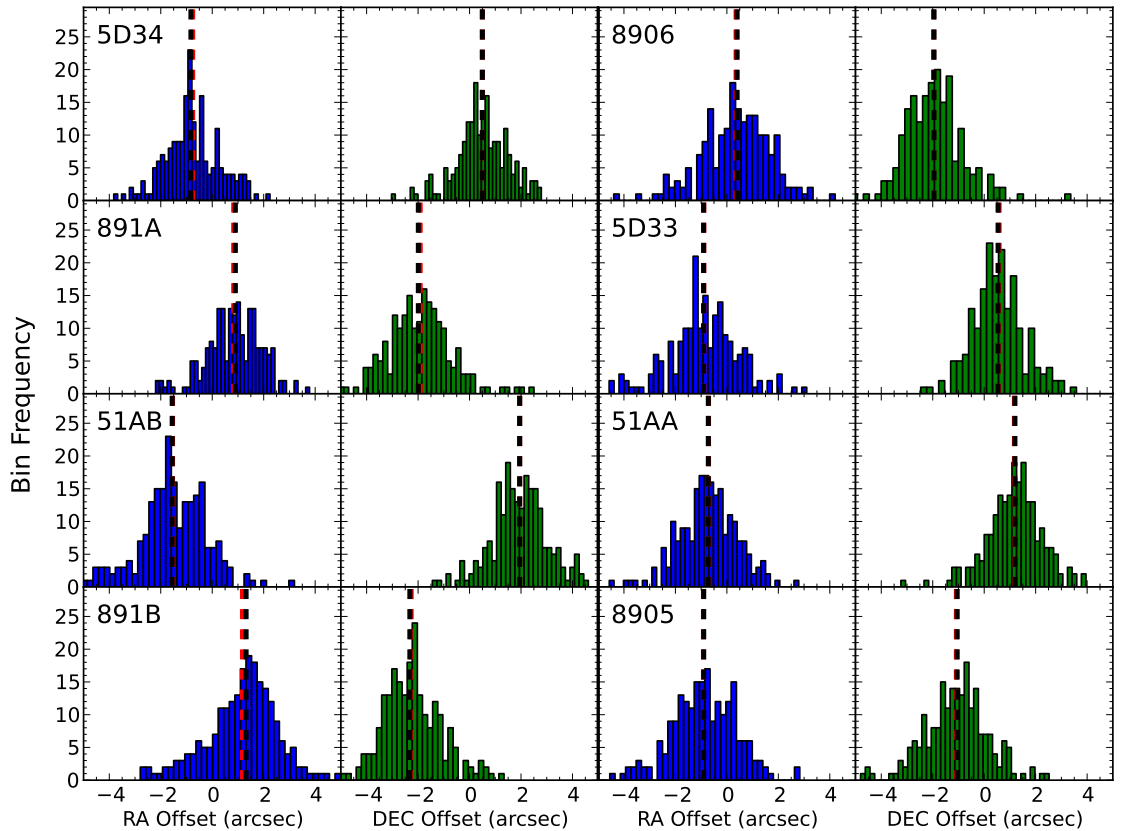


Figure 2.14. The offsets measured between each HeViCS observation and the optical SDSS positions for the eight observations that make up a single $4^\circ \times 4^\circ$ HeViCS image. The RA and DEC offsets are shown by the blue and green histograms respectively and the red and black lines show the mean and median values of the distribution, respectively. The last four digits of the obs-id in hexadecimal are given in the top left corner of each plot.

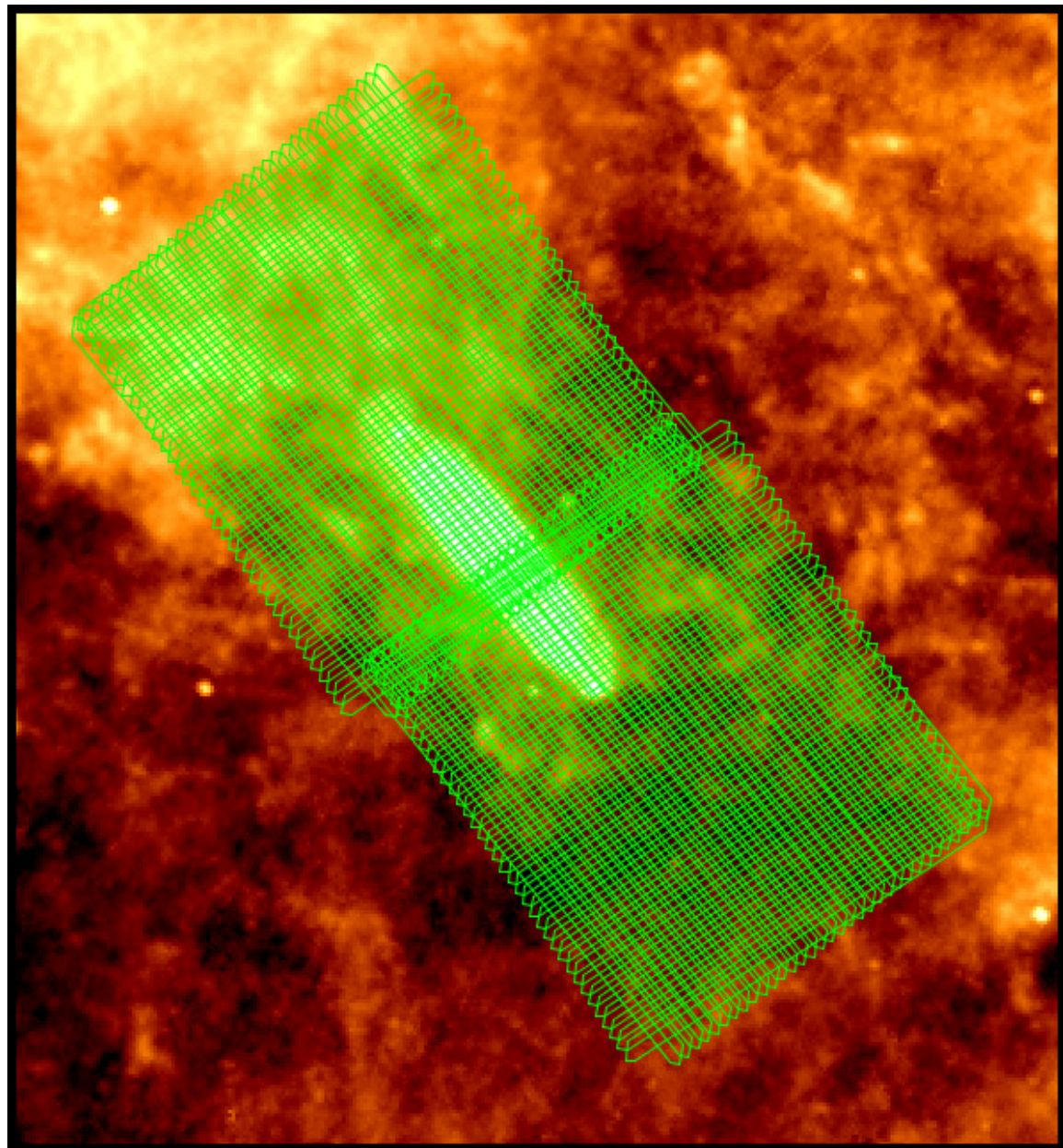


Figure 2.15. An IRAS $100\mu\text{m}$ image with the SPIRE AOR's overlaid in green. For clarity only every second scan-leg has been drawn. The image was created with HSpot, and is approximately $7^\circ \times 8^\circ$.

set to perform the correction every second scan so the beginning and end of each section is not in the galaxy. The thermal correction for the timeline inside the galaxy can then be interpolated from the correction found in the two surrounding regions of the timeline. For the scans perpendicular to the major axis there is no issue as no scan-legs terminate within M 31.

A second problem is caused in the northern half of the galaxy by the large amount of cirrus in this region. There is a north-south gradient in the cirrus structure, which was seen in the observations which ran along this scan direction. The perpendicular scans do not see this gradient as a scan-by-scan baseline subtraction is performed. Large cirrus structures can lead to problems with the thermal drift correction as mentioned in Subsection 2.4.5. To overcome these problems an unusual correction was applied; in addition to the BRIGADE masking an *IRAS* map was used to select a roughly constant level of emission (or cirrus) across the field. This selection was then used as a mask and the thermistor fitting was restricted to only samples in these regions. The choice of regions is somewhat subjective. Ideally one wants as narrow range of cirrus emission as possible but have enough samples to ensure an accurate thermal drift correction. For the north region of M 31 I chose the range of cirrus emission to be between 4–5 MJy/sr which corresponds to 40% of the pixels in the map). This effectively leads to a different zero level in the two halves of the map. To account for this an offset value was calculated from the regions that overlap between the two halves and added to the bolometer timelines of the northern half.

2.9 RELATIVE GAIN CORRECTIONS

The default SPIRE calibration is optimised for point source observations. Therefore corrections have to be made for observations of extended sources (this is discussed in greater detail in Section 3.3). Each bolometer has a slightly different point spread function (PSF) which is accounted for in the SPIRE calibration, but the normalisation changes if an extended source is present. These corrections do not significantly change the flux value of the pixels but do considerably lower the values in the Error extension for regions with extended emission. The Error extension is a map of the standard deviation of the samples that fall within each pixel. The effect of the relative gain corrections applied to an extended source can be seen in Figure 2.16. The relative gains are available inside HIPE from version 8 onwards.

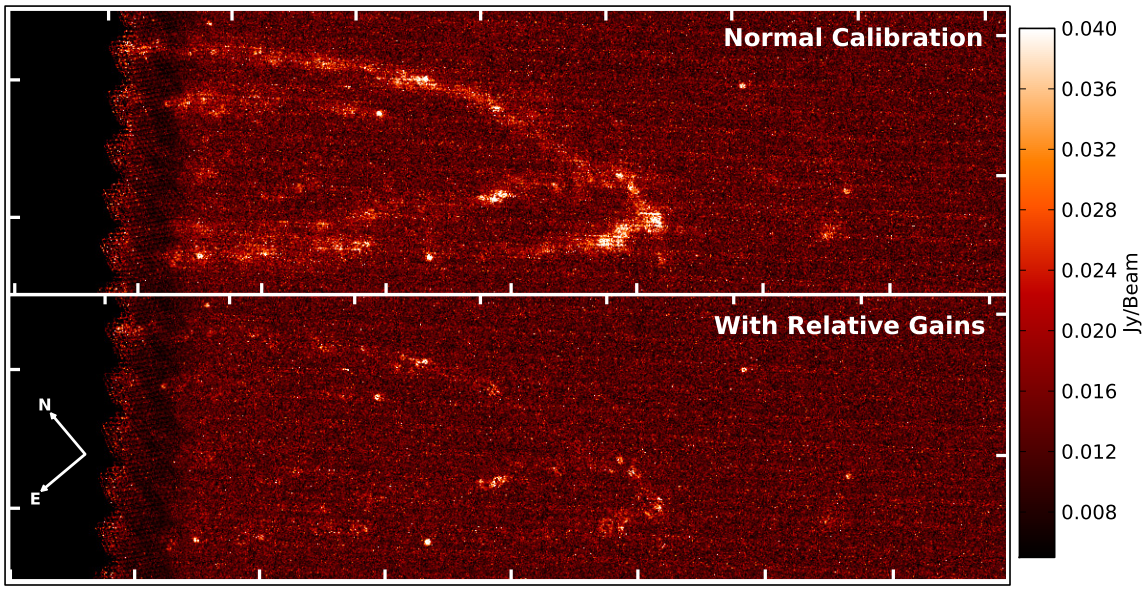


Figure 2.16. The effect of the relative gain corrections on the ‘error extension’ of a SPIRE 250 μm image. Both images are shown on the same colour scale. The top image clearly shows that with the normal calibration there is greater uncertainty for areas with extended emission than when the correct corrections are applied for extended emission (bottom).

2.10 SUMMARY

In this chapter an outline of the standard SPIRE photometer pipeline (HIPE developers build v8.0) and the BRIGADE pipeline has been made. BRIGADE is optimised for the reduction of extra-galactic data and in tests has performed well in comparisons to other available map-making methods. I used this method for the reduction of the SPIRE data for the HRS, Very Nearby Galaxy Survey, Dwarf Galaxy Survey, HELGA, HeViCS, HeFoCS and HEROES.

CHAPTER 3

SPIRE FLUX EXTRACTION AND SED FITTING

“Somewhere, something incredible is waiting to be known.”

Carl Sagan

3.1 INTRODUCTION TO SPIRE SOURCE EXTRACTION AND SED FITTING

This chapter introduces the main concepts and discusses the optimal method of measuring global flux values for galaxies from SPIRE data and fitting spectral energy distributions (SEDs). Extracting fluxes from SPIRE maps can be difficult as the observations are usually limited by the ‘confusion noise’ from galaxies in the FIR background. I developed the error analysis which was used in the photometry of the 323 galaxies in the Herschel Reference Survey (HRS). I also carried out photometry of all the HRS galaxies which was used to test and improve the final set of HRS fluxes produced by the Marseilles group (Ciesla et al., 2012). The program I developed to optimise the SED fitting with *Herschel* fluxes is discussed in Section 3.4.

3.2 POINT SOURCE FLUX EXTRACTION

There are three main methods for estimating fluxes for point sources from SPIRE maps: aperture photometry, map-based point source fitting and estimation of fluxes from the timelines. Both aperture photometry and map-based point source fitting are potentially affected by a pixel-size effect which leads to an underestimate of the global flux. This occurs as the SPIRE calibration is performed using the timelines,

but when making a map the pixel value is created from the average of the samples in that pixel area. Therefore the peak pixel flux is always lower than the real peak flux of the source. The correction factor for a source in the middle of the pixel is given by the SPIRE Observers' Manual (2011) as,

$$P = \frac{\pi}{4 \ln(2)} \left(\frac{\theta_{beam}}{\theta_{pix}} \right) \operatorname{erf}^2 \left[\frac{\theta_{pix}}{\theta_{beam}} [\ln(2)]^{\frac{1}{2}} \right], \quad (3.1)$$

where erf is the error function given by $\operatorname{erf}[x] = \frac{2}{\pi} \int_0^x e^{-t^2} dt$ and θ_{beam} is the symmetrical Gaussian full-width half maximum (FWHM) for that band and θ_{pix} is the pixel width. This correction is not perfect as it relies on the source being in the middle of the pixel and does not account for the source not being covered perfectly by the instrument (i.e., the bolometers may pass either side of the source or straight across the peak). The ICC have tested this correction with calibration observations of Neptune and γ Dra and found that the correction to the fluxes for the 250 and 350 μm data in Equation 3.1 gave good agreement with the fluxes from the timeline method no matter where the sources were positioned in the pixel. However, when comparing the 500 μm results it was found Equation 3.1 was inconsistent with the calibration observations. Instead an empirical relation was derived to be

$$P = 1 - 0.0018 \theta_{pix} - 0.00037 \theta_{pix}^2, \quad (3.2)$$

where θ_{pix} is the pixel size in arcseconds.

In addition for aperture photometry there is an additional ‘aperture correction’ term to account for emission that lies outside the aperture but is not visible due to the noise (both instrumental and confusion arising from background sources). This correction depends on the aperture size chosen and most attempts to correct for it rely on an empirical correction.

The third method to find point source fluxes is to fit the point source in the timeline data. This method for SPIRE data was developed by George Bendo of the SPIRE ICC and is now available within HIPE (sourceExtractorTimeline task). This method is the recommended method by the ICC as it avoids both issues with aperture photometry. The pixel averaging problem is avoided as the timeline fitter uses the right ascension and declination of each sample and no ‘aperture correction’ is needed as the flux is calculated from the best fit model. To use the timeline fitter an initial position is given to the task which then locates all samples in the surrounding region. A Gaussian plus a background is fitted to the data. The peak of the fitted Gaussian in the timeline is the total flux value of the point source.

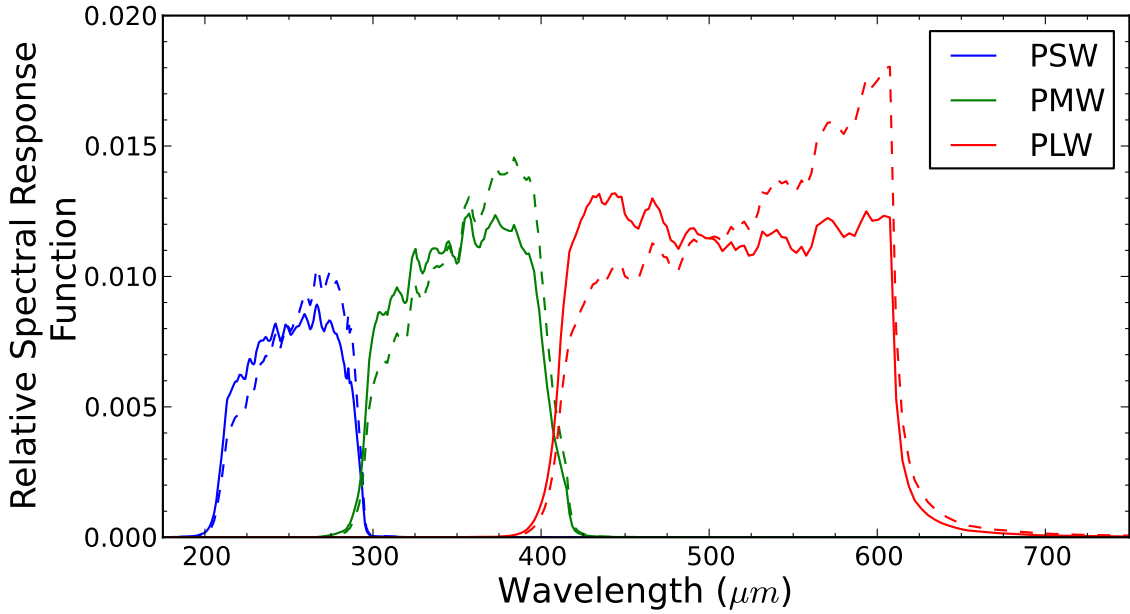


Figure 3.1. The relative spectral response functions (RSRF) for the SPIRE instrument in all three bands. The solid lines represents the profile for a point source and the dashed line is for an extended source. All the profiles have been normalised so the total response is equal to one.

Several options are available including the option of an elliptical Gaussian, options for different background methods and a choice of the maximum allowed width of the point source. By randomly adding point sources with varying brightness to confusion limited observations with the PSW array it is found this method can measure ~ 20 mJy point sources at the 3σ level.

The SPIRE pipeline is optimised for point sources. However, a color-correction needs to be applied to produce estimates of the monochromatic flux densities at 250, 350 and 500 μm . The color-correction accounts for the instrument filters and the slope of the SED across the filter. The filter profiles for the SPIRE bands are shown in Figure 3.1. The monochromatic flux values extracted from the maps are calibrated assuming a $\nu F_\nu = \text{constant}$ spectrum which is not typical of most extragalactic sources. The SPIRE Photometry Cookbook (2011) contains multiplicative corrections to correct for this effect and these values are given in Table 3.1.

3.2.1 CALCULATING POINT SOURCE UNCERTAINTIES

There are two main sources of uncertainty to account for when using the timeline source fitter. The first component is the uncertainty in the amplitude of the peak of the fitted Gaussian estimated by the fitting routine. The second component

Table 3.1
Multiplicative SPIRE Color Corrections

Spectral Index	PSW		PMW		PLW	
	Point	Extended	Point	Extended	Point	Extended
-4.000	0.9820	0.9303	0.9763	0.9306	0.9336	0.8562
-3.500	0.9902	0.9478	0.9852	0.9463	0.9530	0.8864
-3.000	0.9964	0.9626	0.9922	0.9605	0.9693	0.9144
-2.500	1.0005	0.9751	0.9973	0.9731	0.9823	0.9401
-2.000	1.0025	0.9855	1.0003	0.9839	0.9918	0.9631
-1.500	1.0023	0.9938	1.0012	0.9929	0.9978	0.9832
-1.000	1.0000	1.0000	1.0000	1.0000	1.0000	1.0000
-0.500	0.9955	1.0041	0.9967	1.0051	0.9986	1.0134
0.000	0.9888	1.0061	0.9913	1.0181	0.9935	1.0232
0.500	0.9801	1.0059	0.9839	1.0090	0.9849	1.0293
1.000	0.9692	1.0036	0.9744	1.0078	0.9729	1.0316
1.500	0.9564	0.9990	0.9630	1.0045	0.9577	1.0302
2.000	0.9417	0.9924	0.9498	0.9991	0.9395	1.0249
2.500	0.9252	0.9836	0.9347	0.9916	0.9186	1.0161
3.000	0.9070	0.9727	0.9180	0.9821	0.8952	1.0037
3.500	0.8873	0.9598	0.8997	0.9706	0.8698	0.9880
4.000	0.8662	0.9451	0.8800	0.9572	0.8424	0.9692

Notes. The columns are as follows. Column 1: the spectral index (α) where $F_\nu \propto \nu^\alpha$. Columns 2–7: the multiplicative color corrections for point and extended sources for each SPIRE band.

is the contribution to the uncertainty from the confusion of background sources. The values of the uncertainty produced by confusion can be found from the observation or can be taken from Nguyen et al. (2010) who found 5.8, 6.3, 6.8 mJy/beam.

3.3 EXTENDED SOURCES

The only method to estimate the flux of an extended source from a SPIRE image is aperture photometry. An aperture should be selected which covers all the emission of the galaxy but not too large that uncertainties in the background become significant. While a background correction may seem unnecessary for isolated extragalactic sources, given that the standard SPIRE pipelines gives a median of zero for the map, it is still advisable as there may be cirrus contamination, or artefacts present in the map, and even if the mean of the map is zero the background will not be precisely zero unless there are no objects in the map. Choosing a background region is often subjective as a balance must be struck between a large enough region that the statistical error in the estimate of the background is small, but having regions close enough to the galaxy to give good estimates of the background at the position of the galaxy.

The object flux can then be measured from an aperture using the formula

$$F_{\text{object}} = F_{\text{aperture}} - F_{\text{background}} \times \frac{N_{\text{aperture}}}{N_{\text{background}}}, \quad (3.3)$$

where the F_{object} is the measured flux of the object, F_{aperture} is the total emission in the aperture, and $F_{\text{background}}$ is the total flux in the background regions. The background is scaled by the number of pixels in the aperture (N_{aperture}) and the number of pixels in the background region $N_{\text{background}}$. For SPIRE maps the pixels have units of Jy/beam . The units can be converted into Jy/pixel using

$$F_{\text{Jy/pixel}} = F_{\text{Jy/beam}} \times \frac{\text{Area}_{\text{pixel}}}{\text{Area}_{\text{beam}}}, \quad (3.4)$$

where $\text{Area}_{\text{pixel}}$ is the area of the pixel and $\text{Area}_{\text{beam}}$ is the area of the beam.

Dale et al. (2012) for the KINGFISH survey (Kennicutt et al., 2011) also apply an aperture correction to account for emission that lies outside the aperture (e.g., low level emission from PSF smearing) but is hidden by the noise. They calculate these values empirically using *Spitzer* IRAC data to predict the distribution of flux at the longer wavelengths and find that typically the corrections are small, but can be up to a $\sim 10\%$ increase. Our Marseilles collaborators (Ciesla et al., 2012) investigated

this correction for the HRS photometry using simulated galaxies. They found for our typical aperture size the effect is typically less than 2%. As this value is a lot less than current calibration uncertainty (for more details see Section 3.3.2, Point I) we chose not to apply the correction to the HRS photometry.

3.3.1 EXTENDED SOURCE UNCERTAINTIES

To calculate the uncertainty on flux values for SPIRE maps I created a prescription to try and account for all the main sources of uncertainty. The sources of error are:

- 1. Calibration Error:** This can just be added as a fixed percentage of the flux value once measured. For more information on the calibration uncertainty see Subsection 3.3.2, Point I.
- 2. Instrumental Error:** The instrumental error is the uncertainty due to the sensitivity of the instrument and the number of samples contributing to a pixel. This noise is independent from pixel to pixel.
- 3. Confusion Error:** The confusion error is the uncertainty introduced by unresolved background galaxies (i.e., faint point sources). This tends to be a large problem for SPIRE images as the performance of the instrument means that with a very small number of scans the instrumental noise is less than the confusion. The confusion noise is correlated between neighbouring pixels.
- 4. Background Error:** The background regions have the same contributions from the instrumental and confusion errors as mentioned in Points 2 and 3. In addition there may also be an error from cirrus clouds or possibly residual thermal drift. The background region should be chosen to avoid obvious bright sources, and if a large enough area is used to estimate the background the effect of a faint source will be small.

The confusion noise is a problem as unlike the instrumental noise it is not independent from pixel to pixel (as the pixel size is smaller than the beam). I therefore decided to measure the instrumental and confusion noise in two different ways. The standard SPIRE data product contains an ‘error’ map which is the error on the mean of the samples used for each pixel (i.e., the standard deviation of the samples divided by square root of the number of samples within the pixel). This gives a good estimate of the instrumental noise for that pixel. To estimate the contribution of the confusion

noise to the overall uncertainty I used the confusion values from Nguyen et al. (2010) of 5.8, 6.3, 6.8 mJy/Beam for the 250, 350 and 500 μm images, respectively. While cosmic variance could cause this value to vary, similar values have been found for H-ATLAS (Pascale et al., 2011). The HeViCS team have also measured the confusion noise and find similar/slightly lower values.

To estimate the background error, I used the same instrumental and confusion estimates as used for the aperture (but with the instrumental noise estimated from the background region) as well as an estimate of the effect of the cirrus/non-flat background (see below).

There could also be an error if our data reduction method gives inconsistent results for multiple observations of the same object. This seems likely to be negligible (compared to other uncertainties), as tests with our 2 repeated observations give the same flux value to less than 2% of the objects flux.

3.3.2 MATHEMATICAL EXPRESSIONS FOR UNCERTAINTIES

Each contribution to the overall uncertainty is added in quadrature to give the total uncertainty.

$$\sigma_{total} = \sqrt{(\sigma_{Cal})^2 + (\sigma_{Ins})^2 + (\sigma_{Con})^2 + (\sigma_{Back})^2} \quad (3.5)$$

The formula for each individual contributions are given below (N_{ap} is the Number of pixels inside the aperture):

I. Calibration Error

The SPIRE Observers' Manual (2011) provides values for the SPIRE calibration uncertainty for both a component that is correlated and uncorrelated between the SPIRE bands. The correlated uncertainty arises from the models assumed of the primary calibrator (Neptune); for example, if the model is below the real Neptune flux in one band it will be low for all three SPIRE bands. The accuracy of the model is estimated to be approximately 5%. The uncorrelated uncertainty arises from the ability to measure the flux of Neptune in the timelines. From multiple observations of Neptune this uncertainty is estimated at 2% or less. At present the SPIRE ICC recommend adding these two components linearly to give an overall 7% uncertainty (equivalent to adding in quadrature two 5% uncertainties).

$$\sigma_{Cal} = 0.07 \times Flux_{object} \quad (3.6)$$

II. Instrumental Error

The instrumental error for an aperture can be found by adding the uncertainty of all pixels given by the ‘Error’ map (uncertainty on each pixel is denoted by σ_i) within the aperture in quadrature.

$$\sigma_{Ins} = \sqrt{\left(\sum_{i=1}^{N_{ap}} \sigma_i^2\right)} \quad (3.7)$$

An easy method to implement this is to create a variance map by squaring the error map. The total of the pixel variances can then be found using the same aperture and method as for the flux estimate and the final uncertainty is the square root of the result.

III. Confusion Error

The confusion noise (con_{band}) has been estimated by Nguyen et al. (2010) as 5.8, 6.3, 6.8 in units of mJy/Beam for 250, 350 and 500 μ m, respectively. To scale this noise to the aperture, the number of beams present in the aperture must be calculated and the confusion noise scaled for the relevant aperture size. I derived the following formula for the confusion noise (with units of Jy) as:

$$\sigma_{Con} = 0.001 * con_{band} * \sqrt{N_{ap} * Area_{pix}/Area_{beam}}, \quad (3.8)$$

where $Area_{pix}$ is the area of a single pixel, $Area_{beam}$ is the area of the beam and con_{band} is the confusion noise with units of mJy/Beam. The area of an elliptical Gaussian beam can be calculated from the FWHM of the band using

$$Area_{beam_{band}} = 1.1331 \times \theta_{major}\theta_{minor}, \quad (3.9)$$

where θ_{major} and θ_{minor} is the FWHM of the major and minor axis, respectively.

IV. Background Error

This is the most difficult component to quantify because as well as the confusion and instrumental noise there is also the effect of large-scale variations in the background. The total uncertainty is given by adding each of these contributions in quadrature:

$$\sigma_{back} = \sqrt{(\sigma_{back(Ins)})^2 + (\sigma_{back(Con)})^2 + (\sigma_{back(large-scale)})^2}. \quad (3.10)$$

The expression for each contribution is given below.

- The instrumental contribution is the same as in II but with the appropriate scaling to account for the different sizes of the object and background regions; it is given by,

$$\sigma_{back(Ins)} = \frac{\sqrt{\sum_{i=1}^{N_{back}} \sigma_i^2}}{N_{back}} N_{ap}, \quad (3.11)$$

where N_{back} is the number of pixels in the background and the other symbols are the same as previously defined.

- The confusion contribution is the same as in III with an appropriate scaling. This is given by

$$\sigma_{back(Con)} = 0.001 \times con_{band} \times \sqrt{\frac{N_{back} Area_{pix}}{Area_{beam}}} \times \frac{N_{ap}}{N_{back}}, \quad (3.12)$$

which can be simplified to give

$$\sigma_{back(Con)} = 0.001 \times con_{band} \times \sqrt{\frac{Area_{pix}}{Area_{beam}}} \times \frac{N_{ap}}{\sqrt{N_{back}}}. \quad (3.13)$$

- I tried two techniques to assess the uncertainty from large-scale structures in maps. The first method is to split the background annulus radially into two equal area regions and measure the difference between the mean pixel value in the two different background regions and the overall mean. The equation describing the split method is:

$$\sigma_{back(split)} = \begin{cases} |\mu_{reg_1} - \mu_{back}| \times N_{ap} & \text{if } |\mu_{reg_1} - \mu_{back}| > |\mu_{reg_2} - \mu_{back}| \\ |\mu_{reg_2} - \mu_{back}| \times N_{ap} & \text{if } |\mu_{reg_2} - \mu_{back}| > |\mu_{reg_1} - \mu_{back}| \end{cases} \quad (3.14)$$

where μ_{reg_i} is the mean value of region(i). To illustrate this method Figure 3.2 shows the regions used.

In the second method I estimated the background from a number of small regions distributed azimuthally around the galaxy (see Figure 3.2 for an illustration of this). Care is needed to choose the size of these smaller regions; a smaller size allows more regions to be placed but each region has to be of a sufficient size to allow an estimate of the background that is not limited by confusion or instrumental noise. If the background in the image is flat the uncertainty of the background is the error on the mean of the

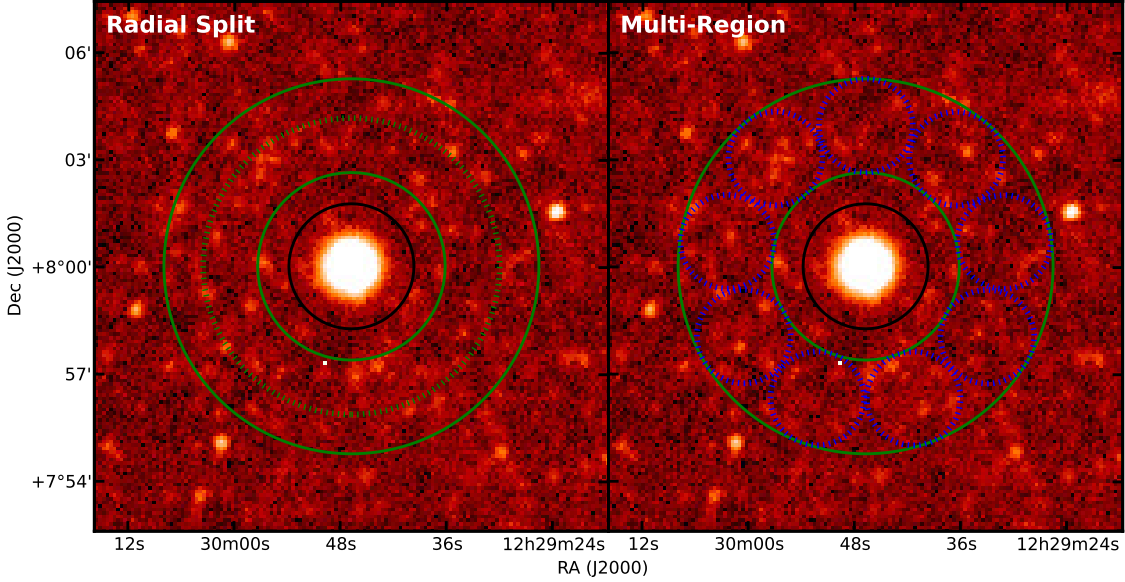


Figure 3.2. Two methods to measure the background uncertainty. In both images the object aperture is given by the black circle and the background value is calculated between the solid green circles. For the left image the uncertainty due to large-scale background variation is estimated by splitting the background region radially with the green dashed line (two areas are equal). For the right image the background region is split into smaller regions and the distribution of background values in each region is used to find the background uncertainty.

background estimates from the different regions. If there are large scale cirrus structure present then the standard deviation of these estimates is a more conservative estimate of the error. This is expressed as

$$\sigma_{\text{back}(regions)} = \begin{cases} \frac{\sigma(\text{regions})}{\sqrt{N_{\text{regions}}}} & \text{if flat background} \\ \sigma(\text{regions}) & \text{if cirrus structure} \end{cases} \quad (3.15)$$

where $\sigma(\text{regions})$ is the standard deviation of the mean value of each region.

3.3.3 EXTENDED CORRECTION FACTORS

The SPIRE pipeline is optimised for point sources rather than extended emission. Therefore certain corrections have to be made. Corrections are needed as the throughput of the feedhorn is proportional to the square of the wavelength, and thus varies across the band. To compensate for this, the filter response function is multiplied by λ^2 (SPIRE Observers' Manual, 2011). To correct for this effect the pipeline

Table 3.2
 K_4 Values for Point and Extended Sources

Source Type	K_4 Values		
	PSW	PMW	PLW
Point	1.0113	1.0087	1.0065
Extended	0.9939	0.9920	0.9773

Notes. The pipeline K_4 values for both point and extended sources for each band. The values are taken from the SPIRE Observers' Manual (2011)

parameter (K_4) which converts the raw instrument response to a flux by assuming a point source with a $\nu F_\nu = \text{constant}$ spectrum should be removed. Once removed a new K_4 parameter can be applied using the modified response function for extended sources. The values of the K_4 for point and extended sources are shown in Table 3.2. The final correction is to apply a color correction but using the values calculated for extended sources, given in Table 3.1.

3.3.4 EXTENDED OR POINT SOURCE?

For most objects it is usually obvious if the source is extended, but for some sources a more detailed test is required. This is important, as if the point source fitter is run on a marginally extended source it could underestimate the flux of the object. The point source timeline-fitter can be used in two ways to identify slightly extended objects. The first method is to look at the parameters returned from the timeline fitter. If the FWHM value is above 20, 29 and 37'', for the PSW, PMW and PLW, respectively, then it indicates the source is wider than a point source. The second method is to use the result from the timeline fitter to subtract the source from the timeline and then remake the map to see if there is any residual emission from the source. An example of this procedure is shown in Figure 3.3. If a source is found to be extended aperture photometry should be used, although it is often advisable to still use the point source K_4 and color-correction if the source is not much larger than (up to $\sim 1.4 \times \text{FWHM}$) the point spread function.

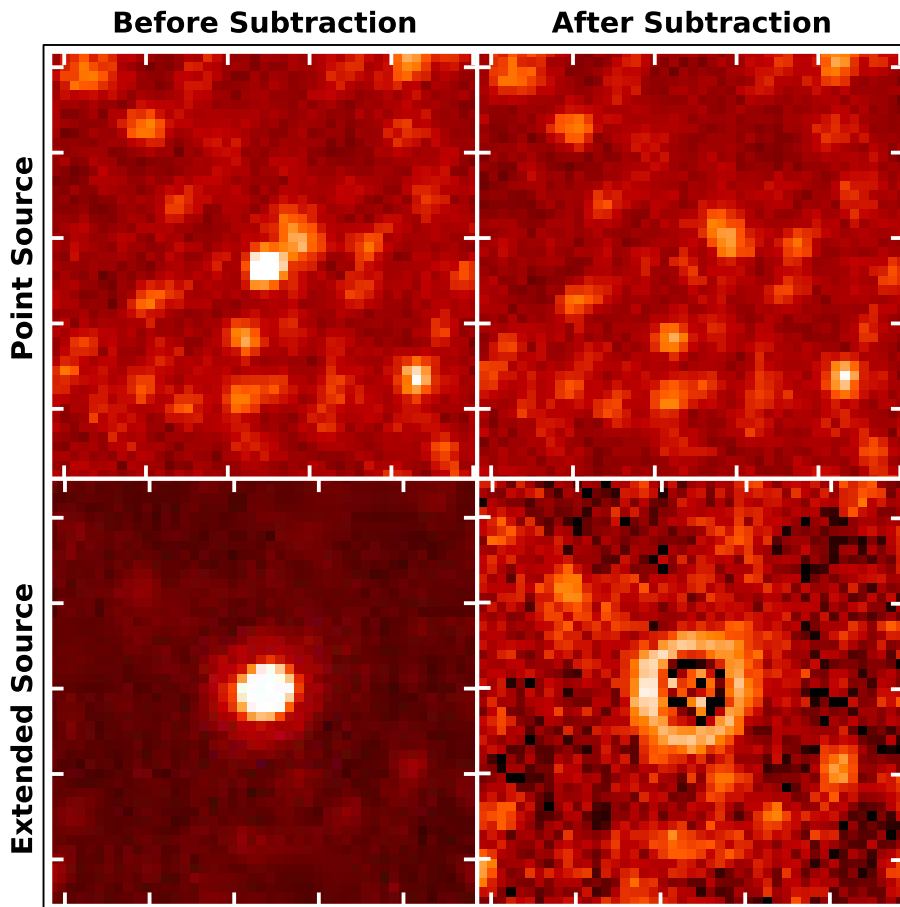


Figure 3.3. Two examples of how the timeline source fitter can be used to test whether a source is extended. The top row shows a point source where no emission is present after subtraction of the source from the timeline and the bottom row illustrates the case for a slightly extended source. All the images are at $350\mu\text{m}$ and the tick size represents $1.2'$.

3.3.5 HRS PHOTOMETRY

The HRS survey is a targeted survey of 323 galaxies with SPIRE, which means there are 969 separate fluxes to be measured. To allow these measurements to be performed on a quick time-scale I wrote a script which measures the global fluxes using the prescription set out in Section 3.3 (the handful of point sources were measured separately) and produce a quick-look catalogue. The program works by placing apertures on the maps derived from the major and minor optical diameters from the Uppsala General Catalog of Galaxies (UGC, Nilson, 1995a) but multiplied by a scaling factor (usually ~ 1.2) to ensure all the emission from the galaxy is included. To ensure that galaxies with optical angular sizes smaller than the beam do not have an aperture smaller than the SPIRE beam, I use a minimum aperture radius of $73.8''$ (for edge-on galaxies this is often important in one dimension but not in the other). I choose an annular background region between two radii (typical values were $1.5 D_{25}$ – $3.0 D_{25}$ in which D_{25} is the optical diameter). For objects with elliptical apertures, I usually set the outer ring to be circular to make the best use of the small images. The position used for each galaxy was taken from the HRS survey paper (Boselli et al., 2010b).

As the HRS covers a range of galaxy type, the aperture chosen by the program is not always appropriate. To provide a quick method to identify galaxies for which the aperture has to be manually adjusted the script outputs a image of the SPIRE map with the apertures overlaid. The images can be quickly cycled through and if required any of the parameters (e.g., centre, radius, background region, position angle) can be adjusted for each object. These manual adjustments are only required for a small fraction of the HRS as most spirals did not have dust emission outside the automated aperture. As a few HRS observations contain more than one HRS galaxy the script automatically masks out the other HRS object from the background region of the object being measured. To allow an in-depth look at particular objects I added in a routine which creates a DS9¹ region file, allowing the apertures used to be plotted on the FITS image and interactively adjusted. The script calculates the fluxes and the uncertainties using the prescription outlined in Subsections 3.3.1 and 3.3.2 and outputs each component separately as well as the combined values.

The official HRS photometry release is published in Ciesla et al. (2012); in this analysis Laure Ciesla performed a careful extraction by eye to define all the apertures chosen. The uncertainties quoted in the paper were calculated using my error analysis and the the automated script I developed but using the apertures that Laure Ciesla defined by eye. For the background uncertainty Ciesla et al. (2012) used a conservative

¹SAOImage DS9 is astronomical data visualisation tool, more information available at <http://hea-www.harvard.edu/RD/ds9/>.

approach of estimating the background uncertainty from the standard deviation of the means in \sim 11–16 boxes (each box 13×13 pixels), using the second conservative option in Equation 3.15. To test this approach I embedded a bright artificial source into 30 HRS maps in which the HRS galaxy had not been detected. This should allow any flux measurement to contain the same uncertainties that would be present for a real observation (except calibration uncertainties). The automatic flux extraction program was run on these observations by splitting the large background region into smaller circular apertures (see Figure 3.2). While these circular regions are larger than the regions used in Ciesla et al. (2012) it is still instructive to see how the uncertainties compare for different methods. In Figure 3.4, I have compared the difference between the input and measured flux (the true error) with the error estimated by Ciesla et al. (2012) and one obtained by using σ/\sqrt{N} , the less conservative option in Equation 3.15. Figure 3.4 shows that for the majority of sources the error estimates by Ciesla et al. (2012) are too high. For \sim 25 of the 30 cases σ/\sqrt{N} would be sufficient. However for \sim 5 of the 30 cases the standard deviation appears to give a more reasonable value of the uncertainty. The published HRS catalogue is therefore a slightly conservative catalogue, although as many of the HRS galaxies are bright the calibration uncertainty is often the limiting factor.

3.4 SPECTRAL ENERGY DISTRIBUTION FITTING

One advantage of *Herschel* over previous observatories is that the large wavelength range and number of photometric bands make it possible to investigate a galaxy’s SED over a wavelength range covering the FIR peak. To make the most of the observations I created a spectral energy distribution (SED) fitting program. As a large fraction of galaxies will have limited ancillary data (i.e. near or mid-infrared) I chose to use a simple model for the dust by using a modified blackbody (with one or two components) and with the possibility of adding an additional synchrotron component (for more details of the models see Subsection 3.4.1). Although it is fairly common to fit models like this to FIR data, my package is the first that incorporates all errors, including calibration errors that are correlated and uncorrelated between bands. The program uses a simplex fitting algorithm from the open-source Scipy² package. Details on some of the features of the SED fitting script are given below.

²More details of Scipy can be found at www.scipy.org.

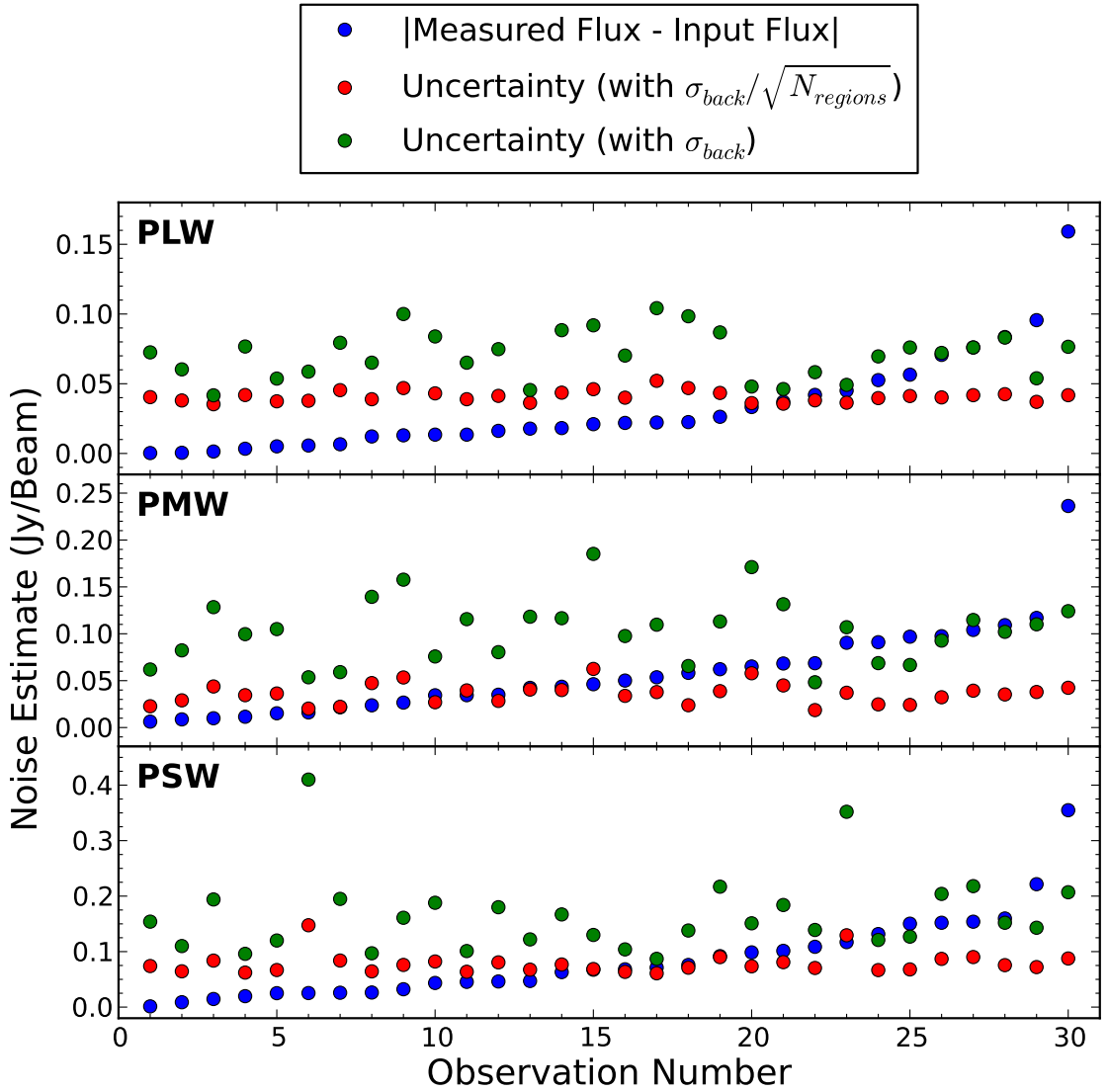


Figure 3.4. The results from tests performed by adding a bright artificial source into the timelines for observations with a non-detection. The blue data points represent the absolute difference of the input to measured flux. The x-axis is just a number assigned to each observation which has been done in ascending order in the discrepancy of the flux returned. Both the green and red points have been calculated using the uncertainty procedure from Section 3.3.1 and 3.3.2. The difference is in how the large scale background uncertainty has been estimated. The green points are calculated from the standard deviation of the background estimates from individual regions while the red points use standard deviation divided by the square root of the number of regions, which effectively assumes that there is no systematic background error.

3.4.1 MODIFIED BLACKBODY MODEL

A modified blackbody model is described as,

$$F_\nu = \frac{\kappa_\nu M_d}{D^2} B(\nu, T_d), \quad (3.16)$$

where F_ν is the flux as a function of frequency (ν), M_d is the dust mass, $B(\nu, T_d)$ is the Planck blackbody function with a dust temperature given by T_d , D is the distance to the galaxy and κ_ν is the dust-opacity coefficient. This model assumes that the dust emission is optically thin; a full proof of this equation is given in Appendix C. The dust-opacity coefficient describes the efficiency with which the dust grain emits as a function of frequency and is assumed to be given by

$$\kappa_\nu = \kappa_0 \left(\frac{\nu}{\nu_0} \right)^\beta. \quad (3.17)$$

Values of β are usually in the range 1.5–2.0 (e.g., Dunne et al., 2011; Planck Collaboration, 2011a; Davies et al., 2012) and it is believed to vary with the size and composition of the dust grains (e.g., Seki & Yamamoto, 1980; Aannestad, 1975).

Some observations show strong evidence for dust components at different temperatures (Dunne & Eales, 2001). The equation describing a two component model is simply,

$$F_\nu = \frac{\kappa_\nu M_{hot}}{D^2} B(\nu, T_{hot}) + \frac{\kappa_\nu M_{cold}}{D^2} B(\nu, T_{cold}). \quad (3.18)$$

For some objects a strong non-thermal synchrotron radio source is present which can contaminate the dust emission in the FIR. While radio measurements could be used to estimate the contribution of the non-thermal emission to the FIR bands, with limited data points it is often better to simultaneously fit the dust and synchrotron emission. The equation for this case is,

$$F_\nu = \frac{\kappa_\nu M_d}{D^2} B(\nu, T_d) + A\nu^\alpha. \quad (3.19)$$

in which α is the radio emission spectral index and A is a constant. For all three model scenarios listed above an example is shown in figure 3.5. The galaxies in the Figure have been taken from either the HRS or the Dwarf Galaxy Survey.

3.4.2 INPUT/OUTPUT MODES

The script can read in the input data in a variety of ways depending on the situation. In the case of a single SED the values can either be inserted manually or

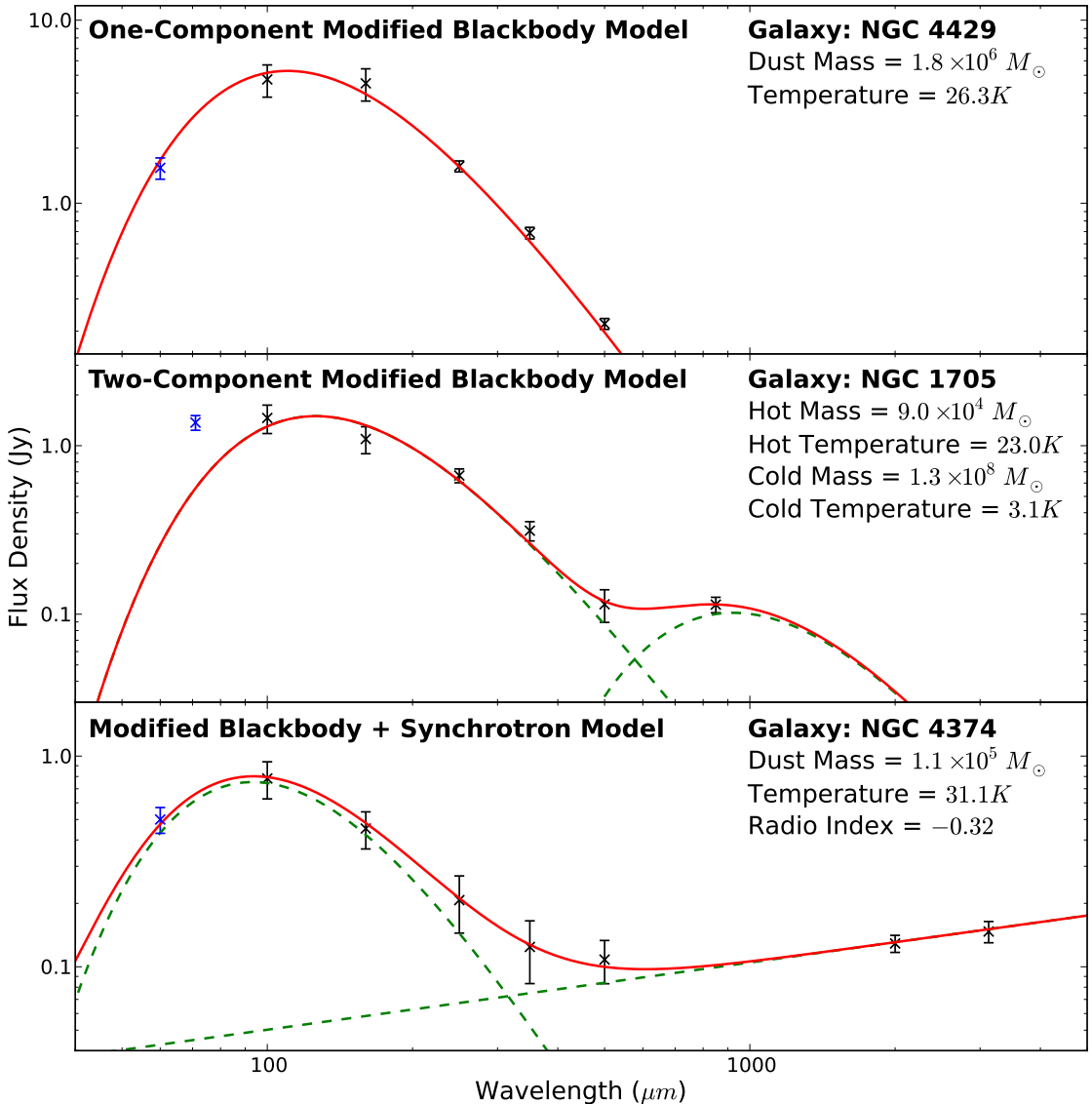


Figure 3.5. Examples of the three models available in the SED fitter. All examples are galaxies from either the HRS or the Dwarf Galaxy Survey. The blue points are fluxes that are used as an upper limit in the fitting process. The red line is the fitted model and the dashed green line shows individual components of the model. For NGC 1705 the excess emission may not be due to cold dust but could have another source. While it is technically more appropriate to plot flux density versus frequency in this thesis wavelength instead of frequency to match the literature (e.g., Dunne et al., 2000).

read in from an ascii file. For the case where multiple SEDs are to be fit the program can either read the data from a list of ascii files or several ‘FITS’ images. The ‘FITS’ mode is the most useful as in this mode the program loads a set of FITS files and fits an SED to each pixel on the map (the input files must have the same WCS) that fulfils the selection criteria specified (i.e., only include data points in which the flux is detected at greater than 5σ). In this mode the fitted results are written out as FITS files with the same co-ordinate system as the inputs. To account for the different redshifts and distances when fitting multiple objects a file can be read in which specifies all the values for each object.

All modes provide an overall ascii result file and an option can be specified to output a result file for each individual fit. For each SED an image of the fitted spectrum with the data points can be created (similar to a single panel in Figure 3.5) and also an image of the distribution of results created by the bootstrapping (for more information see Subsection 3.4.6). For pixel-by-pixel SED fitting this can produce too many images. For these cases a file listing the fluxes that have gone into each fit can be written so individual pixels can be investigated further if desired.

3.4.3 CHOICES

Several parameters need to be set before the fitting routine is run. Firstly the redshift of the spectrum should be entered; the script then shifts the SED to the galaxy’s rest frame. The value of the dust-emissivity, κ_0 , must be set and also the value of the spectral index (β) if it is to be kept constant. Shorter wavelengths can be contaminated by very hot dust in thermal equilibrium or emission from small grains that are not in thermal equilibrium. Therefore an option is provided that allows for data points below a specified wavelength to be used as an upper limit in the fitting algorithm. This is achieved by not including a contribution to χ^2 if the model flux lies below the observed flux.

3.4.4 COLOR-CORRECTION

As mentioned in Section 3.2 and 3.3 a color correction is needed to account for the fact the filter has a finite width instead of a δ -function. As the exact correction depends on the temperature of the dust and the spectral index β , instead of correcting the flux the script takes the trial SED and multiplies it by the filter profile. This is then used in the χ^2 calculation with the flux value modified so the K4 parameter used in the pipeline has been removed.

3.4.5 CORRELATED UNCERTAINTIES

The SPIRE calibration uncertainties are correlated between bands due to the uncertainties in the model used of Neptune (see Subsection I for more details). To account for this in the SED fitter the script uses the χ^2 formula including the full covariance matrix. This is written as,

$$\chi^2 = (F - M)^T Cov^{-1} (F - M), \quad (3.20)$$

where F is a vector containing the measured SPIRE fluxes, M is the model values for the three bands and Cov^{-1} is the inverse of the covariance matrix of the errors which includes both the correlated and uncorrelated errors. If the correlated uncertainties dominate the covariance matrix, the inverse of the covariance matrix becomes unstable (i.e., it is impossible to calculate the inverse of a matrix where all elements are equal to one). This is not a problem for the *Herschel* instrument calibrations at present, but has been a problem for other instruments. For these cases a principal component analysis is used to find the χ^2 value.

3.4.6 BOOTSTRAPPING FOR UNCERTAINTIES

To estimate the uncertainties on the fitted parameters a bootstrap technique is used. This process involves generating N synthetic SEDs by randomly obtaining new flux values for each band from a normal distribution with a mean equal to the measured flux and a standard deviation equal to the error in the flux. To take into account the correlated uncertainties between data points, the script uses a Cholesky decomposition to ensure the simulation has the correct covariance of the system. The resultant distributions for each returned parameter are binned and then plotted (unless specified, e.g., if fitting a large number of data points). An estimate of the uncertainty on the fitted parameters is then found from either the bin that contains the result at $\pm 34\%$ away from the mean or the standard deviation of a fitted Gaussian. The distribution usually follows a normal distribution, but the plot allows the user to see if the uncertainty calculated is appropriate. An example of the bootstrap plot generated by the program is shown in Figure 3.6.

3.4.7 SPEEDING UP THE CODE

For large resolved objects with thousands of independent pixels (such as M31), a bootstrap with ~ 1000 simulated SEDs can quickly become very time consuming.

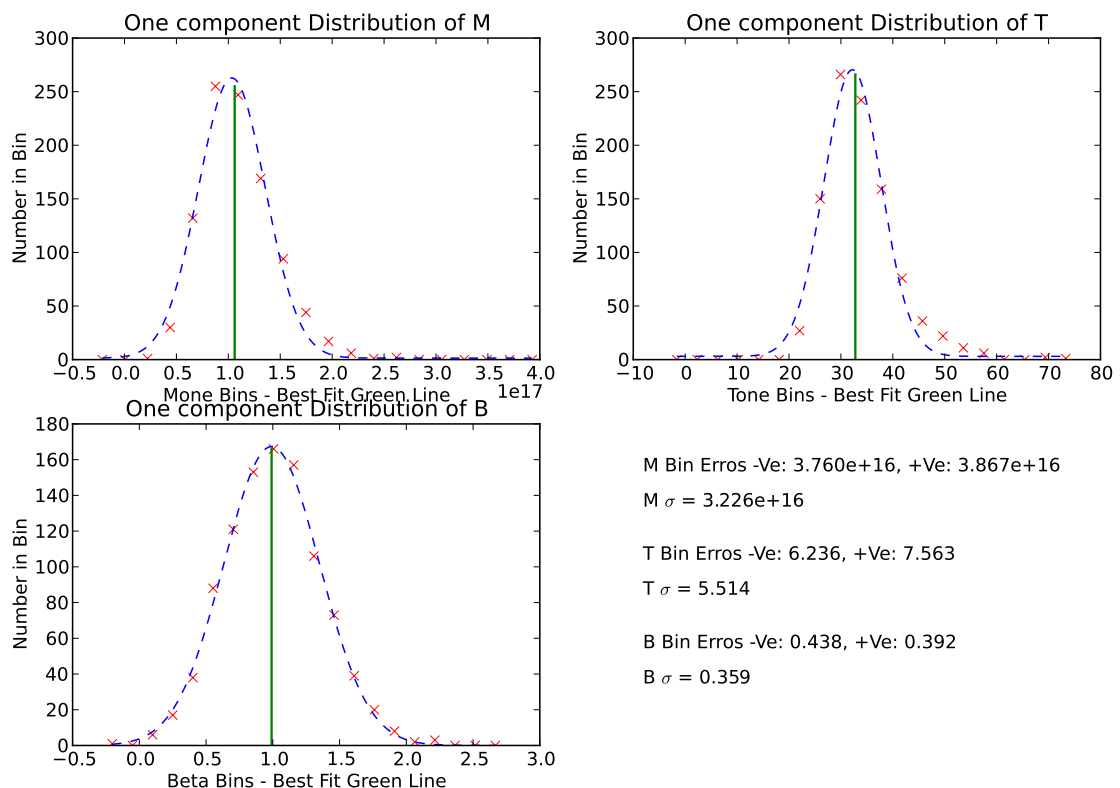


Figure 3.6. An example of the the results of the bootstrap analysis generated by the SED fitter. In this case β is a free parameter and the errors for each parameter are calculated using the method explained in Section 3.4.6.

One method used to speed up the processing is to replace the Python function which calculates χ^2 for every guess with a Fortran function. As Fortran is a low-level code and the fitter calls this function multiple times, this modification results in a $10\times$ increase in speed. A second method is to use PyPy, a Python module which can run the script in parallel on multiple processors (with some adjustments to the script). The SED fitting script can easily be used in parallel as very little memory or data is required to fit an SED (just the wavelengths, fluxes and uncertainties for that particular fit).

3.5 SUMMARY

This chapter describes methods used to measure and estimate the flux uncertainties for both point and extended sources in SPIRE maps. For point sources, fitting of the source in the timeline data is recommended, while for extended sources aperture photometry is the best method. Uncertainties in flux measurements need to account for the instrumental noise, confusion noise, calibration uncertainties and large-scale fluctuations in the background (e.g., cirrus, or reduction artefacts). The development of an optimal way of combining *Herschel* fluxes into a SED fitting routine that can run on a large number of pixels is described.

CHAPTER 4

RESOLVED DUST ANALYSIS OF SPIRAL GALAXIES

“Every atom in your body came from a star that exploded and the atoms in your left hand probably came from a different star than your right hand. It really is the most poetic thing I know about physics; you are all stardust.”

Lawrence M. Krauss

This chapter presents an investigation of the dust properties of three resolved galaxies in the HeViCS survey. This investigation was performed during the *Herschel* Science Demonstration Phase (SDP) and were published in Smith et al. (2010) and entitled “The *Herschel* Virgo Cluster Survey IV. Resolved Dust Analysis of Spiral Galaxies”.

4.1 INTRODUCTION

Infrared data have been widely used to determine the composition and distribution of dust in galaxies since the launch of the *Infrared Astronomical Satellite (IRAS)* in the 1980s. However, dust masses for nearby galaxies calculated from *IRAS* 60 and 100 μm measurements were found to be a factor of ten lower than expected when compared to the Milky Way gas-to-dust ratio of 100–200 (Devereux & Young, 1990). The Milky Way dust mass was calculated by measuring the depletion of metals from the gaseous phase of the interstellar medium (ISM) and by comparing gas column densities to dust extinction (Whittet, 2003), its value implying that most of the dust-mass emits radiation at wavelengths longer than 100 μm (e.g., Devereux & Young, 1990). Analyses of data from the *Spitzer Space Telescope* have determined

gas-to-dust ratios of ~ 150 (e.g., Draine et al., 2007). However, these analyses were generally limited by the number, and low signal-to-noise ratio of data at wavelengths greater than $160\,\mu\text{m}$. These studies therefore had difficulty detecting emission from dust with temperatures lower than 15 K, and their results were biased towards warmer dust temperatures and lower masses. Owing to the difficulties at these wavelengths, high resolution studies of galaxies have been previously limited. These studies are important for understanding how dust interacts with the other phases of the ISM, the sources of dust heating and how the distribution and temperature of dust varies with morphology.

The *Herschel Space Observatory* (Pilbratt et al., 2010, see Section 1.4), with its two photometric instruments, constrains both sides of the peak in the far-infrared spectral energy distribution (SED, see Figure 4.1). The Photodetector Array Camera & Spectrometer (PACS, Poglitsch et al., 2010) has three photometric bands at 70, 100, and $160\,\mu\text{m}$ at superior angular resolutions to those provided by *Spitzer*. The Spectral and Photometric Imaging Receiver (SPIRE, Griffin et al., 2010) also has three photometric bands observing simultaneously at 250, 350, and $500\,\mu\text{m}$ with high sensitivity and angular resolution.

The Herschel Virgo Cluster Survey (HeViCS¹) is a Herschel Open Time Key Project that will observe $\sim 64\,\text{deg}^2$ of the Virgo cluster. This will provide a large sample of resolved galaxies because about 48 late-type galaxies will be observed by HeViCS with optical diameters larger than $3'$. In this chapter, I present an insight into what will be possible with the full HeViCS survey by applying a resolved dust analysis to infer dust temperatures, surface densities, and gas-to-dust ratios for NGC 4501 and NGC 4567/8. These galaxies were chosen because they are among the largest angular size systems in the HeViCS Science Demonstration Phase (SDP) field. In Section 4.2, the observations and data reduction are described, and in Sections 4.3 and 4.4, the analysis and results are presented.

4.2 OBSERVATIONS AND DATA REDUCTION

As part of the Herschel Science Demonstration Phase (SDP), a $4 \times 4\,\text{sq deg}$ field of the Virgo cluster centred approximately on M 87 has been observed in parallel mode, simultaneously at 100 and $160\,\mu\text{m}$ with PACS and at 250, 350, and $500\,\mu\text{m}$ with SPIRE. For details of the observing strategy and data reduction during SDP, see Davies et al. (2010). Following the recommendations given by the PACS and SPIRE instrument control centres (ICCs), the 100 and $160\,\mu\text{m}$ PACS flux densities

¹More details on HeViCS can be found at <http://www.hevics.org>

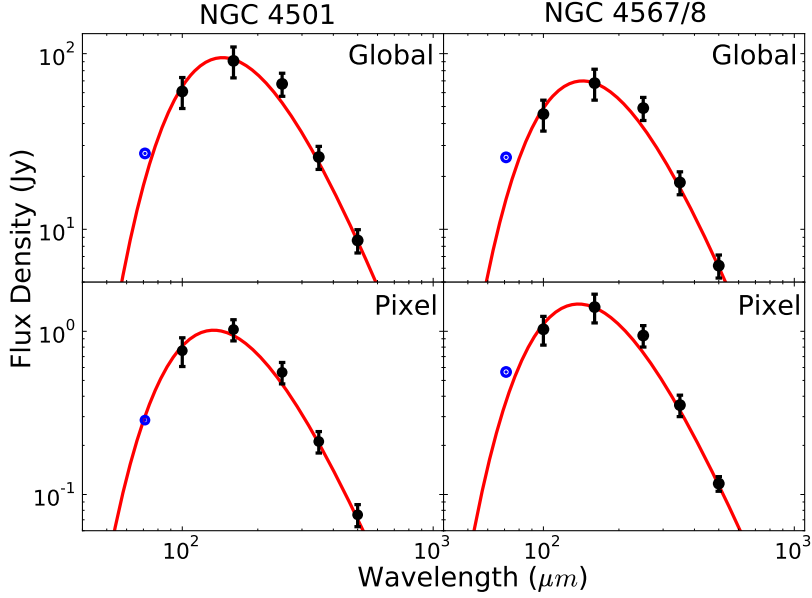


Figure 4.1. Global and example single pixel one component SED fits. If not shown, uncertainties are smaller than the symbol size. The $70\,\mu\text{m}$ point (blue) is used as an upper limit (see Sect 4.3).

were scaled by dividing by 1.06 and 1.29, respectively, and SPIRE flux densities by multiplying by 1.02, 1.05, and 0.94 for the 250 , 350 , and $500\,\mu\text{m}$ bands, respectively. The point spread function (PSF) of the PACS images has a FWHM of $12.70'' \times 6.98''$ and $15.65'' \times 11.64''$ in the $100\,\mu\text{m}$ and $160\,\mu\text{m}$ band, respectively (where the orientation depends on scan direction). The SPIRE PSF has a FWHM of $18.1''$, $25.2''$, and $36.9''$ at $250\,\mu\text{m}$, $350\,\mu\text{m}$, and $500\,\mu\text{m}$, respectively. The calibration error is assumed to be 20% for the PACS band and 15% for the SPIRE bands. The PACS and SPIRE images are shown in Figures 4.2 and 4.3.

This chapter focuses on NGC 4501, which is an Sbc galaxy and has an optical diameter (major axis) of $7.23'$, and the galaxy pair NGC 4567/8, which are both of Sc type with optical diameters of $2.92'$ and $5.1'$, respectively (values taken from GOLD Mine; Gavazzi et al. 2003). As NGC 4501 is on the edge of the SDP field, observations were only obtained in one scan direction.

In addition to the *Herschel* data, I used Spitzer $70\,\mu\text{m}$ data from Kennicutt et al. (2003), Kenney et al. (2006), and Struck et al. (2004), which were reprocessed using the techniques described in Bendo et al. (2010b). The calibration uncertainties were assumed to be 5% at $70\,\mu\text{m}$ (Gordon et al., 2007). I also use GALEX FUV ($\lambda = 1539\text{\AA}, \Delta\lambda = 442\text{\AA}$) data downloaded from the MAST (G4/5) archive. For both NGC 4501 and NGC 4567/8, HI maps were taken from the VIVA HI survey (Chung et al., 2009), and for NGC 4501 a CO($J=1-0$) map from the Nobeyama CO

ATLAS survey (Kuno et al., 2007) is used. The HI and CO images are shown in Figures 4.2 and 4.3. For NGC4567/8, global CO($J=1-0$) measurements from Iono et al. (2005) are used. In the following analysis, neutral atomic hydrogen masses were calculated using $M_{\text{HI}} = 2.36 \times 10^5 D_{\text{Mpc}}^2 FI$ (M_{\odot}), where FI is the integrated HI line flux in units of Jy kms $^{-1}$ (Roberts, 1962) and D_{Mpc} is the distance in Mpc. The distance is assumed to be the same as the centre of the M87 cloud in the Virgo cluster given by Mei et al. (2007) of 16.7 Mpc. To convert a CO integrated line intensity to a value of molecular hydrogen column density, an X-factor of 1.9×10^{20} cm $^{-2}[\text{K km s}^{-1}]^{-1}$ derived from Strong & Mattox (1996) using models of gamma ray scattering is assumed. However, we note that the value of the X-factor is notoriously uncertain and may also vary, for example with metallicity (e.g., Israel, 2000).

4.3 ANALYSIS

A simple model is fitted to the SEDs of each pixel in our galaxies to produce maps of estimated dust temperature and dust mass. All images were first convolved to the resolution of the 500 μm image (which has a PSF of the largest FWHM), using a customised kernel created using the procedure outlined in Bendo et al. (2010b). The images were then regridded to the 14'' pixel size of the 500 μm map. We note that since the pixel size is smaller than the 500 μm beam size, neighbouring pixels are not independent. Owing to lower sensitivities in the PACS 100 μm band and negative artefacts created around the galaxy during the current PACS data reduction process, the analysis is restricted to only pixels with a flux density $>10\sigma$ in the convolved and regridded 100 μm image; the estimated sensitivities are 7.3 mJy pix $^{-1}$ for the cross-scan region and 10.4 mJy pix $^{-1}$ for the single scan (see Davies et al., 2010 for optimal resolution sensitivities). Thus, in the present work the outermost regions of the galaxies are not studied; the full galaxy extent will be considered in future works.

I fit the SEDs in the 70–500 μm range with one and two component modified black-body models. The equation for a one component black body is given by

$$F_{\nu} = \frac{\kappa_{\nu}}{D^2} MB_{\nu}(T). \quad (4.1)$$

Here M is the dust mass, T is the dust temperature, $B_{\nu}(T)$ is the Plank function, D is the distance to the galaxy (see Sect. 4.2), and κ_{ν} is the dust emissivity (for more information see Section 3.4). The dust emissivity is assumed to be a power law in this spectral range, where $\kappa_{\nu} \propto \nu^{\beta}$. The value of κ_0 is assumed to be 0.192 m 2 kg $^{-1}$ at 350 μm (Draine, 2003) and $\beta = 2$, though we note that the values of κ and β are

notoriously uncertain. The best-fit solution is found by minimising the chi-squared (χ^2) function. To adjust for the filter-band passes, the SED is convolved with the filter transmission in the fitting process.

The data in the 100–500 μm range are found to be accurately fitted by a single black-body component. However, for the majority of pixels a significant flux excess is measured at 70 μm relative to this fit. This indicates that a warmer dust component is present, which is consistent with the results found by Bendo et al. (2010a). A two-component model provides a good fit by using the same component through the 100–500 μm data as the one-component model and adding a warm component that fits the 70 μm emission. The warm component, however, is not tightly constrained since a wide range of warm temperatures statistically provide equally good fits, due mainly to the small number of data points on the Wien side of the SED. Therefore, in this work I choose to use a one-component model with the 70 μm data point as an upper limit. This choice has little effect on the total dust mass since the cold component dominates the dust mass. Example global and single-pixel SEDs are shown in Figure 4.1. We note that for most of the SED fits a $\sim 1\sigma$ excess is found for the 250 μm band, which we believe is due to the preliminary calibration available during the SDP.

In addition to maps of dust temperature, maps of dust mass surface density and the gas-to-dust ratio are produced. For NGC 4501, the total gas mass is calculated from $M_{\text{gas}} = M_{\text{HI}} + M_{\text{H}_2}$; for NGC 4567/8, a CO($J=1-0$) map does not exist, so only the HI component of the gas mass is considered.

The uncertainties in the flux densities are calculated by adding in quadrature the calibration uncertainty, background subtraction uncertainty, and the uncertainty from the error map (created by the standard pipeline). For the pixels used in this analysis, the calibration uncertainty dominates for the PACS and SPIRE bands, except for the 500 μm band where the total uncertainty ranges from 15–23%. The average χ^2 value for all the fits is 2.5 with a standard deviation of 1.0, where the 90 % confidence limit is 6.3 for 3 degrees of freedom. To obtain an estimate of the uncertainty in the fitted parameters, a bootstrap technique is used (see Section 3.4.6). This yields an average uncertainty in the pixel-by-pixel fitting of 1.0 K for temperature and 23 % in the dust surface density.

4.4 RESULTS

Maps of the cold dust temperature, dust-mass surface density, and gas-to-dust ratio are shown in Figures 4.2 and 4.3, for NGC 4501 and NGC 4567/8, respectively. The extent of the maps corresponds to ~ 65 % of the optical radius. In each case,

a centrally peaked, symmetrical distribution of dust mass in the galaxies is found. However, the dust temperature does not have the same symmetric distribution and varies across both galaxies, peaking at ~ 22 K and decreasing to ~ 19 K towards the outskirts of the galaxies. For NGC 4501, the peak of the dust temperature distribution corresponds to the bright spiral arm region seen to the southeast of the galaxy in the 70–160 μm images. For NGC 4567/8, the dust temperature distribution is also asymmetric, with higher temperatures in NGC 4568 that are coincident with peaks in the GALEX FUV. For both NGC 4501 and NGC 4567/8, the global temperature is 20 K (and also for NGC 4567 and NGC 4568, individually; an additional uncertainty in the measurements was included to account for the overlap in emission from the two galaxies). In the regions analysed, no evidence was found for any excess of flux at 500 μm that would imply an even colder dust component is present.

The dust-mass surface density distribution for both NGC 4501 and NGC 4568 has a smooth gradient, decreasing by a factor ~ 4 from higher values at the centre to lower values in the outskirts. This is consistent with results found by Muñoz-Mateos et al. (2009), who find exponentially decreasing dust surface densities for the SINGS galaxy sample. For NGC 4501 and NGC 4567/8, I find global dust masses of $(1.2 \pm 0.3) \times 10^8 M_{\odot}$ and $(8.6 \pm 1.8) \times 10^7 M_{\odot}$, respectively ($(1.7 \pm 0.4) \times 10^7 M_{\odot}$ and $(6.6 \pm 1.5) \times 10^7 M_{\odot}$ for NGC 4567 and NGC 4568 individually, respectively).

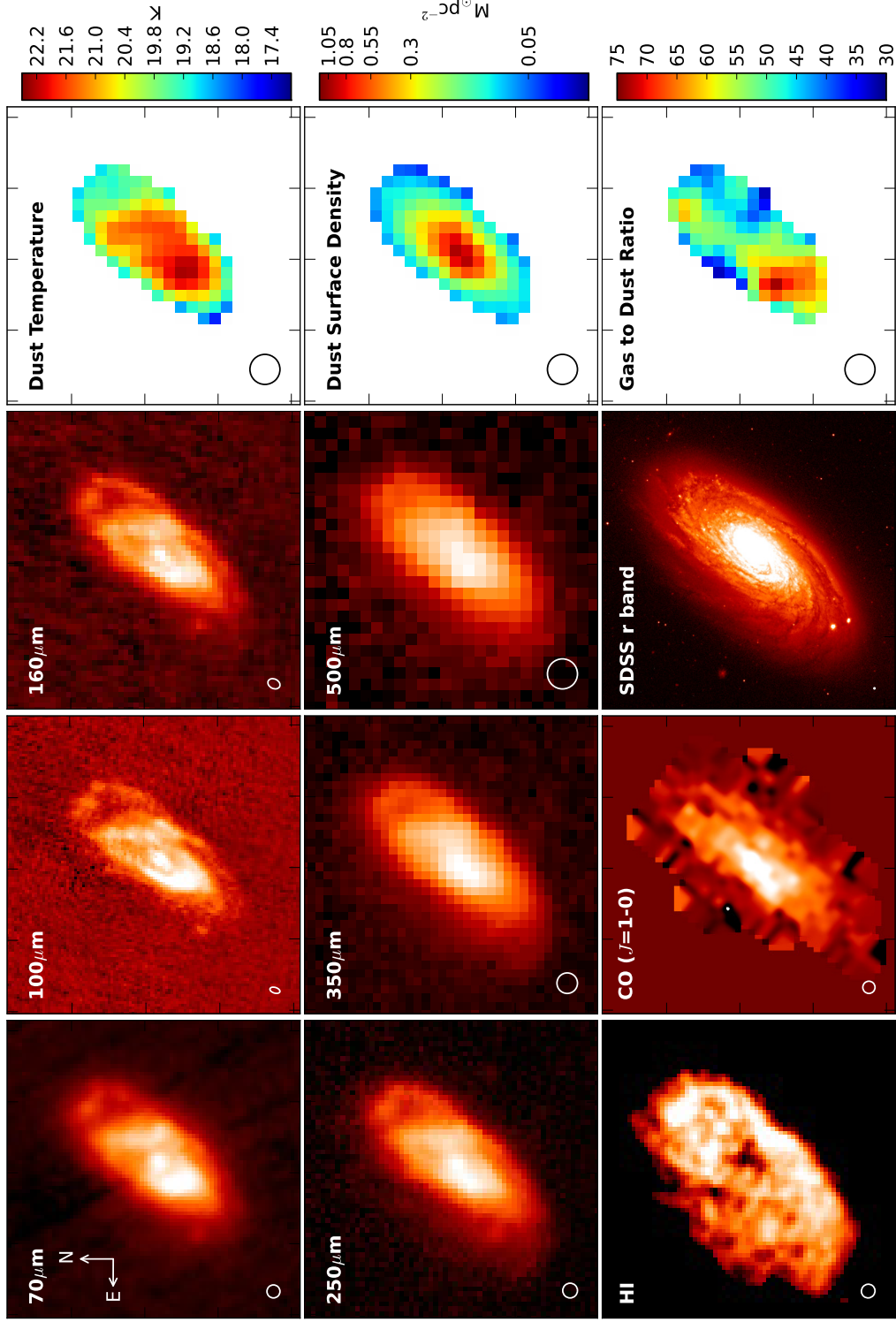


Figure 4.2. Images of NGC 4501 in their native resolution and pixel size. The first three columns show the MIPS 70 μm , PACS, SPIRE, gas and optical images on a log colour scale. The right-hand column shows maps of dust temperature, dust surface density (log scale), and gas-to-dust ratio. Beam sizes for the respective wavelengths are shown. The panels are 6' \times 6' in size and centred on 12h32m00.0s, +14d25m12.0s.

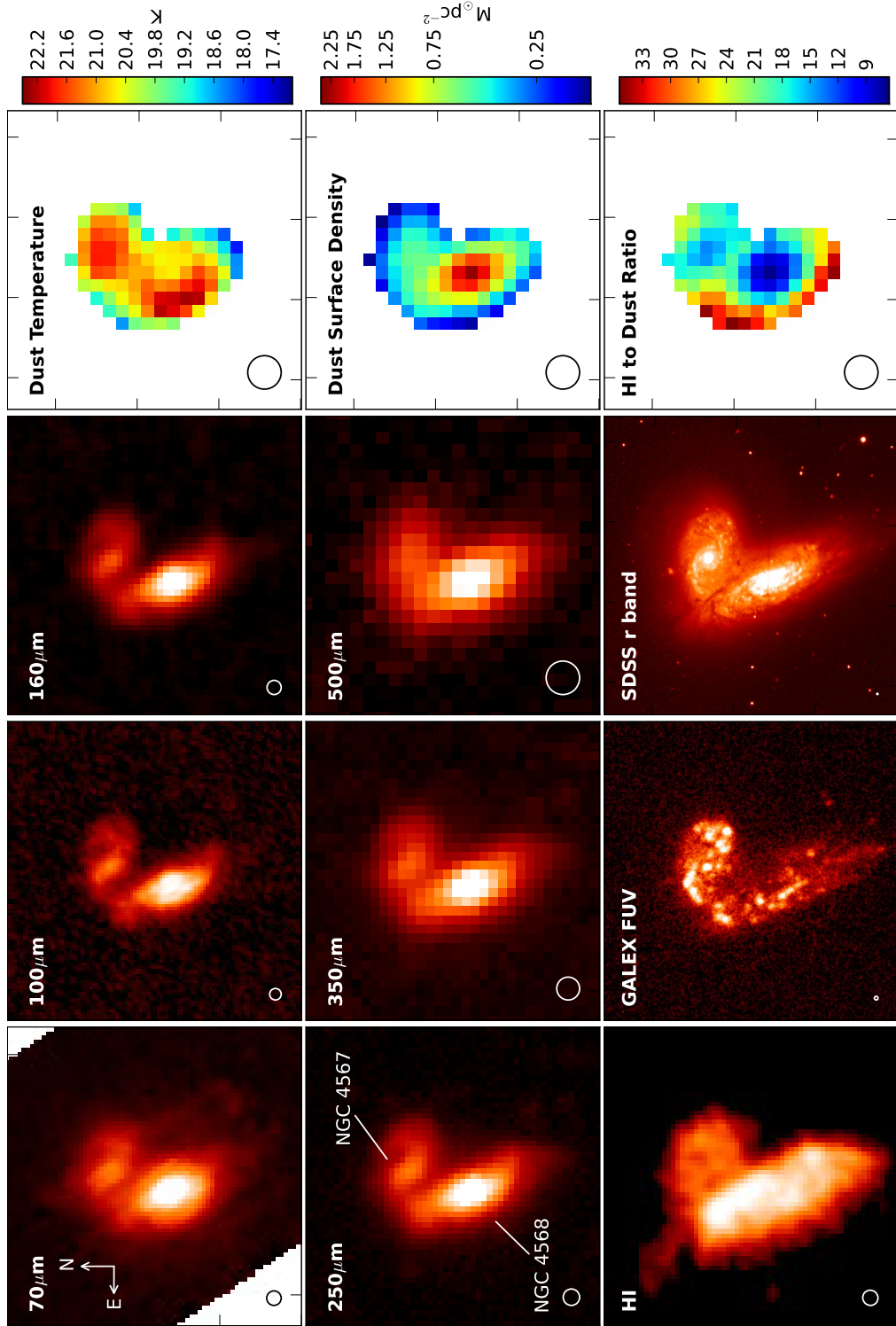


Figure 4.3. Same as Figure 4.2 but for NGC 4567/8. The GALEX FUV image has been smoothed slightly for display purposes. The panels are $5.4' \times 5.4'$ in size and centred on 12h36m33.6s, +11d15m00.0s.

For NGC 4501, the distribution of the gas-to-dust ratio is asymmetric, peaking in the southeast and varying by a factor ~ 2 across the galaxy. The average gas-to-dust ratio for the pixel-by-pixel analysis is 52 ± 13 for NGC 4501, which is in good agreement with the global value of 51 ± 14 . The variation in the gas-to-dust ratio within NGC 4501 is consistent with gas-to-dust profiles within our fitted radius for other Sb galaxies presented in Muñoz-Mateos et al. (2009). For NGC 4568, there is a large reduction in the HI-to-dust ratio in the central regions, which is probably due to higher molecular gas densities. The global (neutral) gas-to-dust ratios for NGC 4567 and NGC 4568 are 32 ± 12 and 39 ± 14 , respectively. Though in all cases the global gas-to-dust ratios are low compared to the Galactic value, they are consistent with the lower end of the range of values in Draine et al. (2007) (correcting for the different X-factor used). In Muñoz-Mateos et al. (2009), Sb and Sc galaxies have higher gas-to-dust ratios at larger radii than found in the current work. For NGC 4501, the global value is in good agreement with the average pixel-by-pixel value, which suggests that a similar increase with radius may not be present for this galaxy. We note that since NGC 4501 and NGC 4568 are mildly HI deficient (0.4–0.6, Chung et al., 2009), low global gas-to-dust values of these Virgo galaxies could arise from the stripping of the outer gas and dust disk caused by environmental effects (Cortese et al., 2010b). For the large sample of galaxies to be observed by HeViCS, we will be able to investigate whether this is a general feature of the cluster environment.

4.5 CONCLUSIONS

I have fitted SEDs on a pixel-by-pixel basis to investigate the dust mass, temperature, and gas-to-dust ratios of NGC 4501 and NGC 4567/8. The distribution of dust surface densities peak at the centre of the galaxy and decrease towards the outer regions. In contrast, the temperature distribution is asymmetric, higher temperatures peaking at some distance away from the centre of the galaxy and then decreasing with increasing radius towards the outskirts. Once the full HeViCS observations are complete, we will be able to extend the analysis to larger radii and lower dust surface densities. For ~ 48 late-type galaxies with optical radii greater than $3'$ to be observed with HeViCS, we will be able to begin to tackle questions about the dominant source of dust heating, how the dust interacts with the other phases of the ISM, and how morphology influences the dust distribution and temperature. By combining the results from HeViCS and the Herschel Reference Survey (Boselli et al., 2010b), we will be able to study how environment affects the dust distribution and other properties of a galaxy.

CHAPTER 5

DUST AND GAS IN ANDROMEDA

“Seize the time, Meribor. Live now; make now always the most precious time. Now will never come again”
Captain Picard - Star Trek: The Next Generation

This chapter presents a study of the dust and gas in Andromeda using data collected by the HELGA survey. This investigation was published in Smith et al. (2012a) and was entitled “The *Herschel* Exploitation of Local Galaxy Andromeda (HELGA) II: Dust and Gas in Andromeda”.

5.1 INTRODUCTION

Astronomy at long infrared wavelengths (20–1000 μm) is a relatively young field due to the need for space missions to avoid the absorption of the atmosphere in this waveband. This waveband, however, is vital for astronomical studies as this is where dust in the interstellar medium (ISM) radiates. This is important for studies of galaxy evolution as star formation regions tend to be dusty, and therefore the use of UV and optical measurements to trace the star formation rate can lead to it being underestimated (see Kennicutt, 1998a; Blain et al., 1999; Calzetti, 2001; Papovich & Bell, 2002; Calzetti et al., 2010). Calibrating the relationship between infrared emission and star formation rate (SFR) has been difficult due to uncertainties from the contribution of the general stellar population to heating the dust, the fact that not all optical/UV emission is absorbed, and uncertainties in the properties of the dust. The dust emission is affected by the composition of the dust and the proportion of non-equilibrium to equilibrium heating. Studies with previous space missions *IRAS*, *Infrared Space Observatory*, *Spitzer*, and *AKARI* tried to address these questions (e.g., Walterbos & Greenawalt, 1996; Boselli et al., 2004; Calzetti et al., 2010; Buat

et al., 2011). However, as they were limited to wavelengths less than $160\,\mu\text{m}$, they were not sensitive to the cold dust ($\leq 15\,\text{K}$) and missed up to 50% of the dust mass in galaxies.

The continuum emission from the dust has been proposed as a potential method of measuring the total mass of the ISM (Hildebrand, 1983; Guelin et al., 1993; Eales et al., 2010b, 2012); traditionally the amount of gas has been measured using HI and CO surveys, but due to sensitivity and resolution issues this method is limited to low redshift and small numbers of galaxies. Smith et al. (2012b) found that for early-type galaxies (E/S0) the ISM was detected for 50% of objects through its dust emission but only 22% through its CO emission. In addition, the conversion of the CO tracer to molecular gas mass is highly uncertain and is believed to vary with metallicity (see Wilson, 1995; Boselli et al., 2002; Strong et al., 2004; Israel, 2005; Narayanan et al., 2012). This is a topical area as recent studies using the Planck all-sky survey and *IRAS* maps have made an estimate of the amount of ‘dark gas’ (Planck Collaboration, 2011a) in the Milky Way (MW). The ‘dark gas’ is thought to be molecular gas which is traced by dust, but not detected with the standard CO method. Previous works have also suggested the presence of ‘dark gas’ by using γ -ray emission from cosmic-ray interactions with clouds of gas (Grenier et al., 2005; Abdo et al., 2010) and by the kinematics of recycled dwarf galaxies (Bournaud et al., 2007).

Herschel is one of the European Space Agency’s flagship observatories and observes in the far-infrared (FIR) in the range $55\text{--}671\,\mu\text{m}$ (see Pilbratt et al., 2010, and Section 1.4). Due to the large space mirror and cryogenic instruments, it has a high sensitivity and unprecedented angular resolution at these wavelengths. *Herschel* has the ability to target both large numbers of galaxies and map large areas of sky. It has two photometric instruments: PACS (Poglitsch et al., 2010) which can observe in three broad bands around 70 , 100 and $160\,\mu\text{m}$ (70 and $100\,\mu\text{m}$ cannot be used simultaneously) and SPIRE (Griffin et al., 2010) which observes simultaneously in filter bands centred at 250 , 350 and $500\,\mu\text{m}$. SPIRE provides flux measurements on the longer wavelength side of the FIR dust peak ($\sim 160\,\mu\text{m}$), allowing us to obtain a full census of dust in nearby galaxies (e.g., Dunne et al., 2011).

Andromeda (M 31) and the MW are the only two large spirals in the Local Group. Studies of Andromeda therefore provide the best comparison to observations of our own Galaxy with the advantage that we get a ‘global’ picture, whereas investigations of the MW are limited by our location within the Galaxy. The total size of M 31 and the scalelength of its disk are both approximately twice those of the MW (see Yin et al., 2009, and references therein). However, the SFR rate of the MW is $\sim 3\text{--}6\,M_{\odot}\,\text{yr}^{-1}$ (Boissier & Prantzos, 1999) compared to only $\sim 0.3\text{--}1.0$ in M 31

(Barmby et al., 2006; Williams, 2003; Ford et al., 2012), despite similar amounts of gas present (Yin et al., 2009). For this reason, M 31 is often labelled as “quiescent”. The dust emission from M 31 is dominated by a dusty star-forming ring at a radius of 10 kpc and was first observed in the infrared by *IRAS* (Habing et al., 1984).

Many projects to map the ISM in M 31 have been undertaken using observations in the mid-infrared (MIR) with *Spitzer* (Barmby et al., 2006), in the FIR with *Spitzer* (Gordon et al., 2006), in the HI atomic line (Thilker et al., 2004; Braun et al., 2009; Chemin et al., 2009), and in the CO($J=1-0$) line (Nieten et al., 2006). Studies of the gas kinematics and dust emission show that M 31 has a complicated structure (e.g., Chemin et al., 2009; Gordon et al., 2006); Block et al. (2006) attribute many of the features observed to density waves from a possible head-on collision with M 32. Tabatabaei & Berkhuijsen (2010) investigated the relation between gas, dust, and star formation using FIR *Spitzer* data. Leroy et al. (2011) used *Spitzer* and gas observations to investigate the conversion between CO($J=1-0$) line flux and molecular hydrogen column density in a sample of nearby galaxies including M 31. In their analysis they found M 31 has the lowest dust temperatures in their sample and therefore would benefit most by including *Herschel* data.

The *Herschel* Exploitation of Local Galaxy Andromeda (HELGA) is a survey covering a $\sim 5.5^\circ \times 2.5^\circ$ area centred on M 31. We use PACS–SPIRE parallel mode, observing at 100, 160, 250, 350, and 500 μm simultaneously. Further details of the observations can be found in Section 5.2.1 and in Fritz et al. (2012). HELGA observations have been used in other works to investigate structures in dust and HI at large radii (Fritz et al., 2012), the relationship between gas and star formation (Ford et al., 2012), and the structure of M 31 and the cloud-mass function (J. Kirk et al., in preparation).

In this chapter, I use the *Herschel* data combined with the wealth of ancillary data to investigate the distribution, emission properties, and the processes heating the dust in M 31 on spatial scales of ~ 140 kpc. There have still been relatively few attempts to map the dust within a galaxy; recent studies with *Herschel* include Smith et al. (2010), Boquien et al. (2011), Foyle et al. (2012), Bendo et al. (2012b), and Mentuch Cooper et al. (2012), but they are often limited to small numbers of independent pixels. The advantage of M 31 over these other studies is the close proximity which allows us to investigate the dust at higher spatial scale and with many more independent pixels. I also apply the Planck method for finding ‘dark gas’ (Planck Collaboration, 2011a) to M 31 and use this method to determine a value of the X-factor—the relationship between the molecular hydrogen column density and the observed CO tracer. In Section 5.2, I present the data used for this analysis and Section

5.3 describes our method for fitting the spectral energy distribution (SED) of dust. Section 5.3.3 presents our maps of the dust properties, including the distribution of dust surface density, temperature, and spectral index. This section also describes a comparison of the distributions of gas and dust and of the search for an excess emission at long wavelengths. In Section 5.5, I discuss the dust properties including the composition of the dust and the processes heating the dust. In this section, I also search for ‘dark gas’ and determine the value of the X-factor. The conclusions are presented in Section 5.6.

5.2 THE DATA

5.2.1 FAR-INFRARED OBSERVATIONS

Herschel observations of M31 were taken using both PACS and SPIRE in parallel mode covering an area of $\sim 5.5^\circ \times 2.5^\circ$ centred on M31. To observe an area this large, the observations were split into two halves with a cross-scan on each half, which produced data at 100, 160, 250, 350 and 500 μm simultaneously (observation IDs: 1342211294, 1342211309, 1342211319, 1342213207). Full details of the observing strategy and data reduction can be found in Fritz et al. (2012).

The PACS data reduction was performed in two stages. The initial processing up to Level-1 (i.e., to the level where the pointed photometer timelines have been calibrated) is performed in HIPE v8.0 (Ott, 2010) using the standard pipeline. To remove low-frequency noise (or drifts) in the arrays, residual glitches and create the final maps we use SCANAMORPHOS (v15; Roussel, 2011, submitted). The final maps have a pixel scale of 2'' and 3'' and a spatial resolution of 12.5'' and 13.3'' full width at half maximum (FWHM) at 100 and 160 μm , respectively.

The SPIRE data were processed up to Level-1 with a custom pipeline script adapted from the official pipeline. The latest flux correction factors from the SPIRE Instrument Control Centre are applied to update the maps to the latest calibration product (SPIRE Observers’ Manual, 2011). For the baseline subtraction we use a custom method called BRIGADE (see Section 2.4) which uses an alternative technique for correcting temperature drifts. The final maps were created using the naive mapper with pixel sizes of 6'', 8'', and 12'' with spatial resolution of 18.2'', 24.5'', 36.0'' FWHM for the 250, 350, and 500 μm maps, respectively. All *Herschel* images are shown in Figure 5.1.

In addition to the *Herschel* data, I make use of the 70 μm *Spitzer* MIPS (Rieke et al., 2004) map published in Gordon et al. (2006). This observation covers a region

of M31 approximately $3^\circ \times 1^\circ$ in size and has an exposure time of ~ 40 s pixel $^{-1}$. The data were processed using the MIPS Data Analysis Tool, version 2.90 (Gordon et al., 2005) and full details of the reduction can be found in Gordon et al. (2006).

5.2.2 GAS MEASUREMENTS

To investigate the atomic hydrogen in Andromeda I use the HI moment-zero map presented in Braun et al. (2009). The observations were made with the Westerbork Synthesis Radio Telescope covering a region of $\sim 6^\circ \times 3.5^\circ$ with a resolution of $18'' \times 15''$. In this work, I present our results using a map which has not been corrected for opacity effects since this correction is uncertain. For the results which make use of the HI map we also test how our results are affected by using an HI map corrected for self-opacity using the prescription outlined in Braun et al. (2009). The uncorrected HI map has a sensitivity of $4.2 \times 10^{18} \text{ cm}^{-2}$.

For the molecular hydrogen gas content we use CO($J=1-0$) observations presented in Nieten et al. (2006) made with the IRAM 30m telescope. This covers an area of $2^\circ \times 0.5^\circ$ with a sensitivity of $\sim 0.35 \text{ K km s}^{-1}$.

All maps other than the *Herschel* images used for this analysis are shown in Figure 5.2.

5.3 THE FIR–SUBMILLIMETER SPECTRAL ENERGY DISTRIBUTION

To investigate how the dust properties vary across M31, we undertake a pixel-by-pixel dust analysis, using the *Spitzer* 70 μm , *Herschel* PACS, and SPIRE images. We first convolve the data to the same resolution as the 500 μm map (our largest FWHM) by using a kernel which matches the point-spread function in a particular band to the 500 μm band. This procedure is described in detail in Bendo et al. (2012b). The images are then re-binned into $36''$ pixels, chosen to be about the same size as the 500 μm beam, so that each pixel is approximately independent of its neighbours. For each band we subtract a background value for the whole map, estimated from regions around the galaxy. The uncertainties on the flux in each pixel are found by measuring the standard deviation of the pixels in these background regions and adding this in quadrature with the calibration uncertainty. The flux errors in the majority of pixels are dominated by the calibration uncertainty which we take as 7% for *Spitzer* 70 μm (Gordon et al., 2007), 10% for PACS (see Fritz et al., 2012) and 7% for SPIRE (see Section 5.3.1 for more details).

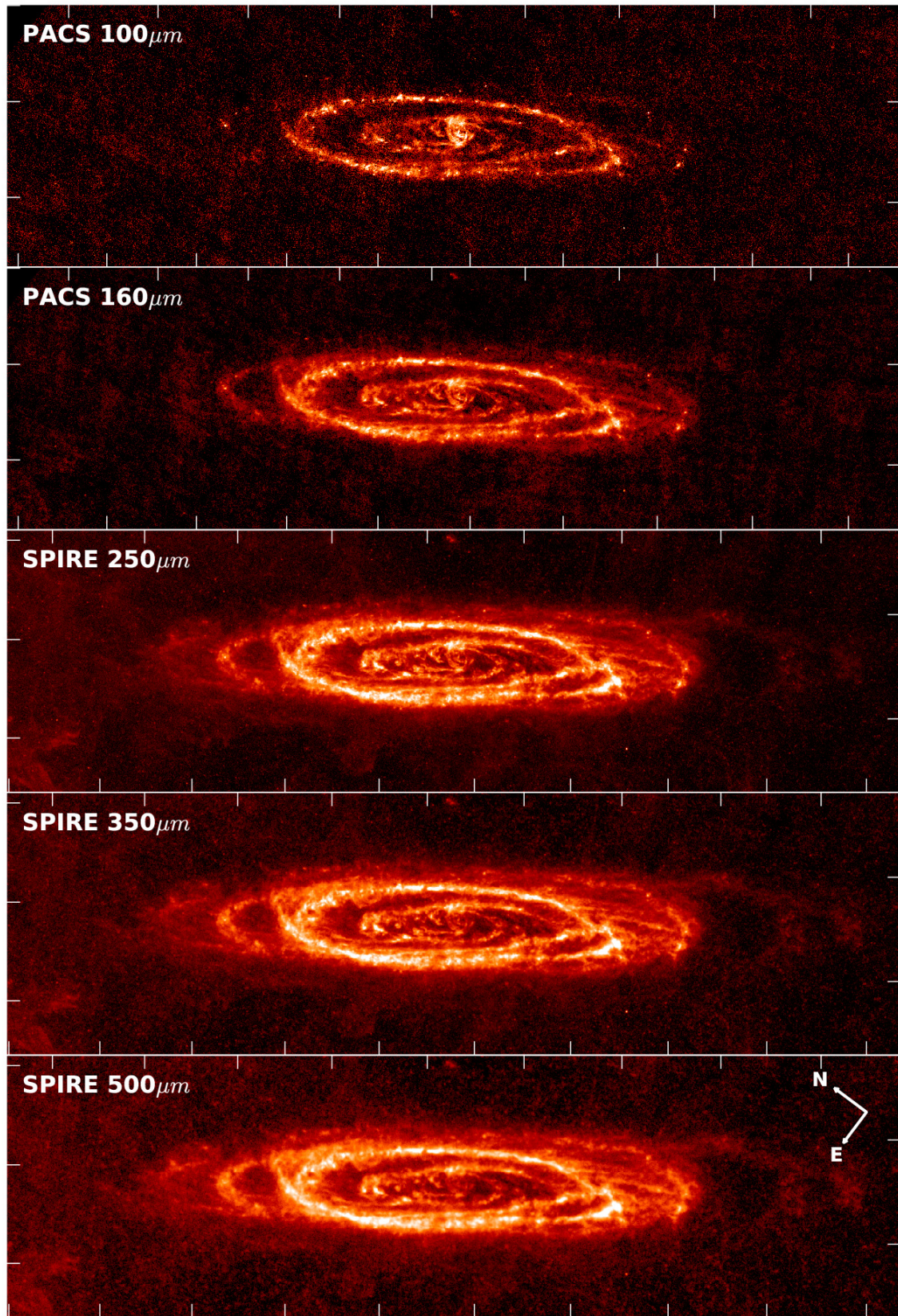


Figure 5.1. *Herschel* images used in the analysis of this paper. The images have dimensions of approximately $4.5^\circ \times 1.3^\circ$, with a tick spacing of $30'$ and centered on $10^{\text{h}}43^{\text{m}}02^{\text{s}}$, $+41^\circ17'42''$. These images are all at their original resolution.

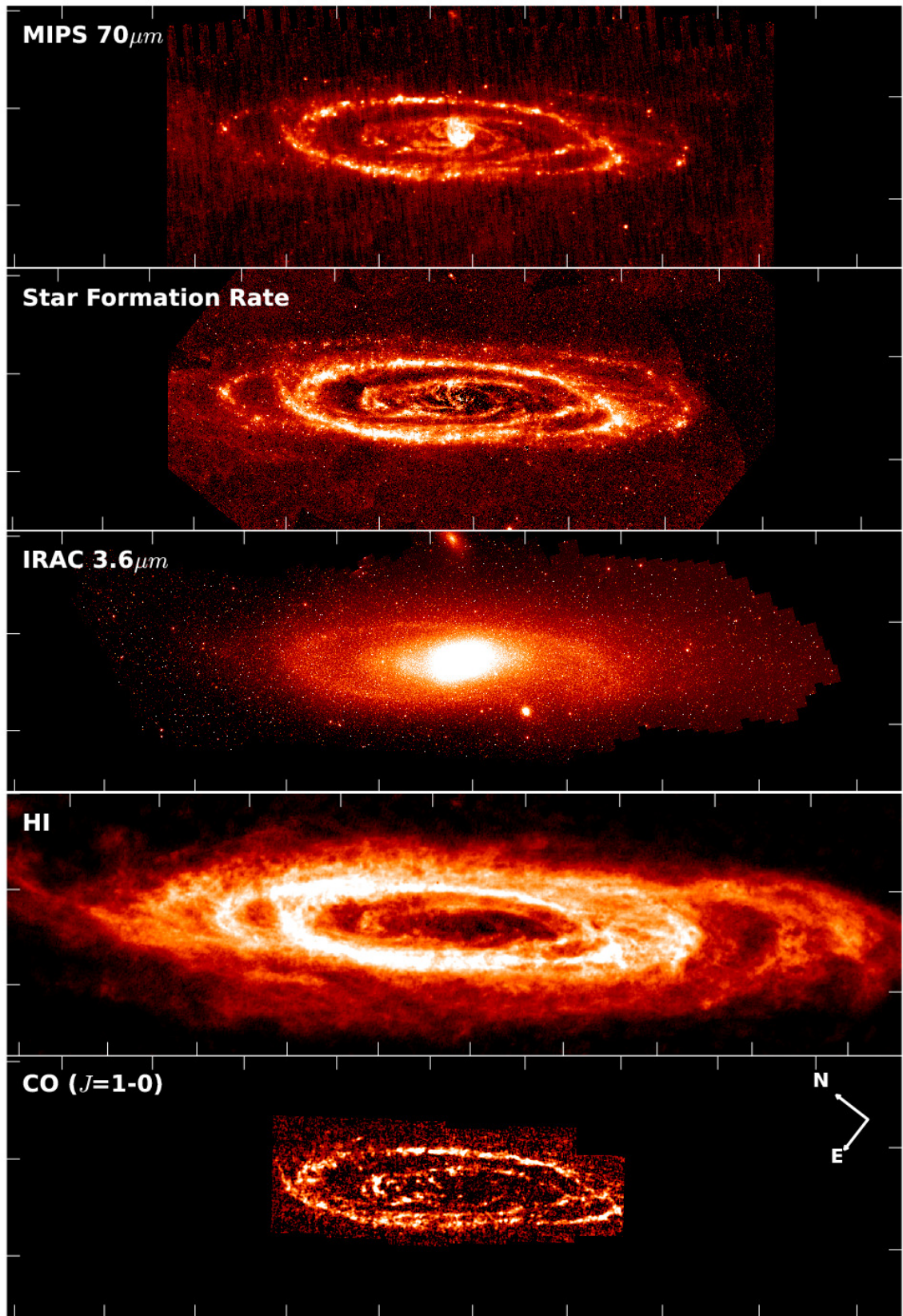


Figure 5.2. Ancillary images for M31. The scale is the same as for the *Herschel* images presented in Figure 5.1. From top: *Spitzer* MIPS $70\mu\text{m}$, the star formation rate (presented in Ford et al., 2012), *Spitzer* IRAC $3.6\mu\text{m}$ (presented in Barmby et al. 2006), HI and CO images as in Figure 5.1. The CO map (used as a tracer of H₂) only covers an area of $2^\circ \times 0.5^\circ$. These images are all at their original resolution.

5.3.1 SED FITTING

For each pixel we fit the far-infrared–submillimetre SED with a one-temperature modified-blackbody model described by

$$S_\nu = \frac{\kappa_\nu M_d B(\nu, T_d)}{D^2}, \quad (5.1)$$

where M_d is the dust mass with dust temperature T_d , $B(\nu, T_d)$ is the Planck function, and D is the distance to the galaxy. κ_ν is the dust absorption coefficient, described by a power law with dust emissivity index β such that $\kappa_\nu \propto \nu^\beta$ (for more information see Section 3.4). We assume a typical value for the ISM of $\kappa_{350\mu\text{m}} = 0.192 \text{ m}^2 \text{ kg}^{-1}$ (Draine, 2003). While the absolute value of κ_ν is uncertain, its value will not affect trends with other parameters as it is a fixed scaling constant. The distance to Andromeda was taken in this work to be $D = 0.785 \text{ Mpc}$ (McConnachie et al., 2005).

We initially used a fixed value of β across the whole galaxy, but we found that with a fixed value it was impossible to adequately fit the SEDs; we therefore let β be a free parameter. To ensure the simplex fitting routine did not get stuck in a local minimum, we ran the SED fitter in two ways: first with all three parameters (M_d , T_d , β) free to vary; second by fixing the value of β while allowing M_d and T_d to vary and repeating the process for all values of β in the range 0.20–5.90 in 0.01 intervals, selecting the result with the lowest χ^2 . Both methods gave consistent results but we created the final maps of the dust properties by choosing the result with the lowest χ^2 for each pixel.

The SPIRE calibration has an overall systematic uncertainty of 5% due to the uncertainty in the prime calibrator Neptune, and a statistical uncertainty of 2% determined from instrumental reproducibility; the SPIRE Observer’s Manual recommends linearly adding these to give an overall uncertainty of 7%. To implement this in practice in our fitting algorithm we increased the uncorrelated uncertainty to give the same overall calibration uncertainty when the errors are added in quadrature. This is implemented in the SED fitting by using the full covariance matrix in the χ^2 calculation (see 3.4.5). Including the full covariance matrix with the correlated uncertainties allows for the SPIRE points to have a systematic shift in flux values compared to data from other instruments.

We apply our own color correction to the *Herschel* maps by removing the *Herschel* pipeline ‘K4’ parameter and then convolving the SED with the filter transmission in the fitting process (for SPIRE the filters appropriate for extended sources are used). This method takes full account of all the wavelength-dependant effects associated with PACS and SPIRE. In previous work (Chapter 4, Smith et al., 2010)

we found that there is a significant contribution from a warmer component of dust at wavelengths $\leq 70\,\mu\text{m}$ and so the *Spitzer* flux at $70\,\mu\text{m}$ is treated as an upper limit in the fitting (i.e., if the flux value is higher than the model it does not contribute to χ^2). The omission of the warm component in the fitting process has a negligible effect on the derived dust mass as the cold component dominates the total dust mass. Bendo et al. (2012b) suggest that a warmer component could influence the dust emission up to wavelengths of $160\,\mu\text{m}$; to test this we repeated the SED-fitting by treating the *Spitzer* and PACS fluxes as upper limits and found it made a negligible difference to our results.

To estimate the uncertainties on the results of our fits we use a Monte Carlo technique. For each pixel we create a set of 1000 artificial SEDs, created by taking the original flux densities and adding a random value selected from a normal distribution with a mean of zero and a standard deviation equal to the uncertainty in the measured flux (the correlations between the calibration uncertainties for SPIRE are also included). We estimate the error in the derived parameters for each pixel from the 1000 fits. We find that for each pixel there is an uncertainty of 20% in our estimate of the surface density of the dust, of $\pm 1.4\,\text{K}$ in our estimate of the dust temperature, and ± 0.31 in our estimate of β .

5.3.2 RESULTS OF THE FITS

In producing the final dust mass, temperature, and β images in this work, we only used pixels where the fluxes in all six bands (five *Herschel* and MIPS $70\,\mu\text{m}$) have a signal-to-noise greater than 5σ . While this potentially causes us to miss the very coldest dust due to weak emission in the shortest wavelength bands, we choose it as a conservative approach to ensure we have accurate estimates of temperature. In practice it is the $100\,\mu\text{m}$ map, which has the lowest sensitivity, which limits the number of pixels in our selection. Despite this very conservative selection, there are still ~ 4000 pixels in our resultant maps. To see if our model is a statistically reasonable fit to the data, we created a histogram of the χ^2 values for all pixels (Figure 5.3). As the $70\,\mu\text{m}$ flux is used as an upper limit (see Section 5.3.1) and is usually higher than the best-fit model it does not usually contribute to χ^2 and therefore we only have 1 degree of freedom ($5_{\text{data points}} - 3_{\text{parameters}} - 1$). The 10% significance level for χ^2 occurs at 2.71 which is shown by the red line in Figure 5.3. We find 9.8% of our fits have χ^2 above this level showing our model is an adequate representation of the data. We have also checked to see if our radial gradients in temperature, β , and dust surface density are affected by lowering the criteria to include fluxes greater than 3σ

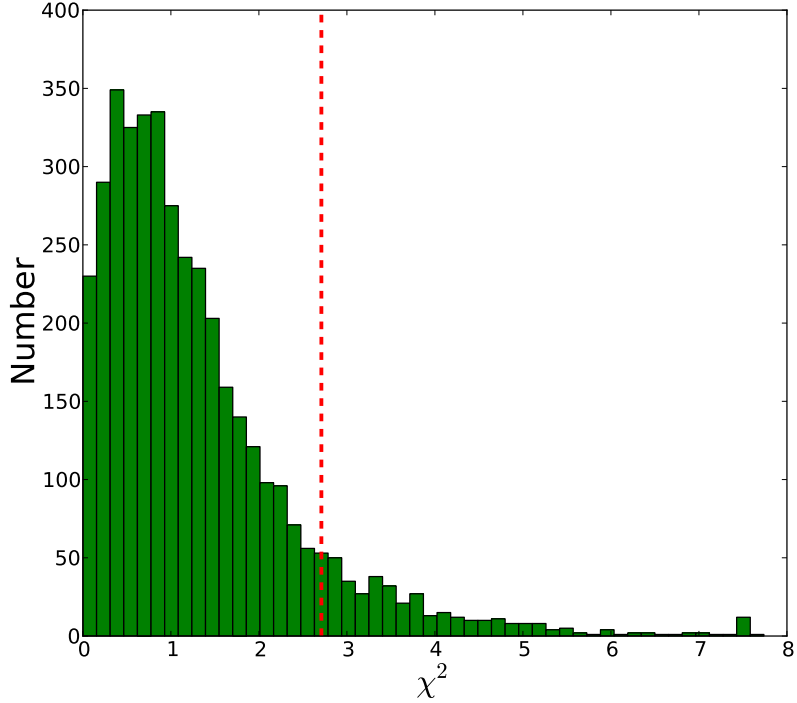


Figure 5.3. Distribution of χ^2 values from pixels fitted with the modified-blackbody model. The red line represents the 10% significance value for 1 degree of freedom.

and find no significant changes.

Recent results from the Key Insight on Nearby Galaxies: A Far-Infrared Survey with *Herschel* (KINGFISH) presented in Dale et al. (2012) have suggested that the one-temperature modified-blackbody model underestimates the dust mass compared to the Draine & Li (2007b) prescription. They attribute this difference to the contribution of warm dust emitting at shorter wavelengths. For our analysis this does not appear to be the case. First when we set the PACS fluxes ($\leq 160 \mu\text{m}$) as upper limits there is no significant change in our results. Second, if multiple temperature components were present this would bias our β values to lower values (since each temperature component peaks at a different wavelength; Shetty et al., 2009b), but we mostly find higher β values than expected (see Section 5.3.3). Third the χ^2 analysis suggests the model is consistent with the data. In addition, Mentuch Cooper et al. (2012), using a similar analysis, have found in M51 that the dust mass distribution is similar when using the Draine & Li (2007b) or the single modified blackbody prescription.

We applied the same fitting technique as outlined in Section 5.3.1 to the global flux densities, measured in an elliptical aperture with a semi-major axis of 2.0° and semi-minor axis of 0.73° . This produces a total dust mass of $10^{7.86 \pm 0.09} M_\odot$ with a dust

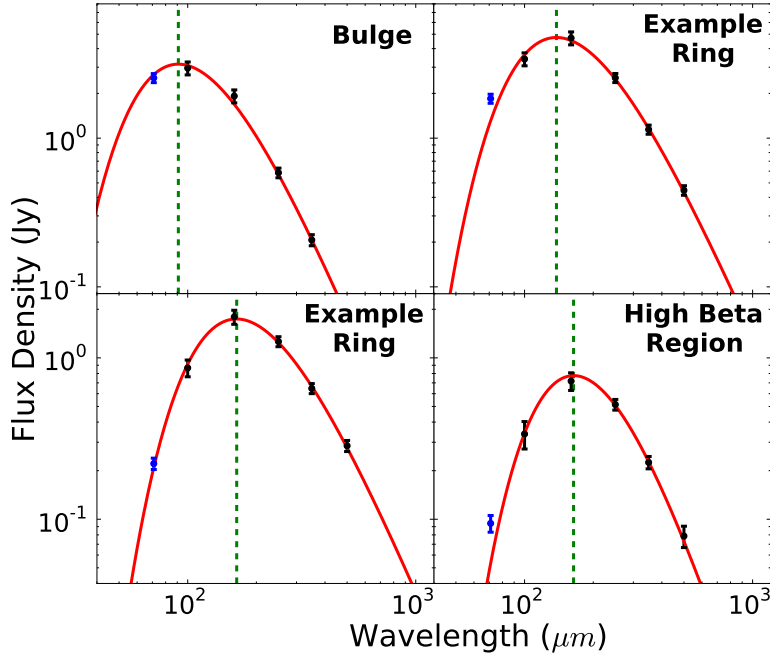


Figure 5.4. Examples of SED fits for pixels in different regions. The $70\,\mu\text{m}$ point (blue) is used as an upper limit and the peak of distribution is shown by the dashed green line.

temperature of $16.1 \pm 1.1\,\text{K}$ and $\beta = 1.9 \pm 0.3$. The total dust mass from summing all the pixels in our pixel-by-pixel analysis gives a value $10^{7.46} M_{\odot}$, a factor of ~ 2.5 lower. This is expected as the fraction of $500\,\mu\text{m}$ flux in the pixels which satisfy our signal to noise criterion is approximately half the global value. Combining our global dust mass with gas measurements, we find a global gas-to-dust mass ratio of 72. The global temperature is consistent with these for other spiral galaxies obtained using similar methods (e.g., Davies et al., 2012). The pixel-by-pixel analysis shows a large range of temperatures and β values as discussed in detail in Section 5.3.3. Examples of fits for individual pixels are shown in Figure 5.4.

5.3.3 SIMULATIONS

To help understand the significance of our results and any potential biases or degeneracies in the parameters, we ran a Monte-Carlo simulation. Assuming the dust emits as a single-component modified blackbody, we generated synthetic flux values for a range of temperatures and β values, with the same wavelengths as our real data. Noise was then added to the simulated fluxes with a value equal to the errors in the real fluxes (excluding the calibration errors) for 2000 repetitions per T, β combination. The calibration error was not included as it would systematically

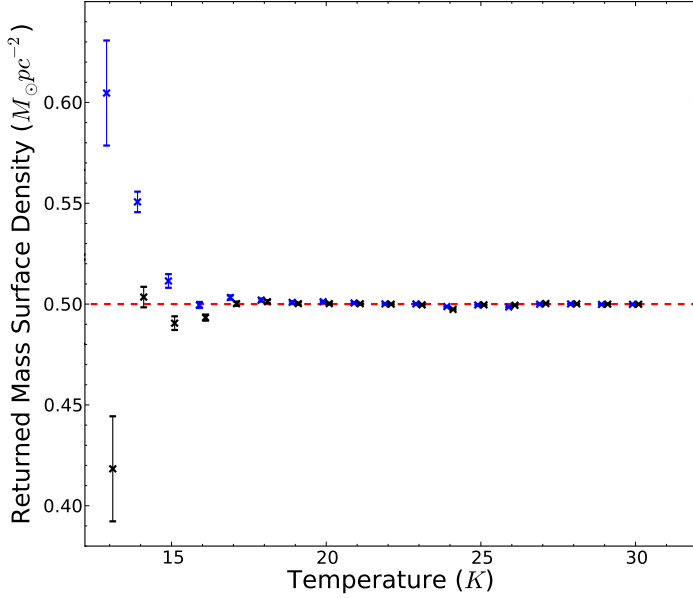


Figure 5.5. Range of mass surface densities returned from the SED-fitting technique vs. the input temperature for the simulated data in Section 5.3.3 with $\beta = 2$ modified-blackbody. The mean of the returned masses is shown by the blue points and the median is shown by the black points. The input mass surface density of $0.50 M_{\odot} \text{ pc}^{-2}$ is shown by the red dashed line. To avoid overlapping data points the blue have been shifted by -0.1 K and the black by $+0.1 \text{ K}$.

shift the fluxes for all pixels. We chose an input mass surface density of $0.5 M_{\odot} \text{ pc}^{-2}$ as this roughly corresponds to the values found in the 10 kpc ring.

The quantity that is most important for our work is the dust mass, which from Equation 5.1 is just a multiplicative term. Figure 5.5 shows the mean and median mass returned for the 2000 repetitions as the input temperature is varied between 12 and 30 K for a β of 2; the error bars show the error on the mean. Between 15 and 30 K, the mean and median dust mass returned matches within the errors the input dust surface density of $0.50 M_{\odot} \text{ pc}^{-2}$.

At dust temperatures of 15 K and below, there are large errors on the returned mass, which is due to the fluxes at the PACS wavelengths not reaching the required sensitivity to be included in the fit. For the actual data, we only included pixels in which there is at least a 5σ detection in all bands, which will avoid the wildly incorrect estimates of the dust mass seen in the simulation. To fully estimate the dust mass and temperature of very cold dust ($T < 15 \text{ K}$), we need flux measurements at $>500 \mu\text{m}$. Nevertheless, the lack of an excess at $500 \mu\text{m}$ (Section 5.4.2) is circumstantial evidence that Andromeda does not contain very cold dust. We investigated if the results in Figure 5.5 were different for a different choice of β but found no systematic differences.

By plotting the difference in the resultant temperature in each pixel compared to the input model temperature, we find that between 15 K and 25 K, the temperature uncertainty is ~ 0.6 K. Above 25 K the uncertainty increases, although in the simulation we did not include a 70 μm point which would likely provide a constraint to our fits if the dust temperature was > 25 K. The simulation suggests that for input β between 1.5 and 2.4, the uncertainty in the returned value of β for each pixel is ~ 0.1 . As expected these uncertainties are lower than returned by the Monte Carlo technique in Section 5.3.1 as we have not included a calibration uncertainty.

A degeneracy is known to exist between temperature and β ; Figure 5.6 shows that if there is an error in one parameter this is anti-correlated with the error in the other parameter. As the distribution is centered on the origin, there is no systematic offset in the returned value of T or β . As there is no systematic offset, the error in the mean values over many pixels will therefore be much smaller than the error for a single pixel.

This simulation is based on the dust emission arising from a one-component modified blackbody. Fitting a one-component modified blackbody to pixels for which there are multiple temperature components would produce a bias toward smaller values of β (Shetty et al., 2009b), although we would hope to detect this by finding high χ^2 values. In Section 5.5.2 we show that different regions of M31 have different β - T relations and discuss why this is unlikely to be due to multiple temperature components.

To summarise, while there is a β - T degeneracy from the fitting algorithm this does not create any systematic offsets in the value returned. If the dust temperature falls below 15 K we are unable to constrain the SED due to the lack of data points beyond 500 μm .

5.3.4 SPATIAL DISTRIBUTION OF DUST MASS, TEMPERATURE, AND EMISSIVITY INDEX

By fitting SEDs to every pixel, we have created maps of dust surface density, temperature, β , and gas-to-dust ratio which are shown in Figure 5.7 (for details on how the gas surface density is calculated see Section 5.4.1). The dust surface density distribution, unsurprisingly, is more similar to the maps of gas and SFR than to the 3.6 μm image (see Figure 5.1 and 5.2), which traces the stellar mass distribution.

The β and temperature maps show significant radial variations. Figure 5.8 shows how the dust column density, temperature, and β vary with radius (the physical radius is calculated assuming an inclination of 77° and P.A. of 38°; Fritz et al. 2012).

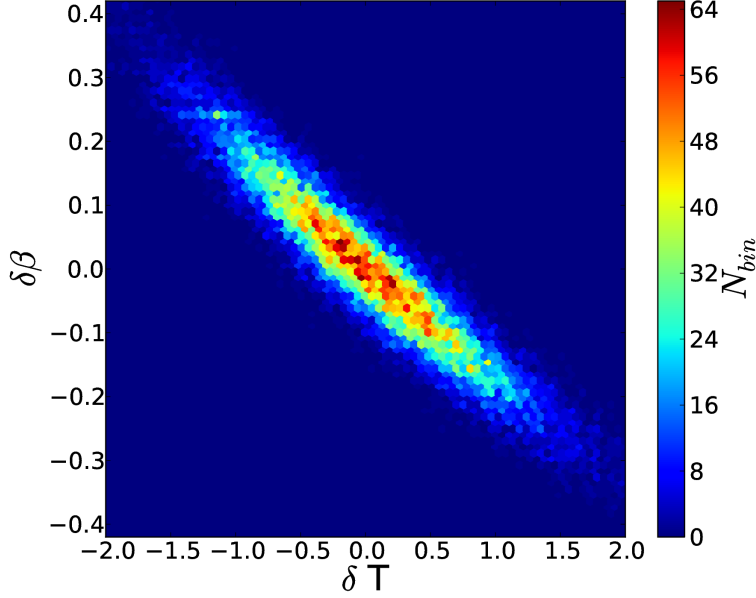


Figure 5.6. Density plot showing the correlated uncertainties between β and temperature. The uncertainties are taken from the simulated data with $T = 17\text{ K}$ and $\beta = 1.8$. A clear anti-correlation is observed with the distribution centred on the correct values. To fully populate this graph we increased the simulation to 20,000 repetitions for this β, T combination.

In the star-forming ring at 10 kpc, β has an average value of ~ 1.8 but increases with decreasing radius reaching a maximum of ~ 2.5 at a radius of $\sim 3\text{ kpc}$. This is higher than found in global studies of galaxies (Planck Collaboration, 2011a; Davies et al., 2012; Dunne et al., 2011). However similarly high values have been reported recently in Foyle et al. (2012) and Bracco et al. (2011) for dust within galaxies. The value for the ring agrees well with early results from Planck (Planck Collaboration, 2011a) for dust in the galactic disk and the solar neighbourhood. The 10 kpc ring has an average dust surface density of $\sim 0.6 M_{\odot} \text{ pc}^{-2}$ with a dust temperature of 18 K. Toward the very center of the galaxy the dust column density decreases to $\sim 0.04 M_{\odot} \text{ pc}^{-2}$, β values fall to ~ 1.9 , and the dust temperature increases to $\sim 30\text{ K}$.

5.4 RESULTS

In Figure 5.8, we see a clear break in the radial variation for both temperature and β at a radius $\sim 3\text{ kpc}$. We fit a model with two straight lines and a transition radius (using a simplex routine) to the β results. The same method is used with the temperature values but we set the transition radius to the value obtained from the fit to the β values, which occurs at 3.1 kpc (shown by the dashed green line in

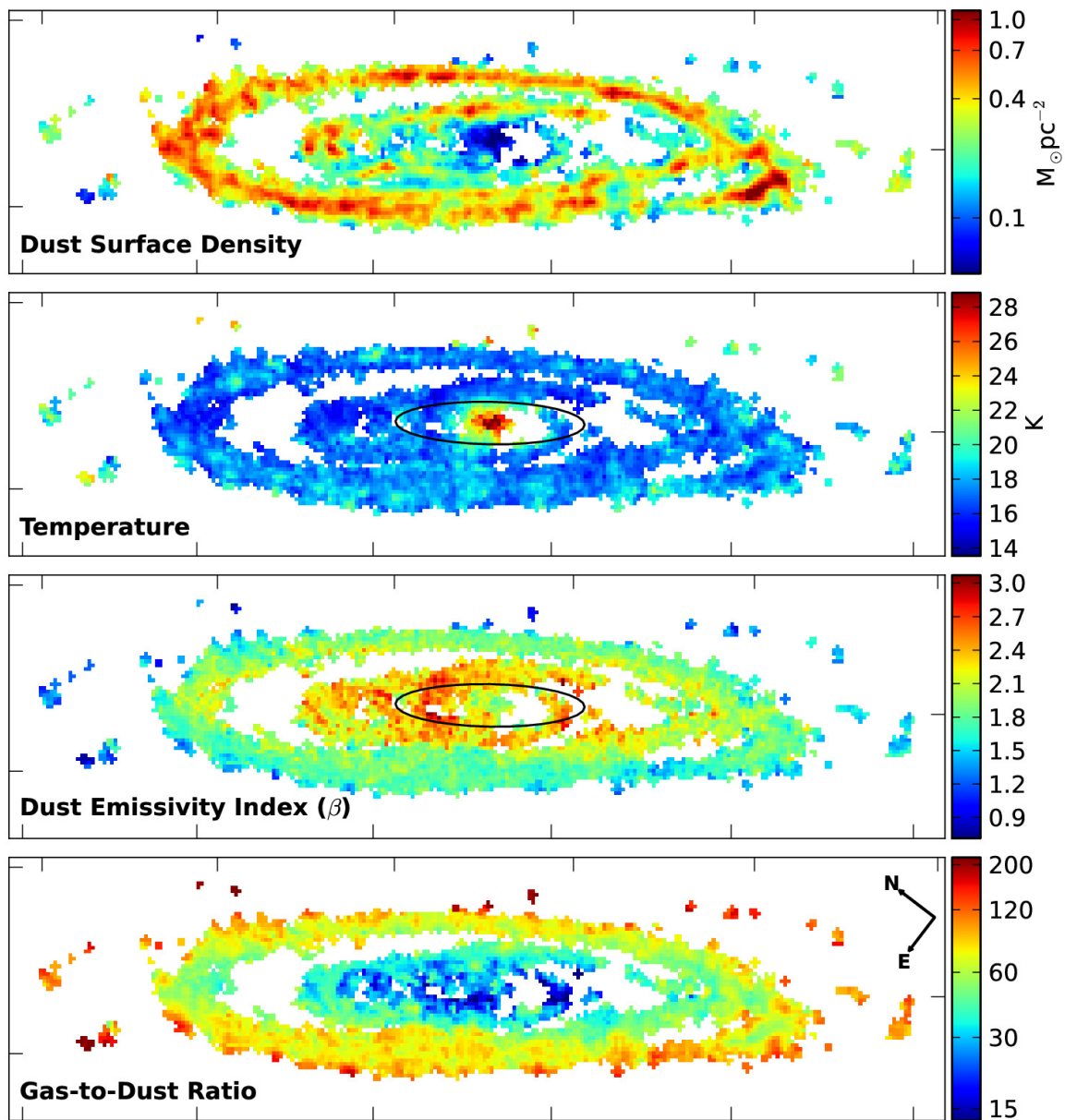


Figure 5.7. Distribution of dust surface density, temperature and β obtained from the SED-fitting technique and the distribution of the gas-to-dust ratio. The temperature and β images include a black ellipse showing a radius of 3.1 kpc. The ticks are plotted at 30' intervals.

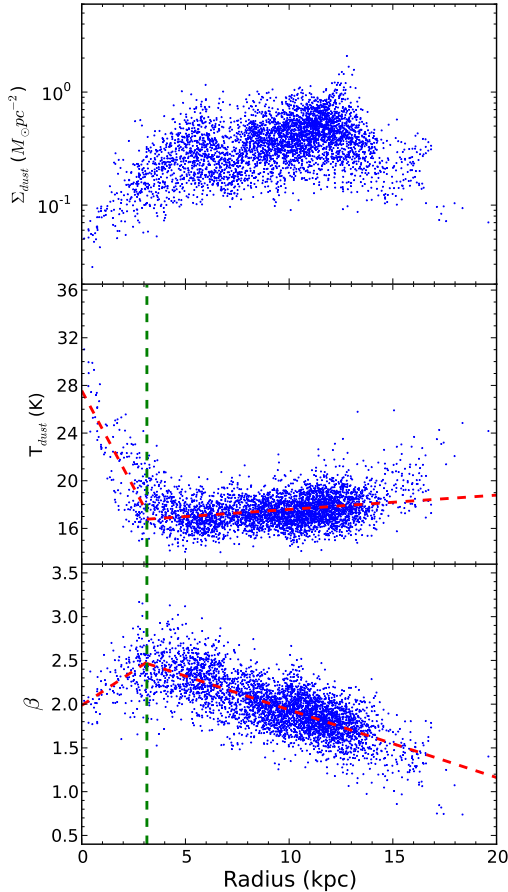


Figure 5.8. Results from the SED fits for each pixel plotted vs. radius. The dashed red lines represent the best-fit linear model (see Section 5.5.1), the dashed green line represents the transition radius (3.1 kpc) found when fitting the β results.

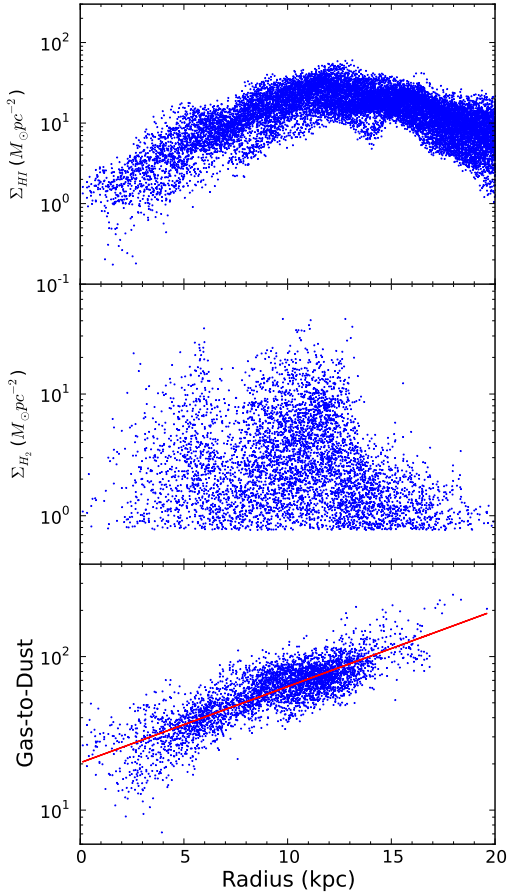


Figure 5.9. Distribution of atomic, molecular and gas-to-dust ratio vs. radius. The two gas maps are plotted for all pixels $> 3\sigma$. The solid red line represents the best-fit exponential profile to the gas-to-dust ratio.

Figure 5.8 or black ellipse in Figure 5.7). At radii smaller than the transition radius, the temperature decreases with radius from ~ 30 K in the center to ~ 17 K, with an associated increase in β from ~ 1.8 to ~ 2.5 . At radii larger than the transition radius the dust temperature slowly increases with radius while β decreases with radius to ~ 1.7 at 13 kpc. The best-fit relationships between T_d , β , and R are shown in Figure 5.8 and listed below:

$$\beta = 0.15R(\text{kpc}) + 1.98 \quad R < 3.1 \text{ kpc} \quad (5.2)$$

$$= -0.08R(\text{kpc}) + 2.70 \quad 3.1 \leq R < 20 \text{ kpc} \quad (5.3)$$

$$T_d = -3.24R(\text{kpc}) + 27.56 \quad R < 3.1 \text{ kpc} \quad (5.4)$$

$$= 0.12R(\text{kpc}) + 16.40 \quad 3.1 \leq R < 20 \text{ kpc} \quad (5.5)$$

We discuss the cause of the temperature and β variations in Section 5.5. For Sections 5.5.1 and 5.5.2, we consider the inner ($R < 3.1$ kpc) and outer regions separately.

5.4.1 RADIAL DISTRIBUTION OF GAS AND DUST

In Figure 5.9 the radial variations of the atomic gas, the molecular gas, and the gas-to-dust ratio are shown. We assume an X-factor of $1.9 \times 10^{20} \text{ cm}^{-2} [\text{K kms}^{-1}]^{-1}$ (Strong & Mattox, 1996) to convert a CO line flux to an H₂ column density, although this value is notoriously uncertain (by a factor of ~ 2) and has been found to vary with metallicity (Strong et al., 2004; Israel, 2005). For our analysis of M31, the choice of X-factor makes very little difference as the total gas is dominated by the atomic phase. Out of the 3974 pixels plotted in the gas-to-dust figure, only 101 have a molecular fraction of $> 50\%$ and globally the molecular gas only constitutes $\sim 7\%$ of the atomic gas (Nieten et al., 2006). To estimate the total gas surface density we include the contribution of the atomic or molecular gas in each pixel if the value is greater than 3σ in their respective maps. Only 86 of our 5σ dust pixels are not covered by the CO($J=1-0$) observations; these pixels are in the outskirts of the galaxy and we assume that the contribution of molecular gas is negligible. We find a tight relation between the gas-to-dust ratio and radius (Spearman rank coefficient of 0.80) as shown in Figure 5.9, which is described by an exponential profile, shown by the red line.

The gas-to-dust ratio increases exponentially from low values of ~ 20 in the center of the galaxy to ~ 110 at 15 kpc typical of the MW in the local environment (see Devereux & Young, 1990, and references therein). Note that the values are

not corrected for helium in the ISM. Metallicity gradients have been estimated from oxygen line ratios $[\text{OIII}]/\text{H}\beta$, $[\text{OII}]/[\text{OIII}]$ and R_{23} by Galarza et al. (1999). They infer a radially decreasing metallicity gradient of $-0.06 \pm 0.03 \text{ dex kpc}^{-1}$ from the R_{23} parameter. Trundle et al. (2002) calculate oxygen abundance gradients based on a set of 11 HII regions from Blair et al. (1982) and find gradients in the range of -0.027 to $-0.013 \text{ dex kpc}^{-1}$ depending on the calibration used. If a constant fraction of the metals in the ISM is incorporated into dust grains (Edmunds, 2001), one would expect the gas-to-dust gradient to be $-1 \times$ metallicity gradient. We find a gas-to-dust gradient of $0.0496 \pm 0.0005 \text{ dex kpc}^{-1}$ consistent within the uncertainties to the gradient measured by Galarza et al. (1999) (if the HI map corrected for self-opacity is used the gradient slightly increases to $0.0566 \pm 0.0007 \text{ dex kpc}^{-1}$). This supports the claim that gas can be well traced by dust if the metallicity is known, as the gas-to-dust ratio varies linearly with the metallicity (similar results have been found by Sandstrom et al., 2012). To see if the uncertainty in the choice of X-factor could affect this result, we carried out the same procedure but limited the analysis to pixels where the molecular hydrogen contribution is less than 10% of the total gas mass. This produced only a small change in the gas-to-dust gradient to $0.0550 \pm 0.0007 \text{ dex kpc}^{-1}$ which is still consistent with the metallicity gradient.

5.4.2 $500 \mu\text{m}$ EXCESS

Searches for a long-wavelength submillimetre excess (i.e., $>500 \mu\text{m}$) have been made in both the MW (Paradis et al., 2012) and for nearby galaxies. A submillimetre excess is important as it could suggest that very cold dust is present ($<15 \text{ K}$) which would dominate the dust mass in galaxies. Other possible explanations of an excess include variations in the dust emissivity index with wavelength (Wright et al., 1991; Reach et al., 1995; Paradis et al., 2012), different dust populations or contamination from a synchrotron radio source. Submillimetre excesses have been reported from observations of low-metallicity dwarf galaxies (see O'Halloran et al., 2010; Grossi et al., 2010; Dale et al., 2012) and spiral galaxies (see Zhu et al., 2009; Bendo et al., 2006). Most detections have been made by combining FIR data with ground-based data at $850 \mu\text{m}$ or 1 mm data rather than from data only at $\leq 500 \mu\text{m}$.

We searched for a submillimetre excess in M31 by comparing the $500 \mu\text{m}$ flux to our best-fit models. A $500 \mu\text{m}$ excess is defined to be any observed $500 \mu\text{m}$ flux that is greater than the expected flux at $500 \mu\text{m}$ from our modified-blackbody fit to the data. Figure 5.10 is a histogram of the ratio of the excess at $500 \mu\text{m}$ and the noise on the $500 \mu\text{m}$ map. The distribution of the excess is consistent with a

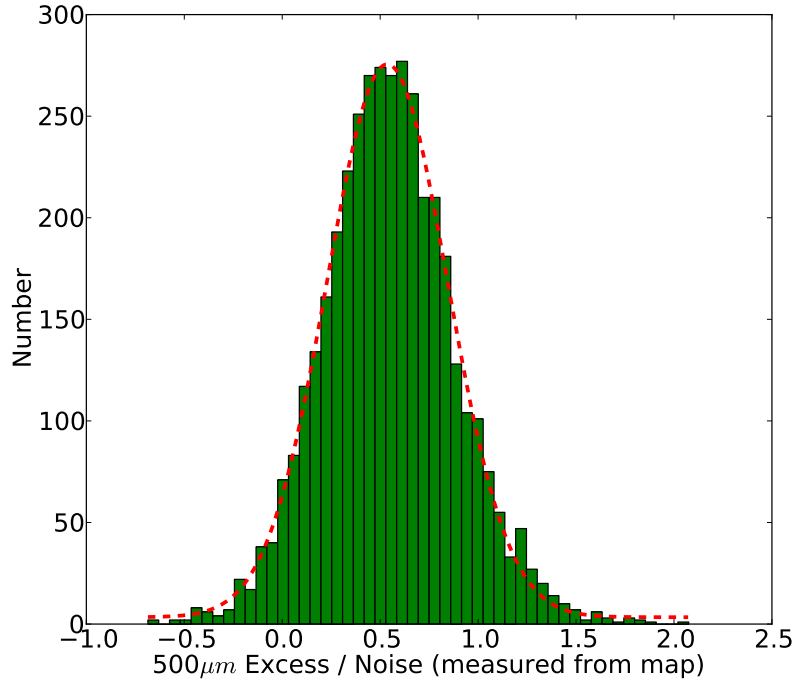


Figure 5.10. Value of the $500\mu\text{m}$ excess, defined as the $500\mu\text{m}$ flux from our blackbody model, divided by the noise. The red line is a Gaussian fit to the histogram.

Gaussian function with a mean of 0.54σ and standard deviation of 0.31σ . The fact the distribution of the histogram is a Gaussian suggests that what we are seeing is random noise with a fixed offset (not centered on zero). Two non-astronomical sources could explain a fixed offset, either an incorrect background subtraction or a calibration error. The background correction applied is quite small (0.2σ), and thus an error in this is unlikely to be the entire explanation of the offset. The distribution of the excess is consistent with the 2% random SPIRE calibration uncertainty, so both factors together could explain the small offset. If the excess is generated from dust with a 10 K temperature and β of 2, the dust mass is $\sim 10^{6.58} M_{\odot}$ in our $>5\sigma$ pixels, which corresponds to only 13% of the mass of the warmer dust. If we used a model containing dust at more than one temperature we would not get a useful constraint on the colder dust component without additional data at longer wavelengths. In particular observations at $\sim 850\mu\text{m}$ (e.g., with SCUBA2) would be useful to determine if any cold dust is present.

5.5 DISCUSSION

5.5.1 HEATING MECHANISMS AND DUST DISTRIBUTION

Recent studies by Bendo et al. (2010a, 2012b) and Boquien et al. (2011) have used *Herschel* colors to confirm previous works (e.g., Lonsdale Persson & Helou, 1987; Walterbos & Greenawalt, 1996) that emission from dust in nearby galaxies at wavelengths longer than $160\,\mu\text{m}$ is mostly from dust heated by the general stellar population. These authors conclude that at wavelengths shorter than $160\,\mu\text{m}$, the emission tends to be dominated from warmer dust heated by newly formed stars. Montalto et al. (2009) in a study of M31 using *Spitzer* MIR/FIR, UV and optical data, also concluded that the dust is mostly heated by an old stellar population (a few Gyr old). To investigate the relation between our derived dust properties and the SFR and the general stellar population, we have used the $3.6\,\mu\text{m}$ map presented in Barmby et al. (2006) to trace the general stellar population (rather than the luminous newly formed stars that dominate the UV) and a map of SFR. The SFR map is created from far-UV and $24\,\mu\text{m}$ images which have been corrected for the contribution of the general stellar population to the emission at these wavelengths (for details see Ford et al., 2012). These maps were all convolved to the same resolution and binned to the same pixel size as all the other maps in our analysis.

We have plotted the fluxes from these maps against the results of our SED fits (see Figure 5.11). In Section 5.3.4, we showed there is a clear break in the dust properties at a radius of 3.1 kpc. Therefore in Figure 5.11 the pixels at a radius less than 3.1 kpc are shown in blue and those at a radius above 3.1 kpc in green. For each graph (and both sets of pixels) the Spearman rank coefficient is computed and an estimate made of its significance (see Table 5.1). With such a large number of pixels, all but one of our correlations are formally significant. In the discussion, below we have concentrated on the strongest correlations as measured by the Spearman correlation coefficient.

There are strong correlations in Figure 5.11 between β and $3.6\,\mu\text{m}$ emission. We believe these are most likely to be caused by radial variations in β seen in Figure 5.8 and the decrease in $3.6\,\mu\text{m}$ brightness with radius. We discuss the possible cause of the radial variation in β in Section 5.5.2.

We find a strong correlation between dust surface density and the SFR in the outer regions, but not with the surface density of total stars traced by the $3.6\,\mu\text{m}$ emission. This correlation is expected as stars are formed in clouds of gas and dust. In the inner region there is an anti-correlation between the dust surface density and the $3.6\,\mu\text{m}$ flux, which seems most likely to be explained by both quantities varying

Table 5.1
Spearman Correlation Coefficients for Properties of M 31

Property A	Property B	Region	Spearman Coefficient	P-value
Dust Surface Density	3.6 μm flux	Inner	-0.73	1.52×10^{-28}
		Outer	-0.16	1.53×10^{-22}
	SFR	Inner	0.31	6.38×10^{-5}
		Outer	0.74	0.00
Temperature	3.6 μm flux	Inner	0.90	6.17×10^{-59}
		Outer	-0.09	7.46×10^{-9}
	SFR	Inner	0.04	5.97×10^{-1}
		Outer	0.14	3.70×10^{-19}
β	3.6 μm flux	Inner	-0.52	8.78×10^{-13}
		Outer	0.56	8.99×10^{-311}
	SFR	Inner	0.16	3.58×10^{-2}
		Outer	-0.24	2.85×10^{-52}

Notes. The Spearman rank-order correlation coefficient and P -value (for the null hypothesis that the two data sets are uncorrelated) for the scatter plots shown in Figure 5.11 (values were calculated using the `scipy.stats` package and checked with IDL `r correlate` routine). The inner and outer regions contain 164 and 3810 pixels, respectively.

with radius: the 3.6 μm emission from the bulge increasing toward the center and the dust surface density decreasing towards the center.

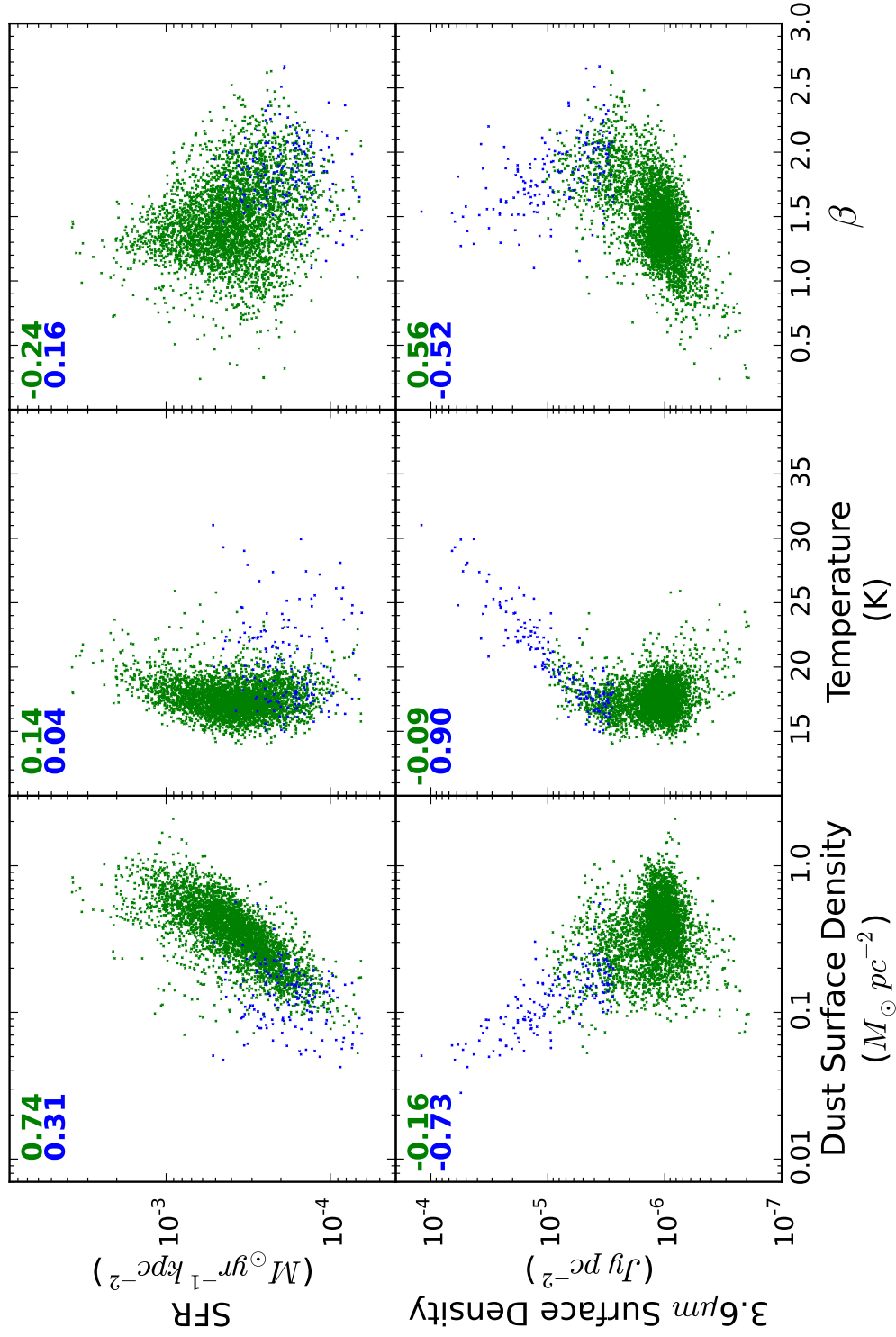


Figure 5.11. Scatter plots showing correlations between dust properties and 3.6 μm flux or SFR. The blue points are results at radii $< 3.1 \text{ kpc}$ and the green data points are results at radii $> 3.1 \text{ kpc}$. The Spearman rank-order coefficients for both sets of points are shown in the top-left corner of each plot.

The strongest correlation is seen between the dust temperature and the $3.6\mu\text{m}$ flux in the inner region. Figure 5.12 shows a log-log graph of the two quantities and a linear fit to the points. The gradient represents the power n where $F_{3.6\mu\text{m}} \propto T_{\text{dust}}^n$ where $n = 4.61 \pm 0.15$. While the correlation suggests the dust in the bulge is heated by the general stellar population, for a modified blackbody with $\beta = 2$ we would expect a gradient of 6. The difference is probably explained by the simplicity of our assumptions: that there is only a single stellar population in the bulge and that the bulge has a constant depth in the line of sight (LOS). If these assumptions are incorrect, the $3.6\mu\text{m}$ surface brightness of M31 will only be an imperfect tracer of the intensity of the interstellar radiation field (ISRF).

Looking at the temperature beyond 3.1kpc , we find a weak, but still highly significant, correlation with SFR, suggesting that the ISRF has a significant contribution from star-forming regions. As most of the star formation in M31 occurs in the 10kpc ring this is to be expected. This correlation can be seen in Figure 5.13 where most but not all of the temperature peaks in the 10kpc ring appear aligned with the peaks in the SFR map. In the same region there is a slight anti-correlation of temperature with the $3.6\mu\text{m}$ flux which could be explained by the radial decrease in the $3.6\mu\text{m}$ flux while the dust temperature increases slightly with radius. The fact that dust temperature increases slightly with radius, while the number-density of stars, traced by the $3.6\mu\text{m}$, is falling with radius suggests that outside the bulge the dust is mainly heated by young stars. Nevertheless, the lack of a strong correlation between dust temperature and either SFR or $3.6\mu\text{m}$ flux suggests that the optical/UV light absorbed by a dust grain is from photons from a large range of distances (e.g., photons from the bulge heating dust in the disk).

Bendo et al. (2012b) have studied FIR colour ratios in M81, M83, and NGC 4203. They find the $250/350\mu\text{m}$ color ratio has the strongest positive correlation with $1.6\mu\text{m}$ emission. An increase in the $250/350\mu\text{m}$ ratio would indicate either an increase in dust temperature or a decrease of β . Bendo et al. (2012b) conclude that the most likely explanation is the temperature effect, with the dust being heated by the general stellar population traced by the $1.6\mu\text{m}$ emission. We find a similar correlation to Bendo et al. (2012b), only we trace the stellar radiation field with the $3.6\mu\text{m}$ band. However, our SED-fitting results suggest that this is caused by a combination of changes in temperature and β . Note that since Bendo et al. (2012b) only use color ratios they are unable to discriminate between changes of temperature and β . At radii greater than 3.1kpc our results suggest that the variation in the $250/350\mu\text{m}$ ratio is mainly caused by a change in β . Bendo et al. (2012b) found that the $70/160\mu\text{m}$ color ratio has the greatest correlation with SFR, which is evidence that there is dust

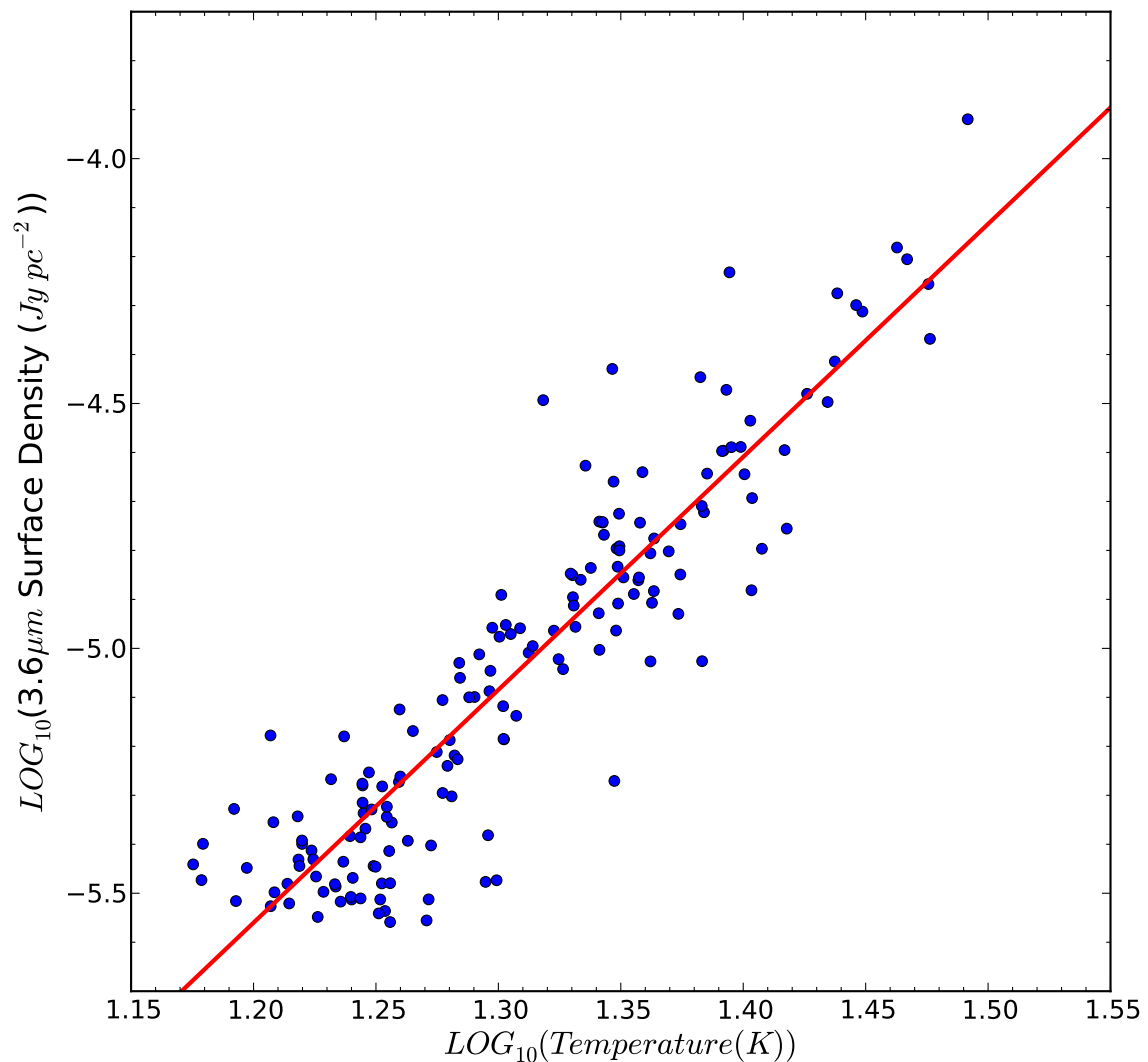


Figure 5.12. $\log(3.6\mu\text{m})$ flux vs. $\log(\text{Temperature})$ for the inner 3.1 kpc. The best-fit linear model is shown by the red line.

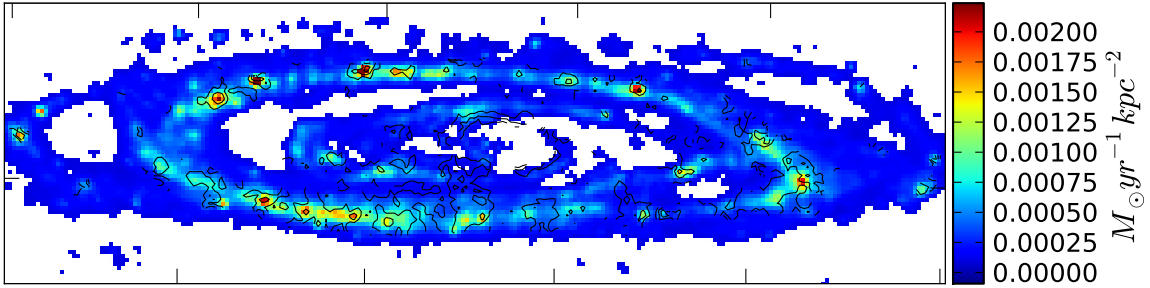


Figure 5.13. Color image shows the SFR image from Ford et al. (2012) which has been smoothed and re-gridded to match the maps presented in Figure 5.7. The contours are from the dust temperature map and drawn at 18.0, 19.5 and 21.0 K values.

at more than one temperature contributing to the 70–500 μm emission. One possible explanation of our failure to find a correlation between the 3.6 μm emission and dust temperature outside 3.1 kpc, instead of the negative correlation between 3.6 μm and β we find, might be if the *Herschel* emission at short wavelengths contains a contribution from a warmer dust component. This would mean our fits of a one-component modified blackbody would produce misleading results. However, as stated in Section 5.3.1 when we attempted the same SED-fitting process but using all flux densities $\leq 160 \mu\text{m}$ as upper limits, we see little difference in our results.

5.5.2 DUST EMISSIVITY AND TEMPERATURE RELATION

The dust emissivity index (β) is related to the physical properties of the dust grains, including the grain composition, grain size, the nature of the absorption process, and the equilibrium temperature of the dust. We would also expect to see a change in β due to environment from the processing of the grains via grain growth (e.g., coagulation, mantle accretion) or destruction through surface sputtering by ions/atoms or shattering by shocks. In M31, we detect an apparent inverse correlation between T_d and β for the inner and outer regions of M31, as shown in Figure 5.14. We find the form of the relation is different for the two regions.

Such an inverse relationship has been observed in the MW with previous FIR-submillimetre experiments and surveys including ARCHEOPS (Désert et al., 2008), which showed β ranging from 4 to 1 with the dust temperature varying between 7 and 27 K, and PRONAOS (Dupac et al., 2003), which shows a variation of β from 2.4 to 0.8 for dust temperatures between 11 and 80 K. Veneziani et al. (2010) used IR-mm data of Galactic high latitude clouds and found a similar trend, and more recently Paradis et al. (2010) with *Herschel* found a similar inverse relationship with

$\beta = 2.7\text{--}1.8$ for $T_d = 14\text{--}21\text{ K}$ for galactic longitude 59° (at longitude $30^\circ \beta = 2.6\text{--}1.9$ for $18\text{--}23\text{ K}$). Recently Bracco et al. (2011) used *Herschel*-ATLAS observations to investigate β variations in low-density, high-latitude galactic cirrus, measuring values of β ranging from 4.5 to 1.0 for $10 < T_d < 28\text{ K}$. These $T_d - \beta$ relationships could be indicative of a problem with the temperature– β degeneracy arising from the SED fitting, the presence of dust with a range of temperatures along the LOS (Shetty et al., 2009b), or real variations of the properties of the dust grains.

On the assumption that the inverse correlations between β and T_d in Figure 5.14 are not simply caused by the two variables being separately correlated with radius, we looked for other possible causes of the relationships:

1. The fitting can lead to a spurious inverse correlation between β and T_d (Shetty et al., 2009a, Section 5.3.3). The most striking feature in Figure 5.14 is the clear separation in points between the inner 3.1 kpc and the outer regions. To test whether these different distributions might be produced by the fitting process, we used the Monte Carlo simulations from Section 5.3.3 to simulate the effect of fitting a modified blackbody for various combinations of β and T_d . The grey lines in Figure 5.15 show the best-fit relationships for different input T_d and β combinations and clearly show that the two different relationships in the two regions cannot be obtained from a single population of dust grains. The green and blue data points represent the range of output T_d and β for an input modified blackbody with $T = 17.0\text{ K}$ (green) and $T = 25.0\text{ K}$ (blue), with $\beta = 2.0$. A comparison of Figures 5.14 and 5.15 shows that in both regions of M31 there is a larger range of temperature and dust emissivity for the real data than that found in the Monte Carlo simulation, indicating there are genuine variations of T_d and β in both regions. Moreover, the fitting artefact cannot explain the observed relationships of β and temperature with radius (Figure 5.8).
2. Artificial inverse $T_d - \beta$ relationships can also be produced if a one-component modified-blackbody model is used to fit dust which contains a range of dust temperatures (Shetty et al., 2009b). Since we are averaging through the disk of a galaxy along the LOS, it is obviously possible that the dust contains a range of dust temperatures. While we cannot fully address this issue, our β values are higher than expected, which is the opposite of what happens from an LOS averaging of temperatures. We also find no statistical evidence from our fits that there is more than one component of dust. Also Paradis et al. (2010) and Anderson et al. (2010) show that inverse $T_d - \beta$ relationships still exist in places

where it is unlikely there is dust at more than one temperature.

3. Variation of β with wavelength has been reported by some authors both from theoretical models and laboratory experiments and from observations (e.g., Meny et al., 2007; Coupeaud et al., 2011), with a transition around $500\,\mu\text{m}$. In Section 5.4.2, we show that there is no evidence for excess $500\,\mu\text{m}$ emission, suggesting that this is not an explanation of our results.

To describe the $T_d-\beta$ relationships we use an empirical model of the form $\beta = AT^\alpha$, commonly used in the literature (e.g., Désert et al., 2008; Paradis et al., 2010; Planck Collaboration et al., 2011) to fit the $T_d-\beta$ anti-correlation. The observed anti-correlation between T and β may arise due to a change in the physical properties of grains including the grain optical constants changing with temperature for amorphous grains or changes in the dust emissivity with wavelength (see Ysard et al., 2012, and references therein). Other possibilities include grain growth or quantum mechanical effects (though these latter grain properties only arise at lower dust temperatures than observed in M 31). The best-fit relationship which describes $T_d-\beta$ for $R < 3.1\,\text{kpc}$ and for $3.1 < R < 15\,\text{kpc}$ are (shown in Figure 5.14)

$$\beta = \begin{cases} 2.30(\frac{T_d}{20})^{-0.61} & R < 3.1\,\text{kpc} \\ 1.58(\frac{T_d}{20})^{-1.57} & 3.1 \leq R < 15\,\text{kpc}, \end{cases} \quad (5.6)$$

where the steeper $T_d-\beta$ relationship at $R > 3.1\,\text{kpc}$ agrees well with the relationship found in the plane of the MW at longitudes of 59° (Paradis et al., 2010) and in low-density, high-latitude cirrus (Bracco et al., 2011). There is some evidence that the $T_d-\beta$ relationship in M 31 is slightly steeper, so that for the same temperature compared to the galactic plane, M 31 has a lower β (but this is only at $\sim 5\%-10\%$ level).

What could be a physical (or chemical) explanation of the different $\beta-T_d$ relationships in the two regions? Typical values of β are in the range 1.5–2.0 for interstellar dust grains and have been found in global extra-galactic studies (e.g., Skibba et al., 2011; Smith et al., 2012b; Dunne et al., 2011) and *average* global values measured in the MW (e.g., Paradis et al., 2010; Bracco et al., 2011; Planck Collaboration, 2011d). Low values of β for large grains would typically represent freshly formed dust grains in circumstellar disks or stellar winds. Alternatively, $\beta \sim 1$ has been observed in regions where small grains dominate (Seki & Yamamoto, 1980). High values of β (> 2) might occur due to grain coagulation or to the growth of icy mantles on the surface of the grains in denser regions (Aannestad, 1975; Lis et al., 1998; Stepnik et al., 2003).

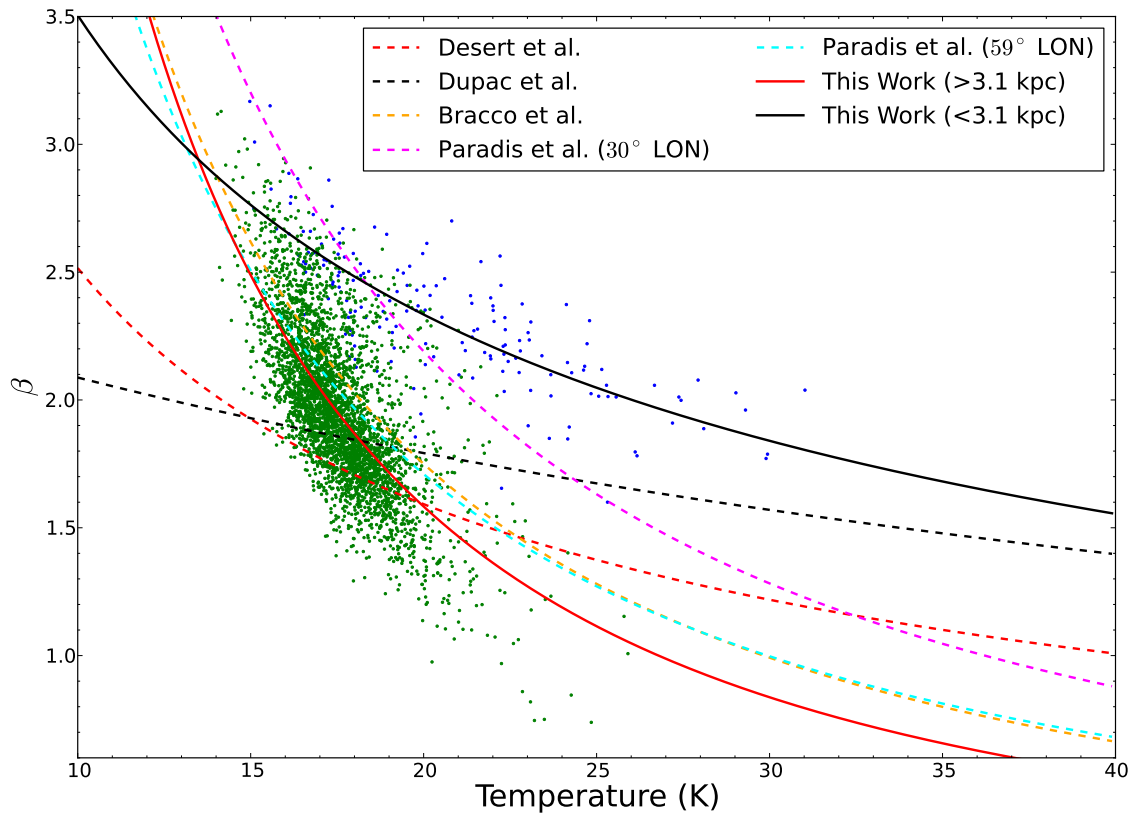


Figure 5.14. Variation of the dust temperature with emissivity index across M31. Data points are colour coded for those within $R < 3.1 \text{ kpc}$ (blue) and those beyond this radius (green). Solid lines show the best-fit relations for $T_d - \beta$ in M31. The $T_d - \beta$ relationships in the literature are indicated by the dashed lines (including Dupac et al., 2003; Désert et al., 2008; Paradis et al., 2010; Bracco et al., 2011).

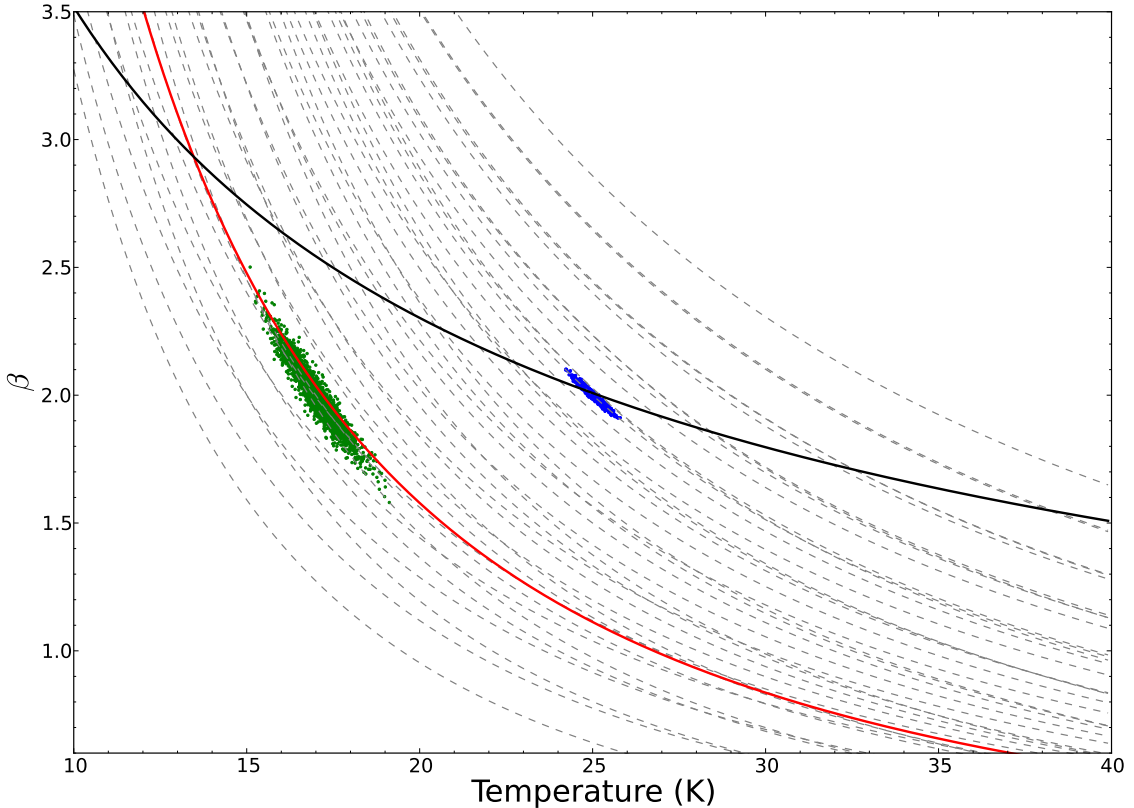


Figure 5.15. Variation of the dust temperature with emissivity index that arise from just the uncertainties in the measurements. The data shown use the simulations of the SED-fitting method, described in Section 5.3.3. The green and blue data points show the recovered values of β and T_d for an input model with $T = 17.0$ K, $\beta = 2.0$ (green) and $T = 25.0$ K, $\beta = 2.0$ (blue). We have carried out the same simulation for input values of T_d and β over the range T_d of 15–29 K in 2 K intervals and in β of 1.6–2.4 in 0.2 intervals. For each group of points we have fitted a line $T_d \propto \beta^n$, which are the grey dashed lines. In these cases we have not shown the recovered values of T_d and β , merely the lines that are the best fit to the points. The red and black solid lines are the best-fit models to the real data as shown in Figure 5.14. When compared with Figure 5.14 it is clear that the uncertainties give a much smaller distribution in the T_d – β relationship, and so cannot account for the distribution in the real data.

Studies have also suggested that high values of β are associated with very cold dust ($T < 12$ K; e.g., Désert et al., 2008) possibly caused by a change in the absorption properties due to quantum effects at low temperatures, increasing self-absorption in amorphous grains via tunnelling (Agladze et al., 1996; Mennella et al., 1998; Meny et al., 2007; Paradis et al., 2012).

The highest value of β is seen at the 3.1 kpc boundary between the two regions. This cannot be caused by changes in the quantum mechanical absorption, since this is only thought to be important for cold dust at temperatures < 12 K. The high β values could be due to efficient grain coagulation or mantle growth in dense molecular clouds, although this too seems unlikely as little CO($J = 1 - 0$) is observed in this region. While there is no obvious explanation for the high β values at this radius, there are many indications that this 3 kpc “boundary” is an interesting regime, we discuss this further in Section 5.5.3.

In the inner region, we suggest that the decrease in β with corresponding increase in T_d might be caused by the increased intensity of the ISRF. Toward the center of M31, we would expect increased sputtering or sublimation of mantles from the increased ISRF, shown by the increased temperature of the dust and the increased X-ray emission observed in the center (Shirey et al., 2001). The lack of gas in the central regions (Figure 5.9) also suggests that dust is less likely to be shielded and thus more efficiently sputtered and leading to smaller grain sizes.

As we mentioned above, a problem with this analysis is that it is difficult to determine which are the causal relationships. For example, we have argued that the radial variation in T_d is due to the radial variation in the ISRF. The radial variation in β might then be due to a physical relationship between T_d and β or it might be the case that there is no causal relationship between these parameters but the radial variation in β is caused by a different effect. For example, an interaction between M32 and M31 might have caused a wave of star formation which has moved out through the galaxy, which might have led (by a number of processes) to the radial variations in β . Therefore, we can rule out some hypotheses but we cannot conclusively determine which is the true explanation using this data set.

5.5.3 WHY A TRANSITION AT 3.1 KPC?

Interpreting the transition in dust properties seen at 3.1 kpc (Figure 5.8) is difficult. One possible clue comes from previous gas kinematics studies. Chemin et al. (2009) found that the HI rotation curve inside a 4 kpc radius is warped with respect to the rest of disk. Stark & Binney (1994) suggest that the inner HI data are consistent

with a bar extended to 3.2 kpc, while a newer analysis by Berman (2001) explains the HI distribution as the result of a triaxial rotating bulge. Block et al. (2006), using *Spitzer* IRAC observations, identified a new inner dust ring with dimensions of 1.5×1 kpc. By using the stellar and gas distributions and from the presence of the 10 kpc ring, they conclude that an almost head-on collision has occurred between M31 and M32 around 210 million years ago. This collision could explain the perturbation of the gas observed in the central 4 kpc. These other observations all show that the inner 3 kpc of M31 is an intriguing region, although it is not clear what are the causes of the difference in the dust properties. The perturbation of the gas may have led to the processing of dust grains, or potentially material from M32 could have been deposited after the interaction. The total dust mass for the pixels in our selection within 3.1 kpc is $10^{4.2} M_{\odot}$ which is a plausible amount to be deposited as recently dust masses of $\sim 10^5 M_{\odot}$ have been reported in Virgo dwarf ellipticals (Grossi et al., 2010).

Another possibility is that the dust properties are affected by the differences between conditions in the bulge and disk. Courteau et al. (2011) decomposed the luminosity profile of *Spitzer* IRAC data into a bulge, disk, and halo. From their Figure 16, we can see that our transition radius of ~ 3 kpc is approximately where the bulge emission begins to become a significant fraction of the optical disk emission. Whether the transition in the dust parameters is due to the changing contribution to the ISRF from the general stellar population and star formation or if there is another influence in the bulge is unknown.

To differentiate between the two possibilities further observations are required. High resolution imaging with interferometers (e.g., Plateau de Bure) of a few CO rotational transition lines would provide information of both the kinematics and heating of the molecular gas. Correlations between the dust emissivity index and the gas temperature would be more consistent with the second interpretation, when changes in the kinematics would suggest one of the possibilities from the first paragraph.

5.5.4 DARK GAS AND X FACTOR

The detection of ‘dark gas’ in the MW was a surprising early result from Planck (Planck Collaboration, 2011a), obtained by combining *IRAS* 100 μm data and the six-band Planck data from 350 μm to 3 mm. The Planck team compared the dust optical depth with the total column density of hydrogen ($N_{\text{H}}^{\text{Tot}}$), where the

optical depth at each wavelength is given by

$$\tau_\nu = \frac{I_\nu}{B(\nu, T_{dust})}, \quad (5.7)$$

where I_ν is the flux density in that band and $B(\nu, T_{dust})$ is the blackbody function. They assumed that at low $N_{\text{H}}^{\text{Tot}}$ the atomic hydrogen dominates over the molecular component while at high column density the molecular hydrogen dominates the emission. For these two regimes they found a constant gas-to-dust ratio, but at intermediate column densities they found an excess of dust compared to the gas. This excess is attributed to gas traced by dust but not by the usual HI and CO lines, and is found to be the equivalent 28% of the atomic gas or 118% of the molecular gas. The excess dust emission was typically found around molecular clouds, suggesting that the most likely cause is the presence of molecular gas not traced by the CO line.

We attempted the same analysis as the Planck Collaboration (2011a) for M 31 using our SED-fitting results from Section 5.3.3. Instead of using Equation 5.7, we compare the column density of gas estimated from the HI and CO with the column density of dust (for convenience we call this Σ_{dust}). We use this parameter as it is calculated with data from all wavelengths, whereas if we used Equation 5.7, small errors in temperature would cause large uncertainties in τ_ν for wavelengths close to the peak of emission.

The Planck team found no radial variation in the gas-to-dust ratio in the MW (see Figure 10; Planck Collaboration, 2011c). In Andromeda, we show that the gas-to-dust ratio does vary radially (Section 5.4.1 and Figure 5.9), as expected from the metallicity gradient. To determine if there is an excess at intermediate column density in dust compared to that expected from the gas we have to correct for the radial change in gas-to-dust ratio. To remove this dependence, we adjust dust column density by using the exponential fit (shown by the red line in Figure 5.9) so the gas-to-dust ratio at all radii has the same value as the center of M 31. To avoid biasing this correction by assuming a value for the X-factor which is highly uncertain, we estimate this relationship from pixels where the atomic hydrogen column density is $> 95\%$ of $N_{\text{H}}^{\text{Tot}}$ (1569 pixels out of the 3600).

In Figure 5.16, we show that the relationship between corrected dust column density (Σ_{dust}) and gas column density is well represented by assuming that the two quantities are directly proportional with no excess in dust column density that could be attributed to “dark gas”. Although only a small proportion of the gas is molecular, we still need to use a value for the X-factor. We can estimate this quantity from the data by finding the values of the X-factor and the constant of proportionality between

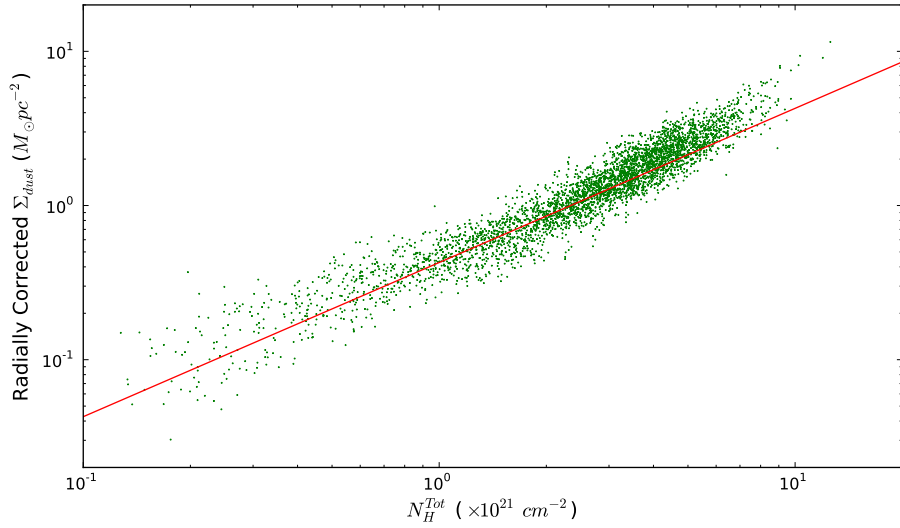


Figure 5.16. Radially corrected Σ_{dust} vs. total column density of gas. The plot is shown using our best-fit value of the X-factor of $(1.9 \pm 0.4) \times 10^{20} \text{ cm}^{-2} [\text{K kms}^{-1}]^{-1}$. The red line represents the best fit model to the data assuming that $\Sigma_{dust} \propto N_H^{Tot}$. The plot shows that, unlike the Planck data for the Milky Way (Planck Collaboration, 2011a), at intermediate gas column densities we do not find an excess in dust column density over the best-fit model which would indicate the presence of gas not traced by the HI and CO ('dark gas').

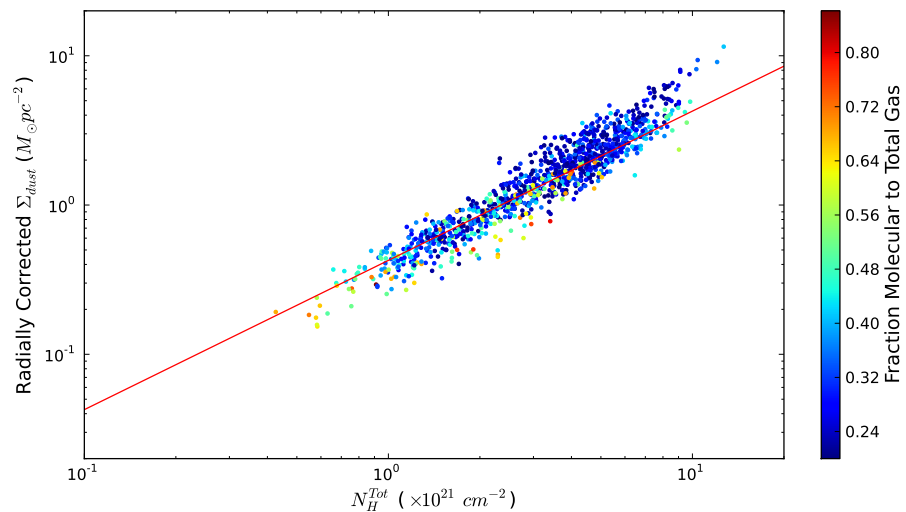


Figure 5.17. Radially corrected Σ_{dust} versus column density of gas for pixels where the molecular fraction is greater than 20%. The data points are colour coded with the fraction of molecular gas compared to total gas. The figure shows that the high column densities are not dominated by regions of molecular gas traced by the CO. The red line is the fitted model from Figure 5.16.

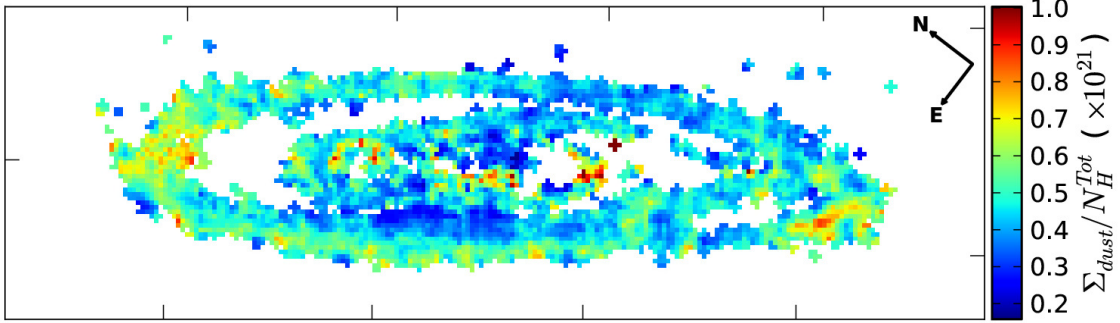


Figure 5.18. Map of $\Sigma_{\text{dust}}/N_{\text{H}}^{\text{Tot}}$ ratio in M 31. Higher values represent areas where there is less gas than predicted from dust measurements. The tick spacing represents $30'$.

the gas column density and the corrected Σ_{dust} that gives the minimum χ^2 value (the fitted line is shown in Figure 5.16.) We find a best value for the X-factor of $(1.9 \pm 0.4) \times 10^{20} \text{ cm}^{-2} [\text{K kms}^{-1}]^{-1}$ (or expressed as $\alpha_{\text{CO}} = 4.1 \pm 0.9 M_{\odot} \text{ pc}^{-2} [\text{K kms}^{-1}]^{-1}$), where the random error is estimated using a Monte Carlo technique (similar to one used in Section 5.3.1). For the dust column densities in each pixel we use the uncertainties provided by the SED fitter as explained in Section 5.3.1, which is on average $\sim 22\%$. Nieten et al. (2006) quote a calibration error of 15% for the CO observations (which directly results in at least a 15% uncertainty in the X-factor) which we combine with the noise in each pixel of our processed moment-zero CO map. For the HI observations we use an uncertainty map provided by R. Braun (private communication, 2012) which has an average uncertainty of 12% on the raw $10''$ map. We also include a 5% systematic uncertainty (e.g., calibration uncertainties). If the opacity corrected HI map is used our best fit X-factor is $(2.0 \pm 0.4) \times 10^{20} \text{ cm}^{-2} [\text{K kms}^{-1}]^{-1}$.

Leroy et al. (2011) find values of the X-factor between 0.97 and $4.6 \times 10^{20} \text{ cm}^{-2} [\text{K kms}^{-1}]^{-1}$ when analysing the southern, northern and inner regions for M 31 with *Spitzer* data. Our average value of the X-factor falls within their range of values. A full analysis of the spatial variations of the X-factor with our data will be undertaken in a future paper.

There are two main problems with this method which could lead us to miss “dark gas”. First, unlike the MW we have to average through the whole disk of M 31 and second, M 31 has a significantly lower molecular gas fraction. The latter prevents us from fitting the model to pixels with just very high and low values of $N_{\text{H}}^{\text{Tot}}$ as the pixels with highest molecular gas fraction are not clustered to high N_{H} values (this is illustrated in Figure 5.17). This suggests Andromeda may not be the best galaxy for this analysis as the molecular contribution to the overall column density is quite low.

However, we can also try an alternative method of looking for ‘dark gas’ because we have one important advantage over the Planck team: we can see M31 from the outside. We can therefore make a map of the ratio of radially corrected dust column density (Σ_{dust}) to gas column density to look for regions of enhancements in this ratio (Figure 5.18). The image clearly shows spatial variations which could either suggest regions of ‘dark gas’ or local variations in the metallicity or emissivity of dust. To distinguish between these scenarios an independent measurement of the ‘dark gas’ is required. On the outskirts of molecular clouds, CO could be photodissociated and the carbon gas would therefore reside in C or C⁺ (Wolfire et al., 2010). Planned observations of the C[II] 158 μm line in Andromeda with *Herschel* could then be a potential test for investigating whether ‘dark gas’ exists in M31.

5.6 CONCLUSIONS

In this chapter, we present the results of an analysis of dust and gas in Andromeda using new *Herschel* observations from the HELGA survey. We have ~ 4000 independent pixels with observations in the range of 70–500 μm . We find the following results.

1. We find that a variable dust emissivity index, β , is required to adequately fit all the pixels in Andromeda. When a variable β is used, the modified blackbody model with a single temperature is found to be a statistically reasonable fit to the data in the range 100–500 μm . There is no significant evidence of an excess of dust emission at 500 μm above our model.
2. There are two distinct regions with different dust properties, with a transition at $R = 3.1 \text{ kpc}$. In the center of Andromeda, the temperature peaks with a value of $\sim 30 \text{ K}$ and a β of ~ 1.9 . The temperature then declines radially to a value of $\sim 17 \text{ K}$ at 3.1 kpc with a corresponding increase in β to ~ 2.5 . At radii larger than 3.1 kpc β declines but only with a small associated increase in temperature.
3. The drop in β toward the center of the galaxy may be caused by increased sputtering or sublimation of mantles from an increased ISRF. The origin of the high β values at 3.1 kpc from the center is less clear but may be indicative of either grain coagulation or an increase in the growth of icy mantles.
4. The dust surface density for our pixels in which flux is detected at $> 5\sigma$ in all

Herschel bands range is between ~ 0.1 and $2.0 M_{\odot} \text{ pc}^{-2}$. We find that the gas-to-dust ratio increases exponentially with radius. The gradient matches that predicted from the metallicity gradient assuming a constant fraction of metals are included into dust grains. The dust surface density is correlated with the SFR rather than with the stellar surface density.

5. In the inner 3.1 kpc the dust temperature is correlated with the $3.6 \mu\text{m}$ flux. This suggests that the heating of the dust in the bulge is dominated by the general stellar population. Beyond 3.1 kpc there is a weak correlation between dust temperature and the SFR.
6. We find no evidence for “dark gas”, using a similar technique as the Planck team. However, we find this technique may not be as effective for M 31 due to poor angular resolution and LOS effects. We have used an alternative technique by constructing a gas-to-dust map after correcting for the radial gradient. We do find regions with enhancements (i.e., higher values of $\Sigma_{\text{dust}}/N_{\text{H}}^{\text{Tot}}$), which may show places where ‘dark gas’ exists, or may be due to local variations in the gas-to-dust ratio. A detection of a potential component of CO-free molecular gas will be possible with future observations to measure the C[II] line planned with *Herschel*.
7. By minimising the scatter between our radially corrected dust column density and the column density of gas inferred from the HI and CO line we find a value for the X-factor of $(1.9 \pm 0.4) \times 10^{20} \text{ cm}^{-2} [\text{K kms}^{-1}]^{-1}$ (or expressed as $\alpha_{\text{CO}} = 4.1 \pm 0.9 M_{\odot} \text{ pc}^{-2} [\text{K kms}^{-1}]^{-1}$).

Our results of Andromeda represent the largest resolved analysis of dust and gas in a single galaxy with *Herschel*. The results of this analysis on M 31 are strikingly different from those obtained by the Planck team in the MW, since we find no clear evidence for “dark gas”, a radial gradient in the gas-to-dust ratio and evidence for radial variation in the dust emissivity index (β). In future work, it will be important to understand these differences between the two big spirals in the local group.

CHAPTER 6

DUST IN EARLY-TYPE GALAXIES

“Science is bound, by the everlasting vow of honour, to face fearlessly every problem which can be fairly presented to it.”

Lord Kelvin

This chapter presents an investigation of the dust in early-type galaxies with the largest sample observed with *Herschel*. This study uses the HRS sample (see Section 1.5.1) and was published in Smith et al. (2012b) and entitled “The *Herschel* Reference Survey: Dust in Early-type Galaxies and across the Hubble Sequence”. The correlation analysis reported in Section 6.4.2 and described in detail in Appendix E was performed by Haley Gomez using luminosities that I provided. In addition, the detailed notes on the ellipticals that were detected by *Herschel* in Appendix D were written by Haley Gomez.

6.1 INTRODUCTION

In the standard theoretical view of galactic evolution, based on the hierarchical paradigm, galaxies may move both ways along the Hubble sequence during their evolution: ellipticals may form as the result of the merging of late-type galaxies (e.g., Cole et al., 2000; De Lucia et al., 2006); disks form as the result of the accretion of gas on to bulges (Cole et al., 2000). There are also plenty of environmental processes that might transform the morphology of a galaxy, just one example among many being ram-pressure stripping in clusters, which would move a galaxy toward the early-type sequence by removing the interstellar medium (ISM; e.g., Corbelli et al., 2012) and thus quenching star formation (Boselli & Gavazzi, 2006).

The observational evidence that galaxy transformation is occurring is mixed, especially for galaxies at the current epoch. The fact that the morphology–density

relation is not just the result of early-type galaxies (ETGs)—ellipticals and S0s—being more common in clusters, but extends over a wide range of environmental density, is evidence that galaxy transformation is not a significant process at the current epoch (Dressler, 1980). However, there is also plenty of observational evidence that merging is still important today. In particular, there is evidence of recent merging or accretion in nearby ellipticals, primarily from obscuration in the optical (Goudfrooij & de Jong, 1995), where fossils of mergers in the form of dust ripples and dust lanes have been detected (Schweizer & Seitzer, 1992). Furthermore, the discovery with the *Infrared Astronomical Satellite (IRAS)* of the ultraluminous infrared galaxies (ULIRGs), which are often late-stage mergers with optical profiles similar to the profiles of ellipticals (Wright et al., 1990), was persuasive evidence that ellipticals are still being formed by mergers at the current epoch. Nevertheless, it is not clear whether all the properties of the eventual merged systems would be the same as present-day ellipticals (Naab & Ostriker, 2009), and many of the distinctive properties of ellipticals seem more naturally explained if ellipticals form in a relatively short early-period in cosmic history (Peebles & Nusser, 2010).

The properties of the ISM in ETGs potentially have something to tell us about the evolution of these systems. Since late-type galaxies are known to contain much more gas and dust than ETGs, any process that moves a galaxy along the Hubble sequence has to change simultaneously the morphology and the ISM of the galaxy. In this chapter, we present *Herschel* observations of continuum emission from the dust in a sample of the most massive ETGs in the nearby universe, which we show is the most sensitive method currently available for estimating the mass of the cool ISM in these galaxies.

Although once thought to be devoid of a cool ISM, optical absorption studies suggested that more than 50% of ellipticals contain some dust (Goudfrooij et al., 1994; van Dokkum & Franx, 1995; Tran et al., 2001; Ferrarese et al., 2006) and therefore molecular gas, though the mass of dust is uncertain from these works. In the last decade, previous far-infrared observations with *IRAS*, the *Infrared Space Observatory (ISO)*, *Spitzer*, and *AKARI* have shown that dust in ETGs is rather common, with dust masses estimated at some 10–100 times larger than those derived from the optical extinction measurements (e.g., Bregman et al., 1998; Ferrari et al., 2002; Kennicutt et al., 2003; Pahre et al., 2004; Xilouris et al., 2004; Temi et al., 2004, 2007a; Panuzzo et al., 2007; Kaneda et al., 2008; Young et al., 2009). Although these observations have probed the peak of the spectral energy distributions (SEDs) of the brightest giant ellipticals and S0s, they are hampered by poor resolution and/or lack of long wavelength coverage.

Our current ideas about the life cycle of dust in ellipticals suggest that it may be possible for us to test the origin of the dust, particularly whether it is provided by internal (via stellar mass loss) or external processes (e.g., fuelled by mergers). As long as dust is not introduced from elsewhere, we essentially have a stellar system in equilibrium: dust is produced in the atmospheres of evolved stars (Athey et al., 2002) and destroyed via sputtering in the hot gas (indeed Bressan et al. 2006 detect silicate features in elliptical galaxies known to be produced in circumstellar envelopes). The dust life cycle in ellipticals may therefore be simpler than that in late-types for the internal origin scenario (Tsai & Mathews, 1996), and the mass of dust predicted to exist in the steady state through production in evolved stars and destruction through sputtering is approximately $10^5 M_\odot$ (Forbes, 1991; Goudfrooij & de Jong, 1995).

An alternative origin for dust in ETGs is accreted material either due to a merger or from a tidally-interacting companion: Centaurus A has long been known to harbour a dusty disk thought to be formed by a merger (recently revealed in the submillimetre (submm)—Leeuw et al., 2002; Auld et al., 2012; Parkin et al., 2012). Forbes (1991) and Temi et al. (2004, 2007a) found no correlation between the dust emission and optical starlight using *ISO* observations of massive ETGs, suggesting that the dust has an external rather than an internal origin. In 2010, Gomez et al. used *Herschel* observations of the elliptical galaxy M 86 to reveal $10^6 M_\odot$ of cold dust coincident with material stripped from the nearby spiral NGC 4438 (Cortese et al., 2010a). A similar process has been seen with the “displaced ISM” of the elliptical NGC 3077 (Walter et al., 2011).

The unprecedented resolution and sensitivity of the recently launched *Herschel Space Observatory* (see Section 1.4 or Pilbratt et al., 2010), combined with the wavelength coverage of the instruments PACS (Poglitsch et al., 2010) and SPIRE (Griffin et al., 2010) from 70 to 500 μm , allow us to address long-standing issues such as the origin and quantity of dust in ETGs. *Herschel* provides us with an unbiased view of the interstellar dust (and therefore the interstellar medium); we are now sensitive to the *total* dust mass in galaxies rather than only to those galaxies which had enough warm dust to be detected by *IRAS* and *Spitzer* (e.g., Dunne et al., 2011). Here, we use observations from the guaranteed time project, the *Herschel* Reference Survey (HRS; see Section 1.5.1 or Boselli et al., 2010b) of 62 ETGs including 23 ellipticals. The HRS is a study of dust in nearby galaxies, crucial for calibrating blind surveys of galaxies with *Herschel* at high redshifts, e.g., HerMES (Oliver et al., 2010) and the *Herschel*-ATLAS (H-ATLAS; Eales et al., 2010a).

Cortese et al. (2012a, hereafter C12) recently used the HRS sample of ~ 300 nearby galaxies to obtain dust scaling relations, finding that the dust is tightly coupled

to the atomic mass and therefore to the cold ISM. C12 measured the dust-to-stellar-mass ratio of galaxies with different morphological types and environment, finding that the ETGs contain less dust mass per unit of stellar mass than the late-type galaxies. In this chapter, I further explore the dust properties of the ETGs in the HRS and measure more precisely the variation of dust content with Hubble type and the origin of this variation. In Section 6.2 I introduce the sample and describe the data reduction techniques. The results are given in Section 6.3 and are used to discuss our understanding of the dust content of early- and late-types in Section 6.4.1 and the link between dust and the hot interstellar medium in Section 6.4.2. I discuss the implications for the evolutionary history of ETGs in Section 6.5. The conclusions are presented in Section 6.6.

6.2 THE SAMPLE

The HRS is a volume-limited sample ($15 \text{ Mpc} < d < 25 \text{ Mpc}$) with *Herschel* SPIRE of 322 galaxies selected by the K -band magnitude (a proxy for stellar mass). The ETGs in the HRS have $K \leq 8.7$, and so our sample consists of the ETGs in this volume of space with the highest stellar masses; contamination from Galactic cirrus is minimized due to the high galactic latitudes of the sample (see Boselli et al., 2010b, for full details). The sample includes different morphological types with 260 late-type galaxies and, in the original catalogue listed in Boselli et al. (2010b), 64 early types. However, after closer inspection of the optical images, we reclassified the galaxies NGC 4438 (HRS 163), NGC 4457 (HRS 173), NGC 4691 (HRS 256), and NGC 5701 (HRS 322) as late types (from S0/a to Sb). We changed two classifications in the other direction, with the Sb galaxies NGC 4179 (HRS 90) and IC 3510 (HRS 202) reclassified to S0 and dwarf elliptical, respectively. The revised catalogue therefore has 62 ETGs, 39 of which are designated S0+S0a galaxies and 23 are ellipticals (Table 6.1) though five of the latter set are morphologically classified as E/S0. The morphological classifications are taken from the Virgo Cluster Catalogue (Binggeli et al., 1985) or are our own if another was not available (Boselli et al., 2010b). The HRS contains galaxies from a range of environments, including isolated field galaxies, pairs and galaxies in the heart of the Virgo Cluster.

Table 6.1.
The Sample

HRS	Other Name	R.A. (h m s)	Decl. (° ' '')	Type	D (Mpc)	D(25) (")	L_B (L_\odot)	L_K (L_\odot)	Membership
3	NGC 3226	10 23 27.01 ^r	+19 53 54.7 ^r	E2;pec;LINER;Sy3	16.7	3.16	10.12	10.59	Leo Cl.
7	NGC 3245	10 27 18.40 ^r	+28 30 26.3 ^r	SA(r)0?;HII;LINER	18.8	3.24	10.08	10.47	Leo Cl.
14	NGC 3301	10 36 56.04	+21 52 55.7	(R*)SB(rs)0/ ^a	19.2	3.55	9.84	10.47	Leo Cl.
22	NGC 3414	10 51 16.19 ^r	+27 58 30.2 ^r	S0 pec;LINER	20.2	3.55	9.98	10.73	Leo Cl.
43	NGC 3608	11 16 58.96	+18 08 54.9	E2;LINER:	15.8	3.16	10.11	10.70	Leo Cl.
45	NGC 3619	11 19 21.51 ^r	+57 45 28.3 ^r	(R)SA(s)0+;	22.1	2.69	9.87	10.57	Ursa Major Cl.
46	NGC 3626	11 20 03.80 ^r	+18 21 24.3 ^r	(R)SA(rs)0+	21.3	2.69	10.12	10.70	Leo Cl.
49	NGC 3640	11 21 06.85	+03 14 05.4	E3	17.9	3.98	10.43	11.06	Leo Cl.
71	NGC 3945	11 53 13.61 ^r	+60 40 32.3 ^r	SB(rs)0+;LINER	18.0	5.25	10.01	11.06	Ursa Major Cl.
87	NGC 4124	12 08 09.64	+10 22 43.4	SA(r)0+	17.0	4.10	9.70	10.38	Virgo Out.
90	NGC 4179	12 12 52.11	+01 17 58.9	S0 ^a	17.0	3.80	9.89	10.60	Virgo Out.
93	NGC 4203	12 15 05.06 ^r	+33 11 50.2 ^r	SAB0-;LINER;Sy3	15.6	3.39	9.89	10.73	Coma I Cl.
101	NGC 4251	12 18 08.31	+28 10 31.1	SB0? sp	15.3	3.63	13.86	10.54	Coma I Cl.
105	NGC 4262	12 19 30.58	+14 52 39.8	SB(s)0?	17.0	1.87	9.69	10.43	Virgo A
123	NGC 4324	12 23 06.18	+05 15 01.5	SA(r)0+	17.0	3.52	9.65	10.38	Virgo S Cl.
125	NGC 4339	12 23 34.94	+06 04 54.2	E0;Sy2	23.0	2.31	9.71	10.34	Virgo B
126	NGC 4340	12 23 35.31	+16 43 19.9	SB(r)0+	17.0	3.60	9.81	10.44	Virgo A
129	NGC 4350	12 23 57.81	+16 41 36.1	SA0;Abs. line	17.0	3.20	9.91	10.64	Virgo A
135	NGC 4365	12 24 28.23	+07 19 03.1	E3	23.0	8.73	10.34	11.26	Virgo B
137	NGC 4371	12 24 55.43	+11 42 15.4	SB(r)0+	17.0	5.10	9.92	10.68	Virgo A
138	NGC 4374, M 84	12 25 03.78	+12 53 13.1	E1;LERG;Sy2	17.0	10.07	10.57	11.26	Virgo A
150	NGC 4406, M 86	12 26 11.74	+12 56 46.4	S0(3)/E3	17.0	11.37	10.66	11.31	Virgo A
155	NGC 4417	12 26 50.62	+09 35 03.0	SB0: s	23.0	3.60	10.08	10.77	Virgo B
161	NGC 4429	12 27 26.56	+11 06 27.1	SA(r)0+;LINER;HII	17.0	8.12	10.23	11.06	Virgo A
162	NGC 4435	12 27 40.50 ^r	+13 04 44.5 ^r	SB(s)0;LINER;HII	17.0	2.92	10.05	10.83	Virgo A
166	NGC 4442	12 28 03.89	+09 48 13.0	SB(s)0	23.0	5.05	10.36	11.12	Virgo B
174	NGC 4459	12 29 00.04 ^r	+13 58 42.2 ^r	SA(r)0+;HII;LINER	17.0	3.36	10.07	10.91	Virgo A
175	NGC 4461	12 29 03.01	+13 11 01.5	SB(s)0+;	17.0	3.52	9.90	10.57	Virgo A
176	NGC 4469	12 29 28.03	+08 44 59.7	SB(s)0/a? sp	23.0	4.33	9.97	10.82	Virgo B

Continued on Next Page..

Table 6.1 (Continued)

HRS	Other Name	R.A. (h m s)	Decl. (° ' '')	Type	D (Mpc)	D(25) (')	L_B (L_\odot)	L_K (L_\odot)	Membership
178	NGC 4472, M 49	12 29 46.76	+08 00 01.7	E2/S0;Sy2	17.0	10.25	10.90	11.59	Virgo S Cl.
179	NGC 4473	12 29 48.87	+13 25 45.7	E5	17.0	4.04	10.15	10.90	Virgo A
180	NGC 4477	12 30 02.17	+13 38 11.2	SB(s)0?;Sy2	17.0	3.60	10.12	13.77	Virgo A
181	NGC 4478	12 30 17.42	+12 19 42.8	E2	17.0	1.89	9.89	10.41	Virgo A
183	NGC 4486, M 87	12 30 49.42	+12 23 28.0	E+0-1 pec;NLRG;Sy	17.0	11.00	10.85	11.43	Virgo A
186	NGC 4494	12 31 24.03	+25 46 29.9	E1-2;Sy	18.7	4.79	10.62	11.20	Coma I Cl.
200	NGC 4526	12 34 03.03 ^r	+07 41 57.3 ^r	SAB(s)0:	17.0	7.00	10.41	11.18	Virgo S Cl.
202	IC 3510	12 34 19.33	+11 04 17.7	dE ^a	17.0	1.10	8.70	9.20	Virgo A
209	NGC 4546	12 35 29.51	-03 47 35.5	SB(s)0-:	15.0	3.31	10.05	10.82	Virgo Out.
210	NGC 4550	12 35 30.61	+12 13 15.4	SB0: Sy;LINER	17.0	3.95	9.66	10.30	Virgo A
211	NGC 4552, M 89	12 35 39.88	+12 33 21.7	E;LINER;HII;Sy2	17.0	7.23	10.29	11.06	Virgo A
214	NGC 4564	12 36 26.99	+11 26 21.5	E6	17.0	4.33	9.86	10.58	Virgo A
218	NGC 4570	12 36 53.40	+07 14 48.0	S0(7)/E7	17.0	3.52	9.96	10.70	Virgo S Cl.
219	NGC 4578	12 37 30.55	+09 33 18.4	SA(r)0:	17.0	3.77	9.71	10.41	Virgo E Cl.
231	NGC 4596	12 39 55.94	+10 10 33.9	SB(r)0+;LINER:	17.0	4.76	10.08	10.79	Virgo E Cl.
234	NGC 4608	12 41 13.29	+10 09 20.9	SB(r)0	17.0	4.30	9.83	10.51	Virgo E Cl.
235	NGC 4612	12 41 32.76	+07 18 53.2	(R)SAB0	17.0	2.16	9.82	10.35	Virgo S Cl.
236	NGC 4621, M 59	12 42 02.32	+11 38 48.9	E5	17.0	7.67	10.32	11.05	Virgo E Cl.
240	NGC 4638	12 42 47.43	+11 26 32.9	S0-	17.0	2.01	9.82	10.49	Virgo E Cl.
241	NGC 4636	12 42 49.87	+02 41 16.0	E _z /S0/1;LINER;Sy3	17.0	9.63	10.51	11.18	Virgo S Cl.
243	NGC 4643	12 43 20.14	+01 58 42.1	SB(rs)0/a;LINER/HII	17.0	3.00	9.98	10.81	Virgo Out.
245	NGC 4649, M 60	12 43 40.01	+11 33 09.4	E2	17.0	5.10	10.73	11.46	Virgo E Cl.
248	NGC 4660	12 44 31.97	+11 11 25.9	E5	17.0	1.89	9.70	10.47	Virgo E Cl.
250	NGC 4665	12 45 05.96	+03 03 20.5	SB(s)0/a	17.0	4.50	10.04	10.80	Virgo Out.
253	NGC 4684	12 47 17.52	-02 43 38.6	SB(r)0+;HII	21.3	2.88	9.82	10.42	Virgo Out.
258	NGC 4697	12 48 35.91	-05 48 03.1	E6;AGN	17.7	7.24	10.55	11.16	Virgo Out.
260	NGC 4710	12 49 38.93 ^r	+15 09 59.1 ^r	SA(r)0+? sp;HII	17.0	4.30	9.91	10.74	Virgo Out.
269	NGC 4754	12 52 17.56	+11 18 49.2	SB(r)0-:	17.0	5.03	10.05	10.81	Virgo E Cl.
272	NGC 4762	12 52 56.05	+11 13 50.9	SB(r)0 sp;LINER	17.0	8.70	10.21	10.85	Virgo E Cl.
286	NGC 4866	12 59 27.14	+14 10 15.8	SA(r)0+;LINER	17.0	6.00	9.84	10.60	Virgo Out.
296	NGC 5273	13 42 08.36 ^r	+35 39 15.1 ^r	SA(s);Sy1.5	15.2	2.75	9.54	10.21	Canes Ven. Spur

Continued on Next Page..

Table 6.1 (Continued)

HRS	Other Name	R.A. (h m s)	Decl. (° ′ ″)	Type	D (Mpc)	$D(25)$ (′)	L_B (L_\odot)	L_K (L_\odot)	Membership
312	NGC 5576	14 21 03.68	+03 16 15.6	E3	21.2	3.55	10.16	10.89	Virgo-Libra Cl.
316	NGC 5638	14 29 40.39	+03 14 00.2	E1	23.9	2.69	10.09	10.72	Virgo-Libra Cl.

Notes. The columns are as follows. Column 1: the number of the source in the *Herschel* Reference Survey (Boselli et al., 2010b). Column 2: other common names for the galaxy. Columns 3 and 4: the right ascension and declination of the galaxy (J2000). This is taken from the NASA Extragalactic Database (NED), except positions with a superscript r are radio positions taken from Wrobel (1991) and Filho et al. (2006). Column 5: morphological type taken from Virgo Cluster Catalogue (Binggeli et al., 1985) or from our own classification. The AGN/Seyfert/LINER classifications were taken from Ho et al. (1997), Schmitt (2001), and Véron-Cetty & Véron (2010). Column 6: distance in Mpc. We assume all objects in Virgo, including those in the outskirts of Virgo, are at a distance of 17 Mpc, except for those in Cloud B, which we assume are at a distance of 23 Mpc. For the other galaxies we have calculated distances from the heliocentric velocity using a Hubble constant of $70 \text{ km s}^{-1} \text{ Mpc}^{-1}$. Column 7: optical isophotal diameter ($25 \text{ mag arcsec}^{-2}$). Column 8: total K -band luminosity measured using $K_{S,\text{tot}}$ from 2MASS (Skrutskie et al., 2006). Column 9: cluster or cloud membership from Gavazzi & Boselli (1999) for Virgo, otherwise from Tully & Fisher (1988) or Nolthenius (1993) wherever available, or failing that our own estimate.

a These sources were morphologically classified by eye using optical images.

The HRS observations were carried out with SPIRE in scan-map mode with a scan speed of 30 arcsec s^{-1} . We chose the size of our maps so that they would be at least as large as the optical disk of each galaxy, defined as the area of the galaxy within an optical isophote with a B -band brightness of $25 \text{ mag arcsec}^{-2}$ (Boselli et al., 2010b, $D(25)$;). In practice, our maps were either 4×4 , 8×8 , or $12 \times 12 \text{ arcmin}^2$, and in most cases are larger than $D(25)$. For each ETG, we made eight pairs of orthogonal scans, resulting in a 1σ instrumental noise in each pixel of 0.35, 0.20 and 0.11 MJy/sr for the 250, 350, and $500 \mu\text{m}$, respectively (integration time of 1199s, 3102s, and 4948s for each map size). We deliberately observed the ETGs in the HRS for at least twice as long as for the late-type galaxies (three pairs of orthogonal scans) because the former are known to contain much less dust on average.

There are a number of sources in the HRS which overlap with galaxies observed as part of the open-time key project the *Herschel* Virgo Cluster Survey (HeViCS; see Section 1.5.2, Davies et al., 2010, 2012), thus the two surveys have a data-sharing agreement for these galaxies. Here we also include data of the duplicate 19 ETGs formally observed as part of HeViCS with both PACS and SPIRE. The SPIRE observations for HeViCS were made in parallel-scan-map mode with a scan speed of 60 arcsec s^{-1} . To cover the Virgo Cluster, four fields with size $4^\circ \times 4^\circ$ were observed with eight cross-scans (see Section 1.5.2 for a complete description). Note that the dust content of all of the ETGs in the Virgo Cluster from HeViCS will be presented in di Serego Alighieri et al. (2012).

6.2.1 DATA REDUCTION AND FLUX EXTRACTION

The HRS and HeViCS SPIRE data were reduced using similar pipeline procedures. The SPIRE data were processed up to Level-1 with a custom script adapted from the official pipeline (*POF5_pipeline.py*, dated 8 Jun 2010) as provided by the SPIRE Instrument Control Centre (ICC)¹. Our custom Jython script was run in the *Herschel* Interactive Processing Environment (HIPE; Ott, 2010) with the continuous integration build number: 4.0.1367. For both surveys we use an optimized deglitcher setting instead of applying the ICC default settings. For the HeViCS data the SIGMAKAPPADEGLITCHER module was used, while for the HRS we applied the WAVELETDEGLITCHER; this module was adjusted to mask the sample following a glitch. For the HRS, after the flux calibration was applied, an additional pass with the WAVELETDEGLITCHER was run, as this was found to significantly improve the

¹See ‘The SPIRE Analogue Signal Chain and Photometer Detector Data Processing Pipeline’ (Griffin et al. 2008 or Dowell et al. 2010) for a more detailed description of the pipeline and a list of the individual modules.

glitch-removal process. Furthermore, we did not run the pipeline default temperature drift correction or the median baseline subtraction. Instead we use a custom method (BriGAdE; see Section 2.4) to remove the temperature drift and bring all bolometers to the same level.

Our final SPIRE maps were created using the naïve mapper provided in the standard pipeline with pixel sizes of 6'', 8'', and 12'' at 250, 350, and 500 μm respectively. The FWHM of the SPIRE beams for this pixel scale are 18.2'', 24.5'', and 36.0'' at 250, 350, and 500 μm , respectively (Swinyard et al., 2010). In addition, the 350 μm data are multiplied by 1.0067 to update our flux densities to the latest v7 calibration product. The calibration uncertainty is a combination of the 5% error due to correlated errors between bands and the 2% random uncertainty; these values are added linearly instead of in quadrature².

The *Herschel* PACS 100 and 160 μm data taken as part of HeViCS were reduced using the standard pipeline (see Davies et al., 2012). In brief, we used a two step deglitching process, first with the standard deglitcher and second using one based on sigma clipping. We masked bright sources and a high-pass filter was used to reduce $1/f$ noise. The orthogonal scans were combined and the naïve mapper was used to create the final maps. Unlike Davies et al. (2012) we use images created using the full HeViCS data set with eight parallel-mode scans per tile. The FWHM beam sizes are approximately 9'' and 13'' with pixel sizes of 3.2'' and 6.4'' for the 100 and 160 μm bands, respectively³. Davies et al. (2012) measured differences in global flux densities of up to 20% between sets of cross-scans, we choose this as a conservative error for our flux estimates as it dominates over other sources of uncertainty, e.g., the calibration⁴.

The 250 μm *Herschel* SPIRE maps for the detected S0+S0a and all of the elliptical galaxies in our sample are shown in Figures 6.1 and 6.2. Most of the objects visible on the images are background galaxies, creating a potential problem for determining whether our targets are detected. Fortunately, these background galaxies are almost always unresolved, whereas virtually all our detections are extended. The full description of the flux extraction process and complete photometry information for all the HRS galaxies including upper limits on the non-detections are provided in Ciesla et al. (2012) and in Chapter 3. The upper limits for the non-detections are estimated using circular apertures with size $0.3 \times D_{25}$ for ellipticals and $0.8 \times D_{25}$ for S0s (chosen as a conservative limit based on the extent of 250 μm emission seen in the detected sample).

²SPIRE Observers' Manual (2011)

³PACS Photometer Point Spread Function Document (2010)

⁴PACS Photometer Calibration Document (2011)

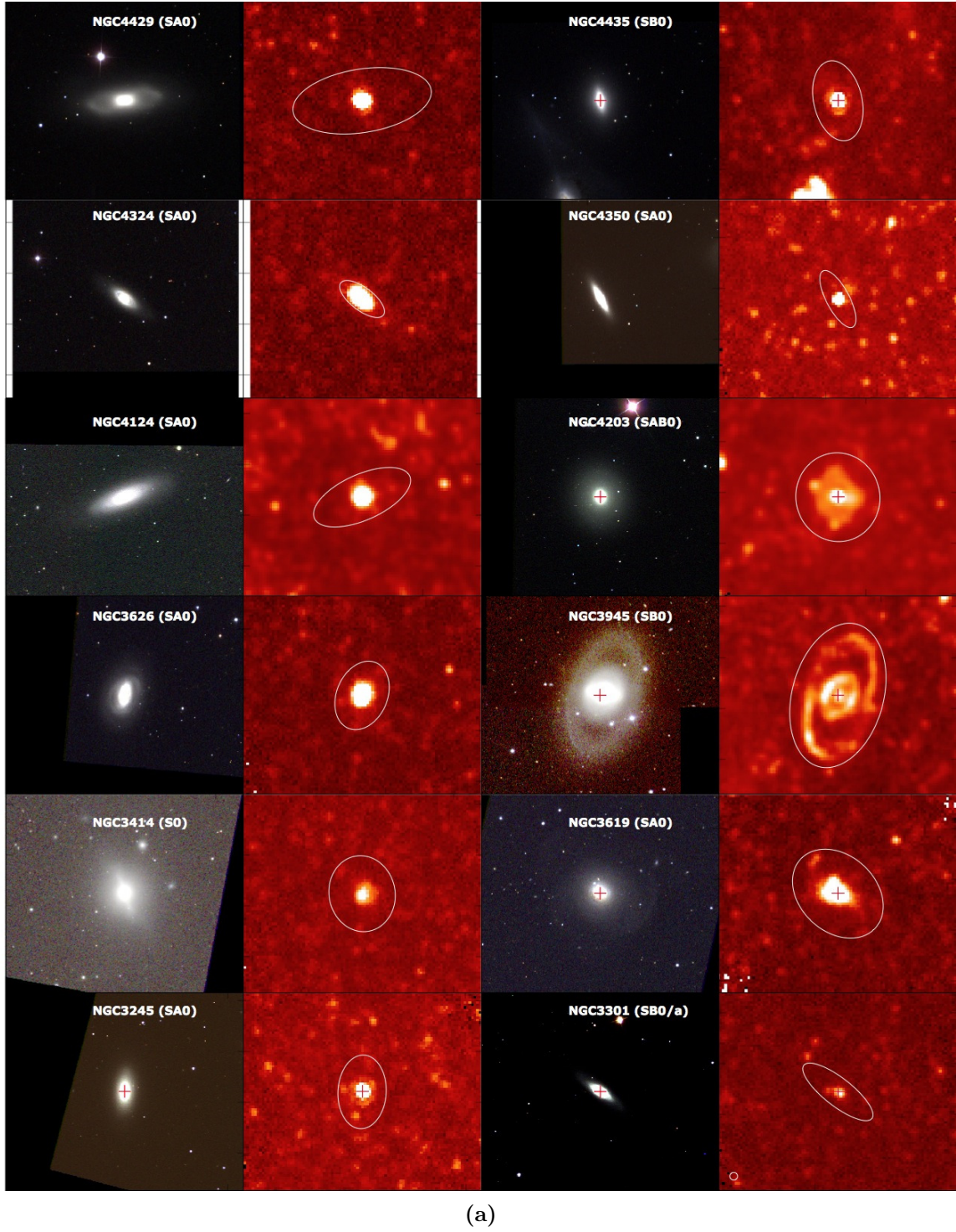


Figure 6.1. SDSS *gri* three-color maps and 250 μm *Herschel* SPIRE maps of the 24 detected S0+S0a galaxies from the *Herschel* Reference Survey. North is up and east is left. The white aperture shows the elliptical optical *B*-band isophotal diameter ($D(25)$ at 25 mag arcsec $^{-2}$ —Table 6.1). The region shown is 8.4' \times 8.4'. Red crosses show the location of the VLA FIRST radio detection. The 250 μm beam is shown in the corner of (a) NGC 3301 and (b) NGC 4469.

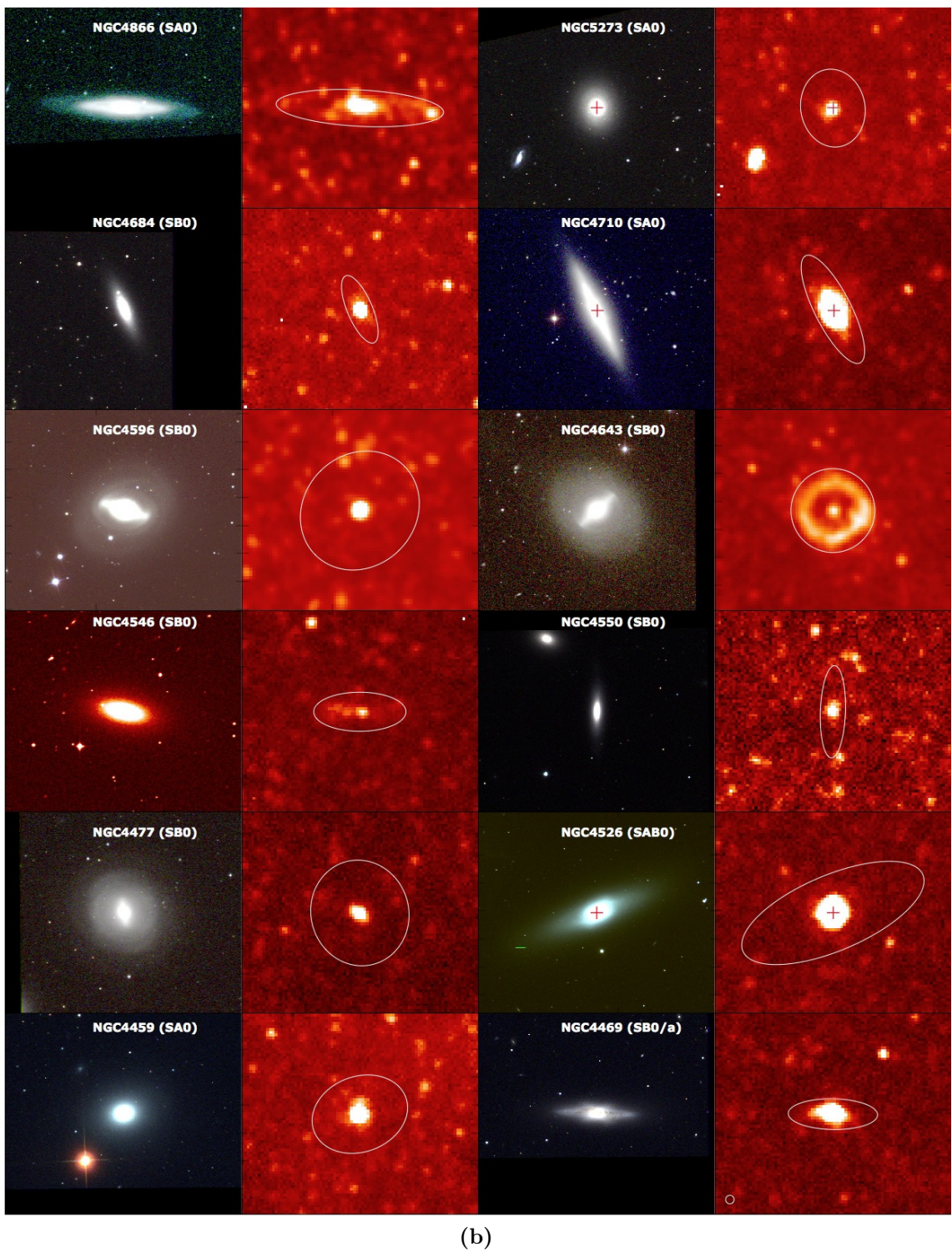


Figure 6.1. (Continued)

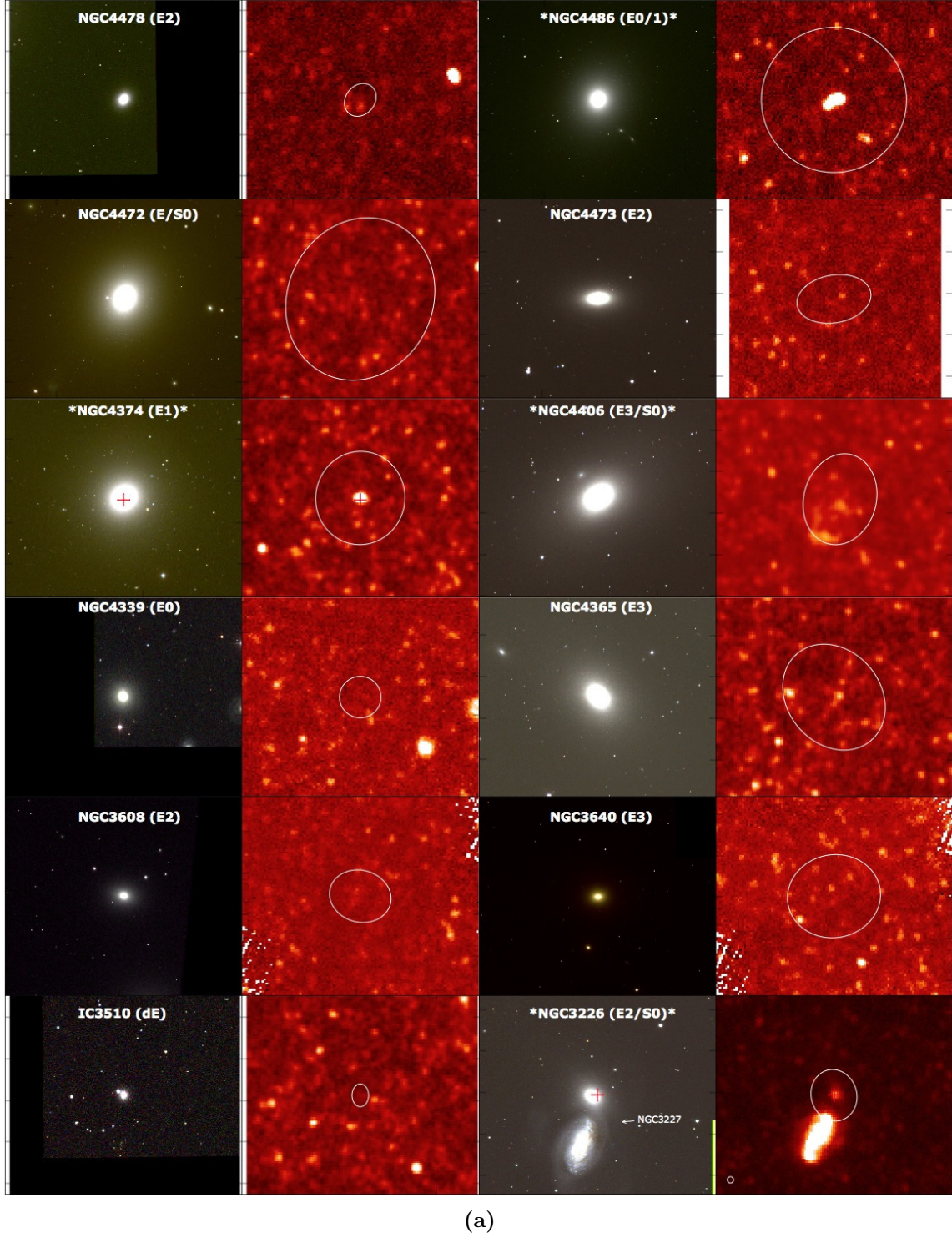


Figure 6.2. SDSS *gri* three-color maps and 250- μm *Herschel* SPIRE maps of the entire sample of 23 elliptical galaxies from the HRS and HeViCS programs (sources denoted with a (*) indicate that it has been detected by *Herschel*). North is up and east is left. The white aperture shows the optical *B*-band isophotal diameter ($D(25)$ at 25 mag arcsec $^{-2}$ —Table 6.1). The boxes are 9.6' \times 9.6'. Red crosses show the location of the VLA FIRST radio detection. The 250 μm beam is shown in the corner of (a) NGC 3226 and (b) NGC 4552.

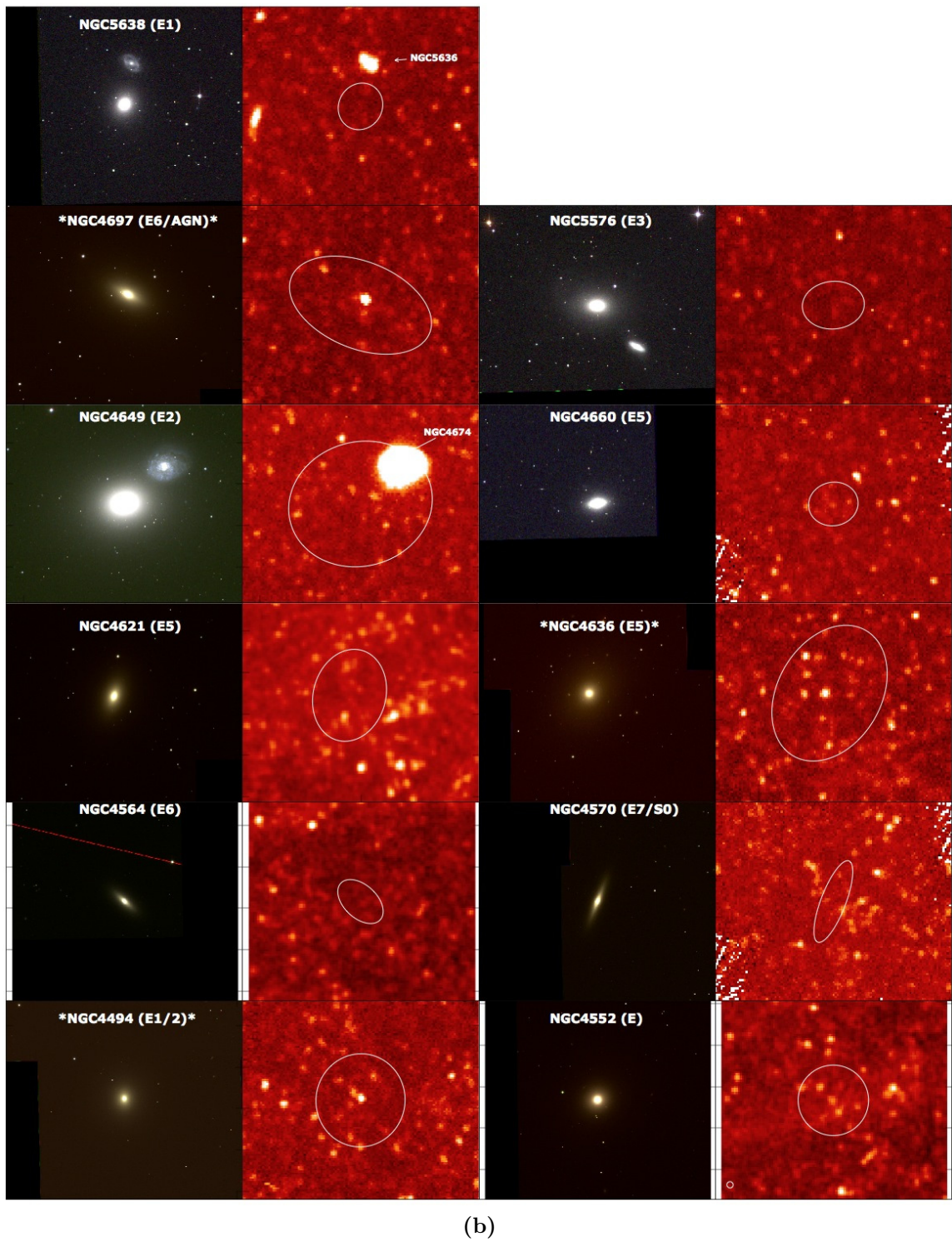


Figure 6.2. (Continued)

We tested the effect of using different definitions of the upper limit on the analysis in this analysis. First, we used simply the statistical noise on the map, taking into account the instrumental noise and confusion to give σ_{rms} . Second, we included the additional uncertainty in the photometry measurement due to the background level (σ_{sky} ; Ciesla et al., 2012), which arises mainly from cirrus contamination. For this work, we use the photometry upper limit as in Ciesla et al. (2012), with $\sigma = 3(\sigma_{\text{rms}} + \sigma_{\text{sky}})$ which is the most conservative limit on the $250\,\mu\text{m}$ flux for our sources. Note that all of the results in this chapter are also valid if we use $3\sigma_{\text{rms}}$ or $5\sigma_{\text{rms}}$ (as a typical 3σ or 5σ detection limit).

For the HeViCS galaxies in our sample the PACS flux densities we used aperture photometry with suitable background regions selected around the source (the assumed uncertainty is outlined in Section 6.2.1). We present the PACS fluxes in Table 6.2.

6.2.2 DATA AT OTHER WAVELENGTHS

In addition to the *Herschel* data, we used $70\text{--}160\,\mu\text{m}$ data from *Spitzer* (Kennicutt et al., 2003), reprocessed using the techniques described in Bendo et al. (2010a) and presented in Bendo et al. (2012a). The calibration uncertainties were assumed to be 5% at $70\,\mu\text{m}$ and 12% at $160\,\mu\text{m}$ (Gordon et al., 2007; Stansberry et al., 2007). We use IRAS 60 and $100\,\mu\text{m}$ measurements originally presented in Knapp et al. (1989) but modified in a private communication to NASA Extragalactic Database (NED, Table 6.2). The calibration uncertainties for *IRAS* were assumed to be 13% at $60\,\mu\text{m}$ and 16% at $100\,\mu\text{m}$ (e.g., Verter & Rickard, 1998). Four of our elliptical galaxies were also detected by *ISO* and we use the fluxes given in Temi et al. (2004).

Optical photometry for the sample was obtained from the Sloan Digital Sky Survey (SDSS) DR7 (Abazajian et al., 2009) database. We estimate stellar masses for the sample from the *i*-band luminosities using the relationship between stellar mass and galaxy color for a Chabrier initial mass function (Zibetti et al., 2009). The full description of this method applied to the entire HRS sample can be found in Cortese et al. (2011) and C12. NUV photometry is available from the *Galaxy Evolution Explorer* (*GALEX*; Martin et al., 2005) from the GR6 data release (see Boselli et al., 2011; Cortese et al., 2011).

X-ray luminosities for 38 of our sources were obtained from the catalogues of O’Sullivan et al. (2001) and Pellegrini (2010). A further 57 of our sources are included in the ATLAS^{3D} sample of ETGs (Cappellari et al., 2011). ATLAS^{3D} includes molecular hydrogen masses estimated from the CO(1–0) intensity ($I(\text{CO})$; Young et al. 2011)

Table 6.2
IRAS Fluxes and *Herschel* PACS for Detected Galaxies.

HRS Name	F60 (Jy)	F100 (Jy)	F100 (Jy)	F160 (Jy)
7	2.09±0.28	3.97±0.64		
14	0.48±0.07	0.92±0.16		
22	0.25±0.04	0.56±0.21		
45	0.38±0.06	1.83±0.37		
71	0.26±0.04	1.36±0.24		
87	0.43±0.07	1.75±0.29		
93	0.59±0.08	2.16±0.36		
101	0.12±0.04	...		
105	0.18±0.04	0.39±0.14	...	2.71±0.54
123	0.41±0.07	1.99±0.32	1.80±0.6	2.42±0.48
126	0.09±0.03	0.37±0.09		
129	0.36±0.06	1.09±0.19		
138	0.50±0.07	1.16±0.22	0.78±0.16	0.46±0.09
150	0.11±0.04	0.33±0.09		
161	1.56±0.21	5.15±0.83	4.74±0.95	4.54±0.91
162	4.48±0.90	3.75±0.75
174	1.87±0.25	4.82±0.78	4.59±0.92	3.78±0.75
176	1.02±0.14	3.40±0.57	3.33±0.67	3.89±0.78
180	0.57±0.09	1.41±0.25	0.94±0.19	0.97±0.19
183	0.39±0.07	0.41±0.12	0.38±0.08	0.60±0.12
186	0.19±0.06	...		
200	5.56±0.72	17.10±2.74	15.81±3.16	15.53±3.11
209	0.26±0.06	0.89±0.26		
210	0.14±0.04	0.25±0.10	0.28±0.06	0.27±0.05
211	0.16±0.05	0.53±0.10		
231	0.40±0.06	0.75±0.13		
243	0.62±0.09	2.06±0.34		
253	1.27±0.17	2.15±0.36		
258	0.46±0.06	1.24±0.21		
260	5.73±0.75	14.79±2.37		
286	0.15±0.06	1.02±0.23		
296	0.90±0.12	1.56±0.28		
312	0.09±0.03	0.21±0.28		
316	...	0.45±0.14		

Notes. The *Spitzer*, and *Herschel* photometry is presented in Temi et al. (2004), Bendo et al. (2012a). Ciesla et al. (2012), respectively. The columns are as follows. Column 1: the number of the source in the *Herschel* Reference Survey (Boselli et al., 2010b). Columns 2 and 3: *IRAS* fluxes at 60 and 100 μ m. Columns 4 and 5: *Herschel* PACS fluxes at 100 and 160 μ m.

with a conversion factor from H₂ to CO of $N(\text{H}_2)/I(\text{CO}) = 3 \times 10^{20} \text{ cm}^2 (\text{K km s}^{-1})^{-1}$ (e.g., Young & Scoville, 1982). The CO data only exist for the central region of the galaxies (i.e., within 30'') and would be an underestimate of the total molecular gas if the real gas distribution is extended, though Young et al. find that there is no strong evidence for extended emission in any of the galaxies except for NGC 4649. Atomic HI masses and upper limits were obtained for 48 sources from the GOLDMINE database (Gavazzi et al., 2003), the ALFALFA survey (Haynes et al., 2011) or Noordermeer et al. (2005) and Springob et al. (2005). The CO and HI masses are presented in Table 6.4. In all cases, these have been corrected to the distances assumed for the ETGs in this study.

6.3 RESULTS

In Figure 6.1 we show the detected S0+S0a galaxies and all of the ellipticals in Figure 6.2; the sources show a variety of morphologies, from small blobs to spectacular ring structures. The difference in the appearance of the S0+S0a and ellipticals at 250 μm is very clear in these figures. The detected S0+S0a sources are brighter than their elliptical counterparts and the FIR emission is more extended within the $D(25)$ isophotes. In general, this appears to be a trend as we move along the Hubble sequence: an aperture of size $0.8 \times D(25)$ is sufficient to include the submm emission from the ETGs, yet Ciesla et al. (2012) require an aperture size of $1.4 \times D(25)$ to incorporate all the emission from the late-type galaxies. This effect was also noticed by Bendo et al. (2007) and Muñoz-Mateos et al. (2009).

The difference between late-types and early-types when viewed in the submm and optical wavebands is quite startling. For example, at optical wavelengths, the giant elliptical NGC 4649 (HRS 245) is extremely bright compared to the smaller, fainter spiral galaxy to the northwest (NGC 4674). At 250 μm (Figure 6.2) however, the situation is reversed, with the spiral galaxy extremely bright in the FIR, but no sign of the elliptical. In Appendix D, we provide brief notes on the elliptical galaxies that are detected by *Herschel*.

6.3.1 DETECTION RATES

We detect 31 out of the 62 ETGs, including 24 S0+S0a galaxies (62%) and 7 ellipticals (30%, Table 6.3). We detect all three of the ETGs classified as ‘peculiar’ (two ellipticals, M 87 and NGC 3226, and one S0, NGC 3414). Our detection rates are higher than published in an *IRAS* study of ETGs (Bregman et al., 1998), which

detected 12%–17%. Although the *IRAS* study excluded peculiar galaxies and active galactic nuclei (AGNs; with approximately half their sample at distances larger than the HRS), the small number of these sources in our sample suggests that the most likely explanation of the large difference in detection rates is that *Herschel* is more sensitive to cold dust than *IRAS*. This is supported by the higher mean dust temperature reported by Bregman et al. (1998). Temi et al. (2004) detected a higher fraction of ETGs (41% of ellipticals and 79% of S0s) with *ISO*, but their sample contains peculiar galaxies and giant ellipticals. The detection rates for the SPIRE and multi-wavelength data for our sample are listed in Table 6.3; these rates are significantly⁵ different for S0s and ellipticals at the 96% level. Our overall detection rate of 50% for the ETGs is higher than the 22% obtained by the ATLAS^{3D} CO study of 260 ETGs (Young et al., 2011), though the ATLAS^{3D} sample has a larger volume out to distances 46 Mpc (compared to 25 Mpc for the HRS). Comparing those galaxies which are in both the ATLAS^{3D} and HRS (i.e., observed in both CO and dust continuum), the detection fraction in CO is a factor of two lower than at 250 μm . Similarly for those galaxies with *Herschel* and HI observations, the detection fraction in HI is ~ 1.5 times lower (Table 6.3). The *Herschel* observations of the continuum emission from the dust are therefore currently the most sensitive way of detecting the ISM in the HRS sample of ETGs.

⁵Using the two-sided Fisher’s exact test, the equivalent of the χ^2 test but for small samples.

Table 6.3.
The Number of Early-type and Elliptical Galaxies Detected with *Herschel*

Type	SPIRE Sample				X-Ray Sample				CO Sample			
	Observed N	Detected N	250 %	Observed N	Detected N	X-ray %	Detected N	250 %	Observed N	Detected N	CO %	Detected N
Total	62	100%	31	50%	38	61%	29	76%	15	52%	56	90%
E	21	34%	5	24%	20	53%	16	80%	4	25%	20	34%
S0	38	61%	23	63%	15	39%	11	77%	9	82%	35	63%
pec	3	5%	3	100%	3	8%	2	67%	2	100%	1	2%
	Hi sample				Environment							
	Observed N	Detected N	250 %	Observed N	Detected N	250 %	Obs. Virgo N	Det. Virgo N	Obs. Not Virgo N	Det. Not Virgo N		
Total	49	79%	17	35%	16	94%	47	76%	21	45%	15	24%
E	15	31%	4	27%	4	100%	17	74%	5	29%	6	26%
S0	34	69%	13	38%	12	92%	30	77%	16	53%	9	23%
pec	0	0%	0	0%	0	0%
	(b/a ≤ 0.5)				(b/a > 0.5)							
	Observed N	Detected N	Det. Virgo %	Not Virgo %	Observed N	Det. Virgo %	Not Virgo %	Observed N	Detected N	Det. Virgo %	Not Virgo %	
S0	18	46%	12	67%	13/17	76%	1/1	100%	21	54%	12	57%
Barred	11	28%	6	55%	5/10	50%	1/1	100%	13	33%	6	46%

Notes. Top Panel: the detection numbers for the 250 μm , X-ray, and CO samples in this work. Columns are as follows. Column 1: morphological type for the sample. Columns 2–5: SPIRE-detected sources including—Column 2: number of sources observed; Column 3: percentage of the observed sample which falls into the different types; Column 4: number of sources detected with SPIRE; Column 5: percentage detected with

Continued on Next Page...

Table 6.3 (Continued)

SPIRE compared to the observed sources in each morphological class. Columns 6–11:*X-ray sources including*—Columns 6 and 7: number of sources in our sample observed in X-ray from the literature and the percentage which falls into each morphological class (O’Sullivan & Ponman, 2004; Pellegrini, 2010); Columns 8 and 9: number and percentage of the observed X-ray sources which are detected in X-ray; Columns 10 and 11: number of sources detected in X-rays *and* detected with SPIRE. Columns 12–17:*CO sources including*—Columns 12 and 13: number of sources in our sample observed in CO from the literature and the percentage which falls into each morphological class (Young et al., 2011); Columns 14 and 15: number and percentage of the observed CO sources which are detected in CO; Columns 16 and 17: number of sources detected in CO *and* detected with SPIRE. Middle Panel: the detection numbers for the HI and 250 μm sample, and for the entire 250 μm sample split by environment. Columns are as follows. Column 2–7:*HI sources including*—Columns 2 and 3: number of sources in our sample observed in HI from the literature and the percentage which falls into each morphological class; Columns 4 and 5: number and percentage of the observed HI sources which are detected in HI; Columns 6 and 7: number of sources detected in HI *and* detected with SPIRE. Columns 8–15:*Environment*: the number and percentage in each subset defined as within the Virgo Cluster (Columns 8–11) and outside (Columns 12–15). Given the small numbers in the Virgo/non-Virgo samples, we do not separate the peculiar galaxies in this analysis. Bottom Panel: the detection numbers for S0+S0a and barred S0 galaxies split into regimes depending on their axial ratios, where $b/a < 0.5$ and $b/a > 0.5$, indicating edge-on or face-on galaxies, respectively. Columns are as follows. Columns 2–9:*Edge-on galaxies including*—Columns 2 and 3: number and percentage of edge-on sources ($b/a < 0.5$); Columns 4 and 5: number and percentage of these sources which are detected with SPIRE. Columns 6 and 7: number of sources detected with SPIRE inside the Virgo Cluster and Columns 8 and 9 for those outside Virgo. Columns 10–17:*Face-on galaxies*—Columns 10 and 11 – number and percentage of face-on sources ($b/a > 0.5$); Columns 12 and 13: number and percentage of those sources which are detected with SPIRE. Columns 14 and 15: number of sources detected with SPIRE inside the Virgo Cluster and Column 16 and 17 for those outside Virgo.

Given the small number of ellipticals that have been detected by *Herschel*, it is interesting to ask the question of what makes these special. Twenty of the ETGs in our sample are classified as having low-ionization narrow emission line regions (LINERs). The origin of LINER activity in ETGs can be ionizing photons from the old stellar population (e.g., di Serego Alighieri et al., 1990; Sarzi et al., 2010), heating by the hot ISM (Sparks et al., 1989) or AGN heating (e.g., González-Martín et al., 2009). At least 12 of the HRS sample have bright radio cores (Figure 6.1) suggesting AGN photoionisation is important for at least 20% of the sample. For the most massive ellipticals, the hot ISM could be a significant photoionising source; nine of the detected LINER sources in our sample have X-ray luminosities well above that expected from the discrete stellar population i.e., $L_X/L_B \sim 10^{29.5}$ (O’Sullivan et al. 2001; Section 6.4.2) suggesting that a significant fraction of the LINER emission may originate from the hot ISM rather than an AGN source. Of the seven detected ellipticals, two are classified as LINERs, two as Seyferts and a further two are unambiguously identified as containing a bright AGN (Ho et al., 1997; Schmitt, 2001; Véron-Cetty & Véron, 2010). Only one of the seven, NGC 4406 (HRS 150) is a ‘pure’ elliptical with no sign of an active nucleus, but this galaxy has acquired dust and atomic gas through a recent interaction (Gomez et al., 2010). Nine other ‘pure’ ellipticals in our sample are not detected at $250\mu\text{m}$.

Another way to look at this question is to compare the properties of the detected and undetected sources in other wavebands. The distribution of the B -band luminosities for the sample is shown in Figure 6.3 along with the distributions of the detected sources. The figure shows that while there is no tendency for the detected S0 galaxies to be optically luminous, the detected elliptical galaxies are optically the most luminous ones.

Figure 6.3 shows a similar comparison for the X-ray luminosities. In this case, one might suspect that the galaxies with the highest X-ray luminosities from the hot halo are the least likely to be detected by *Herschel* because of sputtering. The figure shows that the elliptical galaxies detected at $250\mu\text{m}$ tend to have higher X-ray luminosities so that elliptical galaxies more luminous in X-rays and optical (i.e., the most massive stellar systems) tend to be detected by *Herschel*. The detected S0 galaxies span a wide range of L_B and L_K , indicating that the stellar mass of these systems is not the critical factor for detection by *Herschel*.

In contrast to the X-rays, we find that galaxies containing large masses of cool gas are more likely to be detected by *Herschel* (Figure 6.3). CO observations of our sources taken from the ATLAS^{3D} survey (Young et al., 2011) suggest that 28% of our ETGs have molecular gas (Table 6.3), similar to the detection rate of 22% for the

entire ATLAS^{3D} sample of 260 ETGs. Atomic hydrogen observations are available in the literature for 79% of our sample, although only 35% of these galaxies are detected.

We can also consider whether certain morphological types are more likely to be detected. Eighty percent of the undetected galaxies are morphologically classified as barred systems (NED, Table 6.1), which at first glance suggests that barred galaxies have less dust content than galaxies without a bar. However, we actually detect 50% of the barred sources from the HRS sample (Table 6.3), suggesting that the presence of a bar does not determine whether it is detected at $250\mu\text{m}$. Finally, we investigated whether the inclination angle might affect whether or not the galaxy was detected by *Herschel* using the measured axial ratios of the galaxies (minor axis/major axis— b/a). The detection rate for edge-on galaxies ($b/a < 0.5$) is 67% and for face-on galaxies ($b/a > 0.5$) is 57% though this is not statistically significant. Whether a galaxy has rings, bars or high inclination angles therefore does not affect whether it is detected by *Herschel*.

One important effect on whether we detect ETGs with *Herschel* is environment. It has long been known that galaxies in dense environments are depleted in atomic gas, and recent *Herschel* observations have shown that this is also true of dust (Cortese et al., 2010b, ; C12). Gravitational interactions might also either remove or add gas and dust to a galaxy. We can do a rough comparison of the detection rates in different environments using the cluster or cloud membership listed in Table 6.1. Following C12, we split our sample into two sets: one set includes galaxies inside the Virgo Cluster and its outskirts ($N = 47$ galaxies) and the other set includes galaxies outside Virgo ($N = 15$). We detect 53% (16/30) of the S0s and 29% (5/17) of the ellipticals within the Virgo Cluster. Outside Virgo, we detect 89% (8/9) and 33% (2/6) respectively (Table 6.3). The detection rates are therefore lower for galaxies within the Virgo Cluster, but this is not at a significant level.⁵

6.3.2 RESIDUAL STAR FORMATION?

We now discuss if our galaxies are truly quiescent or show signs of recent star formation. We use the NUV– r color, as it is a useful measure of the specific star formation rate (SFR/M_*) since the NUV is a tracer of recent star formation and the r band is a proxy for the stellar mass (e.g., Wyder et al., 2007). The NUV band is used instead of the FUV as it is less affected by the absorption of dust, although it can be contaminated by the emission of evolved hot stars (the UV-upturn e.g, Greggio & Renzini, 1990; Yi et al., 2011; Ford et al., 2012). Blue, star-forming galaxies have $\text{NUV} - r < 3.5$ (i.e., the ‘blue cloud’, Kaviraj et al., 2007) while red passive ETGs

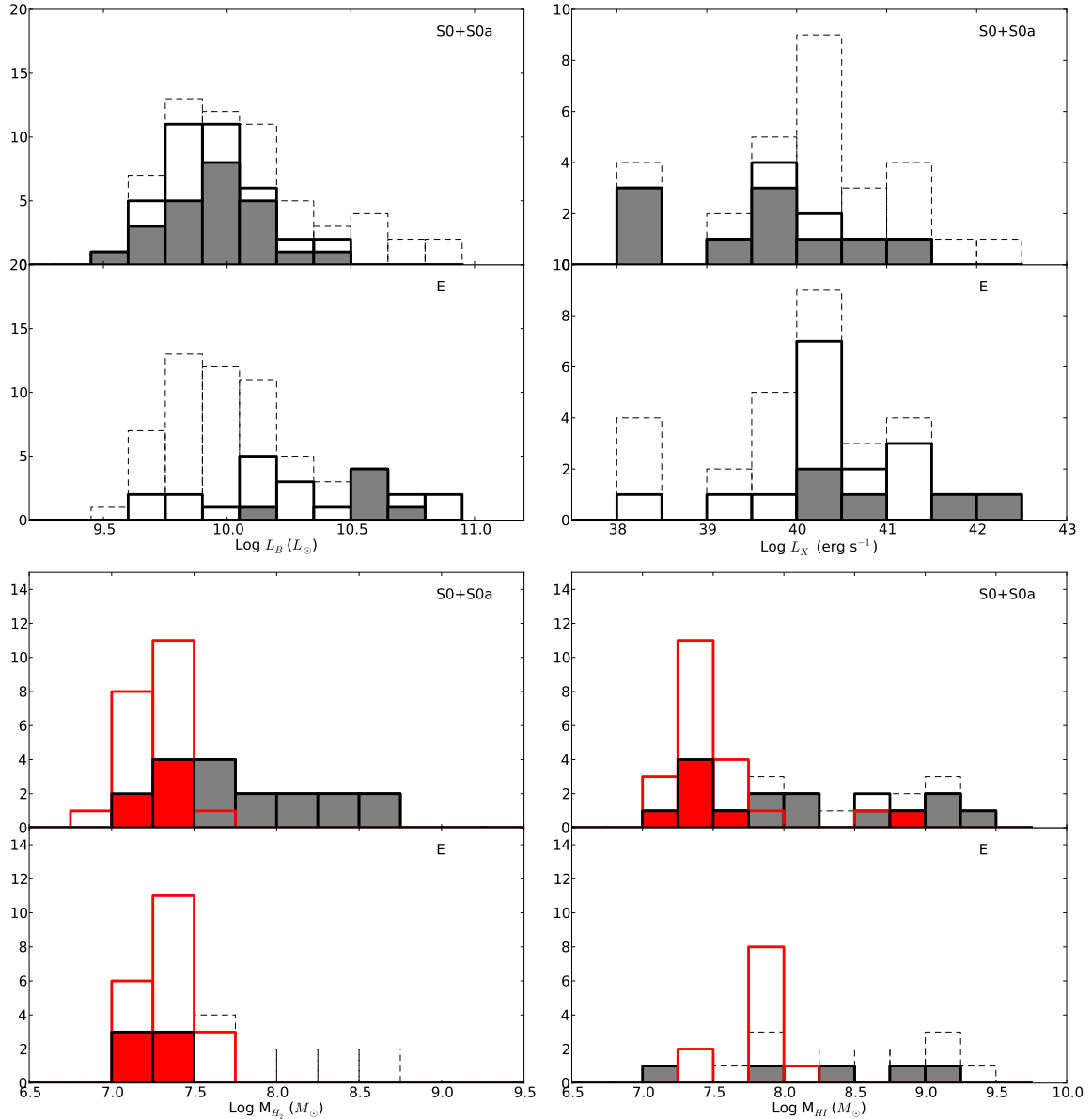


Figure 6.3. Top left: the range of B -band luminosities; top right: X-ray luminosities for the S0+S0a (top) and elliptical (bottom) galaxies. The outer dashed histogram shows the range of the whole sample (S0+S0a or E combined), the thick black unfilled histograms are the subsamples (S0+S0a and E separated out), and the detected sources are shaded gray. Bottom left: the molecular gas mass estimated from CO observations; bottom right: the atomic gas mass from HI. The red histograms show the upper limits on the gas mass obtained from the CO (HI), i.e., these are sources in our sample not detected either at $250\mu\text{m}$ or CO (HI). The red shaded histogram shows the sources detected at $250\mu\text{m}$ but *not* detected in CO (HI).

occupy the region $\text{NUV}-r > 4.5$ (the ‘red sequence’). While a $\text{NUV}-r > 4.5$ is often used to select galaxies on the ‘red sequence’, passive galaxies are significantly redder than this. For example Saintonge et al. (2011) found that galaxies with $\text{NUV}-r > 5$ contain little molecular gas and Kaviraj et al. (2007), Schawinski et al. (2007) and Yi et al. (2005) have shown ‘passive’ (quiescent/non-starforming) ETGs have $\text{NUV}-r > 5.4$.

The NUV should be corrected for both dust extinction (as we detect dust in almost 50% of objects) and for the ‘UV upturn’. There may also be a bias due to any LINER-type activity present. Due to the complexity of these corrections we leave this to future work. Following Schawinski et al. (2007) we simply classify galaxies as quiescent if $\text{NUV}-r > 5.4$ and possibly undergoing recent star formation (RSF) if $\text{NUV}-r < 5.4$. Figure 6.4 shows the $\text{NUV}-r$ color for the entire HRS sample where the values are taken from C12 and Cortese et al. (2012b). The galaxies detected by *Herschel* are outlined by black circles.

Most of our ETG sample are clustered around the line $\text{NUV}-r = 5.5$, with only two objects falling below $\text{NUV}-r = 4.5$. The ETGs with $\text{NUV}-r < 5.4$ might be due to the ‘UV-upturn’ rather than residual star formation. A famous case of this in our sample is NGC 4552 which has no residual star formation, but has a $\text{NUV}-r \sim 5.2$. Excluding NGC 4552, 12 out of 18 S0s lying below this boundary are detected with *Herschel* and 2 out of 7 ellipticals. The two ellipticals have either an AGN (NGC 4486, HRS 138) or an (unusual) X-ray source (NGC 4636, HRS 241) which could contribute to their NUV emission. Approximately 40% of our ETG sample is classified as RSF, including 30% of ellipticals. These figures agree with the fraction of RSF ETGs in the SDSS (Schawinski et al., 2007).

Figure 6.4 clearly shows that a large number of ETGs that lie on the ‘red sequence’ and in the quiescent region are detected by *Herschel*. Objects on the ‘red sequence’ are often assumed to contain very little inter-stellar material. A detection of dust in $\sim 50\%$ of our sample indicates that galaxies on the ‘red sequence’ can contain significant amounts of interstellar material, agreeing with recent CO observations in ETGs (Young et al., 2011).

6.3.3 DUST MASSES AND TEMPERATURES

The global IR-submm SEDs of the detected S0+S0a and elliptical galaxies with available data from 60 to $500\mu\text{m}$ are presented in Figures 6.5 and 6.6, respectively. NGC 4486 (M 87) and NGC 4374 are both bright radio sources and their SEDs are well fitted by a power law at the longer FIR wavelengths. For the former, we find no

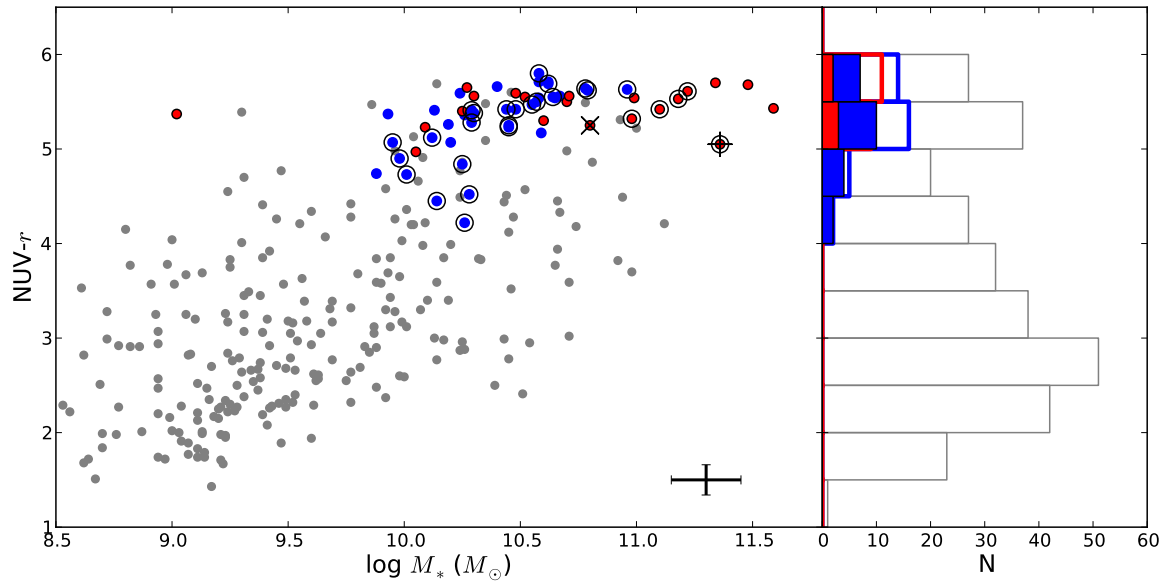


Figure 6.4. Left: the $\text{NUV}-r$ color vs. the stellar mass of the HRS sample (Cortese et al., 2012b) including our morphologically classified spirals (gray, C12), S0+S0a (blue), and elliptical galaxies (red). The S0+S0a and elliptical galaxies detected with SPIRE are highlighted with the outer black circles. Note that the galaxy NGC 4486 is shown as detected in this plot but we do not see evidence for dust (above the synchrotron emission), NGC 4486 is highlighted with “+”. The well-known galaxy with no evidence for star formation (NGC 4552) but with somewhat bluer $\text{NUV}-r$ color than the average elliptical in our sample is highlighted with a “ \times ”. UV photometry exists for 87% of the ellipticals and 95% of the S0 sample. Right: the distribution of $\text{NUV}-r$ colors for the observed samples split into spirals (gray), S0+S0a (blue), and ellipticals (red; unfilled histograms) including detections for the early -types (shaded histograms).

evidence for dust emission above the power-law synchrotron component (in agreement with Baes et al., 2010b). In NGC 4374, we do see a strong excess from dust emission in the FIR. We fit the SEDs from 100 to 500 μm with a modified blackbody model, where

$$S_\nu = \frac{\kappa_\nu M_d B(\nu, T_d)}{D^2}, \quad (6.1)$$

M_d is the dust mass, T_d is the dust temperature, $B(\nu, T_d)$ is the Planck function and D is the distance to the galaxy. κ_ν is the dust absorption coefficient described by a power law with dust emissivity index β , such that $\kappa_\nu \propto \nu^\beta$. For $\beta = 2$ (typical of Galactic interstellar dust grains), we use $\kappa_{350\mu\text{m}} = 0.19 \text{ m}^2 \text{ kg}^{-1}$ (Draine, 2003). Although κ is notoriously uncertain, virtually all of our analysis relies on κ being constant between galaxies rather than on its absolute value.

We assumed $D = 17 \text{ Mpc}$ for the Virgo Cluster (Gavazzi & Boselli, 1999) and 23 Mpc for the Virgo B cloud; for all other galaxies, we estimated D from the recessional velocities using a Hubble constant of $H_o = 70 \text{ km s}^{-1} \text{ Mpc}^{-1}$.

We found the best-fit solution by minimizing the chi-squared (χ^2) difference between the model and the measured fluxes, involving the model with the filter transmission functions. To account for the uncertainties in the fluxes that are correlated between the SPIRE bands (5%), we used the full covariance matrix in the χ^2 calculation. The covariance matrix has diagonal elements with the total variance of each band and non-diagonal elements consisting of the covariance between bands from the correlated calibration uncertainties. We treated flux measurements at wavelengths $\leq 70 \mu\text{m}$ as upper limits for the cold dust emission as previous works (Smith et al., 2010; Bendo et al., 2010a) found that there is a significant contribution at these wavelengths from a warmer component of dust. We estimated uncertainties in the dust temperatures and masses using a bootstrap technique, in which we generated artificial sets of fluxes from the measured fluxes and errors, and then applied our fitting technique to each set of fluxes. The dust temperatures, and therefore dust masses, depend on the choice of β ; $\beta = 1.5$ would yield slightly higher dust temperatures for the whole sample (Bendo et al., 2003) and therefore lower dust masses.

The SED for NGC 5273 (Figure 6.5) is the only one which appears to have an additional component present. Using the $\beta = 2$ one-temperature component described above provides an adequate fit to the photometry data if an additional synchrotron component is present. The SED is also adequately fit with a one temperature dust component model with β as a free parameter, $\beta = 0.9$, or with a two-temperature dust component model. To fit the data with the latter model would require an additional component of $\sim 9 \text{ K}$ dust which would increase the dust mass

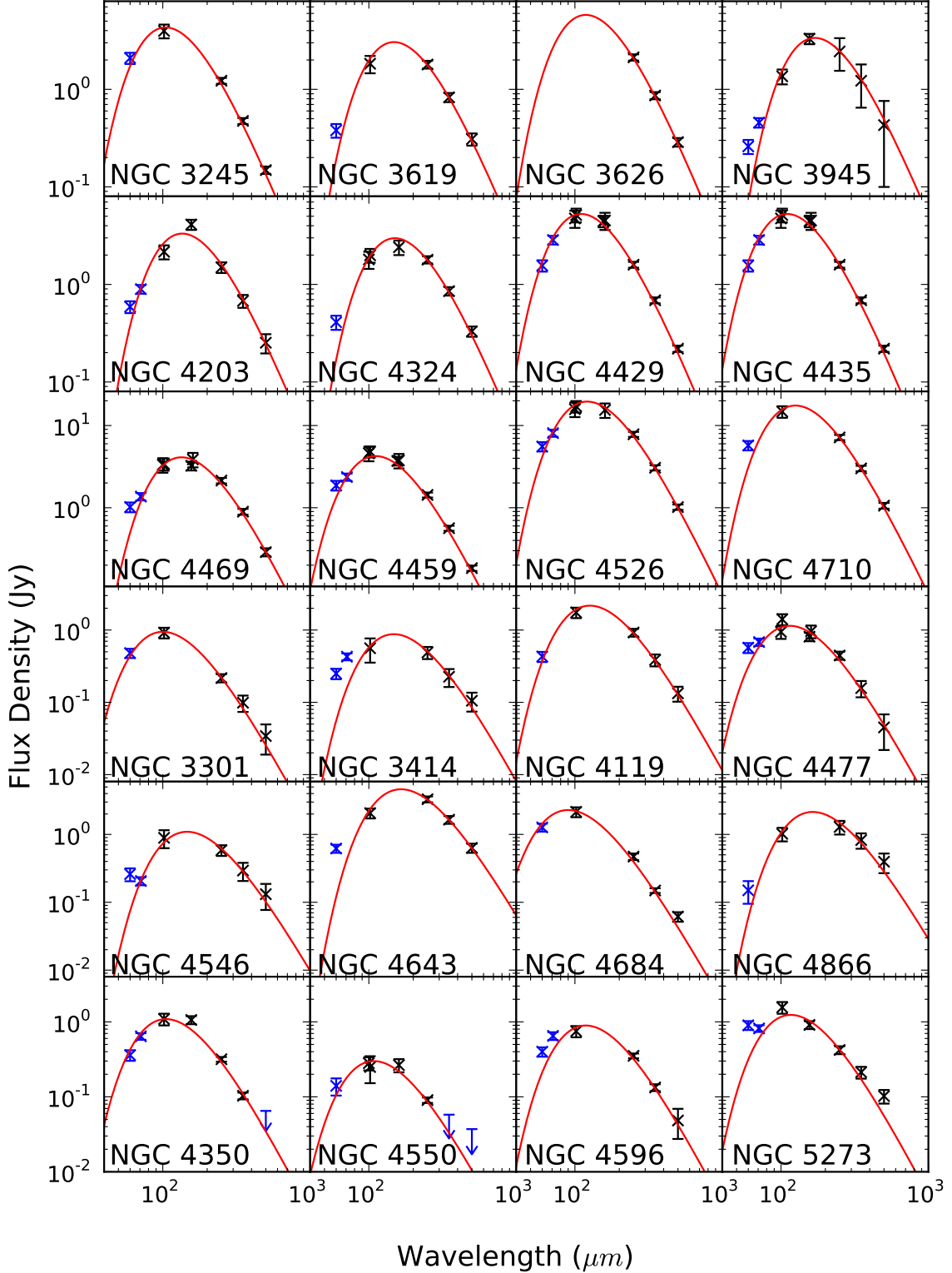


Figure 6.5. Spectral energy distributions of the 24 detected S0+S0a galaxies in our sample. The red solid line is the best-fit modified blackbody, blue points are fluxes used as upper limits, and black crosses are the photometry used for the cold dust component, including *Herschel* SPIRE fluxes and PACS, *IRAS*, and *Spitzer* where available. Errors shown also include calibration errors (Ciesla et al., 2012). The best-fit model parameters are provided in Table 6.4.

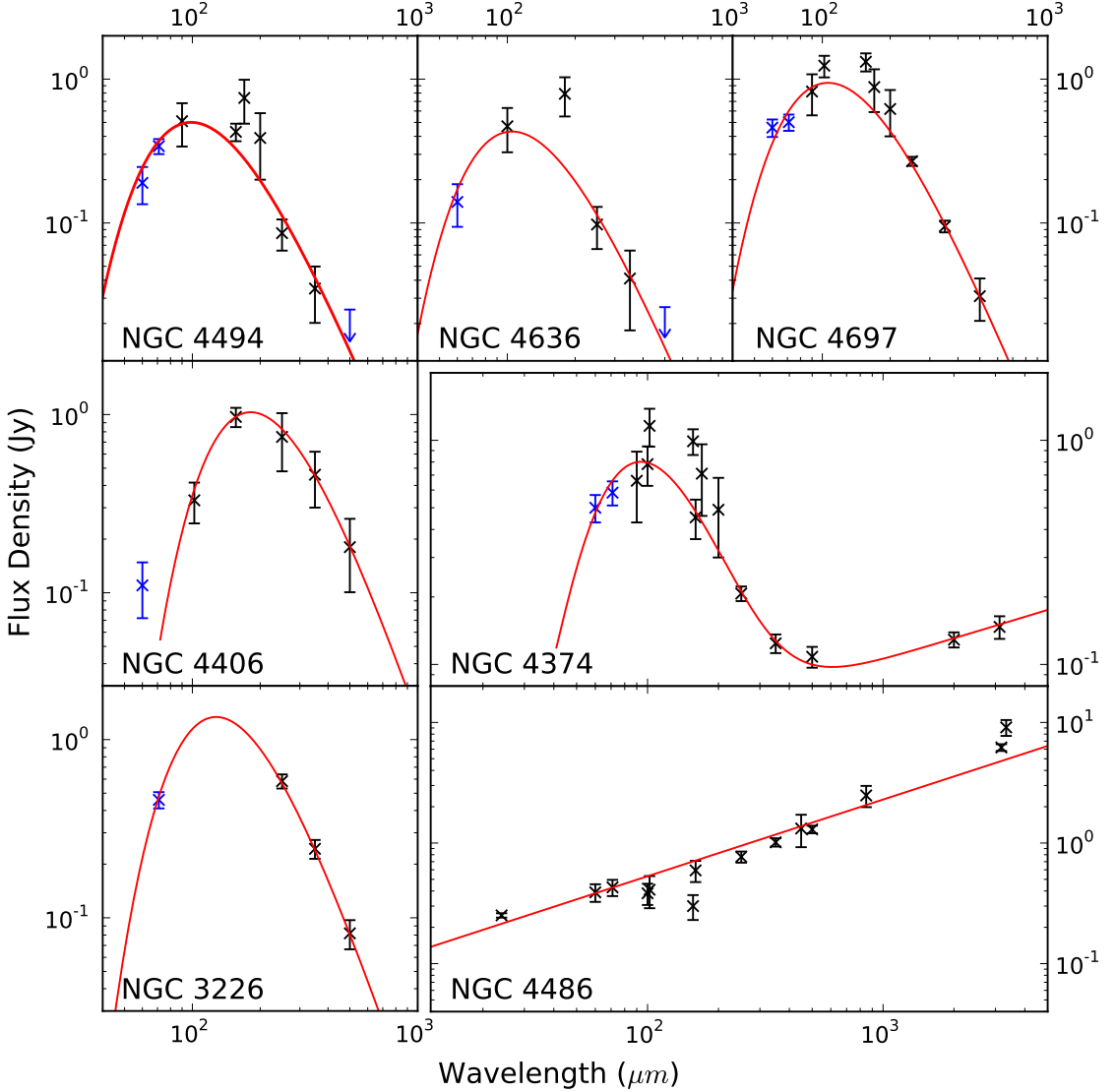


Figure 6.6. Spectral energy distributions of the seven detected ellipticals in our sample. Blue points are those fluxes used as upper limits and black crosses are the photometry used for the cold dust component, including *Herschel* SPIRE and PACS, *IRAS*, *ISO*, and *Spitzer* where available. Radio fluxes are also shown by black points for NGC 4374 and NGC 4486 (M 87). The red solid line is the best fit to the data and includes a modified (single temperature component) blackbody with $\beta = 2$ and a synchrotron component. Errors shown also include calibration errors (Ciesla et al., 2012). These galaxies are discussed in more detail in Appendix D and the best-fit model parameters are listed in Table 6.4.

by an order of magnitude. Both the $\beta = 2 +$ synchrotron model and $\beta = 1$ model give a dust mass of $10^{5.45} M_{\odot}$ which is somewhat lower than the dust mass estimated using the $\beta = 2$ one-temperature dust component without synchrotron ($10^{5.65} M_{\odot}$) but within the errors (Table 6.4). As no millimetre data are available for this source, we cannot rule out synchrotron contamination, so in this analysis we have chosen to stick with the $\beta = 2$ one-component model to be consistent with the other sources.

We have estimated upper limits to the dust masses for the galaxies undetected by *Herschel* using the flux upper limit at $250 \mu\text{m}$ (including the noise on the image, an estimate of confusion noise and background variance in the map as described in (Ciesla et al., 2012) and the average temperature for the detected galaxies.

The dust masses and temperatures are presented in Table 6.4, and we show the range of dust temperatures, masses, and stellar masses for the S0+S0a and elliptical detected sample in Figure 6.7. These range from $M_d = 10^{5.0-7.1} M_{\odot}$ and $16 - 32 \text{ K}$ with mean values of $10^{6.14} M_{\odot}$ and 24 K , respectively (Table 6.5). The stellar masses of these galaxies (C12) range from $10^{9.9-11.2} M_{\odot}$ with an average of $\langle \log M_*(M_{\odot}) \rangle = 10.89$; the average dust-to-stellar-mass ratio is $\log(M_d/M_*) = -4.33 \pm 0.14$. The M_d/M_* ratios are plotted in Figure 6.8 and clearly shows that, at the same stellar mass, there is a sharp fall in the dust-to-stellar-mass as we move from spirals to S0s (by roughly a factor of 10), and that this fall continues as we move from S0s to ellipticals (again, by a factor of 10). The two ellipticals with anomalously high values given their stellar mass are NGC 3226 (HRS 3) and NGC 4406 (HRS 150). Both galaxies show signs of a tidal interaction (see Appendix D), suggesting that the dust may have been acquired as the result of an interaction with a dust-rich galaxy.

6.4 DUST, STARS AND GAS

In this section we compare the dust temperatures, masses, and dust-to-stellar ratios with other *Herschel* results of late-type and early-type galaxies. First, the temperatures for the HRS ETGs are generally higher than temperatures for the galaxies detected in blind submm surveys or in other samples of nearby galaxies (see Planck Collaboration, 2011b; Dunne et al., 2011) when corrected for different choices of β . We have tested whether the temperatures of ETGs are systematically higher than those of late types by comparing our dust temperatures with those of 71 Virgo galaxies in Davies et al. (2012) who used an identical method. We find that the temperatures of the early types are systematically higher (with $U = 1638$, $n_1 = 70$, $n_2 = 30$ and

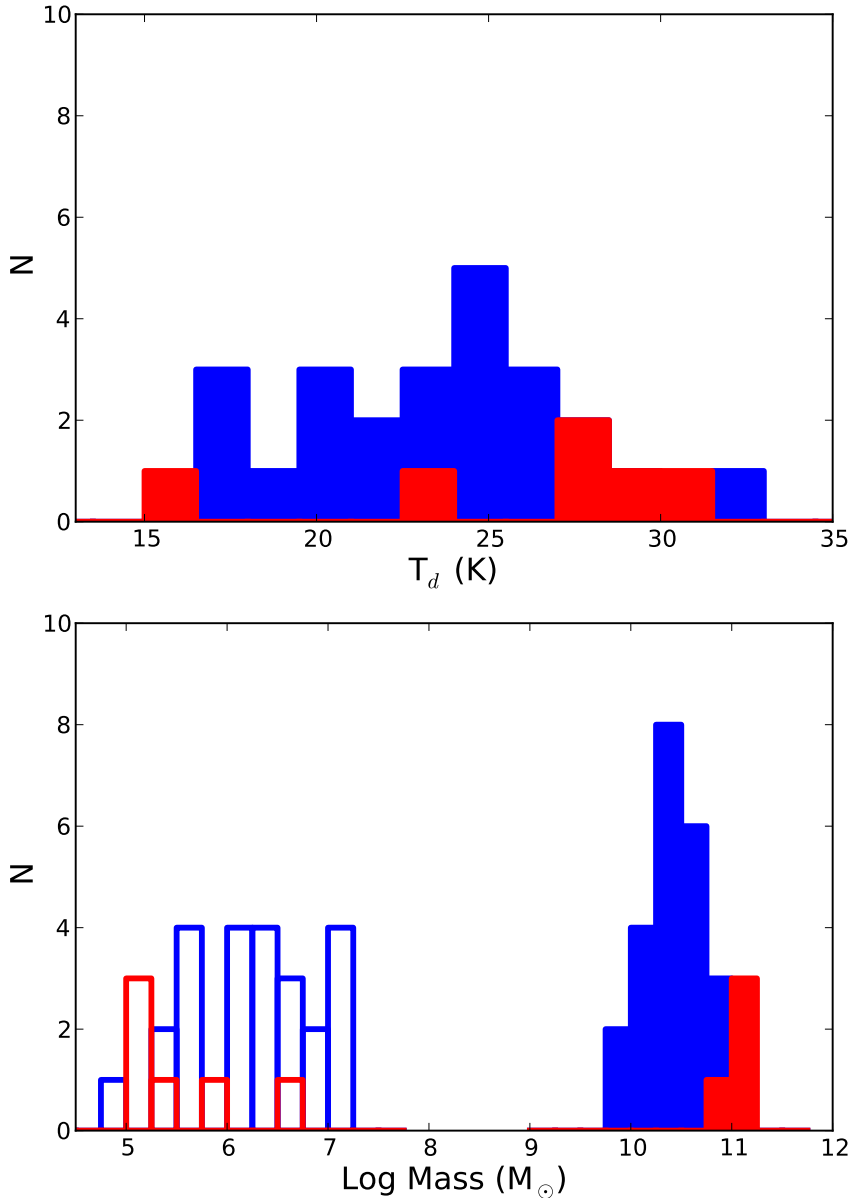


Figure 6.7. Top: histogram of the dust temperatures based on single modified blackbody fits; bottom: dust (left) and stellar masses (right shaded; Cortese et al. 2012b) for the detected ellipticals (red) and S0+S0a galaxies (blue)—see Table 6.4. The populations of the dust and stellar masses of the detected ellipticals and S0s are different with significance level $P > 97.9\%$ (M_d) and $P > 99.9\%$ (M_*) using a Mann–Whitney U-test.

$P > 99.99\%$ using the Mann–Whitney U statistic⁶), in agreement with the result that the ETGs in the HRS have warmer IR colors than late types (Boselli et al. 2010a ; see also Bendo et al. 2003; Engelbracht et al. 2010).

In Figure 6.8, we compare the ratio of dust-to-stellar-mass for the HRS ETGs with the *Herschel* KINGFISH (Kennicutt et al., 2011) results based on 10 nearby early types (Skibba et al., 2011). They find warmer dust temperatures, with a mean of $\langle T_d \rangle = 30$ K (mostly due to the use of a lower emissivity index $\beta = 1.5$ compared to this work), and their sample has a lower average stellar mass compared to the HRS. Though their dust masses are similar, the dust-to-stellar-mass ratios are higher in KINGFISH than for the HRS. This may be a result of the different environments (a large fraction of the HRS galaxies are in a rich cluster) and/or the selection of the sample (KINGFISH ETGs may include unusual galaxies rather than the flux-selected ETGs in the HRS).

Rowlands et al. (2012) detected only $\simeq 5\%$ of ETGs in a blind submm survey with *Herschel* at $250\,\mu\text{m}$, finding a median dust mass for their detected galaxies (in their lowest redshift bin) of $10^{7.8} M_\odot$ with average dust temperature consistent with the HRS ETG sample. Their dust mass is significantly higher than the dust masses of the HRS ETGs and their mean value of their dust-to-stellar mass ratio ($\log(M_d/M_*) = -2.95$, Figure 6.8) is also larger. Many of their sources have bluer UV–optical colors than the HRS (with a significant fraction lying below $\text{NUV}-r < 4$: their Figure 15), suggesting that the larger amount of dust in the H-ATLAS galaxies is associated with increased star formation (Rowlands et al., 2012). The simplest explanation of the differences is that the H-ATLAS study is picking up the rare, very dusty ETGs, which the HRS misses, partly because it is not large enough, and possibly also because it is dominated by the ETGs in the Virgo Cluster. A possible local example of these rare dusty ETGs is the local elliptical Cen A (Parkin et al., 2012). Since the depth of the SDSS images used for the morphological classification in the H-ATLAS study made it impossible to distinguish between ellipticals and S0s, it is also possible that some of the ETGs detected in H-ATLAS are S0s or early-type spirals rather than ellipticals.

⁶Using the Mann–Whitney U statistic, appropriate when comparing two groups where the underlying distribution of the data is not necessarily normal. The statistic assumes that the observations are independent and are continuous (i.e., able to be ranked) and is more robust than the Student’s t -test.

Table 6.4.
SED Parameters and Gas Masses

HRS Name	Type	$\log L_{\text{FIR}}$ (L_{\odot})	T_d (K)	$\log M_d$ (M_{\odot})	$\log M_{\text{H}_2}$ (M_{\odot})	$\log M_{\text{HI}}$ (M_{\odot})	Rotator
3	E	8.50	22.7 ± 1.29	5.96 ± 0.09	<7.13	...	F
7	S0	9.20	27.7 ± 1.5	6.14 ± 0.05	7.20	...	F
14	S0	8.57	29.0 ± 1.9	5.41 ± 0.12	<7.31	7.80^3	F
22	S0	8.42	19.6 ± 2.0	6.26 ± 0.21	<7.02	...	S
43	E	<7.56	...	<4.88	<7.28	...	S
45	S0	9.04	19.6 ± 1.0	6.89 ± 0.07	8.11	8.89^3	F
46	S0	9.38	24.4 ± 4.0	6.65 ± 0.17	8.29	9.02^3	F
49	E	<7.88	...	<5.20	<7.25	...	F
71	S0	8.84	17.1 ± 1.1	7.05 ± 0.18	<7.28	...	F
87	S0	8.73	22.9 ± 1.0	6.17 ± 0.09	7.91	...	F
90	S0	<8.38	...	<5.70	<7.31	$<7.68^1$	F
93	S0	8.81	21.4 ± 0.6	6.43 ± 0.07	7.63	9.44^4	F
101	S0	<8.41	...	<5.73	<6.92	$<7.39^1$	F
105	S0	<8.12	...	<5.44	<7.16	8.71^1	F
123	S0	8.79	19.3 ± 0.6	6.68 ± 0.07	7.72	8.73^1	F
125	E	<7.85	...	<5.17	<7.2	$<7.84^1$	F
126	S0	<8.48	...	<5.80	...	$<7.31^1$	F
129	S0	8.51	27.6 ± 0.6	5.47 ± 0.04	<7.27	$<7.38^1$	F
135	E	<8.85	...	<6.17	<7.62	$<8.18^1$	S
137	S0	<8.91	...	<6.23	<7.29	$<7.38^1$	F
138	E	8.4	31.1 ± 1.0	5.05 ± 0.06	<7.16	8.96^1	S
150	E	8.25	16.0 ± 1.1	6.63 ± 0.16	<7.4	7.95^2	S
155	S0	<8.71	...	<6.03	<7.54	$<7.64^1$	F
161	S0	9.18	26.3 ± 0.6	6.26 ± 0.04	8.05	$<7.44^1$	F
162	S0	9.13	25.0 ± 1.2	6.34 ± 0.10	7.87	$<7.31^1$	F
166	S0	<9.06	...	<6.38	<7.48	$<7.64^1$	F
174	S0	9.11	26.4 ± 0.6	6.18 ± 0.03	8.29	$<7.61^1$	F
175	S0	<8.29	...	<5.61	<7.23	$<7.13^1$	F
176	S0	9.25	21.6 ± 0.7	6.83 ± 0.05	...	$<7.64^1$	F
178	E	<8.45	...	<5.77	<7.25	$<7.92^1$	S
179	E	<7.87	...	<5.19	<7.16	$<7.92^1$	F
180	S0	8.49	25.2 ± 1.6	5.68 ± 0.11	7.54	$<7.31^1$	F
181	E	<7.53	...	<4.85	<7.31	...	F
183	E	S
186	E	8.28	29.3 ± 1.3	5.08 ± 0.11	<7.35	8.26^1	F
200	S0	9.7	23.9 ± 0.6	7.03 ± 0.04	8.62	7.13^1	F
202	E	<7.61	...	<4.93	...	$<7.37^1$	F
209	S	8.26	19.8 ± 0.8	6.08 ± 0.11	<7.05	...	F
210	S0	7.94	26.8 ± 1.8	4.97 ± 0.08	<7.32	8.79^1	S
211	E	<8.35	...	<5.67	<7.36	$<7.92^1$	S
214	E	<7.98	...	<5.30	<7.33	$<7.79^1$	F
218	E	<8.35	...	<5.67	<7.47	$<7.31^1$	F
219	S0	<8.41	...	<5.73	<7.24	$<7.24^1$	F
231	S0	8.37	24.5 ± 1.3	5.64 ± 0.08	7.34	$<7.19^1$	F
234	S0	<8.55	...	<5.87	<7.33	$<7.44^1$	F
235	S0	<7.95	...	<5.27	<7.22	$<7.38^1$	F
236	E	<8.44	...	<5.76	<7.24	$<7.92^1$	F
240	S0	<8.20	...	<5.52	<7.30	$<7.44^1$	F

Continued on Next Page...

Table 6.4 (Continued)

HRS Name	Type	$\log L_{\text{FIR}}$ (L_{\odot})	T_d (K)	$\log M_d$ (M_{\odot})	$\log M_{\text{H}_2}$ (M_{\odot})	$\log M_{\text{HI}}$ (M_{\odot})	Rotator
241	E	8.11	27.6 ± 2.2	5.06 ± 0.19	<7.02	9.0 ¹	S
243	S0	8.94	17.5 ± 0.7	7.08 ± 0.07	7.30	8.06 ¹	F
245	E	<8.08	...	<5.40	<7.59	<7.92 ¹	F
248	E	<7.53	...	<4.85	<7.30	<7.92 ¹	F
250	S0	<9.14	...	<6.46	...	<8.66 ¹	F
253	S0	9.1	32.2 ± 1.4	5.65 ± 0.06	7.63	8.22 ³	F
258	E	8.48	27.4 ± 0.7	5.46 ± 0.04	<7.25	...	F
260	S0	9.64	23.1 ± 1.2	7.06 ± 0.05	8.72	7.76 ²	F
269	S0	<8.95	...	<6.27	<7.23	<7.44 ¹	F
272	S0	<9.16	...	<6.48	<7.23	<7.92 ¹	F
286	S0	8.61	17.7 ± 1.2	6.73 ± 0.17	...	9.13 ¹	F
296	S0	8.43	24.8 ± 2.6	5.65 ± 0.20	7.26	...	F
312	E	<8.19	...	<5.51	<7.46	...	S
316	E	<7.91	...	<5.23	<7.54	...	F

Notes. Column 1: HRS ID; Column 2: morphological classification; Columns 3 and 4: the FIR luminosity (of the cold dust component) and dust temperature; Columns 5: dust masses estimated using $\beta = 2$ and $\kappa_{350} = 0.19 \text{ m}^2 \text{ kg}^{-1}$, 3σ upper limits (Ciesla et al., 2012) are quoted where the source is not detected using the mean dust temperature; Columns 6 and 7: molecular masses estimated from CO (Young et al., 2011) and HI masses (references below); Columns 8: low (S) or fast (F) rotator as defined by ATLAS^{3D} (Emsellem et al., 2011).

References. (1) Gavazzi et al. (2003); (2) Haynes et al. (2011); (3) Springob et al. (2005); (4) Noordermeer et al. (2005).

^a No SDSS data are available for HRS 209 or HRS 186.

Rowlands et al. (2012) were also able to estimate the dust masses of the ETG population *as a whole* using a stacking analysis. They estimated a mean dust mass of $10^{6.3} M_{\odot}$, with a mean dust temperature of 25 K and a mean dust-to-stellar-mass ratio of $\log(M_d/M_*) = -4.87$. This is in reasonable agreement with the average parameters of the early-type sample from this work and in particular, with the S0+S0a sample and our most dusty ellipticals (Figure 6.8).

6.4.1 DUST AND STELLAR MASS ALONG THE HUBBLE SEQUENCE

The average dust mass for the S0+S0a and elliptical galaxies detected by *Herschel* is $10^{6.3} M_{\odot}$ and $10^{5.5} M_{\odot}$ (Figure 6.7, Table 6.5) with average dust temperatures of 23.5 and 25.7 K, respectively. The dust masses for the two morphological groups are significantly different (Mann–Whitney $U=117$ with $n_1 = 6$, $n_2 = 24$ at $P > 99.7\%$ for two-sided test).⁶ This does not take into account the large number of upper limits so we have used the Astronomical Survival Analysis programs (Feigelson & Nelson, 1985), implemented through the IRAF STSDAS STATISTICS package, to compare the two samples. Using three different tests we find that the probabilities that the

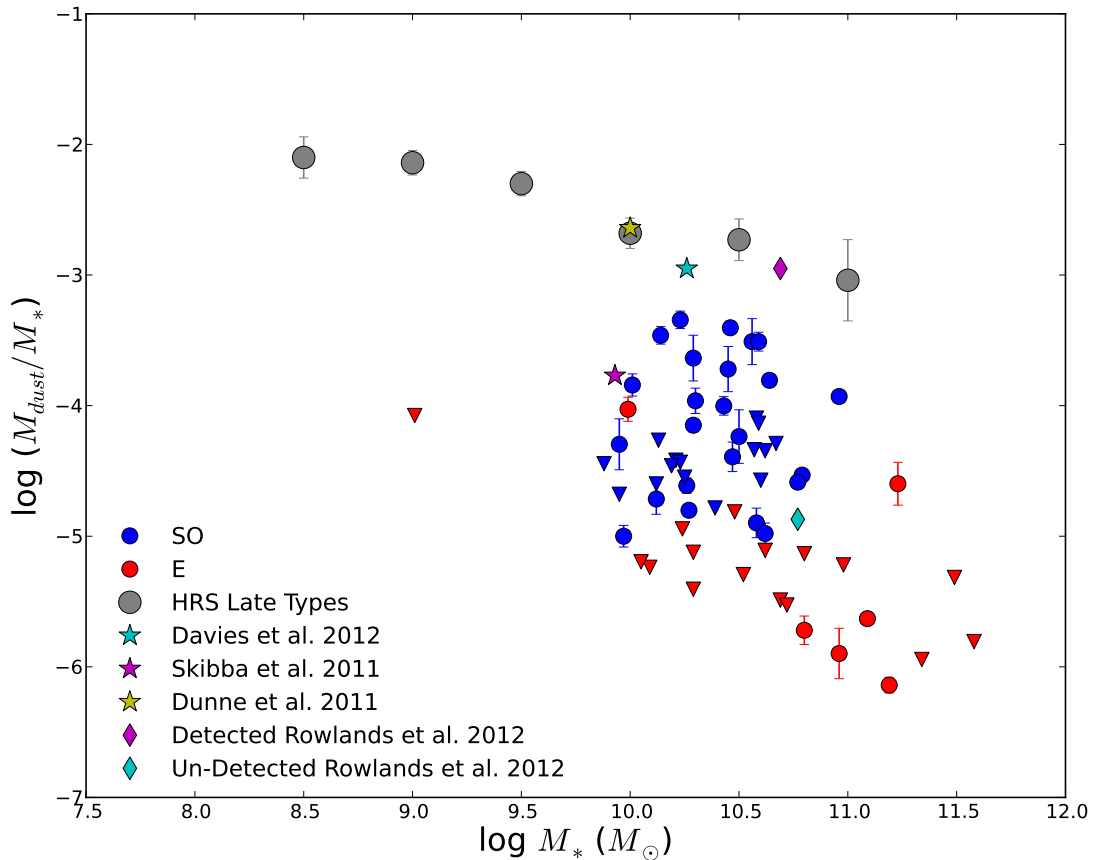


Figure 6.8. Dust-to-stellar-mass ratio vs. stellar mass. Blue points are the detected S0+S0a galaxies, with red points for the ellipticals. Upper limits on the dust mass are shown with triangles. The mean M_d/M_* for the HRS spirals in each stellar mass bin is shown with gray circles (see C12, his Figure 5) with error bars indicating the error on the mean. We also compare the mean M_d/M_* results of late types in HeViCS (blue star; Davies et al. 2012) and H-ATLAS (yellow star; Dunne et al. 2011), early types with H-ATLAS (Rowlands et al. 2012 for detected (purple diamond) and undetected (cyan diamond) early-type populations), and early types with KINGFISH (purple star; Skibba et al. 2011). The stellar masses are from Cortese et al. (2012b).

Table 6.5
Mean Parameters for the Sample

Type	N	T_d (K)	$\log M_d$ (M_\odot)	$\log M_*$ (M_\odot)	$\log M_d/M_*$	$\log L_X$ (erg s^{-1})	$\log M_{\text{H}_2}$ (M_\odot)	$\log M_{\text{HI}}$ (M_\odot)
Detected sample:								
Total	31	23.9 ± 0.8	6.12 ± 0.12	10.49 ± 0.07	-4.33 ± 0.13	40.02 ± 1.17 (15)	...	8.40 ± 0.17 (15)
E (+E/S0+pec)	7	25.7 ± 2.5	5.54 ± 0.28	10.89 ± 0.19	-5.26 ± 0.24	40.96 ± 3.11 (5)	< 7.21 (0)	8.26 ± 0.14 (5)
S0 (+pec)	24	23.5 ± 0.8	6.26 ± 0.13	10.40 ± 0.06	-4.13 ± 0.12	39.34 ± 1.90 (10)	7.84 ± 0.25 (16)	8.47 ± 0.19 (10)
Entire sample:								
Total	62	...	5.59 ± 0.09	10.09 ± 0.12	-5.12 ± 0.14	39.89 ± 0.18	7.13 ± 0.67 (57)	7.57 ± 0.11 (48)
E (+E/S0+pec)	22	...	5.21 ± 0.09	10.66 ± 0.13	-5.83 ± 0.11	40.13 ± 0.24	7.02 ± 1.29 (21)	7.72 ± 0.17 (15)
S0 (+pec)	39	...	5.87 ± 0.13	10.38 ± 0.04	-4.42 ± 0.10	39.25 ± 0.24	7.25 ± 0.75 (36)	7.58 ± 0.13 (33)

Notes. Top: the mean parameters for the detected sample of early types. Bottom: the mean parameters estimated using survival analysis, including the upper limits. The error quoted is the standard error of the mean. The columns are as follows.
 Column 1: morphological type. Column 2: the number of sources. Column 3: the average dust temperature. Column 4: the average dust mass (dust masses are estimated using a single temperature modified blackbody with $\beta = 2$ and $\kappa_{350} = 0.19 \text{ m}^2 \text{ kg}^{-1}$). Column 5: the average stellar masses using the optical colors Cortese et al. (2012b). Column 6: the average dust-to-stellar-mass ratio. Column 7: average X-ray luminosity—the numbers in brackets give the number of sources with X-ray and 250 μm detections. Column 8: the average molecular gas masses estimated from the CO data. Column 9: the average atomic gas masses estimated from HI data.

elliptical and S0+S0a dust masses are drawn from the same population are 0.0005, 0.0006, and 0.004, and for M_d/M_* , the probabilities are zero (Table 6.6); these parameters for S0+S0a and ellipticals in our sample almost certainly arise from different distributions. We have used the Kaplan–Meier estimator⁷ to estimate the mean⁸ for the two samples, making the necessary approximation that the lowest upper limit is actually a detection. With this approximation, we find that the mean dust mass for the S0s is $10^{5.87} M_\odot$ and the mean dust mass for the ellipticals is $10^{5.21} M_\odot$ (Table 6.5).

C12 has recently shown that the dust-to-stellar-mass ratio decreases when moving from late- to early-type galaxies, but used a conservative approach by treating non-detections as upper limits. Here we incorporate the information in the upper limits on the non-detected sources and quantify the change as we move along the Hubble sequence. We estimate that the mean value⁸ of the dust-to-stellar-mass for the ellipticals is $\log(M_d/M_*) = -5.83 \pm 0.1$ and for the S0s is -4.42 ± 0.1 (Table 6.5).

Following C12 (his Figure 5), we plot the dust-to-stellar-mass ratio against morphological type in Figure 6.9. We split the late-type sample into the subgroups: Sa+Sab, Sb+Sbc, Sc+Scd and Sd+Sdm. The figure also shows the strong drop in mean dust-to-stellar mass ratio from early-type spirals to S0s (and the further decline as we move to ellipticals). Figure 6.9 suggests that the variation in this ratio is larger for early types than late types. This is particularly true for early-type spirals and S0+S0a galaxies with M_d/M_* ranging by a factor of approx. 50. Although ellipticals probably have a similarly wide range in dust-to-stellar-mass, the high number of non-detections make it difficult to be sure of this.

6.4.2 THE ORIGIN OF DUST IN ETGS

With detections of dust in 50% of our ETGs, a big question is what is the origin of the dust? There are three possible sources of dust in these objects:

1. Dust is formed by the old stellar population, in the atmospheres of AGB stars.
2. Dust is acquired externally either by merger events or tidal interactions.

⁷It is likely that the censoring in this data set is not random: the censored data are a multiple of the noise in the data and we have observed to a flux limit in K with shorter integration times for the S0+S0a sample compared to the ellipticals. The censored data may have some randomisation introduced by the SED-fitting technique since the SED can have different distributions but still give the same M_d . We note that the censored data could be biased.

⁸The median of the distribution function returned by Kaplan–Meier estimator is well defined if the censored data are restricted to less than half of the sample. Given the small sample size of the ellipticals which is dominated by upper limits (70% of the data) we use the mean in this work.

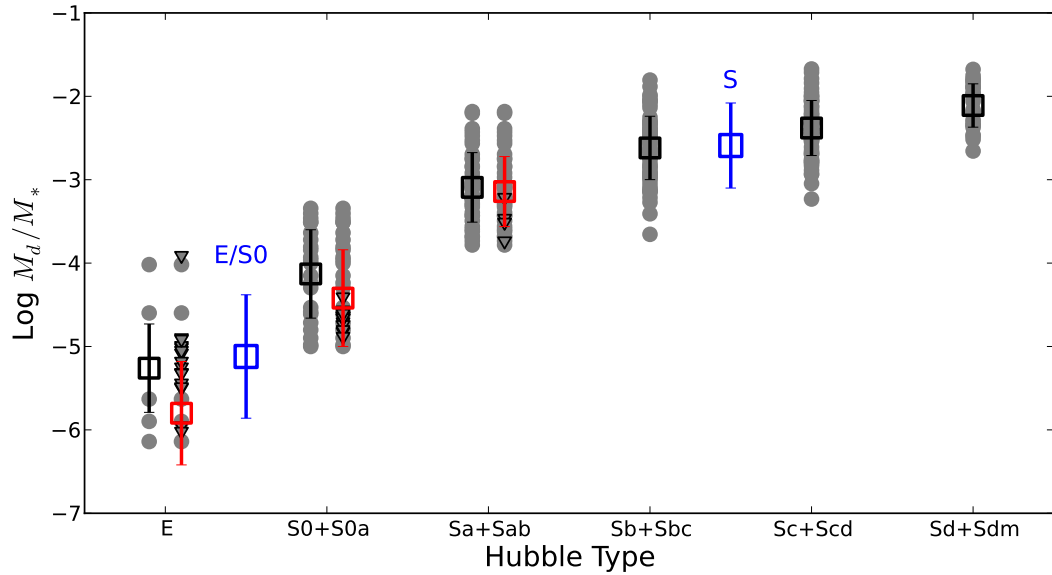


Figure 6.9. Dust-to-stellar-mass ratio vs. morphological type for the detected and undetected sources. Gray circles show the M_d/M_* estimated for detected sources, with upper limits highlighted with gray triangles. The mean and standard deviation of M_d/M_* for the *detected* samples are highlighted with black boxes and error bars. Offset from the detected sources, we also show the entire HRS sample in each Hubble type including both detected sources and upper limits. The mean and standard deviation for the samples *including* the upper limits are shown with the red squares and error bars (see Table 6.5). We also compare the mean and standard deviation of the complete early-type galaxies (S0+S0a and E) and the complete sample of spiral galaxies (C12) in blue. The stellar masses are from Cortese et al. (2012a).

Table 6.6
Results of the Two-sample Tests

Sample	Parameter	P(GGW)	P(LR)	P(PPGW)
S0 × E	M_d	0.0005	0.0006	0.004
	M_d/M_*	0.000	0.000	0.000
	$M(\text{H}_2)$	0.007	0.009	0.003
Virgo × not Virgo	M_d	0.14	0.09	0.14
	M_*	0.189	0.151	0.165
	M_d/M_*	0.055	0.082	0.078
	$M(\text{HI})$	0.008	0.011	0.005

Notes. The S0–S0a versus elliptical (top) and Virgo versus non-Virgo galaxy samples tested for the probability they are drawn from the same population. The tests include GGW: Gehan's Generalized Wilcoxon test; LR: log-rank test; PPGW: Peto and Peto Generalized Wilcoxon test. These are determined using the IRAF STSDAS task TWOSAMPT.

3. The dust could be formed by grain growth in the ISM or dust production in supernova (e.g., Barlow et al., 2010; Matsuura et al., 2011; Gomez et al., 2012).

Of the three possibilities (1) has the most testable predictions. If the source of the hot gas is from the mass loss of stars, we would expect the X-ray luminosity (L_X) to correlate with the optical luminosity (L_B); this is found in our sample (Appendix E, Equation (E.1)). Using the same reasoning, if the source of dust is from stellar mass loss a correlation between the FIR luminosity (L_{FIR}) and the optical luminosity should exist.

The FIR luminosity, L_{FIR} (Table 6.4) was determined by integrating over the SED (Figures 6.5 and 6.6). (This is an underestimate of the total IR luminosity as the $70 \mu\text{m}$ fluxes are treated as upper limits in our SED fitting; we estimate that including a warm temperature component to fit the MIR– $70 \mu\text{m}$ emission would contribute (on average) 3% to the FIR luminosity, though for some sources this can be up to 17%— see also Muñoz-Mateos et al. 2009.). The mean ratio of FIR to optical luminosity $\log(L_{\text{FIR}}/L_B)$ for S0s is -1.1 ± 0.1 and -2.2 ± 0.1 for ellipticals. Therefore ellipticals have less FIR luminosity per unit blue luminosity than S0s (also seen in an IRAS sample of isolated galaxies - Lisenfeld et al. 2007). There is no evidence for a correlation between L_{FIR} and L_B or L_X (Figure 6.10, Appendix E). The large scatter between L_{FIR} and L_B suggests that the dust may have been acquired externally. The FIR luminosity strongly depends on the temperature of the dust (as $L_{\text{FIR}} \propto T^6$), it is therefore instructive to compare the dust mass with the optical and X-ray luminosity. The dust mass has a weak correlation with both L_B and L_X but these are not statistically significant (Figure 6.10, Equations (E.4) and (E.5)).

Another way to test possibility (1) is to compare our dust masses with models of stellar mass loss from evolved stars and dust destruction from sputtering (Goudfrooij & de Jong, 1995, Figure 6.10)⁹. The amount of gas lost in these winds is estimated by Faber & Gallagher (1976) as $\dot{M}_{\text{gas}} = 1.5 \times 10^{-11} (L_B/L_\odot) M_\odot \text{yr}^{-1}$. For our sample this gives a stellar mass loss of 0.005 to $0.75 M_\odot \text{yr}^{-1}$. The dust destruction in a hot plasma probably occurs on timescales of $\tau_d \sim 10^6\text{--}10^7 \text{ yr}$ (Draine & Salpeter, 1979), although a plausible maximum destruction timescale is $\tau_d \sim 10^{7.5} \text{ yr}$ (Goudfrooij & de Jong, 1995), since this corresponds to electron densities in the hot X-ray plasma of $n_{\text{H}} < 10^{-3} \text{ cm}^{-3}$. The results of the models are plotted in Figure 6.10 for values of $\log_{10}(\tau_d)$ from 6.5 to 7.5. The ETG sample detected by *Herschel* have dust masses comfortably above the models, suggesting that an alternative source of dust is required. Longer dust timescales may be possible for objects that contain a

⁹We assume that the gas-to-dust ratio in the stellar winds of evolved stars is ~ 150 .

significant component of cool gas (see Section 6.4.3); for example in the Milky Way destruction timescales are of the order $\log_{10}(\tau_d/\text{yr}) = 8.5$. Three of our detected elliptical galaxies have dust masses consistent with the boundary marked by the maximum destruction timescale ($\log_{10}(\tau_d/\text{yr}) = 7.5$). The upper-limits for 50% of ETGs in our sample could be consistent with dust originating from the mass loss of evolved stars (Clemens et al., 2010).

To summarise, scenario (1) where the dust is from the mass loss of evolved stars appears unlikely as there are no statistically significant correlations between the FIR luminosity and the optical or X-ray luminosity, and the detected amounts of dust are far higher than the most generous assumptions of dust production and destruction. In addition, if the dust was formed in old AGB stars there should be a small range in M_d/M_* . However, Figures 6.8 and 6.9 show that the scatter is much larger than observed in late-type galaxies; this is particularly true for S0s where the value of M_d/M_* varies by a factor of ~ 50 . Scenario (3) where dust forms from supernova seems unlikely as most of galaxies have NUV– r colors in the quiescent region of the red sequence. Finally, another argument against hypotheses (1) and (3) is that they predict the dust will be distributed in a similar way to the stars. However, for five of the six ellipticals that have been detected by *Herschel* (excluding M87), the absorption in optical or near-IR continuum emission is distributed differently than the stellar distribution (see Appendix D).

The evidence therefore supports the idea that the dust in our ETG sample has been acquired from mergers or tidal interactions. This is supported by other recent studies; for example Davis et al. (2011) have used the misalignment between the kinematics of the stars and gas in ETGs to conclude one-third of ETGs have acquired much of their ISM by this means.

6.4.3 A COOL INTERSTELLAR MEDIUM IN EARLY-TYPE GALAXIES?

In the last decade, it has become clear that a significant fraction of ETGs do contain a cool ISM similar to that of spirals. Morganti et al. (2006) detected HI in 70% of their sample of nearby ETGs (see also Oosterloo et al., 2010; Serra et al., 2009; di Serego Alighieri et al., 2007) and detections of molecular gas have been made in many (Sage et al., 2007; Lucero & Young, 2007; Combes et al., 2007). A number of studies indicate ongoing star formation in a significant fraction of ETGs (Kaneda et al., 2005, 2008; Panuzzo et al., 2007, 2011; Temi et al., 2007a,b) and the detection of dust in 50% of our sample strongly supports the conclusion that a significant fraction of ETGs contain a cool ISM.

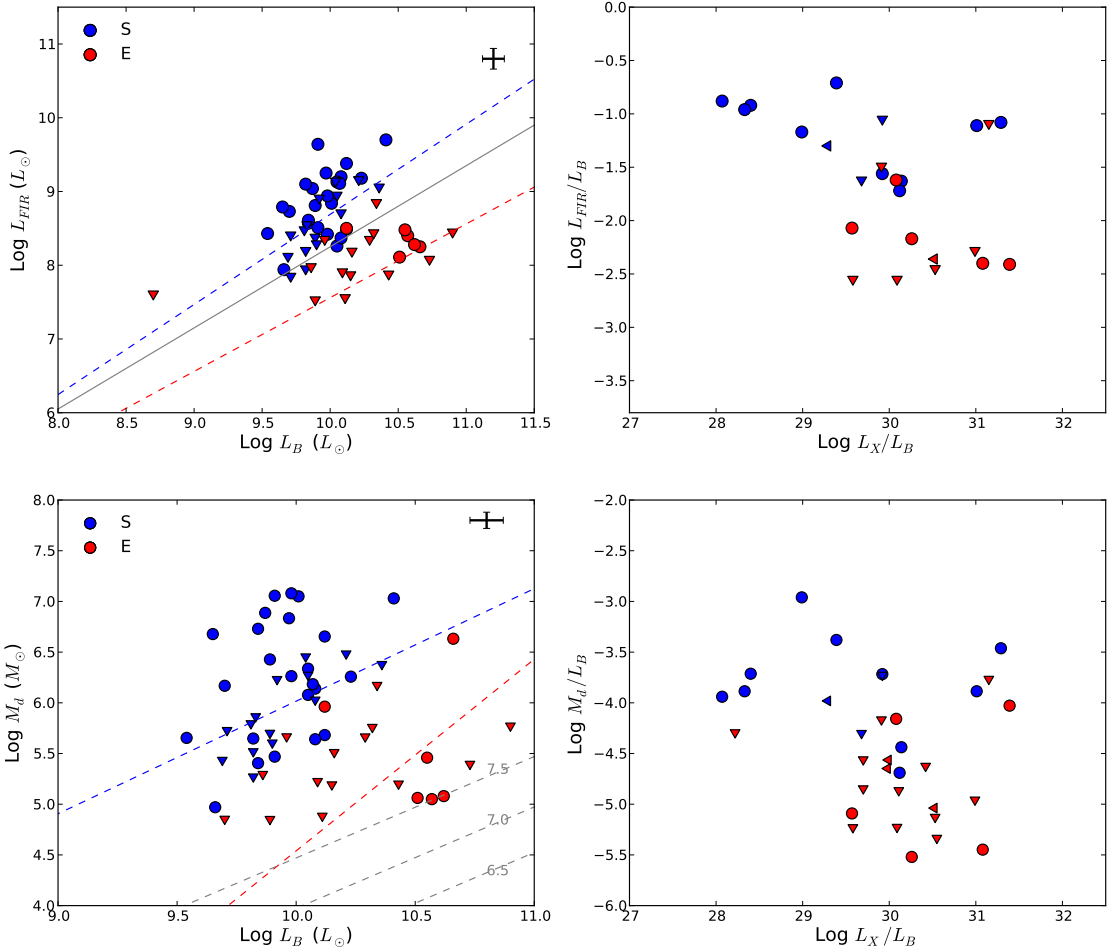


Figure 6.10. Top panel: the FIR luminosity from the cold dust component $L_{\text{FIR}}(\text{cold})$ vs. the B -band luminosity (left). Blue points are S0+S0a galaxies and red points are the ellipticals. Upper limits are plotted as downward-pointing triangles. The gray solid line shows the expected relationship (arbitrarily normalized) for $L_{\text{FIR}} \propto L_B^{1.1}$ if the FIR emission is produced by dust from stellar atmospheres. The best-fit line to the S0+S0a sample including the upper limits is shown by the dashed blue line ($m = 1.22$, $c = -3.53$, $\sigma_r = 0.39$) as estimated from the Buckley James method. The correlation parameters for ellipticals are shown by the dashed red line ($m = 1.00$, $c = -2.44$, $\sigma_r = 0.3$). Right: the FIR emission vs. X-ray luminosity (L_X) normalized by the blue luminosity (L_B). Bottom panel: the dust mass M_d vs. the B -band luminosity (left) and vs. X-ray luminosity (right). The $\log M_d$ vs $\log L_B$ relationship is described with $m = 1.11$, $c = -5.08$, $\sigma_r = 0.58$ for the S0+S0a (blue dashed) and $m = 1.89$, $c = -14.40$, $\sigma_r = 0.97$ for the ellipticals (red dashed). The dashed gray lines represent the loci where dust is replenished by stellar mass loss and destroyed by dust sputtering in the hot gas (the labels represent the log of the dust destruction timescale assumed). This model assumes a gas-to-dust ratio of 150. The errors on the dust mass are similar to the symbol size for most galaxies, and a representative error bar is shown.

We can compare the ISM in the ETGs with that in late types in two other ways. First, using the measurements of the dust, atomic, and molecular gas that exist for eight galaxies from our sample (Table 6.4), we estimate that the mean gas-to-dust ratio is $10^{2.08 \pm 0.08}$, similar to the typical value for late-type galaxies: $\sim 100\text{--}200$.

Second, in late-type galaxies there is a tight correlation between FIR and radio emission (Wrobel & Heeschen, 1988; Helou et al., 1985; Devereux & Eales, 1989). This is usually explained as the result of a correlation between the FIR emission and the SFR, with FIR emission originating either from dust heated by young stars (e.g., Vlahakis et al. 2007 and references therein; Ford et al. 2012) or due to dust itself tracing the gas mass, which in turn fuels star formation (Rowan-Robinson et al., 2010; Bendo et al., 2012b). The radio emission is then also correlated with the SFR as it originates from relativistic electrons produced by supernova remnants after the young stars die. Whether or not this correlation is truly caused by the SFR, we can at least see whether the ETGs in our sample have a similar ratio of FIR–radio as spiral galaxies. Sixteen ETGs are detected at 1.4 GHz (see Figures 6.1 and 6.2) by the Faint Images of the Radio Sky at Twenty centimeters (FIRST) radio survey (Becker et al., 1995). For these sources we have estimated the value of the parameter, q , introduced by Helou et al. (1985), defined as

$$q = \log \left(\frac{L_{\text{FIR}}}{3.75 \times 10^{12} \text{ W m}^{-2}} \right) - \log \left(\frac{L_{1.4 \text{ GHz}}}{\text{W m}^{-2}} \right), \quad (6.2)$$

where L_{FIR} and $L_{1.4 \text{ GHz}}$ are the FIR and radio luminosities, respectively. Yun et al. (2001) found a median value for nearby galaxies of $q = 2.64 \pm 0.02$, with most star-forming galaxies having values of q between 2 and 3. Wrobel & Heeschen (1988), and more recently Combes et al. (2007) and Lucero & Young (2007), have found similar values of q for ETGs in which star formation is occurring.

Two of our galaxies (NGC 4636, NGC 4374) have $q < 1.8$, which suggests they host radio-loud AGNs. Thirteen out of 16 sources with FIRST detections in our HRS sample have $2.15 < q < 3.32$, similar to star-forming late types. Nine of these sources also have CO detections (Table 6.4) and therefore 70% of the galaxies for which the q values are suggestive of star formation also have a reservoir of molecular gas. These galaxies lie below the ‘quiescent’ UV–optical boundary defined as $\text{NUV}-r < 5.4$ (Section 6.3.2) and a literature search reveals evidence of residual star formation in seven out of the nine galaxies, with signatures including mid-IR emission (Panuzzo et al., 2007; Shapiro et al., 2010), line diagnostics (Sil’chenko et al., 2010; Crocker et al., 2011), and UV emission (Cortese & Hughes, 2009).

Converting the q ratio into SFRs for ETGs is extremely complex due to the

difficulty in disentangling the AGN component, other processes that may be heating the dust, and the thermal contribution to the radio emission. If the $q \sim 2$ ratios for those galaxies with molecular gas are an indication of star formation, then there is not only cool gas and dust in these galaxies but also stars forming at a measurable rate for at least 15% of the sample. We defer a full analysis of SFRs for future work, though we note that a literature search reveals SFRs ranging from 0.03 to $0.40 M_{\odot} \text{ yr}^{-1}$ in 23% of the HRS ETG sample (see references listed above).

In summary, although the mass of the ISM in ETGs is less than the mass of the ISM in late types, observations of the radio continuum, CO, and HI are consistent with the ISM in ETGs being quite similar to that found in late types. The only difference is that, on average, the dust in ETGs has a temperature that is a few degrees higher, possibly due to the dust grains in early types being exposed to a more intense interstellar radiation field or from the more centrally distributed dust emission in ETGs (Sauvage & Thuan, 1992; Bendo et al., 2012b, e.g.).

6.5 DISCUSSION

6.5.1 EVIDENCE FOR DUST-DEPLETED DISKS IN S0s

Figures 6.8 and 6.9 both show that S0s contain a smaller mass of ISM per mass of stars than early-type spirals (i.e., those with Hubble type ranging from Sa to Sbc). However, the bulge-to-total mass ratio is known to be larger for S0s than early-type spirals: is the fall in the dust-to-stellar-mass ratio we observe here simply a reflection of the more massive bulges of S0s? We can test this idea by making the assumptions that (1) bulges do not contain dust and (2) the dust-to-stellar-mass ratio is the same for all disks. With these assumptions, to explain the factor of 10 decrease in the dust-to-stellar-mass ratio of S0s relative to early-type spirals, the bulge-to-total stellar-mass ratio must change by a very large factor. If the bulge-to-total stellar-mass ratio is 0.1 for early-type spirals, it must be 0.91 for S0s. For larger values of the bulge-to-disk stellar-mass ratio for the early-type spirals (Sa–Sc), even larger ones are required for the S0s. Weinzierl et al. (2009) have found that the proportion of the total mass of a galaxy that is in the bulge increases from ~ 0.1 for Sbc galaxies to ~ 0.2 for S0+S0a galaxies (their Figure 14). In larger samples, Graham & Worley (2008) and Laurikainen et al. (2010) find values for this ratio of approximately 0.1–0.2 for Sab–Sbc galaxies and 0.3–0.5 for S0 galaxies (their Figure 4), a somewhat larger change but still too low to explain the different dust-to-stellar-mass ratios.

Another way to investigate this is to compare the ratio of the submm diameter

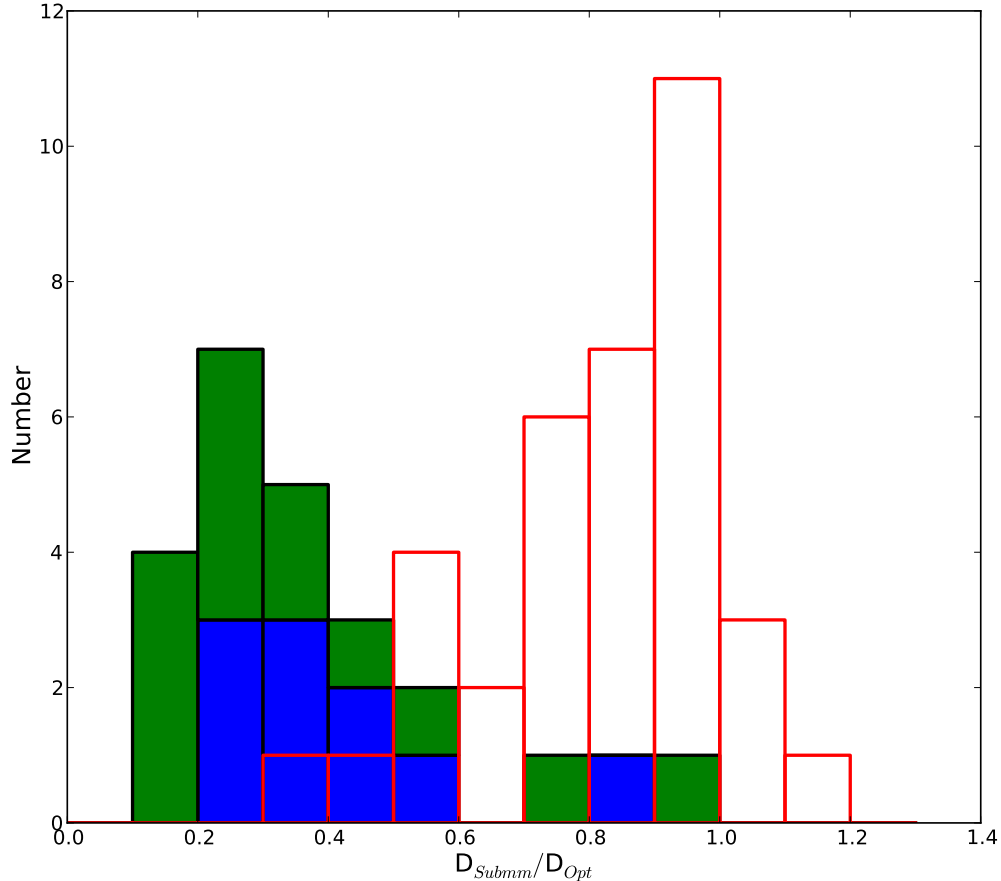


Figure 6.11. Ratio of the submm and optical sizes for the HRS sample. The red histogram shows the distribution of $D_{\text{submm}}/D_{\text{opt}}$ for the early-type spiral galaxies (Sa-Sbc) with the same color cut as the S0 and ellipticals, i.e., $K < 8.7$ (the original sample of early types is presented in Cortese et al. (2010b) and C12). The green shaded histogram shows the distribution for the S0s in this analysis, with the blue shaded histogram showing the S0s that are not in one of the Virgo clouds or the outskirts of Virgo (Boselli et al., 2010b).

to the optical diameter (e.g., Cortese et al., 2010b), where the optical diameter is likely to be a good measure of the size of the disk. We measured this ratio for two samples: (1) all of the S0 galaxies and (2) all early-type spiral galaxies in the HRS with $K < 8.7$ (the limit used for ETGs). For the optical size of the galaxy we used θ_{major} , the diameter along the major axis measured to the standard B 25th mag arcsec $^{-2}$ isophote ($D(25)$). For the submm size, we used the same definition, finding the ellipse that provided the best fit on the 250 μm image to an isophotal brightness of 6.7×10^{-5} Jy arcsec $^{-2}$. Figure 6.11 shows the distributions of $D_{\text{submm}}/D_{\text{opt}}$ for the S0+S0a galaxies and the early-type spirals with the same K -band magnitude selection; these populations are significantly different ($P < 0.001$ level¹⁰). We do not apply a correction for beam smearing, which increases the angular sizes of the objects, an effect which is biggest for the objects with smallest angular size. If a correction was made for this bias, the difference between S0+S0a and early-type spiral populations seen in Figure 6.11 would increase. We have also compared the submm-optical sizes for the S0 galaxies outside of Virgo in Figure 6.11. The values for these are still clearly different from the early-type spirals, strongly suggesting that the dust-depleted disks of S0s are not caused by a current cluster-environmental effect.

Both approaches imply that the dust-to-stellar-mass ratio is lower for the disks of S0 galaxies than the disks of early-type spirals, suggesting that the disk of an S0 contains a smaller mass of ISM than the disk of an early-type spiral with the same stellar mass. This is not an entirely surprising result, since for the last 40 years the working definition of an S0 galaxy is that it is a galaxy with a disk but no sign of spiral arms or, if it is an edge-on galaxy, of a dust lane (Sandage, 1961). Nevertheless, even if the qualitative result is not surprising, *Herschel* has allowed us to determine how little ISM the disks of S0 galaxies do contain.

6.5.2 ELLIPTICALS AND S0S OR SLOW ROTATORS AND FAST ROTATORS?

So far in this chapter, we have classified ETGs based on their optical morphology into ellipticals and S0s. Based on the ATLAS^{3D} study of the stellar kinematics of 260 ETGs, Cappellari et al. (2011) have argued that a physically more meaningful way is to divide ETGs into slow rotators and fast rotators. Emsellem et al. (2011) found that 66% of the galaxies in ATLAS^{3D}, which are traditionally morphologically classified as ellipticals, have disk-like kinematics and are therefore fast rotators. Given the similarity in the kinematics, the suggestion is then that early-type fast rotators

¹⁰Using the Kolmogorov–Smirnov two-sample test.

are part of the same evolutionary sequence as the late types, but are at different stages of their evolution. Slow rotators are defined as galaxies with bulge-like properties, likely to be the end-point of systems that have undergone complex merger histories; these are massive, lie on the red sequence, and contain very little cool interstellar material.

Eleven (18%) of the ETGs in our sample are slow rotators, including nine ellipticals (39% of the ellipticals) and two S0s (5%). In Figure 6.12(a), we plot dust-to-stellar-mass ratio versus the quantity $\lambda_{R_{e/2}}/\sqrt{\epsilon_{e/2}}$, where ϵ is the ellipticity of the galaxy and R_e is the effective radius. This parameter is suggested by the ATLAS^{3D} team as appropriate to separate out the slow and fast rotators since it is a good measure of the projected stellar angular momentum per unit mass (Emsellem et al., 2007). There is no sign of a correlation between the two parameters for galaxies in our sample. Indeed, with *Herschel* we have detected dust emission from 50% of the slow rotators, including four ellipticals, which is not very different from the detection fraction for all the ETGs (Table 6.3).

The fact that there is a clearer distinction in the dust properties of the ETGs when they are put in morphological classes (Figures 6.8 and 6.9) than when they are put into kinematic classes does not mean that the kinematic division is not physically meaningful. It is possible that the morphological classification is more connected to the mass of ISM in a galaxy than the kinematic classification, although the kinematic definition may be telling us more about the evolutionary state of the galaxy. As *Herschel* detects a number of slow rotators and given the lack of correlation seen in Figure 6.12(a), this may be additional evidence that the cool ISM in ETGs is acquired by random gravitational encounters. Again, the amount of dust may not be connected with the evolutionary state of the galaxy. In Figure 6.12(b), we show the same diagram but this time labelling the galaxies by their HI mass. There is a tendency for galaxies with larger atomic gas masses to have higher dust-to-stellar mass ratios. Since the 21 cm morphologies have often been adduced as evidence for an external origin of the ISM (e.g., Serra et al., 2009), this figure may be additional evidence that the mass of the ISM is rather unconnected to the evolutionary history of the stellar populations in the galaxies.

Finally, we note that connections between the dust properties and stellar kinematics of the ETGs may become evident in a larger sample. The HRS sample of ETGs is a statistically complete quasi-volume-limited sample, but the volume contains the rich environment of the Virgo Cluster and is therefore not a representative sample of the local universe. The HRS ETGs also cover a limited range of stellar mass (Section

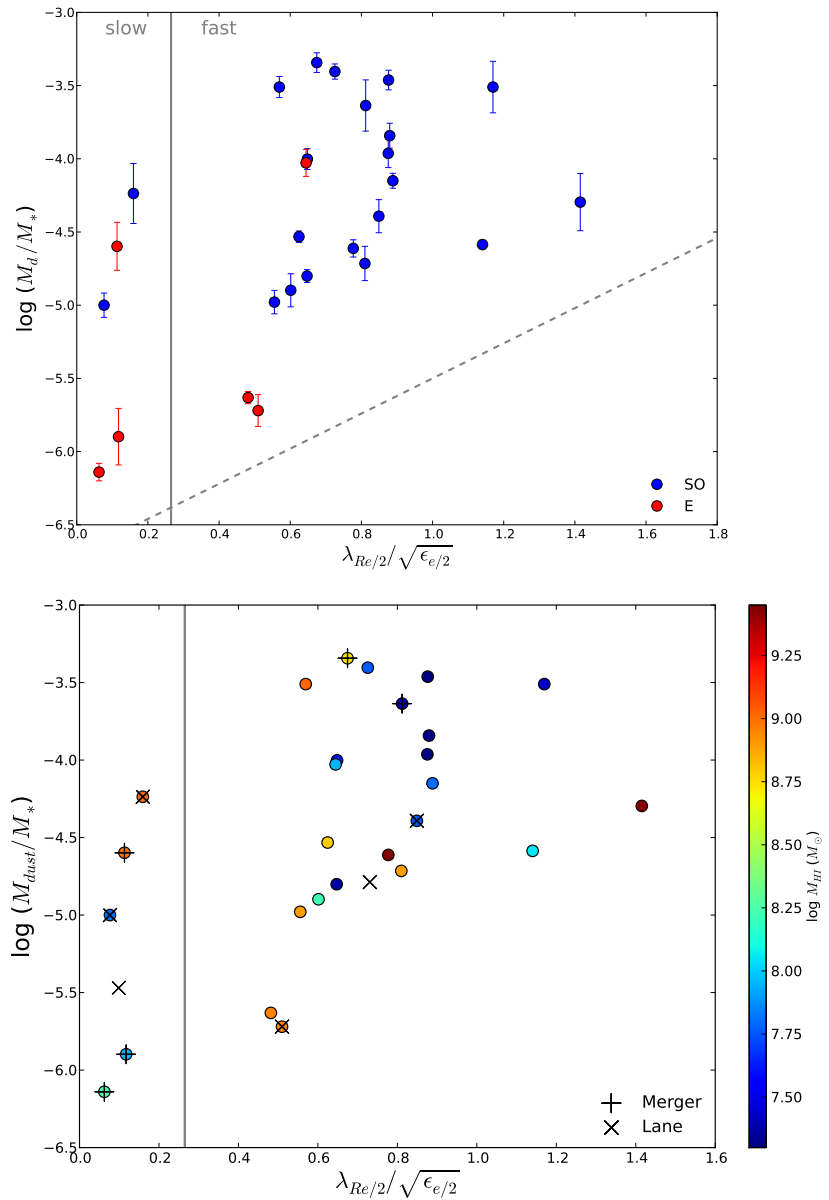


Figure 6.12. Top: the dust-to-stellar-mass ratio vs. the kinematical parameter $\lambda_{Re/2} / \sqrt{\epsilon_{e/2}}$, where $\epsilon_{e/2}$ is the ellipticity measured within an aperture defined at $0.5R_e$ and R_e is the effective radius of the galaxy. λ_R is a proxy for the angular momentum per unit stellar mass and the $\sqrt{\epsilon_{e/2}}$ term accounts for the shape of a galaxy since a more flattened galaxy would be expected to have a stronger anisotropy. Blue points are S0+S0a galaxies and red points are ellipticals. The gray solid line marks the region defined as the boundary between fast and slow rotators (Emsellem et al., 2011), i.e., between galaxies with disk-like rotation and bulge-like kinematics. Bottom: as above but color-coded with respect to the HI mass. Galaxies which are known to be mergers or have obvious dust lanes in the optical are indicated with + (mergers) and \times (dust lanes). Galaxies without filled circles are the *Herschel*-detected galaxies that have no corresponding HI observations. Many of the galaxies at the lower end of the HI mass scale are upper limits (Table 6.4). The gray dashed line roughly marks the detection limit of the survey and note that NGC 4486 (HRS 183) is not shown in these plots.

6.3, Figure 6.3). An important future project would be to observe the dust in a sample of ETGs containing more galaxies in low-density environments and with a wider range of stellar mass.

6.5.3 GALAXY EVOLUTION

We can use the results from the *Herschel* observations to make an inference about the evolution of early types. On the assumption that the dust we observe is delivered to the galaxies externally, we can make a rough estimate of the effect such an interaction would have on the stellar mass of the ETG. We use the mean values of M_d/M_* shown in Figure 6.9 (Table 6.5) for the different morphological classes, ($10^{-5.9}$ for ellipticals, $10^{-4.4}$ for S0s, and $\sim 10^{-3.0}$ for spirals). On the assumption that all the dust we detect in an ETG is the result of a past merger with a spiral, the ratio of the mass of the spiral to the original ETG must be ~ 0.05 for an elliptical and ~ 0.1 for an S0. These estimates suggest that such interactions are only minor mergers and do not represent significant galaxy-building events. The estimates are also upper limits because the dust may have been acquired by a tidal interaction without the galaxies necessarily merging, and some of the dust may also have been produced inside the galaxy.

6.6 CONCLUSIONS

We present the FIR and submm observations with *Herschel* of 62 ETGs, including 23 ellipticals and 39 S0+S0a galaxies. We find the following results:

1. We detect 24% of the ellipticals and 62% of the S0s. The optical and X-ray luminosities of the detected sources show we are detecting the most massive ellipticals, though the S0 sample is representative of the general population. Of the ten ‘pure’ ellipticals in our sample only one is detected by *Herschel* (M86), while six of the eleven ‘impure’ ellipticals are detected. The detection rate for the ETGs outside Virgo appears to be higher than for those inside the cluster but this is not statistically significant.
2. The mean dust masses for the detected galaxies are $\log M_d = 6.3 \pm 0.1$ and $5.5 \pm 0.3 M_\odot$ for the S0+S0a and E population, with average dust-to-stellar-mass ratios of $\log(M_d/M_*) = -4.1 \pm 0.1$ and -5.3 ± 0.2 . Including the upper limits, the average dust masses for the detected *and* undetected S0+S0a and elliptical sources are $\log M_d(M_\odot) = 5.9 \pm 0.1$ and 5.2 ± 0.1 , with dust-to-stellar-mass ratios of $\log(M_d/M_*) = -4.4 \pm 0.1$ and -5.8 ± 0.1 .

3. The mean dust temperature for the ETGs *detected* by *Herschel* is $\sim 24\text{ K}$, warmer than the dust in late-type galaxies. The *entire* early-type sample, including non-detections, has a dust mass of $\log M_d = 5.6 \pm 0.1$ and $\log(M_d/M_*) = -5.1 \pm 0.1$. In comparison, the average dust-to-stellar mass ratio for spiral galaxies in the HRS is -2.59 ± 0.03 . The dispersion in the dust-to-stellar mass ratio is much greater for ETGs than spirals.
4. The NUV– r colors show that virtually all the ETGs lie close to the red sequence, but there is evidence from UV and optical colors, radio continuum observations, and literature searches that $\sim 20\%$ of the sample have had a recent star-forming epoch or have significant residual star formation. However, the NUV colors have not been corrected for extinction or contamination from the old stellar population. Our ETGs are redder in NUV– r with lower dust-to-stellar mass ratios than the ETGs detected in the H-ATLAS survey.
5. We show that the detection of cold dust, the ratio of far-infrared to radio emission, and the gas-to-dust ratios all indicate that many ETGs contain a cool ISM in which stars are forming, similar to that seen in spiral galaxies.
6. We find no evidence for a correlation between the FIR luminosity or dust mass of ETGs with the optical luminosity, suggesting that the main source of the dust in the galaxies detected by *Herschel* is not mass loss from evolved stars. This, together with the large spread in the dust-to-stellar-mass ratio of ETGs, suggests a significant fraction of the dust in these galaxies is acquired externally via mergers or tidal interactions.
7. We use the results from the ATLAS^{3D} survey to divide our sample into fast and slow rotators. We show that the difference in dust properties between S0s and ellipticals is more obvious than the difference between slow and fast rotators. We suggest that this may be additional evidence that the dust in ETGs has been acquired by gravitational encounters and may not tell us much about the evolutionary state of the galaxy.
8. The low dust-to-stellar-mass ratios of S0s compared with early-type spirals cannot be explained by the larger bulge-to-disk ratios of S0s. The relative sizes of the dust sources in S0s are also smaller than seen in early-type spirals. These suggest that the disks in S0s contain much less dust (and presumably gas) than spiral disks with a similar size. This effect is probably not being caused by current environmental processes adding to the weight of evidence that early-type

spirals are not being transformed into S0s in significant numbers at the current epoch.

9. If the cool ISM in ETGs is acquired as the result of a tidal interaction or merger, an upper limit on the increase in the stellar mass of the ETG due to the interaction is 1% for the ellipticals and 10% for the S0s, suggesting that the interactions are not significant galaxy-building events.

Our sample of ETGs has lower dust-to-stellar-mass ratios and dust masses compared to previously published *Herschel* samples. The results from our sample are important for interpreting chemical evolution models which model the production and destruction of dust in ellipticals as well as providing a low-redshift benchmark for understanding the evolution of dust and gas in high redshift surveys (e.g., Rowlands et al., 2012; Dunne et al., 2011). Finally, we note that to obtain a better understanding of some of these issues it will be important to follow-up our statistical study with detailed observational studies of individual ETGs, for example with ALMA.

CHAPTER 7

EXTENDED DUST IN THE FULL HRS

“The scientists of today think deeply instead of clearly. One must be sane to think clearly, but one can think deeply and be quite insane”

Nikola Tesla

7.1 INTRODUCTION

One of the original aims of the Herschel Reference Survey (HRS, see Section 1.5.1) was to try and detect dust outside the optical radii of galaxies. There are good reasons to suggest that cold dust would exist outside the optical disk of galaxies. Dust can get driven out of the disk by radiation pressure or supernova winds (Madau et al., 2001; Bianchi & Ferrara, 2005). Alternatively dust could be formed in galaxy halos if local star formation is occurring (e.g., Bigiel et al., 2010).

The presence of dust outside the galaxy disk has been found by both the reflection of UV emission (e.g., Hoopes et al., 2005) and from the absorption of quasar spectra (Ménard et al., 2010). Ménard et al. (2010) use ~ 85000 quasars at redshift greater than one from the Sloan Digital Sky Survey (York et al., 2000) and the positions of 24 million local galaxies to detect the presence of dust from between 20 kpc and 10 Mpc from the centres of galaxies. They calculate that the dust content in galactic halos and large scale structures is comparable to the mass in galactic disks.

Detecting dust emission outside of a galaxy’s optical radius before *Herschel* was very difficult, due to the likely coldness and the expected low surface density of the dust. One claim of a detection of extended dust was by (Davies et al., 1999) who created radial profiles of NGC 6946 at 200 μm from *ISO* data and at optical wavelengths. They claimed that as the logarithmic scale length of the 200 μm emission ($160 \pm 16''$) is larger than in the optical (in B-band, $141 \pm 6''$) that the dust is more extended.

The difference in scalelength is marginal and is sensitive to the exact smoothing kernel applied to match the optical with the far-infrared observations. With *Herschel* Cortese et al. (2010a) investigated the perturbed spiral galaxy NGC 4438 and found extra-planar dust up to 5 kpc from the galaxy’s disk. NGC 4438 has been disturbed due to interactions with NGC 4436 and possibly M 86. The extra-planar dust is co-incident with both atomic gas (H I) and H α +[NII] emission and Cortese et al. argue it is a feature created by the external disruption.

This chapter presents an initial analysis to see if any dust outside galactic disks is present in a representative sample of galaxies in the nearby universe.

7.2 STACKED RADIAL PROFILES

To provide the highest sensitivity to low-surface brightness dust and to go beyond the confusion limit I created radial profiles for each late-type galaxy in the HRS. Galaxies were not included in the sample if:

- The galaxy was identified as a non-detection in the HRS flux catalogue (Ciesla et al., 2012).
- The galaxy is listed as a point source in the HRS flux catalogue.
- There is another bright extended object within the SPIRE image of the galaxy.
- The image is listed in the HRS flux catalogue as having significant cirrus contamination.
- The galaxy has an inclination greater than 60°.

After the selection, there are still \sim 130 galaxies in the sample, potentially providing an order of magnitude increase in sensitivity over that for a single object. A radial profile for each galaxy is created by firstly calculating the physical radius of each pixel from the centre of the galaxy by using the pixel coordinate, inclination, distance to the galaxy (Cortese et al., 2012a), position angle and the optical centre. The optical diameter (D_{25} , where D_{25} is defined as the optical isophotal diameter corresponding to a brightness magnitude in the B-band of 25 mag arcsec $^{-2}$) and the coordinates of the centre of the galaxy is taken from Table 1 in Boselli et al. (2010b). The position angle and the inclination (calculated using the major and minor optical diameters) are taken from the Uppsala General Catalogue (UGC, Nilson, 1995b).

Before the radial profile can be computed the maximum radius allowed by the observation must be found. The maximum radius is found based on the number of

‘NaN’ pixels (i.e., pixels for which there is no data) that would be included at a given radius. The profiles are extended to a radius which includes 20 ‘NaN’ pixels; 20 is chosen so the profile is not cut early from an individual isolated ‘NaN’ pixel. The pixel values are converted to mJy arcsec⁻² and a correction is applied to adjust the surface brightness to that of a face-on galaxies (assuming optically thin emission). The radius for each galaxy is calculated in units of R_{25} .

The profiles are then averaged to give an average profile for the whole sample. To remove any residual background a constant is removed from each profile based on the mean value of the surface brightness between $2.6 \leq R_{25} < 3.0$ (a couple of profiles do not extend as far as $3.0 R_{25}$). The final profile is then put into radial bins and the uncertainty of each bin is calculated using σ/\sqrt{N} , where N is the number of data points in the bin and σ is the standard deviation of these data points (tests have shown correlations between pixels is not a significant effect for the stacked profiles). The results of the stacked profile are shown in Figure 7.1. When plotting the radial profile to a radius much larger than shown in Figure 7.1 some fluctuations were found in the data points which were larger than the formal uncertainties on each data point. I therefore estimated the standard deviation of the data points between $3.0 \leq R_{25} < 7.0$ to get a better estimate of the true uncertainty. The horizontal red lines in Figure 7.1 show the 3σ level (calculated from this estimate) and a good indication of the valid range of the radial profiles. This measured noise is a conservative estimate as many of the individual profiles do not extend to $7.0 R_{25}$. The median distance and optical diameter are 17.0 Mpc and 2.4', respectively, which means the R_{25} equates to a physical radius of 5.9 kpc.

7.3 THE EXTENT OF DUST IN GALAXIES

The stacked radial profiles (Figure 7.1) clearly show that dust emission is detected to much larger radii than R_{25} . At 250 μm dust is detected at a 3σ level to $2.1 R_{25}$ while at 500 μm is about $1.8 R_{25}$. The drop off between 250 and 500 μm may be due to the lower sensitivity of the SPIRE bands towards longer wavelengths rather than a change in the dust properties. An important consideration is whether the profiles are just measuring the point spread function (PSF) of the images? To test this I took calibration images of Neptune which is a very bright point source in the SPIRE images. The radial profile of Neptune were found using the same method and scaled assuming the median D_{25} of the sample (2.2'). The Neptune profile has been normalised to the same central surface brightness as the galaxy profile and is shown by the green data points in Figure 7.1. The difference between the two profiles

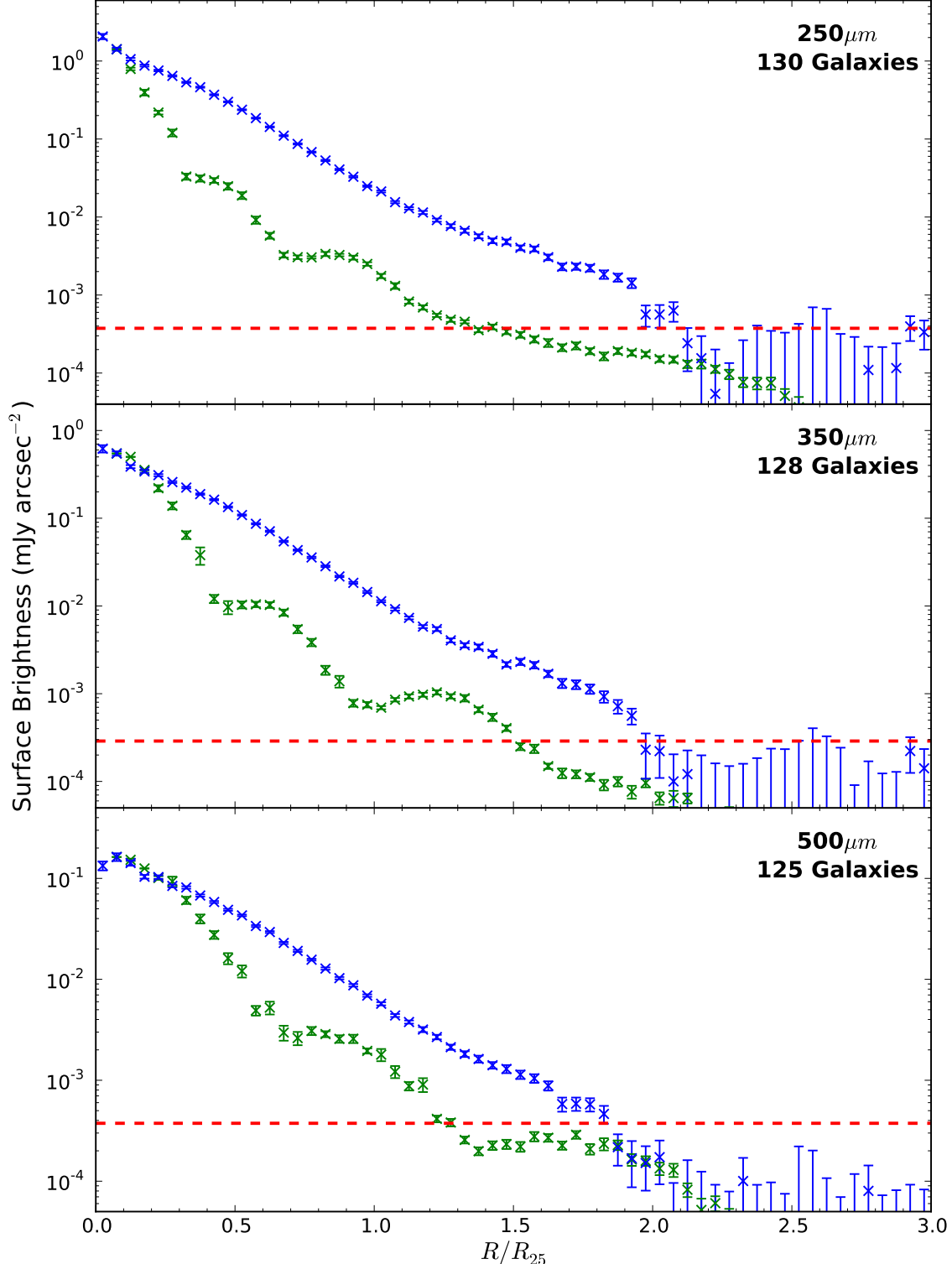


Figure 7.1. The average radial profile of late-type galaxies in the HRS. The blue data points show the average radial profile for each SPIRE band. The wavelength and number of galaxies that has been used in each plot are shown in the top-right corner. The green data points represent the profile of a point source (see Section 7.3). The dashed red line shows the 3σ sensitivity limit of our profiles (see Section 7.2 for more details).

is generally over an order of magnitude indicating that the stacked HRS profile is not a PSF effect.

The comparison with the point source shows that the emission is not solely from an unresolved source. However, it does not discount that the observed emission is from dust out to the optical radius which is then extended out by the *Herschel* beam. To test the true extent of the dust emission I fit an exponential model with a cut-off radius convolved with the 250 μm beam (the most resolved band) to the exponential disk. The preliminary analysis suggests that the dust emission must extend to at least $1.8 R_{25}$ to explain the emission in Figure 7.1 and will be investigated in detail in future work.

One important question is what fraction of dust is present outside the optical disk? To provide a rough estimate of this value the percentage of dust emission between 1.0–2.5 R_{25} compared to the total dust emission within 2.5 R_{25} was calculated for each band. I found values of 6.6, 8.0 and 10.6% for the 250, 350 and 500 μm band, respectively by using a linear interpolation between data points. An alternative method is to fit an exponential model to the surface densities and then compare the fraction of dust emission outside the optical disk to the total amount from a radius of 0– ∞ . This method gives consistent results with the first method, with the fraction of dust emission outside the optical disk of 6.8, 8.9 and 12.8% for the 250, 350 and 500 μm band. These results suggests that a significant amount of dust is either transported or created outside the optical disk (see Section 7.1). The higher percentage of emission outside the optical disk at longer wavelengths may indicate that the dust is colder at larger radii, or possibly be an effect of the larger PSF at longer wavelengths.

The quantity of dust emission found in this analysis can be compared to that reported from the absorption analysis of (Ménard et al., 2010). As Ménard et al. (2010) traced dust to much larger scales than is possible with the HRS observations, the comparison can only be made with their measurement on the smallest physical scale (15 kpc). Converting the mean surface density at 15 kpc from Figure 8 of Ménard et al. (2010) (adjusting to a $H_0 = 70 \text{ km s}^{-1} \text{ Mpc}^{-1}$) to a surface brightness at 250 μm results in a surface brightness density of $5.7 \times 10^{-3} \text{ mJy arcsec}^{-2}$. This is assuming a temperature of 17 K (from average global temperature of bright late-type galaxies reported in Davies et al., 2012) and the same dust emissivity index and opacity as used in Chapter 6. This surface brightness equates to a radius of 7.5 kpc in the averaged 250 μm radial profile, significantly short of the 15 kpc of Ménard et al. (2010). The global temperature of 17 K is likely to be an overestimate of the dust temperature outside the optical radius as the dust in the centre is likely to be hotter than the dust at the large radii. As the luminosity of dust scales as T^6 the central emission can

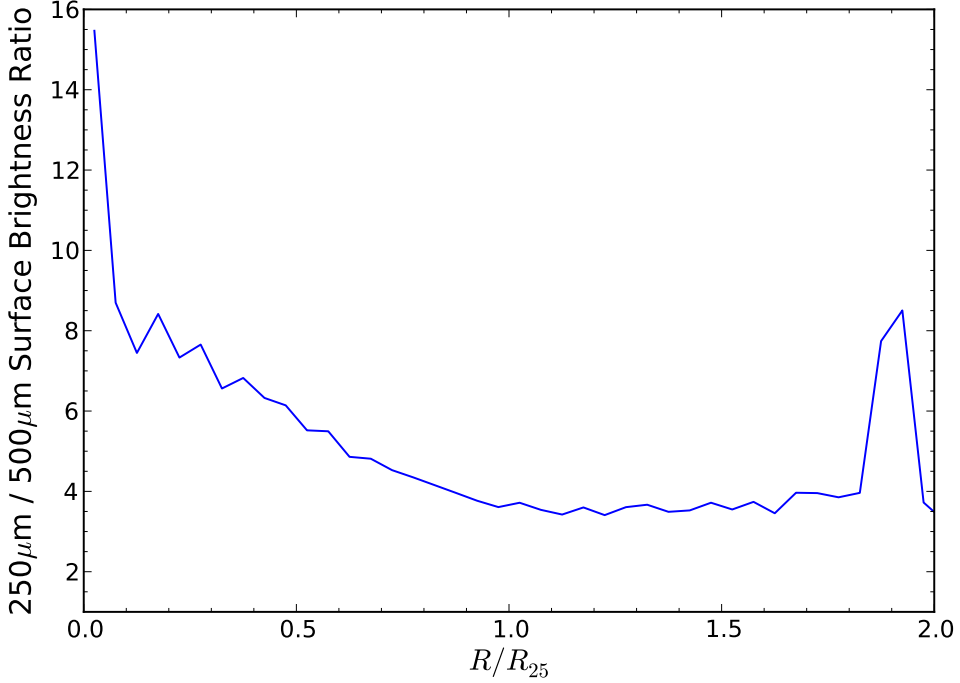


Figure 7.2. The radial profile of the $250\mu\text{m}/500\mu\text{m}$ surface brightness ratio. The decline in values between $0.0\text{--}1.3 R_{25}$ indicate the dust temperature is falling.

dominate any fit to the global spectral energy distribution.

Ideally PACS measurements would be available to obtain an accurate temperature of the dust, but a reasonable estimate of the dust temperature can be made with just SPIRE measurements. A full analysis would require smoothing the shorter wavelength maps to the same spatial resolution as the $500\mu\text{m}$ images which will be done in future work. A rough indication of the temperature can be found from the current data. Figure 7.2 shows the 250 to $500\mu\text{m}$ surface brightness ratio for the averaged profiles. High values would represent high dust temperatures; the decline to large radii suggests a decline in dust temperature. The profile past $1.7 R_{25}$ is quite noisy which is expected as the $500\mu\text{m}$ profile reaches the 3σ noise limit. Using the surface brightness values at $1.5 R_{25}$ for all wavelengths and fitting a modified-blackbody model (see Section 3.4) with dust emissivity index (β) of two, a temperature of 13.9 K is obtained. Figure 7.2 suggests that the temperature is largely constant out to $2.0 R_{25}$ but this is past the 3σ limit of the radial profiles.

Using a dust temperature of 13.9 K to compare our average $250\mu\text{m}$ profile and the dust surface density from quasar absorption at 15 kpc gives an equivalent distance of $\sim 10\text{ kpc}$. Given the uncertainties in trying to compare the results from dust emission and the dust surface density from quasar absorption, the rough agreement is very encouraging.

7.4 COMPARISON WITH HI-DEFICIENCY

One of the first results of *Herschel* was from a study which investigated the size of the dust disk compared to the galaxy's HI-deficiency (Cortese et al., 2010b). The HI-deficiency (HI_{def}) is defined as the difference between the measured HI mass and the value expected for an isolated field galaxy (adjusted for morphology and optical size) in logarithmic units (Haynes & Giovanelli, 1984). Cortese et al. (2010b) found in a sample of 15 Virgo galaxies that the ratio of the dust to optical disk size in highly HI deficient objects ($\text{HI}_{\text{def}} > 0.95$) is significantly lower than objects with little HI deficiency ($\text{HI}_{\text{def}} < 0.3$).

To see if the same trends are found from the radial profiles I used the $250 \mu\text{m}$ band (as it is the most sensitive) and split the galaxies into bins of varying HI-deficiency. The values of the HI-deficiency for the HRS sample were taken from Cortese et al. (2011). When making the radial profiles any galaxy that only contained a lower limit on the HI-deficiency was omitted. The same definition of the size of the dust disk was used as in Cortese et al. (2010b) and corresponds to an isophotal radius where the $250 \mu\text{m}$ surface brightness is $6.7 \times 10^{-2} \text{ mJy arcsec}^{-2}$. The average profiles split into bins of different HI deficiency are shown in Figure 7.3, where the dust disk size is shown by the vertical green lines.

While a trend is found for galaxies with higher HI deficiencies to have smaller disk sizes the result is not as pronounced as that shown in Cortese et al. (2010b). The variation in the dust disk size of this analysis of $0.8\text{--}0.6 R_{25}$ is significantly less than $1.2\text{--}0.7 R_{25}$ from Cortese et al. (2010b). At first glance this could suggest an issue with our analysis, but a comparison of the two objects in common show that for those individual objects the results from our profiles are in good agreement with those of Cortese et al. (2010b). The difference may lie in that this analysis has far better statistics or that the Cortese et al. (2010b) analysis includes some objects with a much higher inclination than this work. To test whether the difference is significant between the low ($\text{HI}_{\text{def}} < 0.0$) and high ($\text{HI}_{\text{def}} > 0.9$) HI deficiency bin I applied a Mann–Whitney U statistic and found the samples are significantly different (with $U = 520$, $n_1 = 39$, $n_2 = 16$ and $P > 99.99\%$).

7.5 DEPENDENCE ON MORPHOLOGY?

As well as splitting the profiles by HI-deficiency the radial profiles can be binned into different morphologies. The average radial profile at $250 \mu\text{m}$ split by morphology is shown in Figure 7.4. The morphology classifications have been taken from

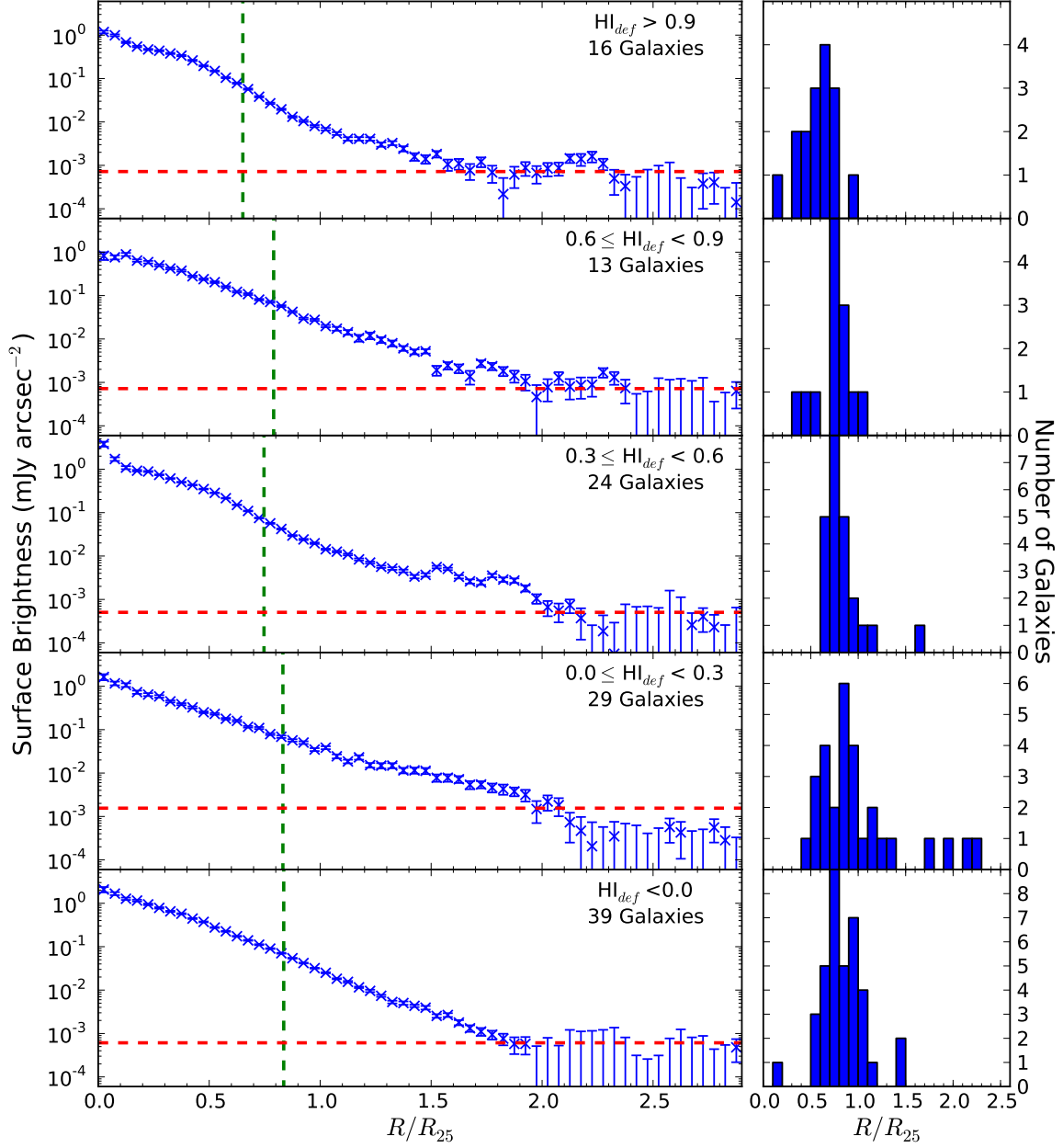


Figure 7.3. *Left:* The average radial profiles at 250 μm of late-type galaxies in the HRS split into bins of HI-deficiency (HI_{def}). The number of galaxies that has been used in each plot is shown in the top-right corner. The green line represents the size of the dust disk as defined in Section 7.4. The dashed red line shows the 3σ sensitivity limit of our profiles (see Section 7.2 for more details). *Right:* A histogram of the size of the dust disk for the individual objects used to make the averaged radial profiles on the left.

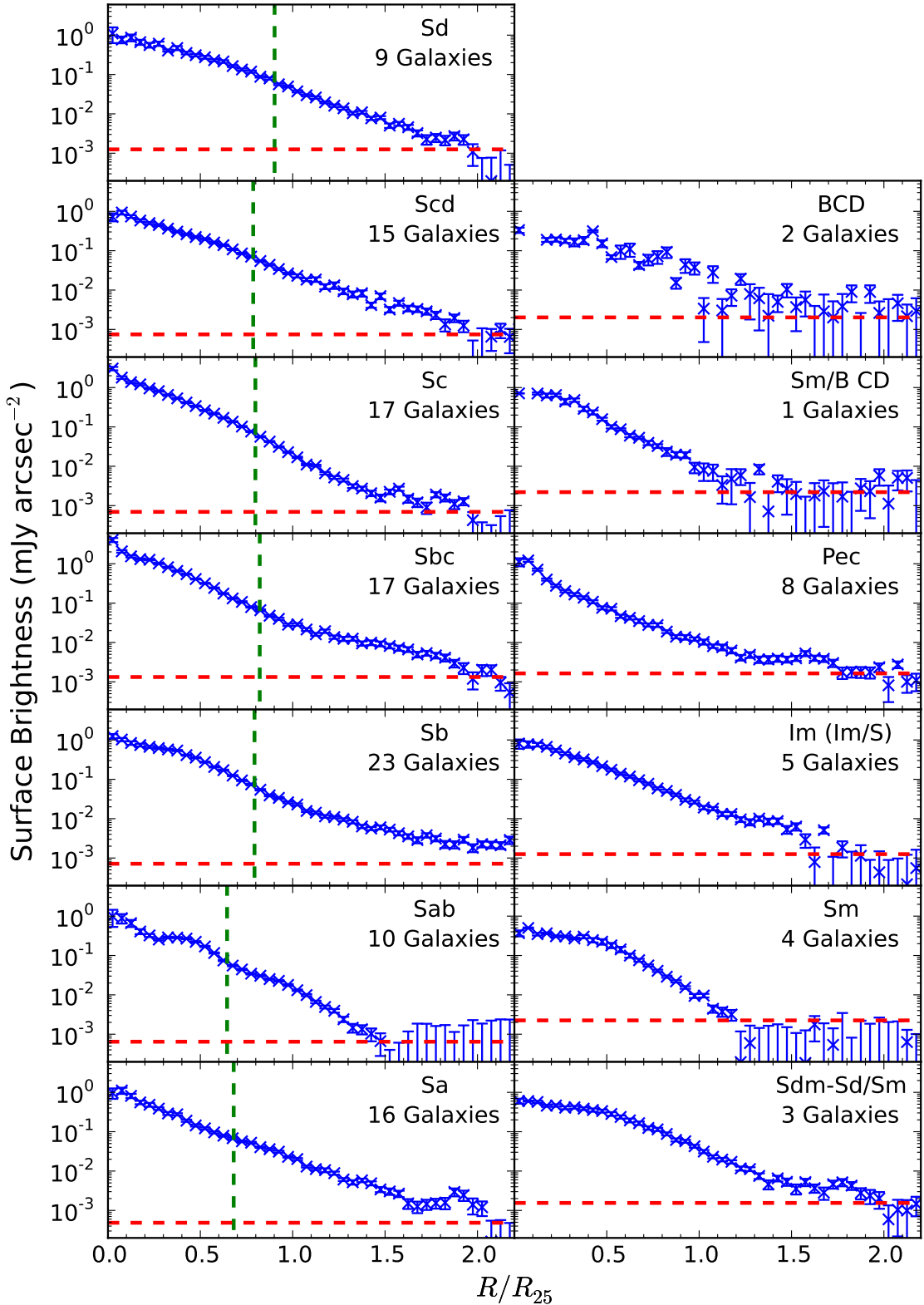


Figure 7.4. The average radial profiles at 250 μm of late-type galaxies in the HRS split by morphology. The number of galaxies that has been used in each plot is shown in the top-right corner. The green line represents the size of the dust disk as defined in Section 7.4 for the galaxies with nine objects or more. The dashed red line shows the 3 σ sensitivity limit of our profiles (see Section 7.2 for more details).

Cortese et al. (2012a) who used the Goldmine classification scheme (Gavazzi et al., 2003). One interesting feature is that there is remarkable consistency in the peak surface brightness with the surface brightness for all bins peaking $\sim 2.0 \text{ mJy arcsec}^{-2}$. The average disk sizes are not very different, although Sa/Sab galaxies appear to have on average a smaller disk size than Sb–Sd spirals by $\sim 0.2 R_{25}$. As shown in Figure 6.9 in Chapter 6 Sa/Sab galaxies have a lower dust-to-stellar mass ratios than other spirals, which is consistent with these findings.

7.6 CONCLUSIONS

This chapter has presented the first detection of dust emission outside the optical disk for a representative sample of galaxies in the local universe. At $250 \mu\text{m}$, dust emission is found above the 3σ level to a radius of $2.0 R_{25}$. The dust is most likely to be associated with gas or star-formation regions in the outskirts, but could also arise from dust being ejected from the optical disk. Further studies into the distribution of the dust will be able to distinguish between these possibilities. A rough temperature estimate at R_{25} suggests the dust is about 14 K which would put the dust emission estimates in reasonable agreement with those measured through the absorption of quasar spectra by Ménard et al. (2010). A more detailed comparison including the dust mass surface density will be possible in future work when a more rigorous estimation of the dust temperature is performed.

To extend these profiles to larger radii, observations of larger areas, and a greater number of galaxies are required. While HeViCS does provide larger areas the higher density of galaxies in the cluster may lead to the profiles overlapping. A good survey for this project, however, is H-ATLAS which covers ~ 500 square degrees with PACS and SPIRE (see Figure 7.5 for the areas observed), which has thousands of local galaxies and a large continuous area. The two potential disadvantages with using H-ATLAS are that the galaxies have smaller angular sizes and the observations are less sensitive than the HRS.

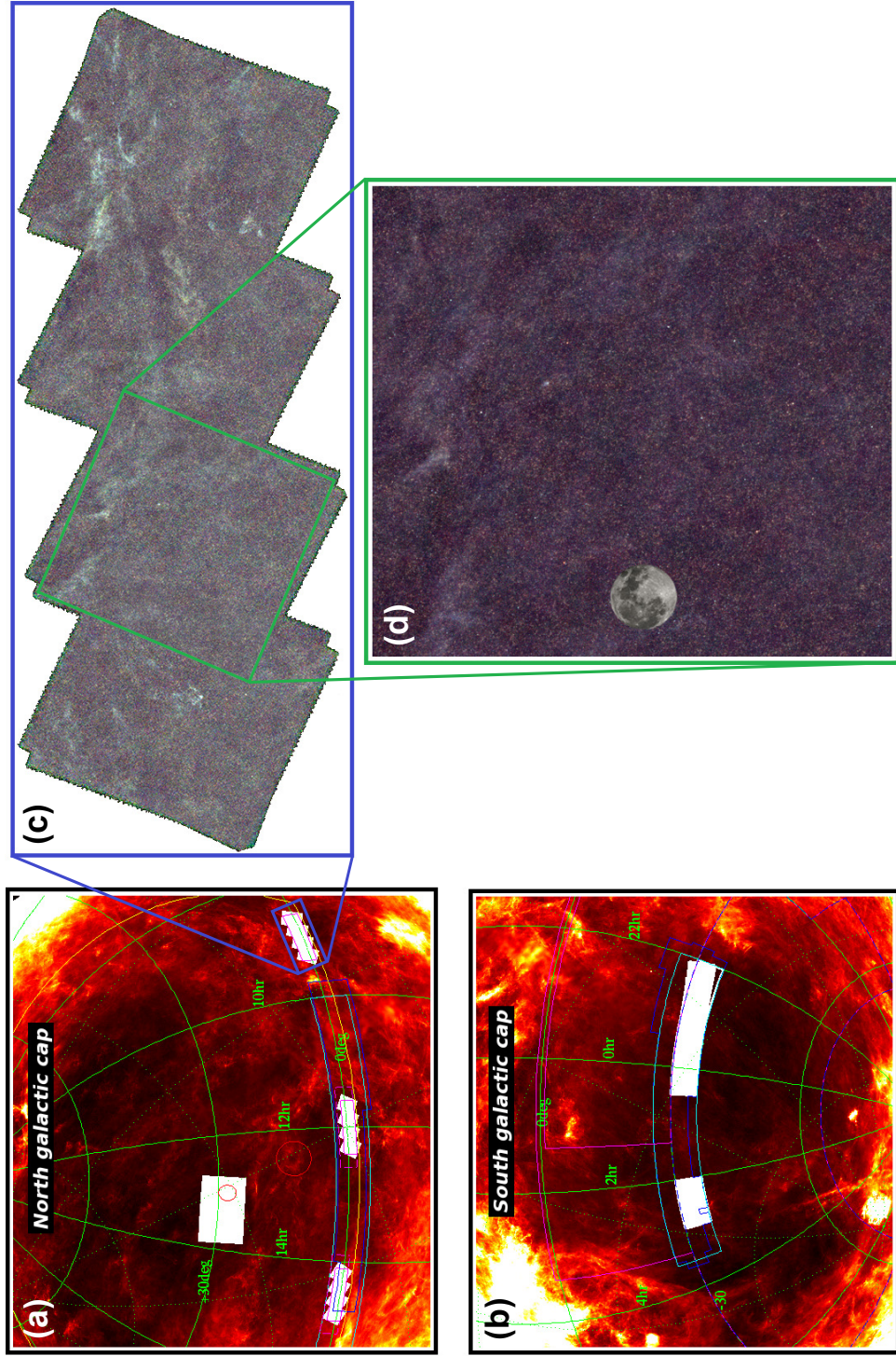


Figure 7.5. The Herschel Astrophysical Terahertz Large Area Survey. Panels (a) and (b) in white show all the regions observed as part of the survey. Panel (c) is a SPIRE 3 color image of the GAMA-9 field and a zoom of the science demonstration phase field is shown in panel (d). The large area of the survey is illustrated in panel (d) by the angular size of the moon drawn to scale.

CHAPTER 8

DISCUSSION & CONCLUSION

“When you think about it, nothing ever exists, in fact. I was working this out in the post office as I was waiting for that woman to finish twanging her elastic bands. The future doesn’t exist because it hasn’t happened yet; the past doesn’t exist because it’s already over. But the present doesn’t exist, because as soon as you start to think about it it’s already in the past. Which doesn’t exist any more.”

Victor Meldrew - One Foot in the Grave

8.1 THESIS OVERVIEW

The aim of this thesis was to use new data from the *Herschel Space Observatory* to investigate dust and the ISM in nearby galaxies. As *Herschel* was launched at the beginning of this study a lot of work has been done to optimise the data and maximise the scientific return of the observations. The two main contributions I made to this effort is an extra-galactic data reduction pipeline (BRIGADE) and a routine to fit spectral energy distributions which is optimised for use with *Herschel* data. In this work I have used observations of local galaxies to investigate the distribution, heating, origins and composition of dust within galaxies.

This thesis has mainly relied on three *Herschel* surveys of the local universe: the HRS, HeViCS and HELGA. The HRS is a volume limited sample of 323 nearby galaxies ($15 < D < 25$ Mpc) with SPIRE observations at 250, 350, 500 μm . HeViCS is a blind survey of the Virgo Cluster covering an area of 80 square degrees covering the full 100–500 μm wavelength range. The HELGA survey has produced the most detailed (in area, wavelength coverage and sensitivity) survey of dust in Andromeda.

8.2 KEY RESULTS

The key results of this work are:

- For no galaxy studied in this thesis is there any conclusive evidence of an excess of dust emission at $500\mu\text{m}$. Such an excess could indicate the presence of a large quantity of very cold dust ($\sim 10\text{ K}$) and has been found in low-metallicity dwarf galaxies with *Herschel* (e.g., Grossi et al., 2010).
- The distribution of dust within a galaxy varies between objects. For both NGC 4501 and NGC 4567/8 the dust is symmetrically distributed, while for S0 galaxies many ring and uneven distributions are found. In Andromeda the dust surface density is found to be highly correlated with the star-formation rate rather than the stellar distribution.
- In Andromeda a radial gradient in the gas-to-dust ratio is found, with the ratio varying from ~ 20 in the centre to ~ 200 at 18 kpc. The gradient is consistent with that predicted from the metallicity gradient assuming a constant fraction of metals is incorporated in dust grains.
- The investigations of Andromeda, NGC 4501 and NGC 4567/8 showed the dominant source of dust heating depends on the local conditions. In regions with a high density of stars (e.g., the bulge of Andromeda) the dust is heated by the general stellar population. While in regions with higher star-formation the dust temperature is weakly correlated with the star-formation rate.
- The properties of the dust grains vary throughout Andromeda as the dust emissivity index (β) changes with radius. The value of β varies between ~ 1.0 and ~ 2.5 ; high values of β may be due to efficient grain coagulation or mantle growth.
- A search in Andromeda for the presence of ‘dark gas’ using a similar method to that used by the *Planck* team for the Milky Way (Planck Collaboration, 2011a) was unsuccessful. This may be due to the low CO emission, poor angular resolution or line-of-sight averaging effects. By plotting the ratio of dust surface density to hydrogen column density, I find regions of enhancements which suggest either the presence of ‘dark gas’ or a change in the local gas-to-dust ratio. The method did yield a value for the constant of proportionality between the CO($J = 1 - 0$) line flux and molecular hydrogen column density, which is $(1.9 \pm 0.4) \times 10^{20} \text{ cm}^{-2} [\text{K kms}^{-1}]^{-1}$

- Dust emission is the most efficient way of detecting the ISM in nearby galaxies. A comparison of the detection rates for early-type galaxies found many more objects are detected in dust than in surveys of the HI and CO emission, which require much longer integration times.
- The HRS contains the largest targeted survey of early-type galaxies with *Herschel*. Out of the sample of 62 galaxies, 24% of ellipticals and 62% of S0's are detected. Elliptical galaxies have a dust-to-stellar mass ratio an order of magnitude lower than their S0 counterparts and two orders of magnitude lower than late-type objects.
- The lack of a correlation between dust mass or FIR luminosity with optical luminosity and the large spread of dust-to-stellar mass ratios in early-type galaxies suggests that the dust in early-types is external in origin. Events like merging may deposit the ISM in these objects but would not be a significant effect on the stellar population.
- By combining the radial profiles of the late late-type galaxies in the HRS, I have detected the emission of dust out to $2.0 \times R_{25}$. This is the first detection of dust far outside the optical disk in a representative sample of galaxies in the nearby universe. The fraction of dust emission between 1.0 and $2.5 R_{25}$ is 6.6%, 8.0% and 10.6% of the total emission between 0.0 and $2.5 R_{25}$ for the 250, 350 and 500 μm bands, respectively.
- When averaging the radial profiles for galaxies in bins of HI deficiency, I found that highly HI-deficient objects have a smaller dust disk than those with very low HI-deficiencies. However, the difference was smaller than found in previous study by Cortese et al. (2010b) who looked at 16 objects in the Virgo Cluster.

8.2.1 DUST IN LATE-TYPE GALAXIES

Herschel has provided the first large samples of nearby galaxies with coverage at wavelengths longer than the FIR peak of dust emission. A pixel-by-pixel dust analysis has been performed on M31, NGC4501 and NGC4567/8 and has found dust temperatures in the range between 15 and 25 K. The typical dust temperature of ~ 17 K is lower than previous studies which just use data at $\leq 160 \mu\text{m}$. I found dust masses which give gas-to-dust ratios similar to that found in the Milky Way. The heating of the dust can be due to either the general stellar population or young stars

in star-formation regions depending on the local conditions. In these objects no large quantities of cold dust (~ 10 K) have been detected.

For the first time this work has detected dust emission out to at least a radius of $2.0 \times R_{25}$. The dust has a temperature about 14 K. The quantity of dust out to this radius is only approximately 10% of the total dust mass within the galaxy. Previous satellite observations did not have the wavelength coverage and SCUBA did not have the sensitivity to detect this dust. The dust has either formed in star-formation regions inside the optical disk and has been transported out of the disk or is created by star-formation in the halo. This result could have important implications for the enrichment of the inter-galactic medium.

The dust spectral index varies with radius in Andromeda. In the main ring at 10 kpc β is consistent with that found by the *Planck* team for the local environment in the Milky Way (~ 1.8). However in the inner regions β increases to ~ 2.5 , much higher than expected. This is evidence that the grain composition within galaxies is not uniform, which may lead to a bias in global studies. However, for Andromeda dust mass estimated from the global fluxes was found to be consistent with the dust mass found from the total of individual pixels.

Can Dust Trace Gas?

With the measurements of Andromeda the idea that dust can be used to trace the gas in a galaxy has been tested with unprecedented accuracy. Andromeda is an unusual case in that very little of its gas is in the molecular form and so the uncertainties in the conversion from a CO line flux to the column-density of molecular gas are not too important. A radial gradient is present in the gas-to-dust ratio which matches that predicted from the metallicity gradient (assuming a constant fraction of metals are within dust grains). This suggests it is possible to trace the total gas content in galaxies from the dust measurements but only if the distribution of metallicity is also known. Further observations are required to confirm if ‘dark gas’ is present.

8.2.2 DUST IN EARLY-TYPE GALAXIES

Using the Herschel Reference Survey (HRS), I have undertaken the first complete un-biased census of dust in early-type galaxies (ETGs) with *Herschel*. Our overall detection rate of 50% is higher than that found by other surveys with time consuming HI and CO measurements, suggesting that dust is a much more efficient method to detect the ISM in galaxies. There is an order of magnitude reduction in dust mass as a fraction of stellar mass as you move from spirals to S0s and a further

order of magnitude decrease to elliptical galaxies. This difference between the S0s and early-type spirals cannot be explained by the difference in bulge-to-disk ratio. All the evidence supports the scenario that much of the dust in early-type galaxies has been acquired from mergers. With these galaxies I find a higher average dust temperature (23.9 K) for the ETGs with respect to the sample of late-type galaxies measured in the Virgo cluster (Davies et al., 2012). As early-type galaxies have little or no star-formation this shows that heating of dust from the general stellar population can be significant.

Recently optical studies of 260 ETGs by the ALTAS^{3D} team (Cappellari et al., 2011) have found that ETGs do contain a rotational component and there appears to be gradual progression in their properties from ‘fast rotators’ to ‘slow rotators’. However, when investigating the dust in these objects there is a much cleaner distinction when the ETGs are grouped by morphology than by their optical kinematic properties.

8.3 FUTURE WORK

This thesis has presented some of the first investigations of nearby galaxies using observations from *Herschel*. However, it is only now that many of the samples of galaxies are complete and that many in-depth studies can be performed. Chapter 7 presented an initial search and detection of dust outside the optical disk of a galaxy. Similar stacking studies have been made with both molecular gas and star-formation tracers (Schruba et al., 2011). By combining the multiple wavelengths a more detailed analysis which compares the radial gradients may be able to distinguish if the dust outside the optical radius (R_{25}) is from dust driven out of the optical disk or associated with gas and star-formation in the outskirts of galaxies.

Results from quasar absorption (Ménard et al., 2010) suggest that dust extends over very large scales (up to 10 Mpc) which is beyond the scales possible with the HRS. While stacking a larger sample (e.g., with H-ATLAS) of galaxies may help increase the sensitivity of dust profiles at higher radii a fundamental limit from the point spread function of the central source may be reached. A potential way to avoid this problem is to either choose a sample of galaxies with large angular size by combining observations from many different *Herschel* surveys or to attempt a study with higher resolution but less sensitive PACS data. One aim of the HeViCS team is to detect extra-cluster dust, however the maps are contaminated by emission from cirrus clouds in our own galaxy. A possible way to correct for this is to use HI observations that have velocity information to differentiate which structures are from the Milky Way

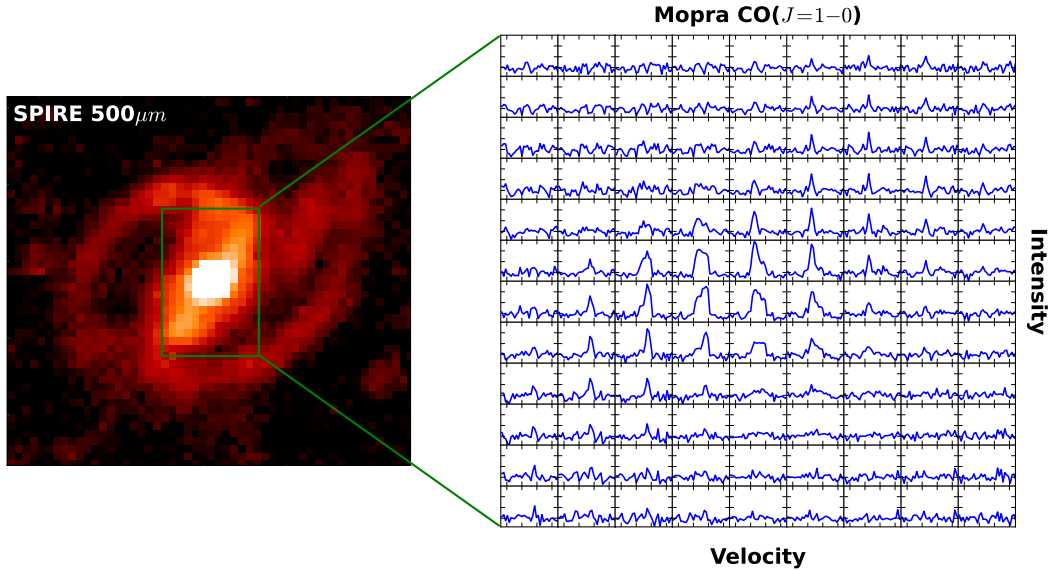


Figure 8.1. An example of a CO($J = 1 - 0$) map taken with Mopra. The image on the left is a *Herschel* 250 μm map and on the right is the data cube showing CO($J = 1 - 0$) emission.

and which are from inter-cluster dust.

In this thesis an attempt to detect ‘dark gas’ (i.e., gas not traced by the usual HI and CO tracers) was unsuccessful. However, regions were identified as potentially containing ‘dark gas’ or areas in which the gas-to-dust ratio is different. Surveys in Andromeda of C[II] emission, will distinguish between the possibilities. This is an important question as many studies of local galaxies require a good knowledge of the total surface density of gas. The relative strength of the C[II] line makes it a very important tracer for higher redshift objects (where it is possible to observe from the ground), so understanding how it relates to the molecular gas mass and dust in the local universe is crucial to investigate the early universe.

The studies of Andromeda and HeViCS galaxies showed that the dust temperature and dust emissivity index can vary considerably in a galaxy. The obvious extension to the Andromeda analysis is to see if those trends are repeated in other galaxies. Many galaxies with a large angular size have been observed with *Herschel* that would be ideal for such a study. One of the major limits to performing this study is the availability of CO maps to trace the molecular gas. In the last couple of years surveys of the HRS in CO($J = 3 - 2$), HeFoCS in CO($J = 1 - 0$) and KINGFISH in CO($J = 2 - 1$) have begun to fill this void (an example of a CO map recently obtained by me is shown in Figure 8.1).

For the HRS there are now many global metallicity values and by combining

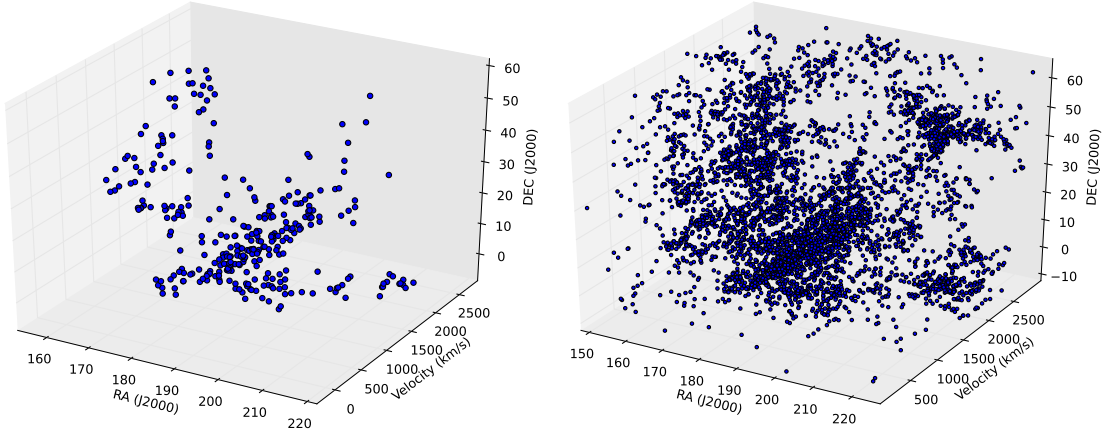


Figure 8.2. *Left:* The distribution of the HRS galaxies inside the volume used to define the sample. The impact of the Virgo cluster can be seen with its large velocity range. *Right:* The distribution of all galaxies from the HyperLeda database identified within the HRS volume.

this data with many global gas and dust measurements it might be possible to calibrate a method for estimating the gas mass from the dust emission. This could then be used to find the gas masses for the thousands of galaxies detected by *Herschel* and for which measurements of the HI and CO are difficult. With knowledge of the gas it would be possible to identify whether a Kennicutt-Schmidt relation holds at higher redshifts and what factors affect the star-formation efficiency of galaxies.

It is known that environment can dramatically affect the quantity of the gas in a galaxy. I found a small change in the sizes of the dust disks but a full analysis of how the environment affects the dust properties has yet to be carried out. *Herschel* has now observed several clusters including Virgo, Coma and Fornax, so the effect of cluster size and mass can be studied. An alternative approach to quantify a galaxy's local environment is to use optical data to find the local number density of all galaxies in the surrounding region. Figure 8.2 shows the distribution of the HRS galaxies and all the galaxies from the HyperLeda database (Paturel et al., 2003) in the volume covered by the survey. A future project would be to use the HyperLeda database to quantify the variation in the local density of galaxies and compare it to the dust properties of the galaxies. It is currently unclear whether the distance to a galaxies nearest neighbours (e.g., the closest one or two galaxies) or the environment as a whole (e.g., field or cluster) has the most prominent effect on a galaxy. Figure 8.2 shows that the HRS volume does contain large variations in the local environment and so observations of the dust and gas maybe able to differentiate between the two cases.

The new generation of ground based instruments/telescopes has now started operations. The Atacama Large Millimeter Array (ALMA) will observe at wavelengths between $350\,\mu\text{m}$ – $9.5\,\text{mm}$. With its fifty 12 m dishes it will have un-paralleled sensitivity and angular resolution. While ALMA does not have the mapping speed to cover large areas of sky it will be able to follow up targets from *Herschel* in unprecedented detail. SCUBA2 is now observing at 450 and $850\,\mu\text{m}$ at the JCMT and has a much greater mapping speed than its predecessor, allowing large maps of the cold dust emission to be created. The longer wavelengths will make it possible to fully constrain the dust emissivity index, both globally and in specific regions of a galaxy. This will give a better understanding of the composition and the mass of dust by finding more precise measurements of the dust-opacity coefficient (κ) and identify if it varies with different dust emissivity indexes.

8.4 CONCLUDING REMARKS

Herschel has provided the most detailed understanding of dust in the universe to date. The observatory’s helium coolant will run out in 2013 after a lifetime of \sim 3–4 years, but the legacy value of its data will mean *Herschel* observations will be used for many years to come.

APPENDIX A

IMAGES OF GALAXIES IN THE HERSCHEL REFERENCE SURVEY

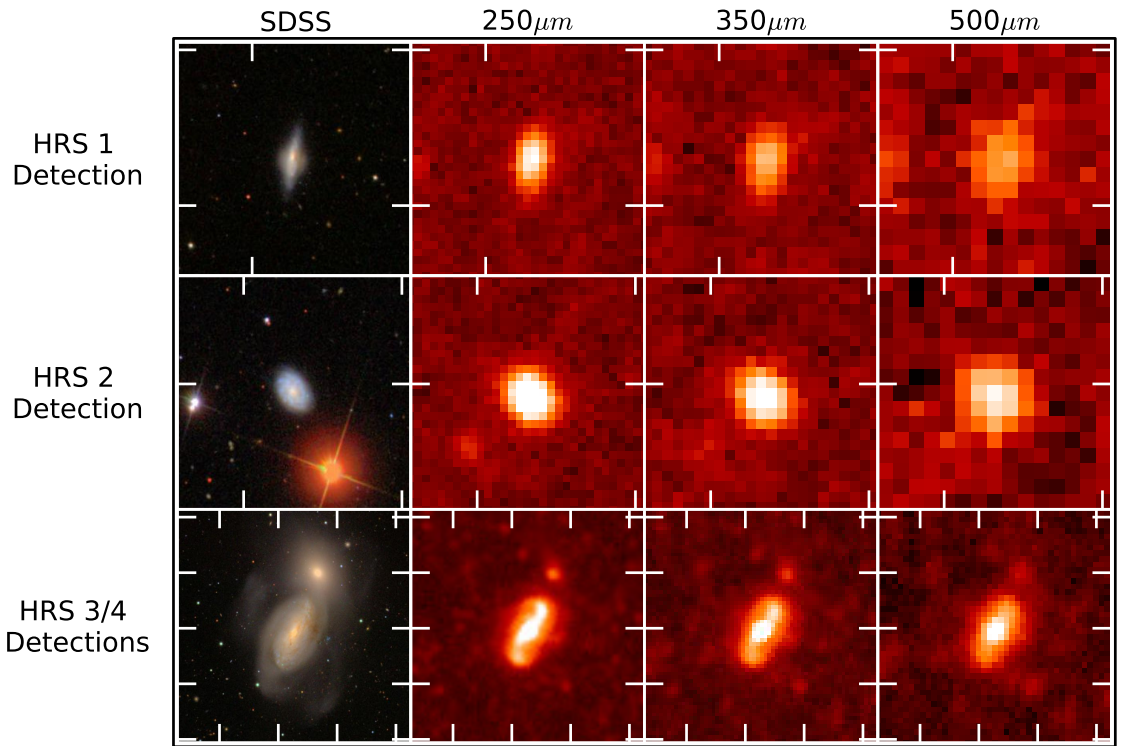


Figure A.1. Images of the galaxies that comprise the Herschel Reference Survey. The label for each row indicates the HRS number and whether the galaxy was detected by SPIRE. The left hand column is a 5 band colour image taken from the SDSS survey except for images that have a '*' in the top left hand corner which are made from the blue, red and IR images from the DSS. All images are $1.5 \times D_{25}$ with a minimum width of $3'$. The tick size represents $2'$.

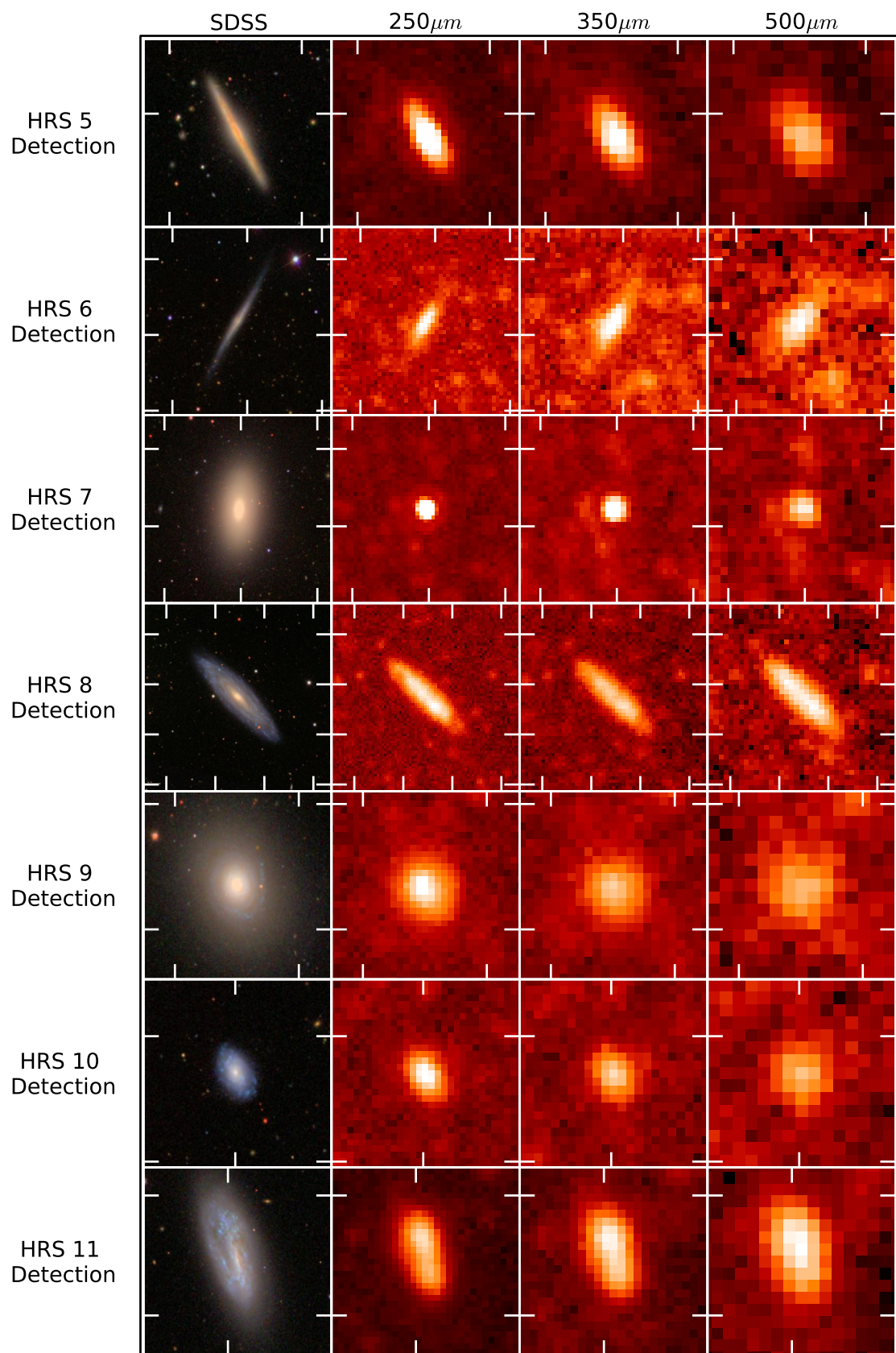


Figure A.1. (*Continued*)

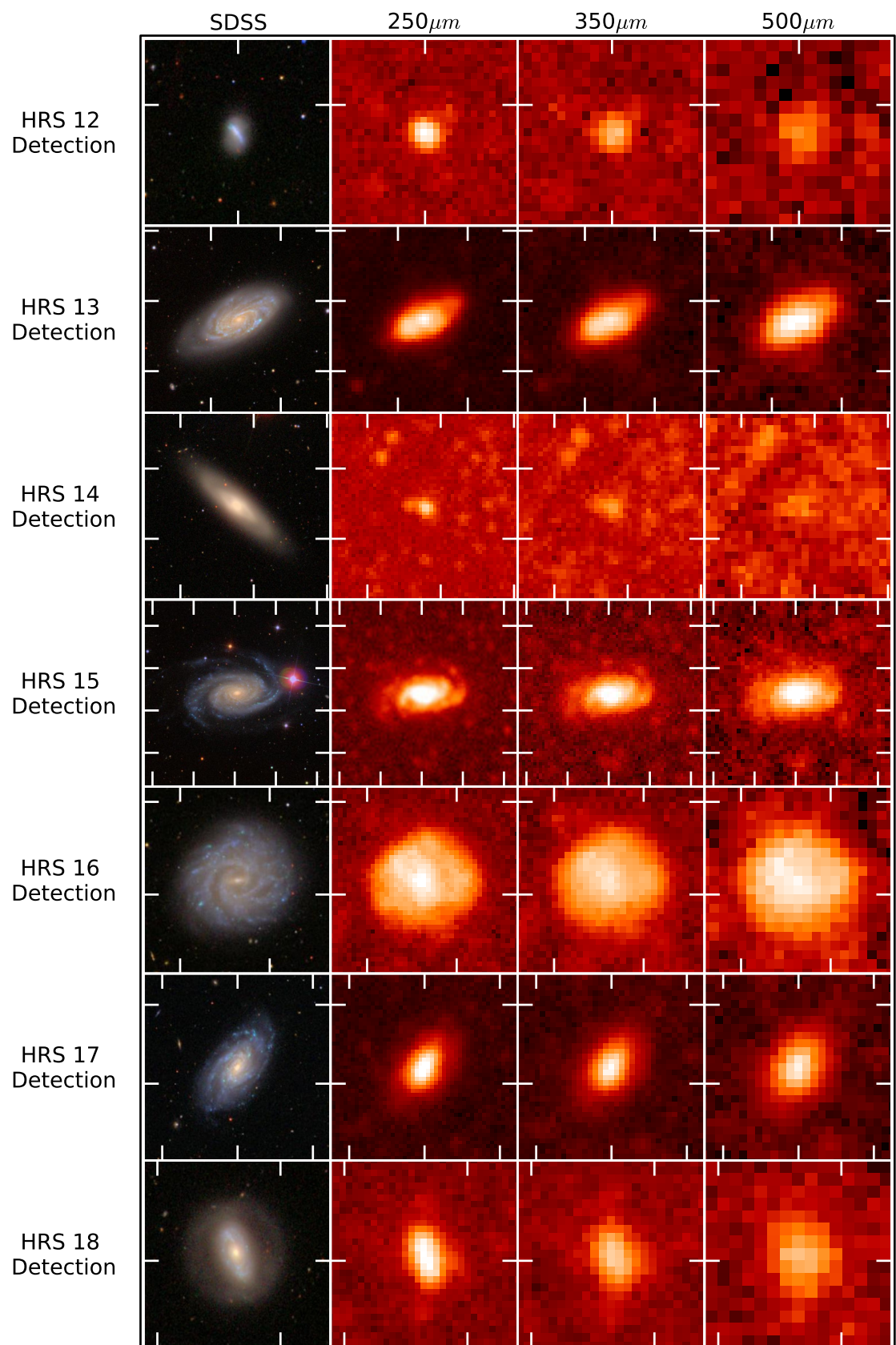


Figure A.1. (*Continued*)

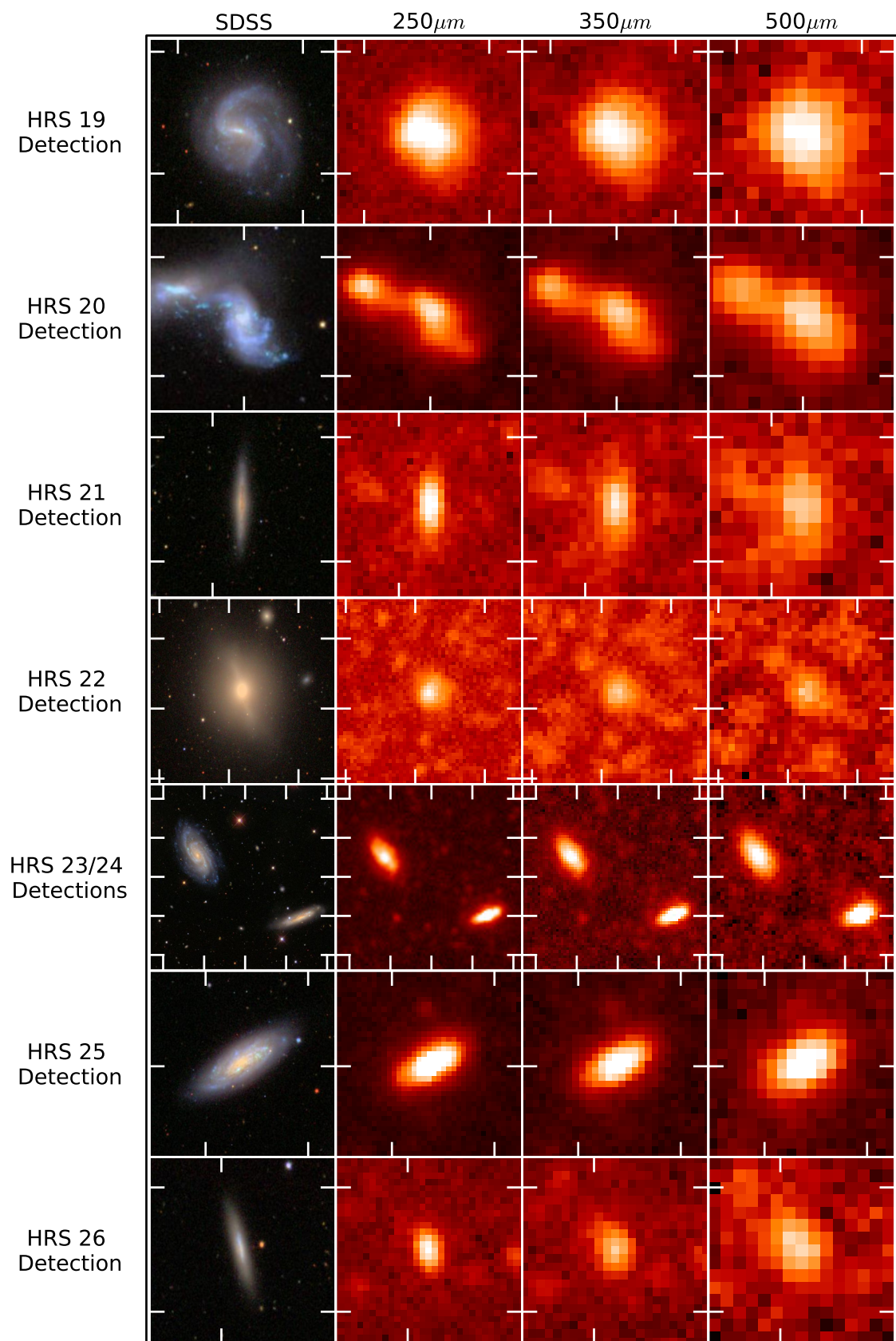


Figure A.1. (*Continued*)

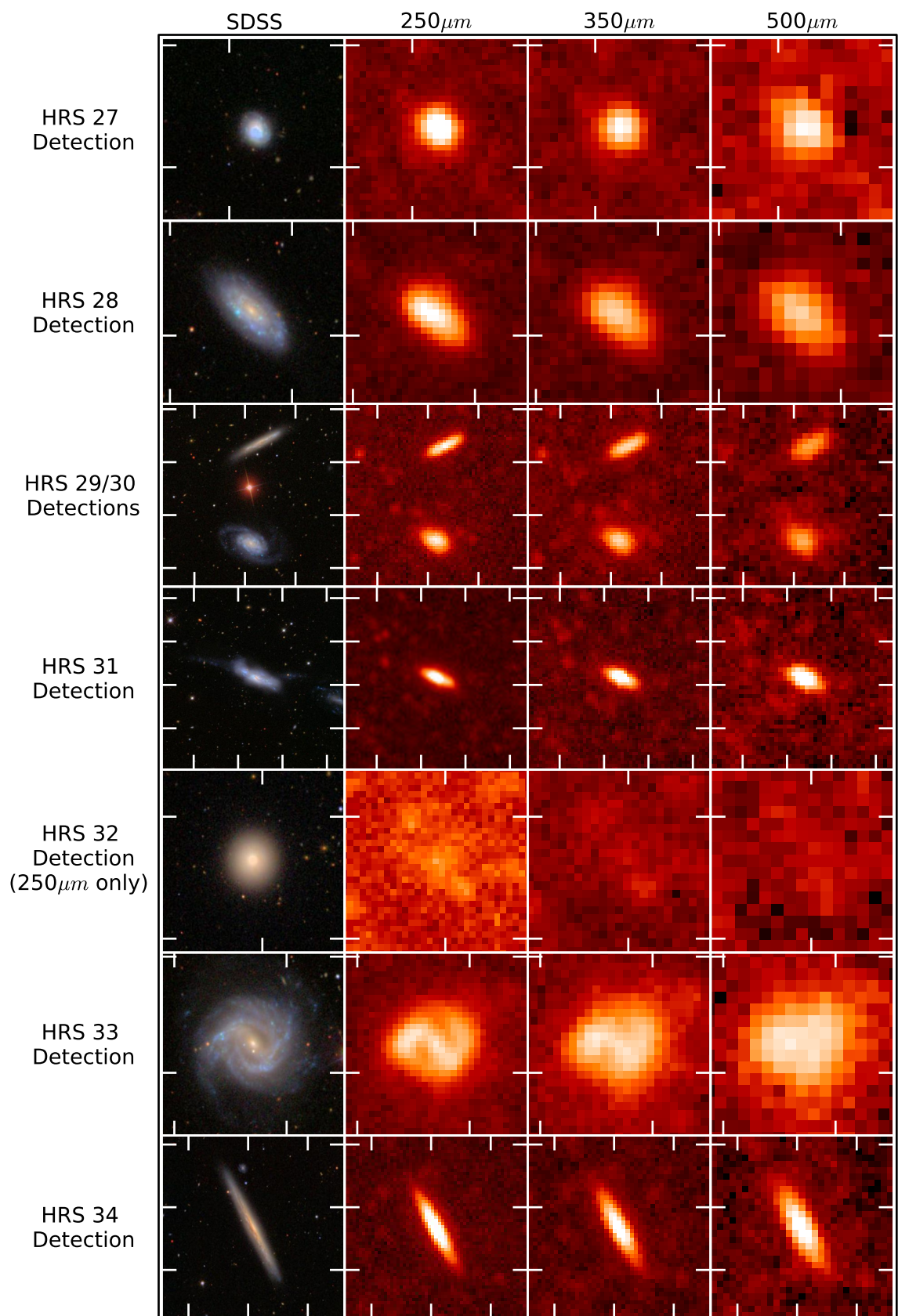


Figure A.1. (Continued)

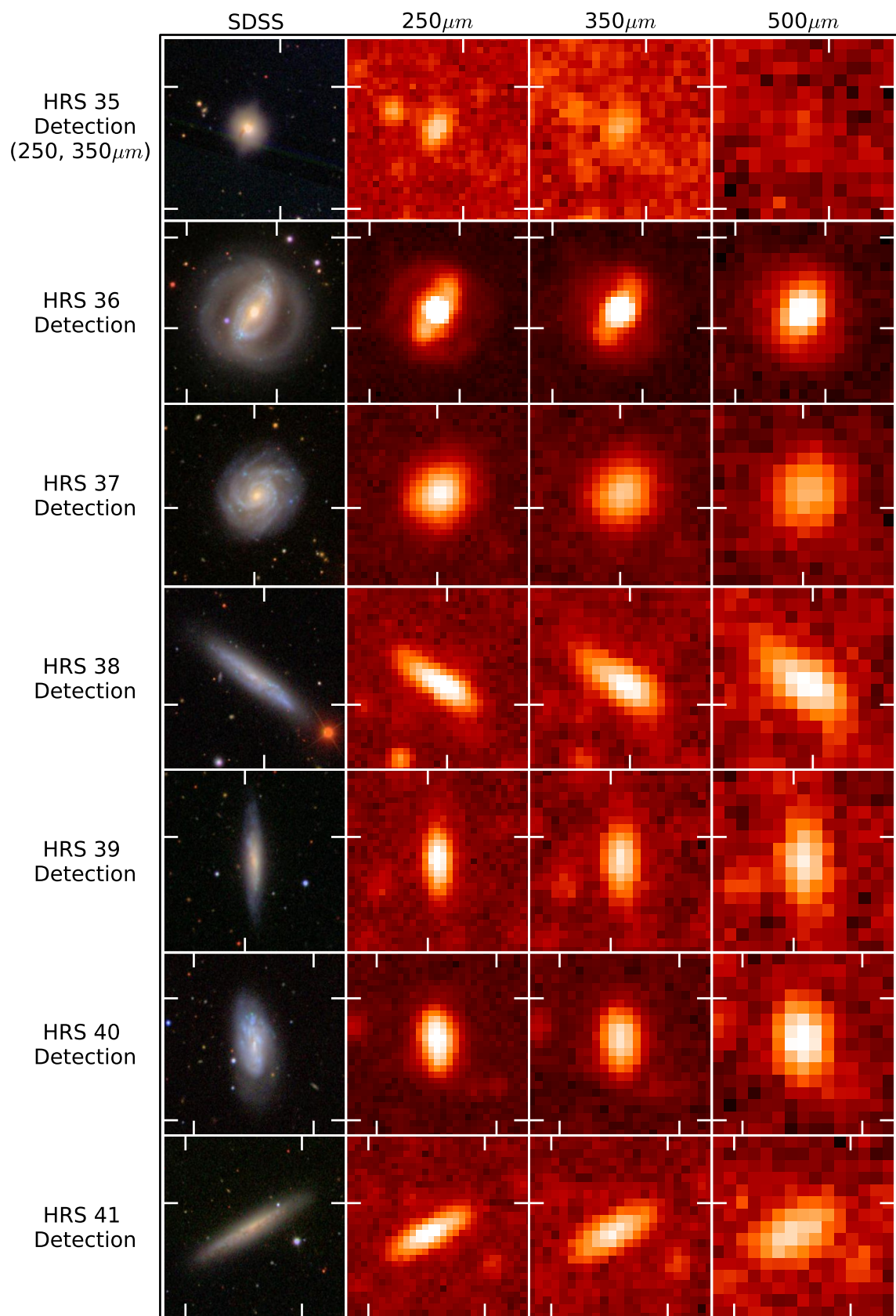


Figure A.1. (*Continued*)

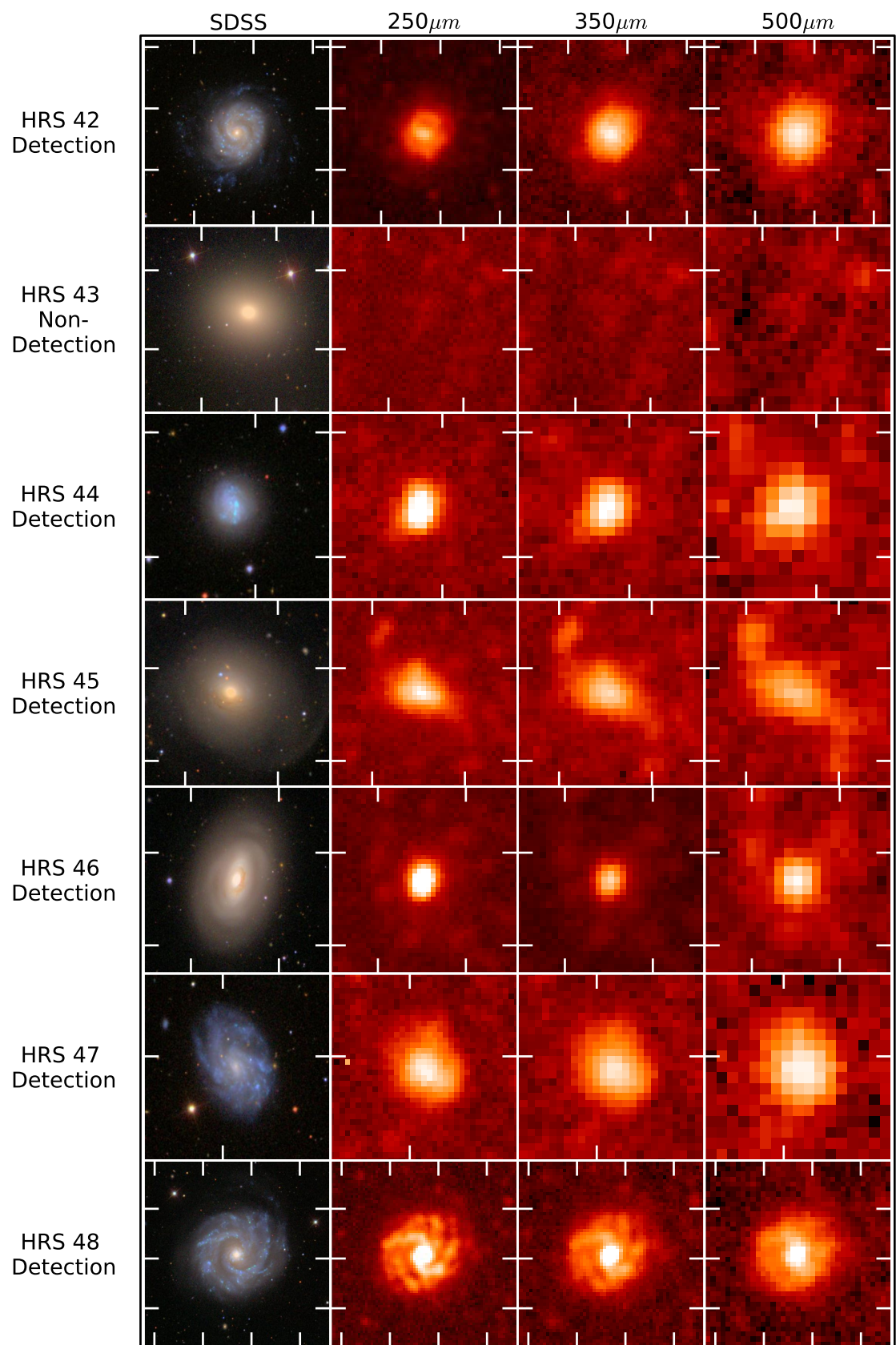


Figure A.1. (*Continued*)

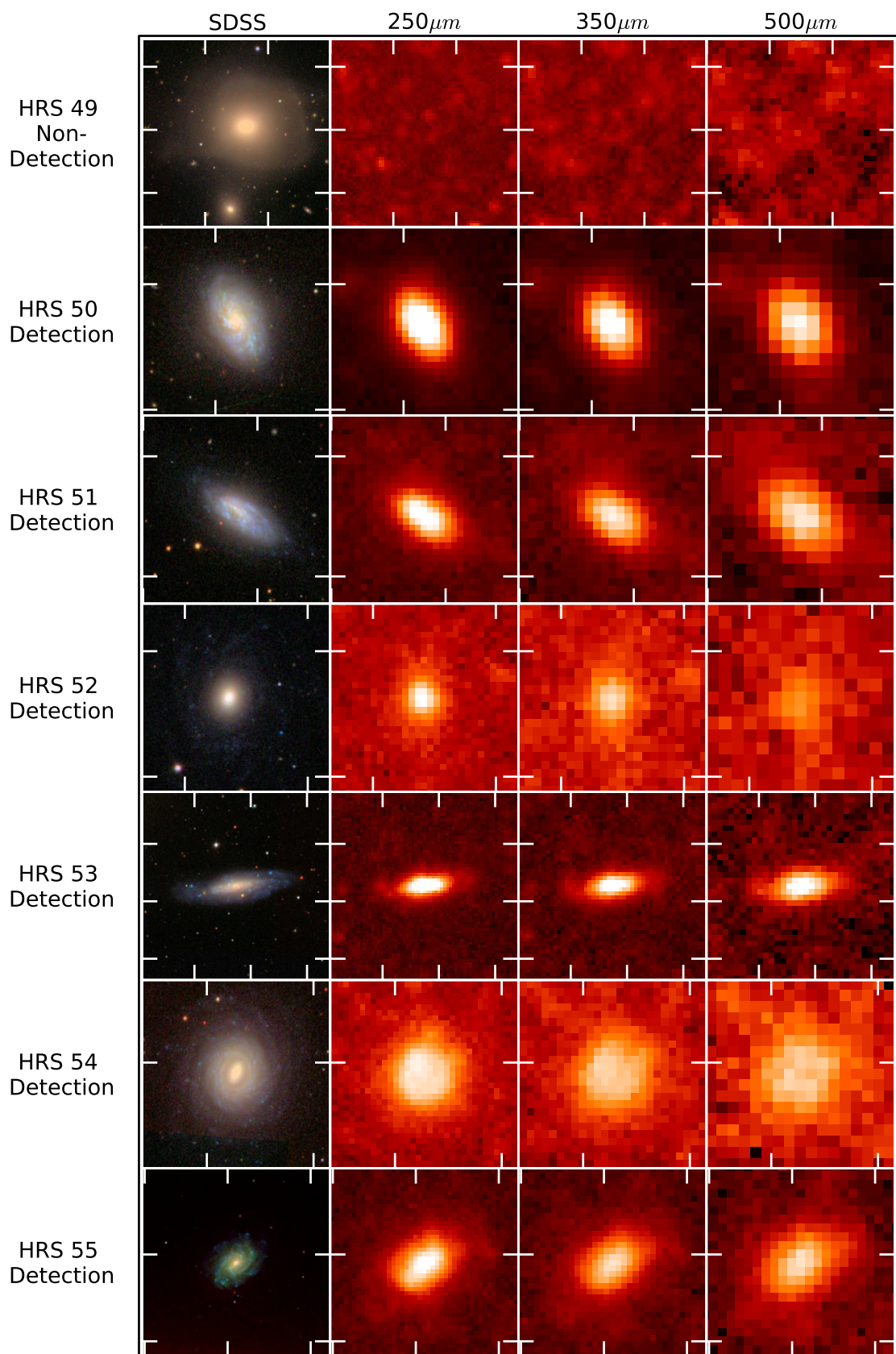


Figure A.1. (*Continued*)

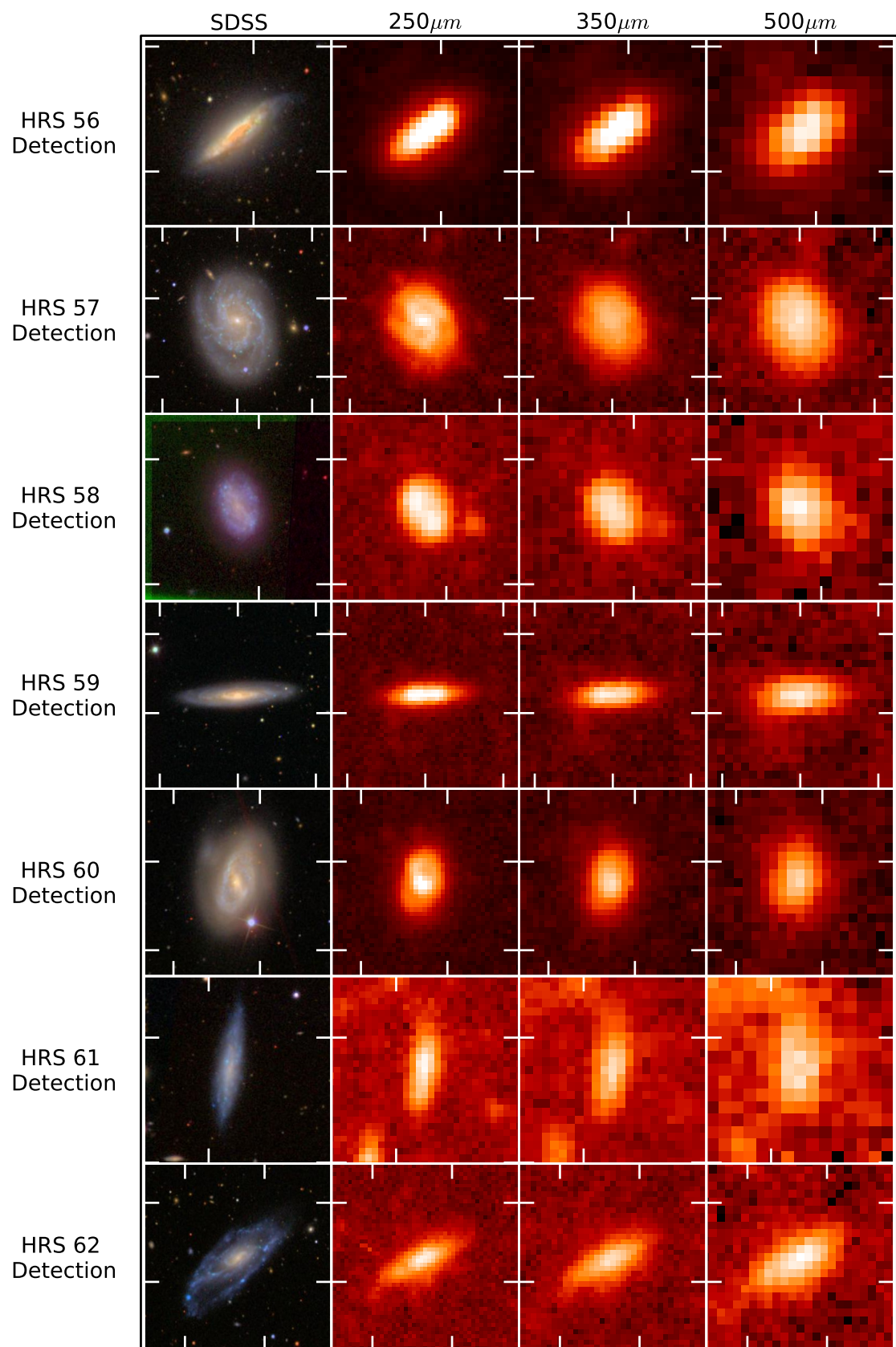


Figure A.1. (Continued)

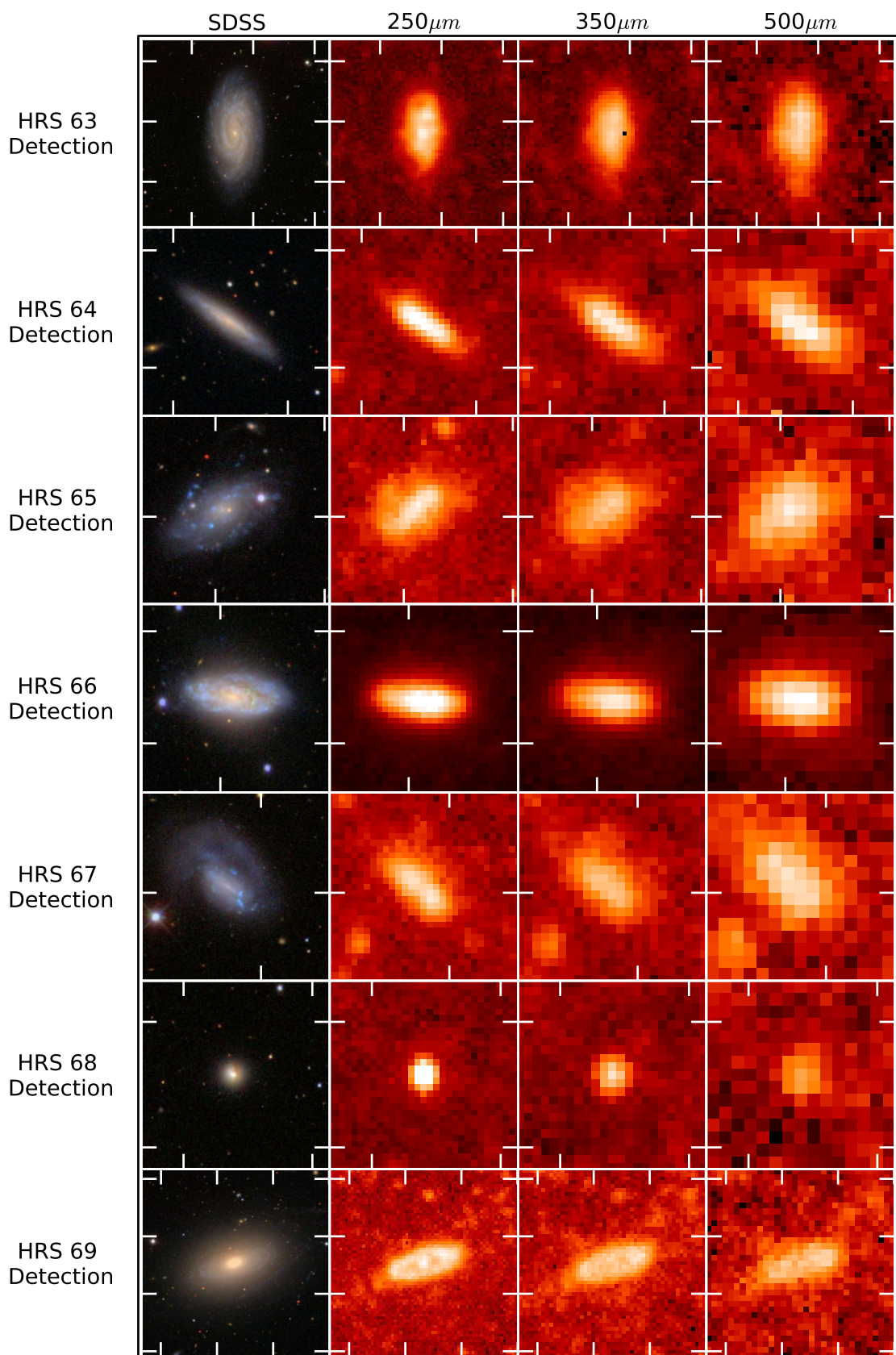


Figure A.1. (*Continued*)

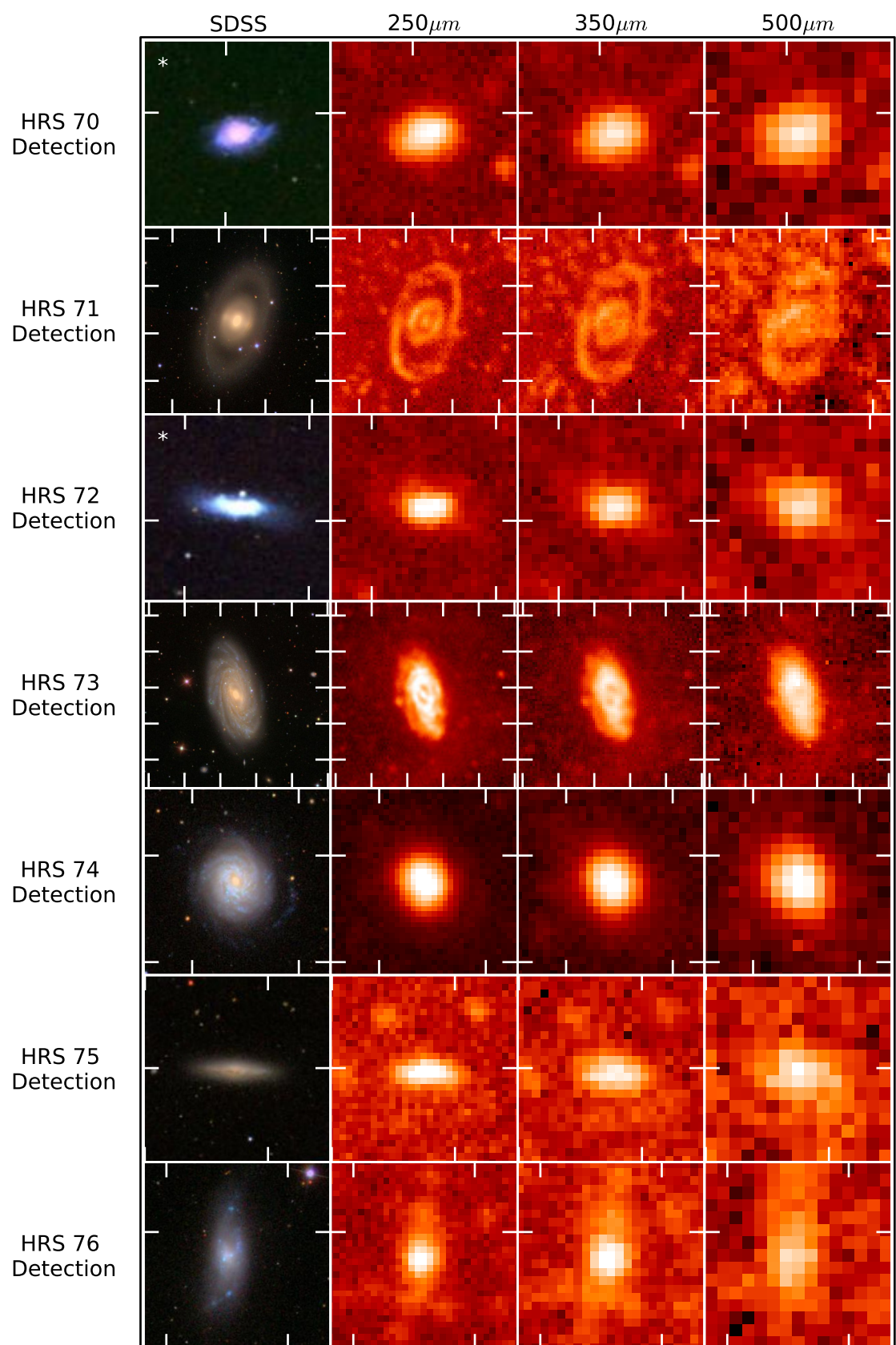


Figure A.1. (Continued)

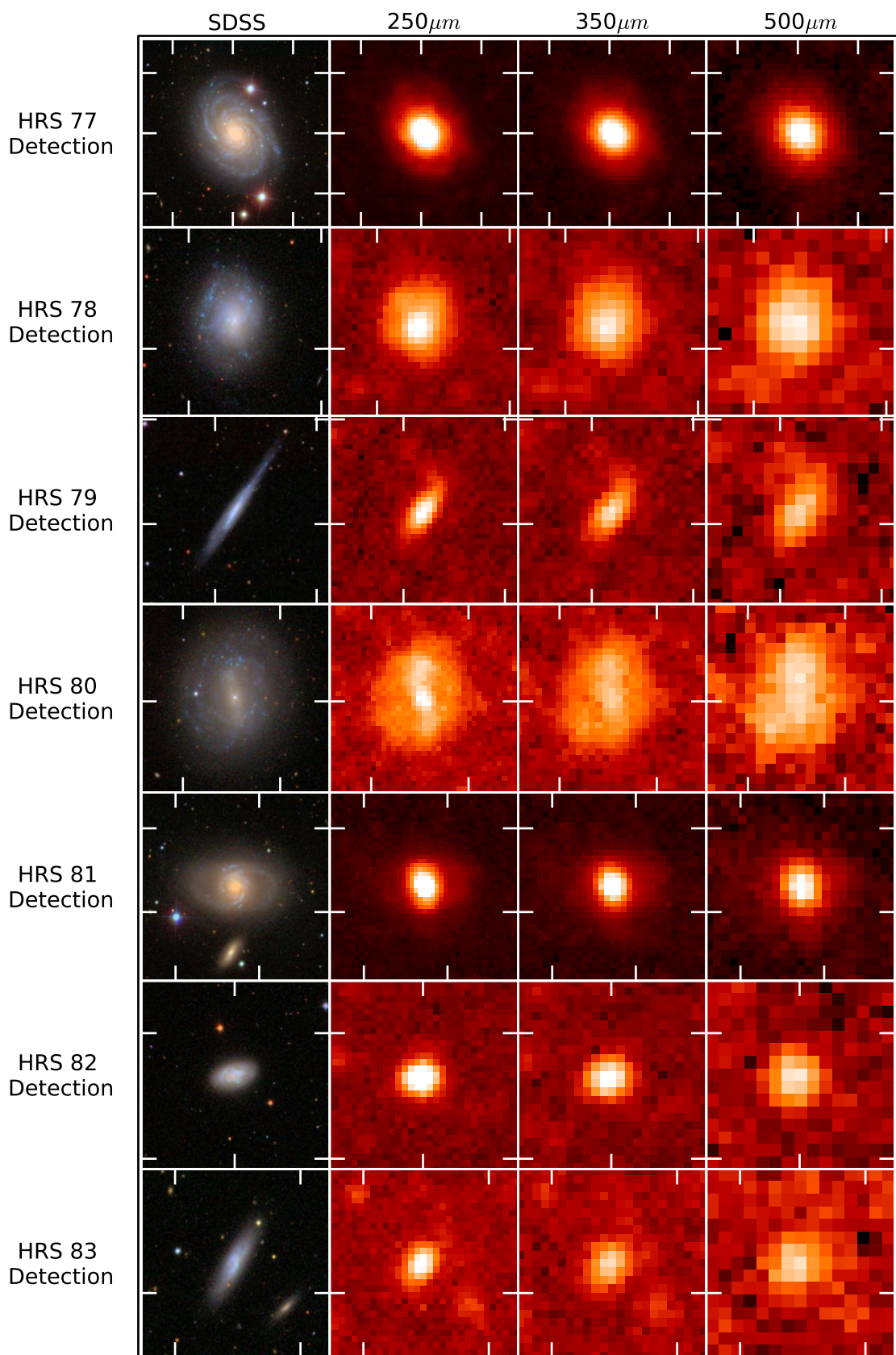


Figure A.1. (*Continued*)

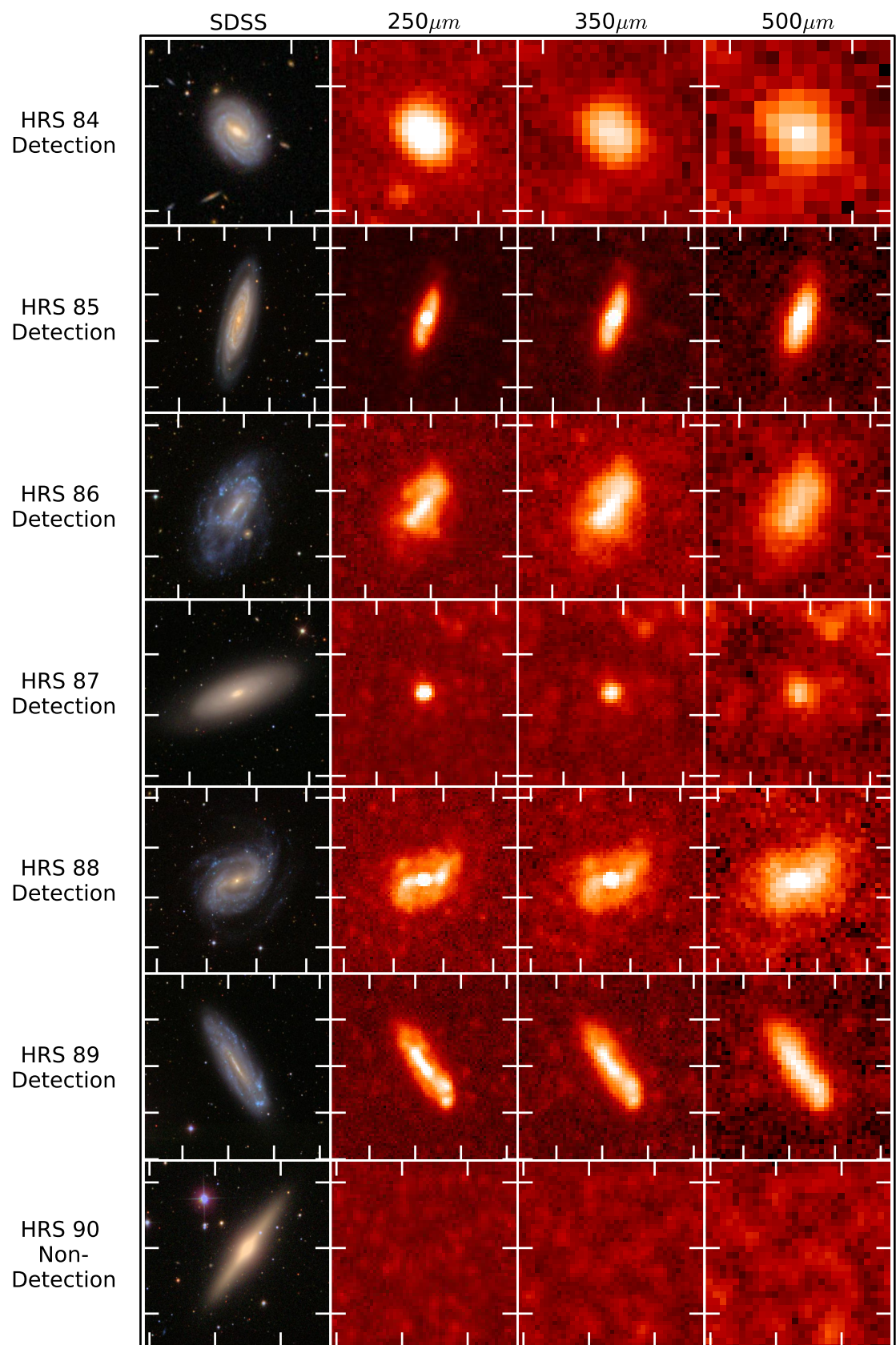


Figure A.1. (Continued)

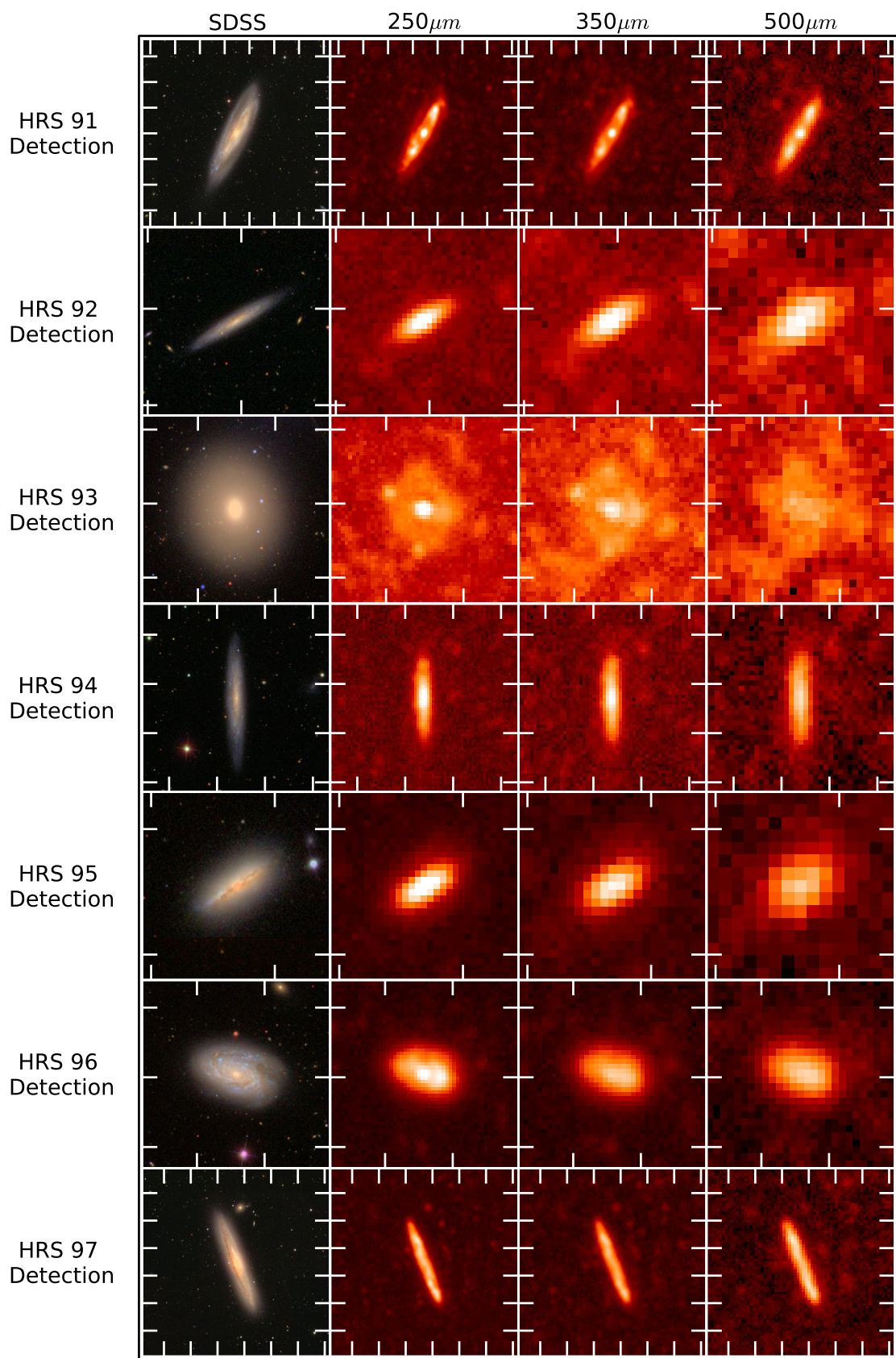


Figure A.1. (*Continued*)

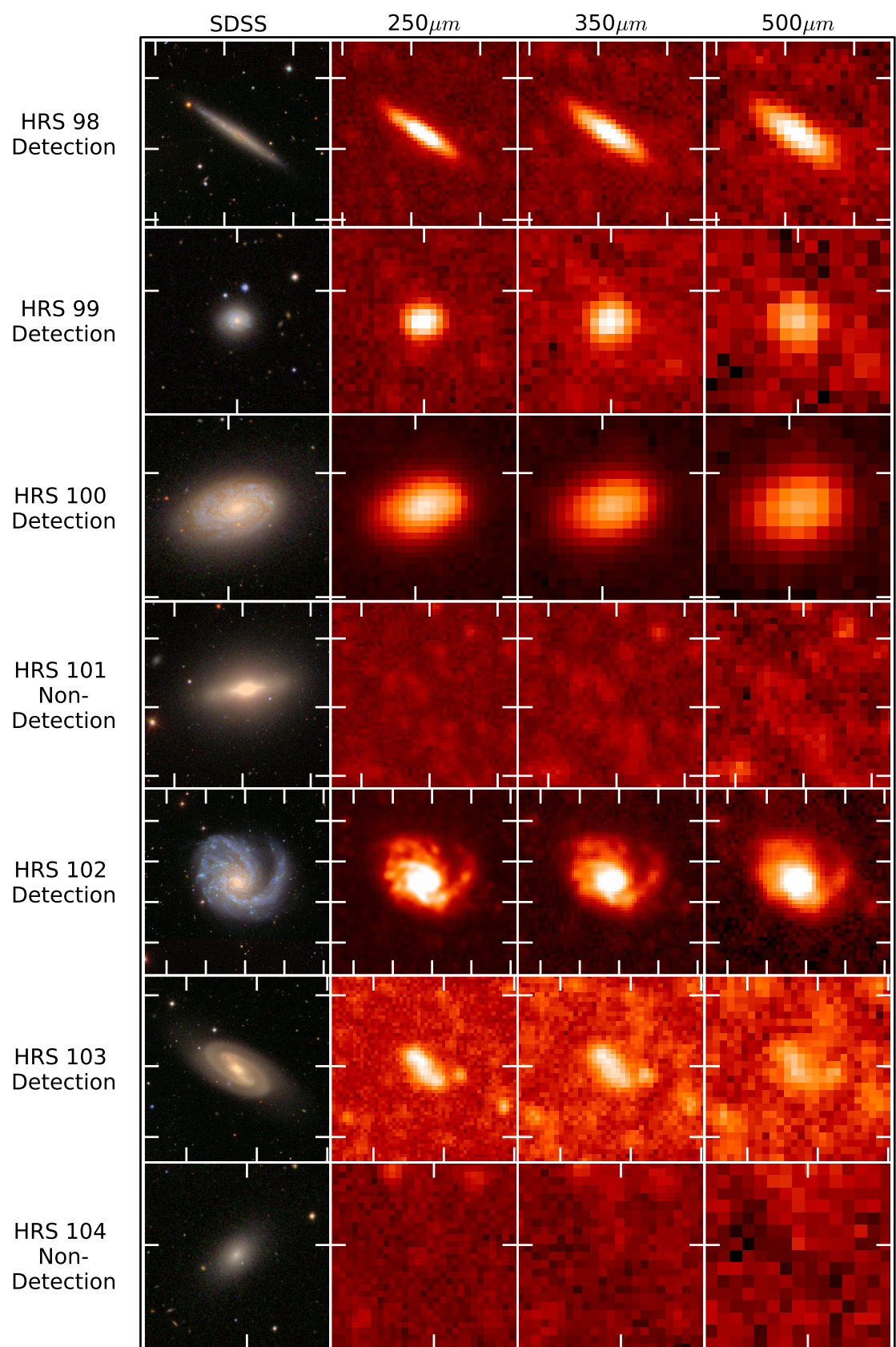


Figure A.1. (*Continued*)

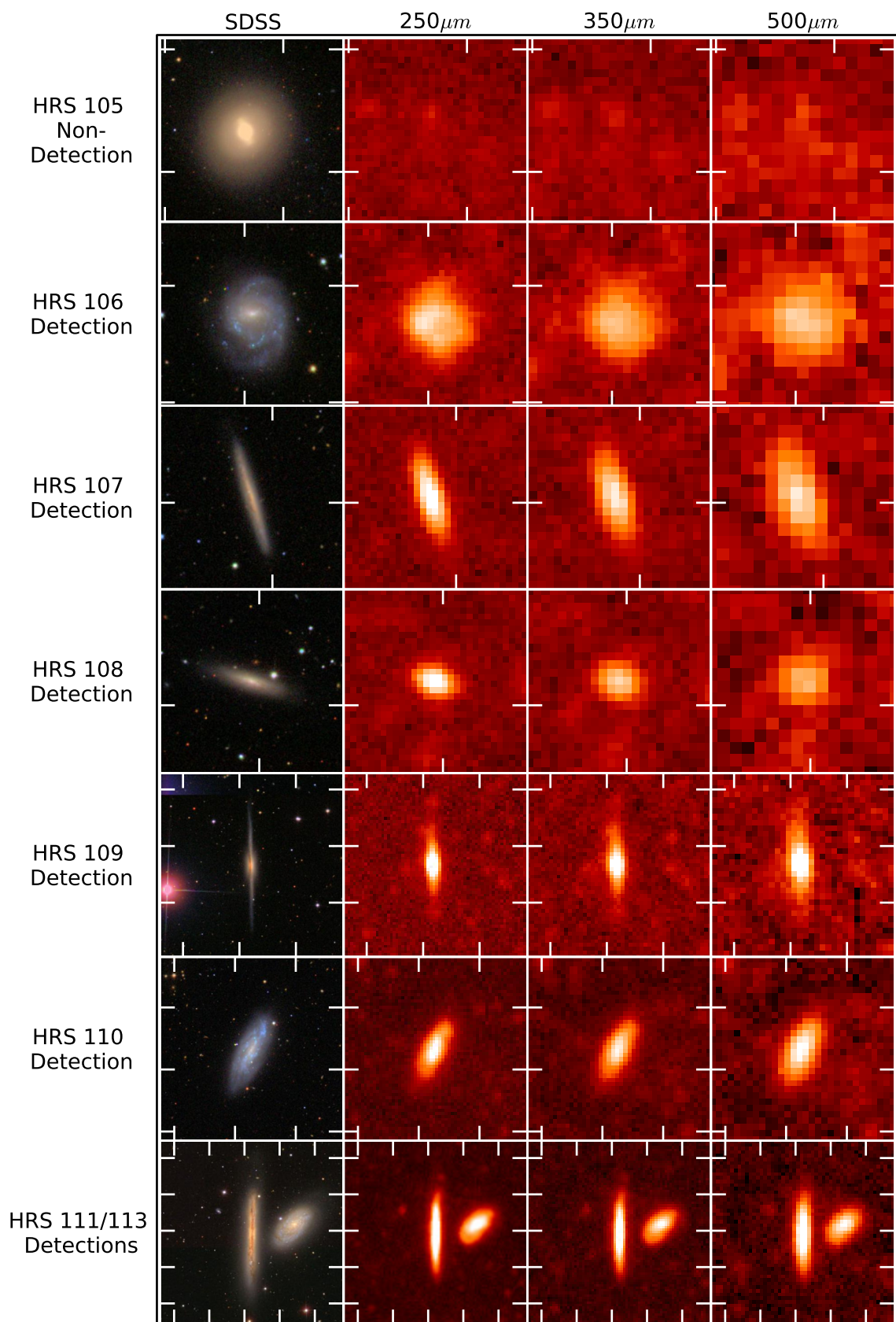


Figure A.1. (*Continued*)

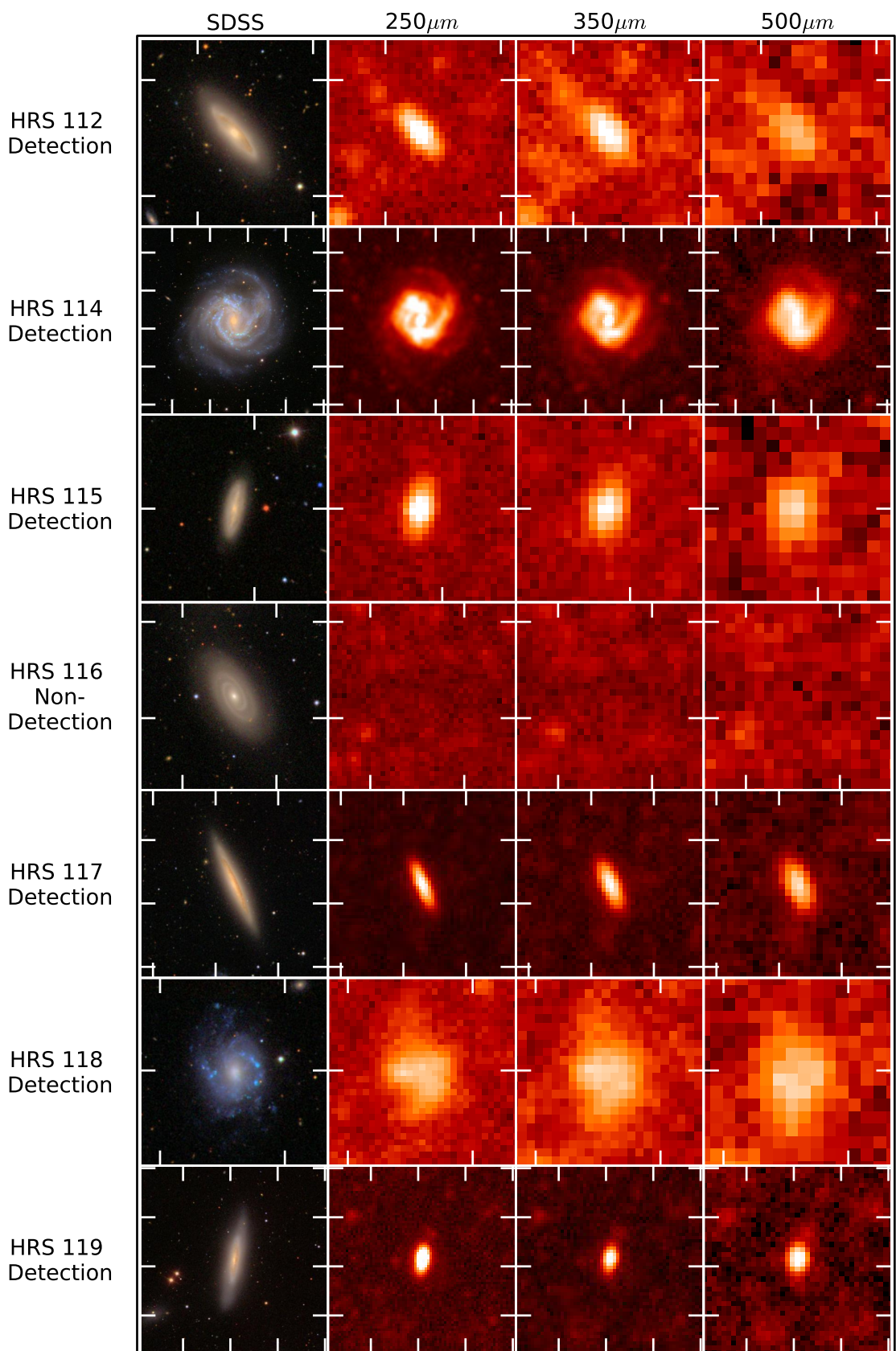


Figure A.1. (*Continued*)

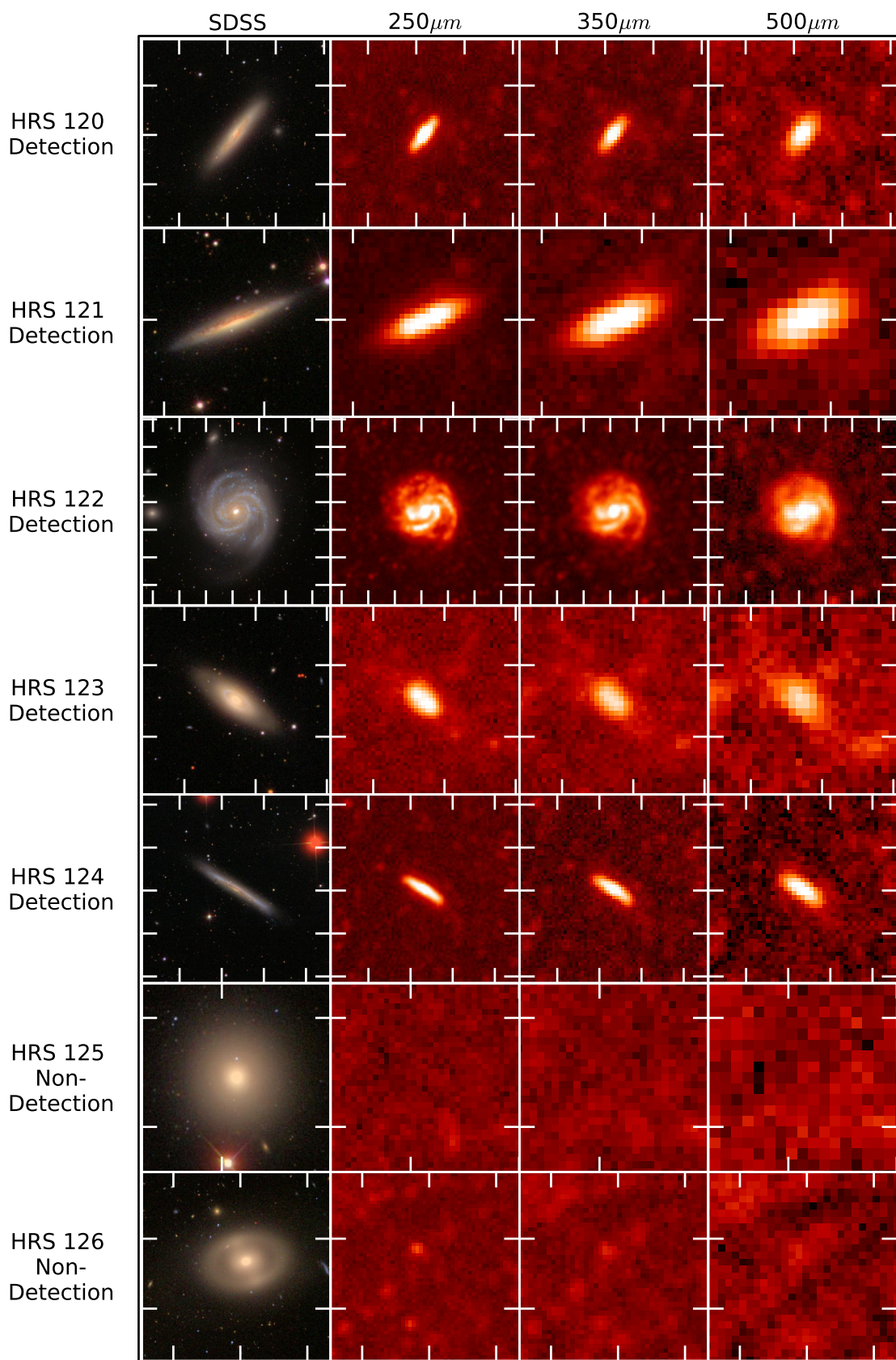


Figure A.1. (*Continued*)

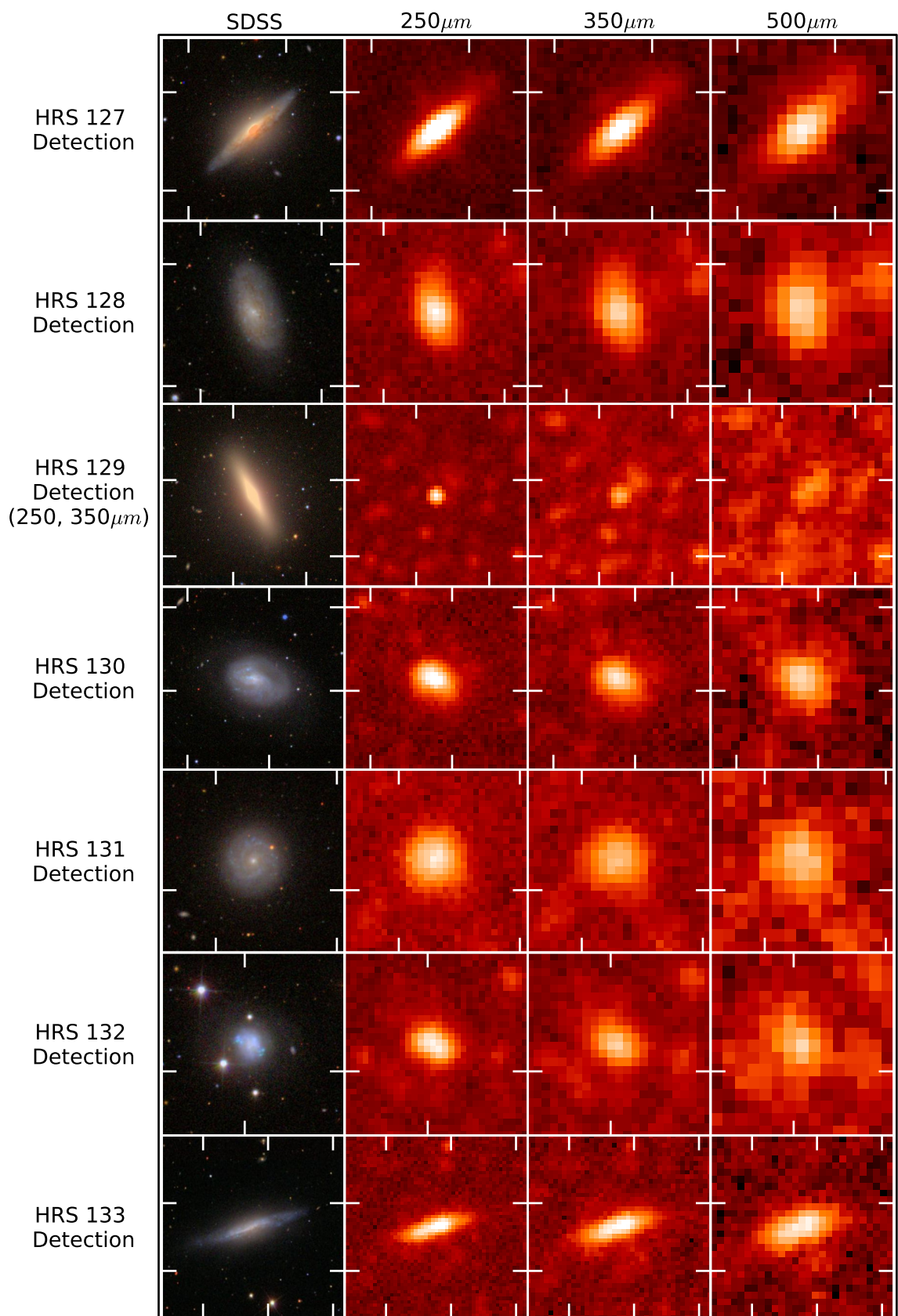


Figure A.1. (*Continued*)

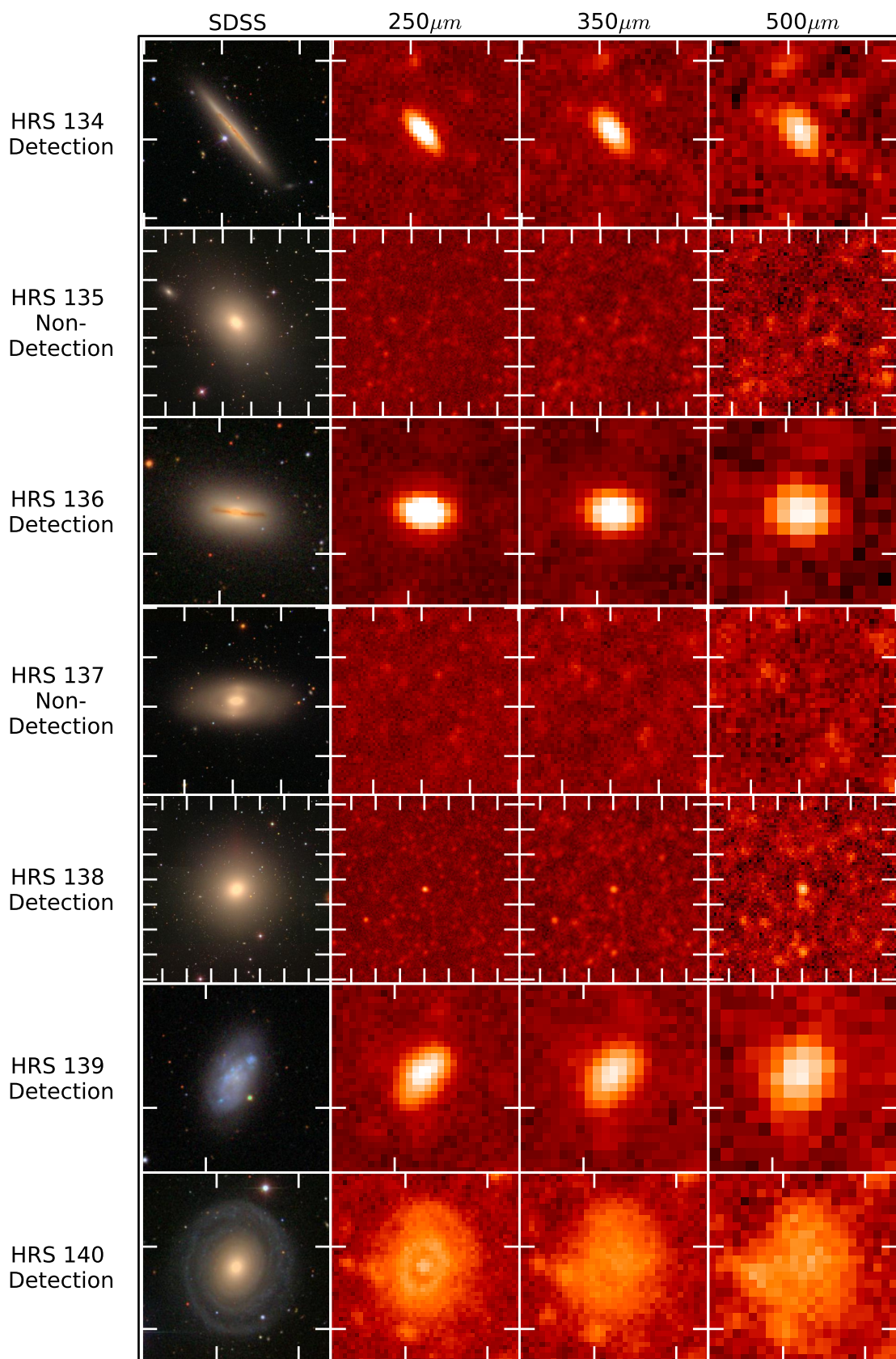


Figure A.1. (*Continued*)

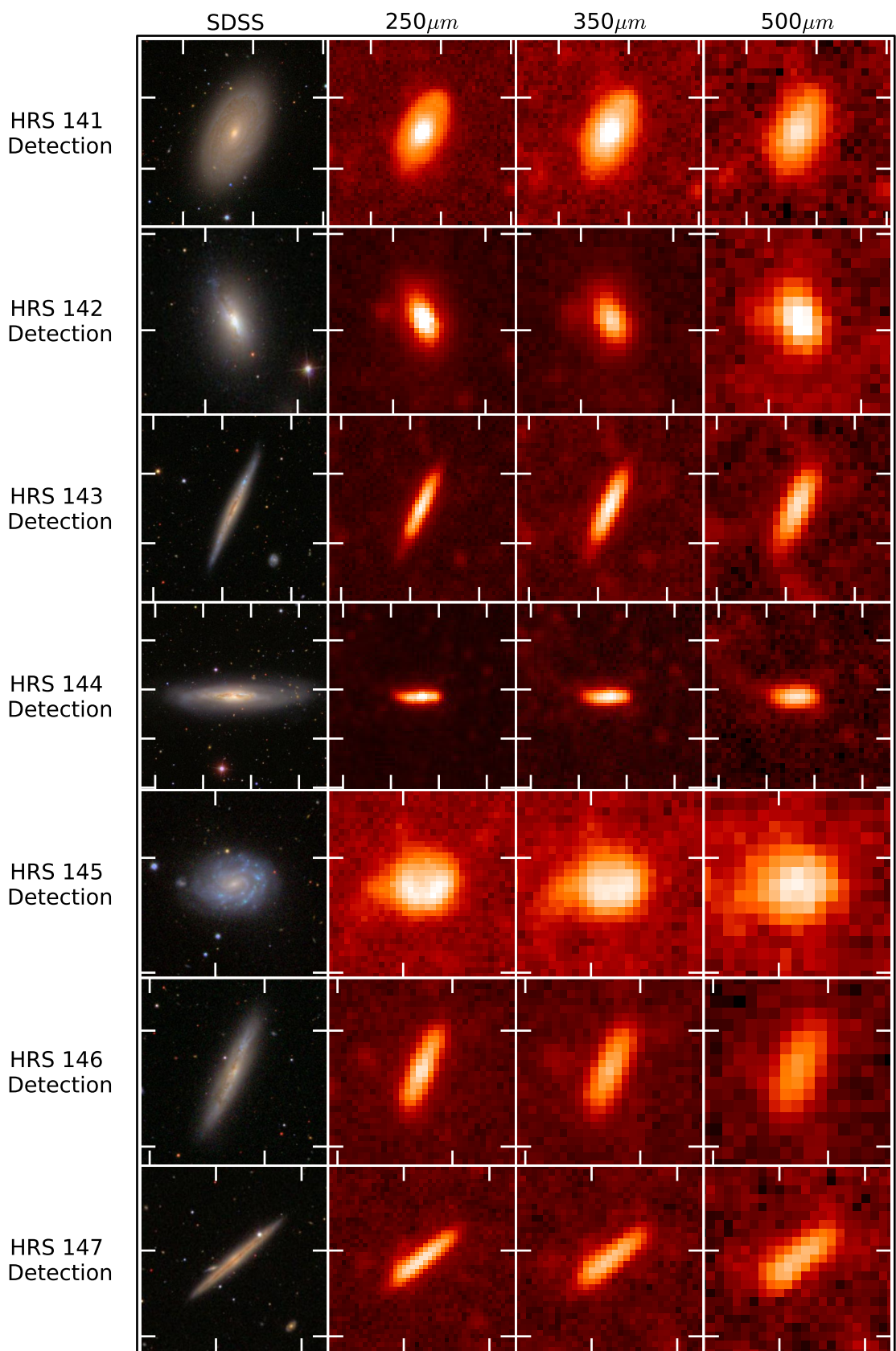


Figure A.1. (Continued)

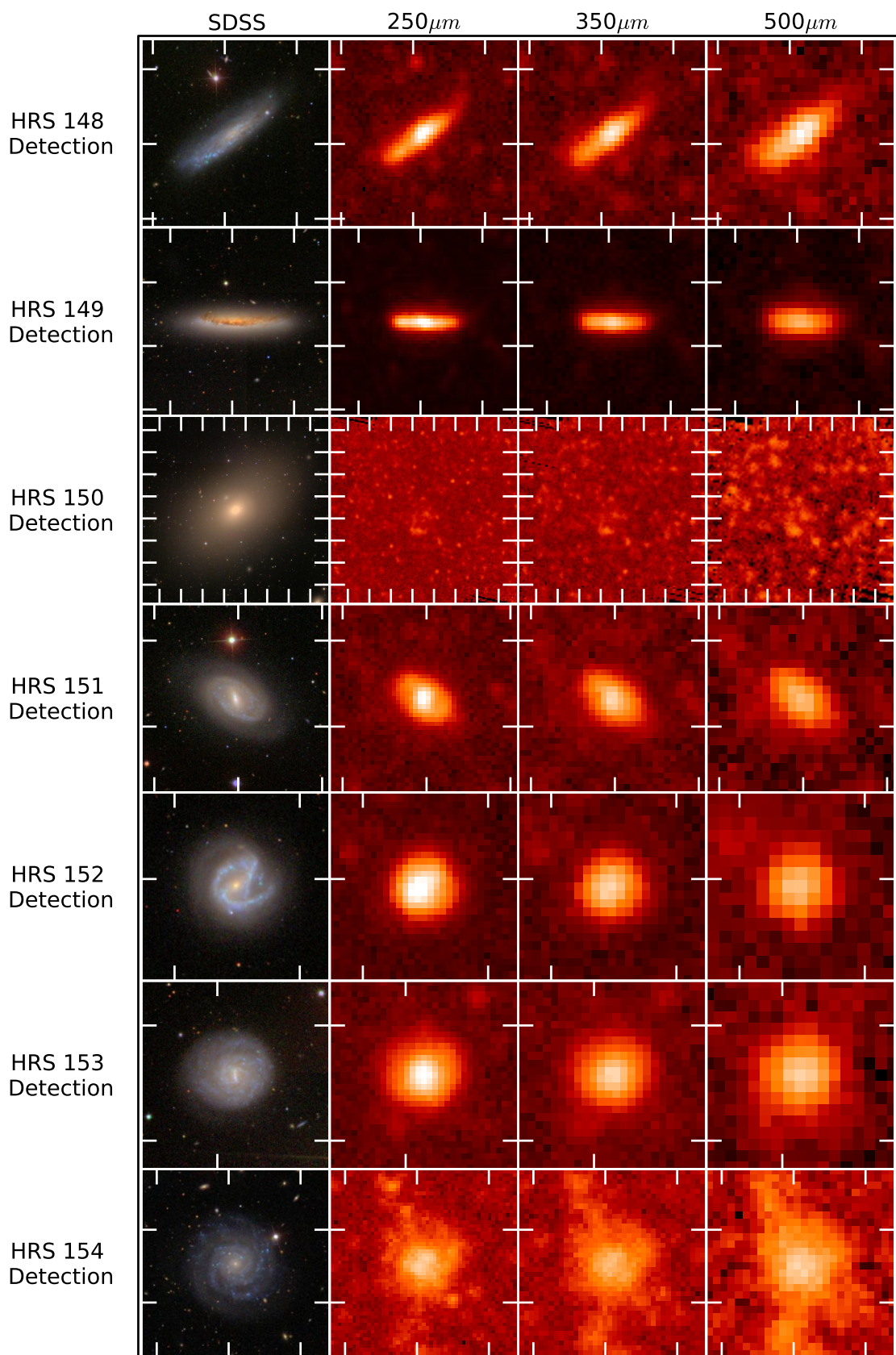


Figure A.1. (*Continued*)

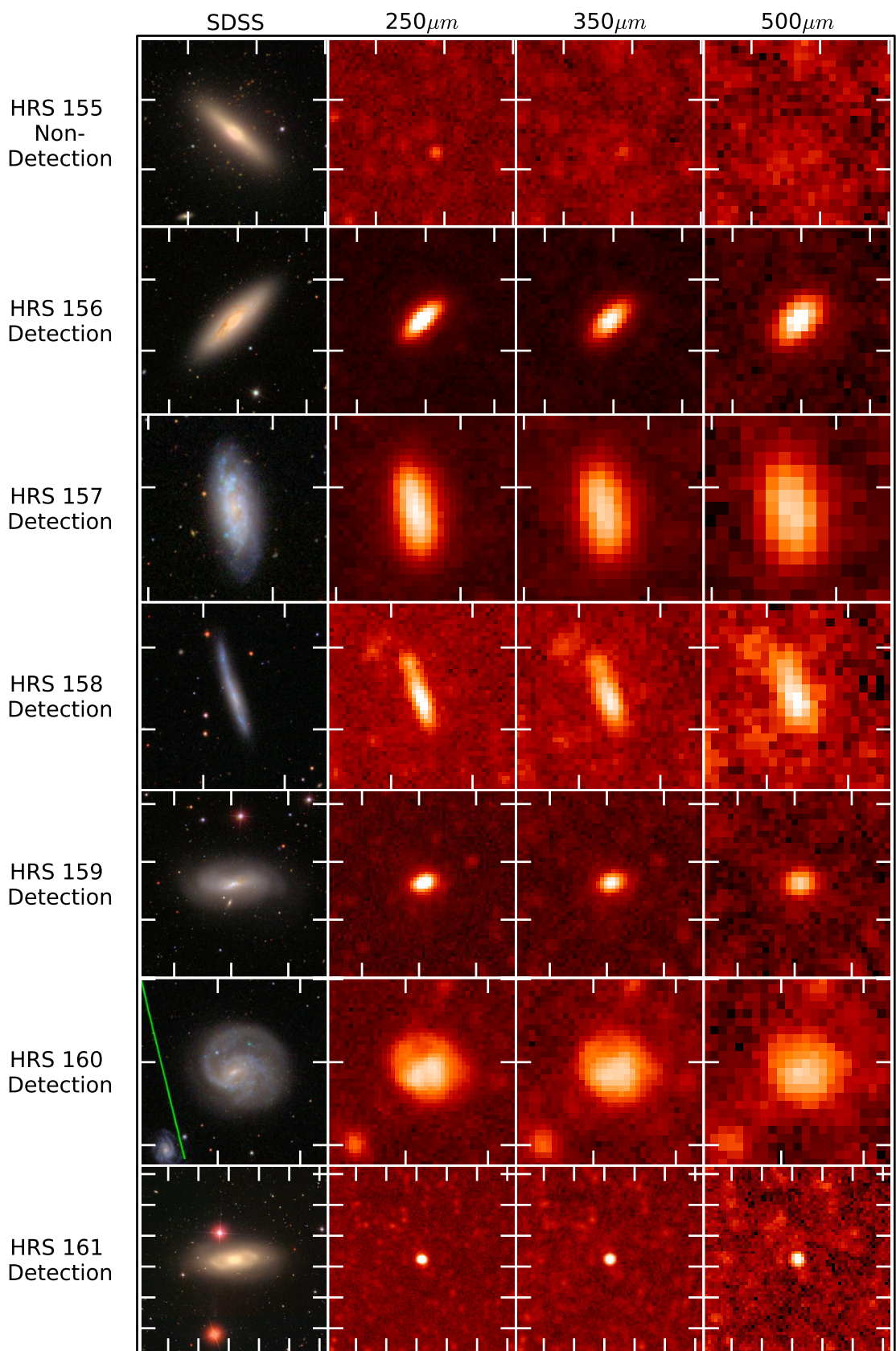


Figure A.1. (Continued)

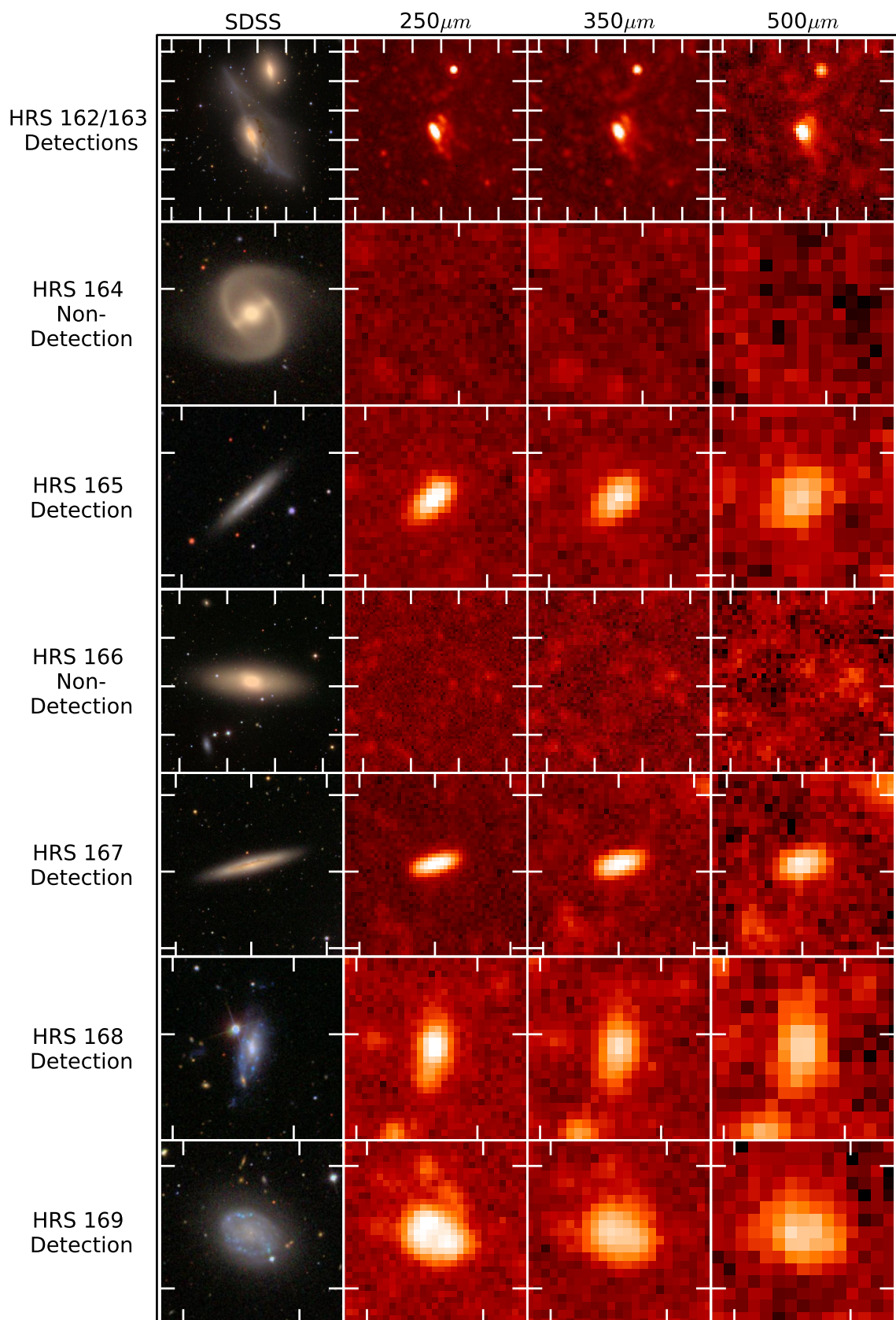


Figure A.1. (*Continued*)

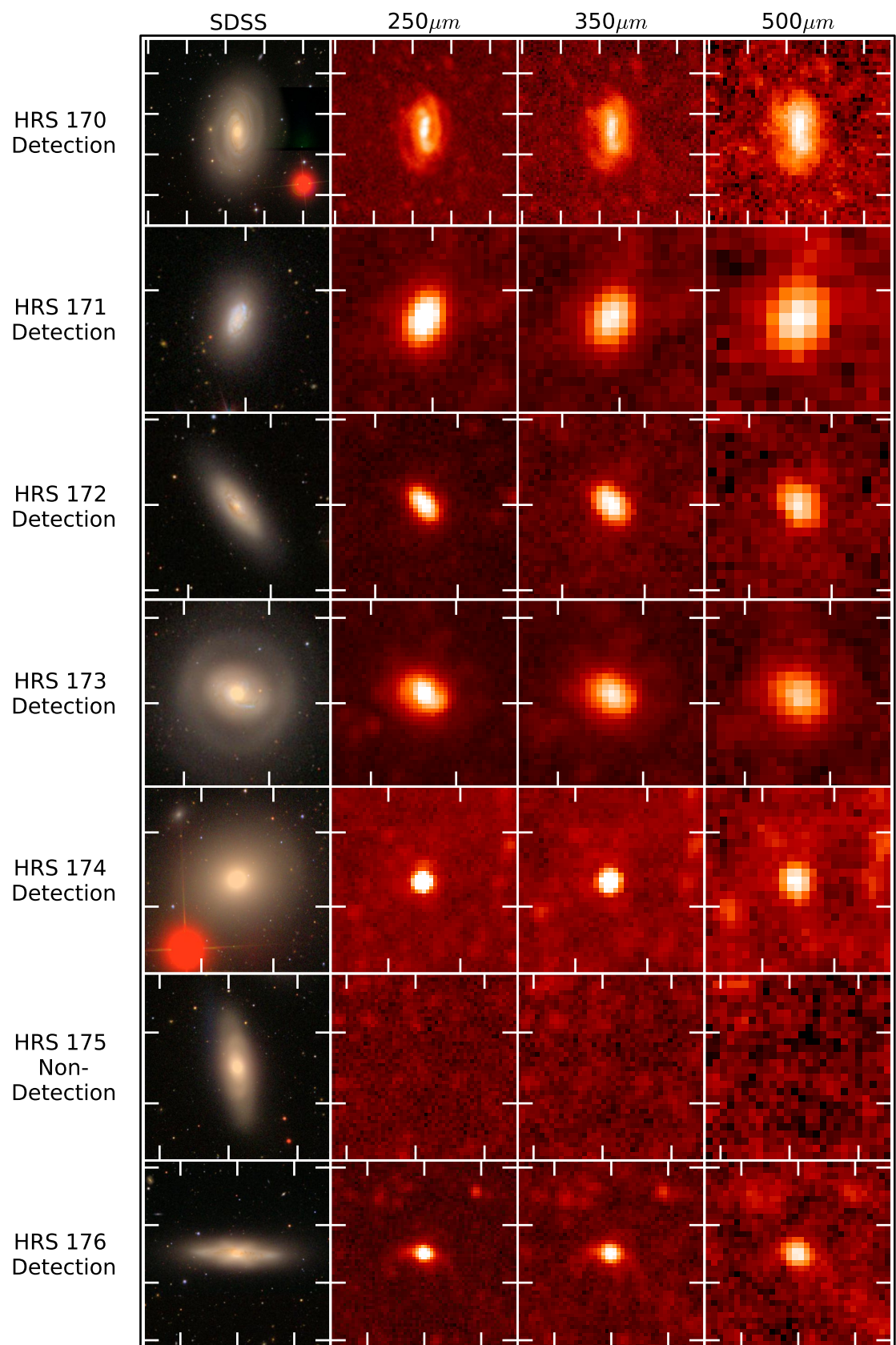


Figure A.1. (Continued)

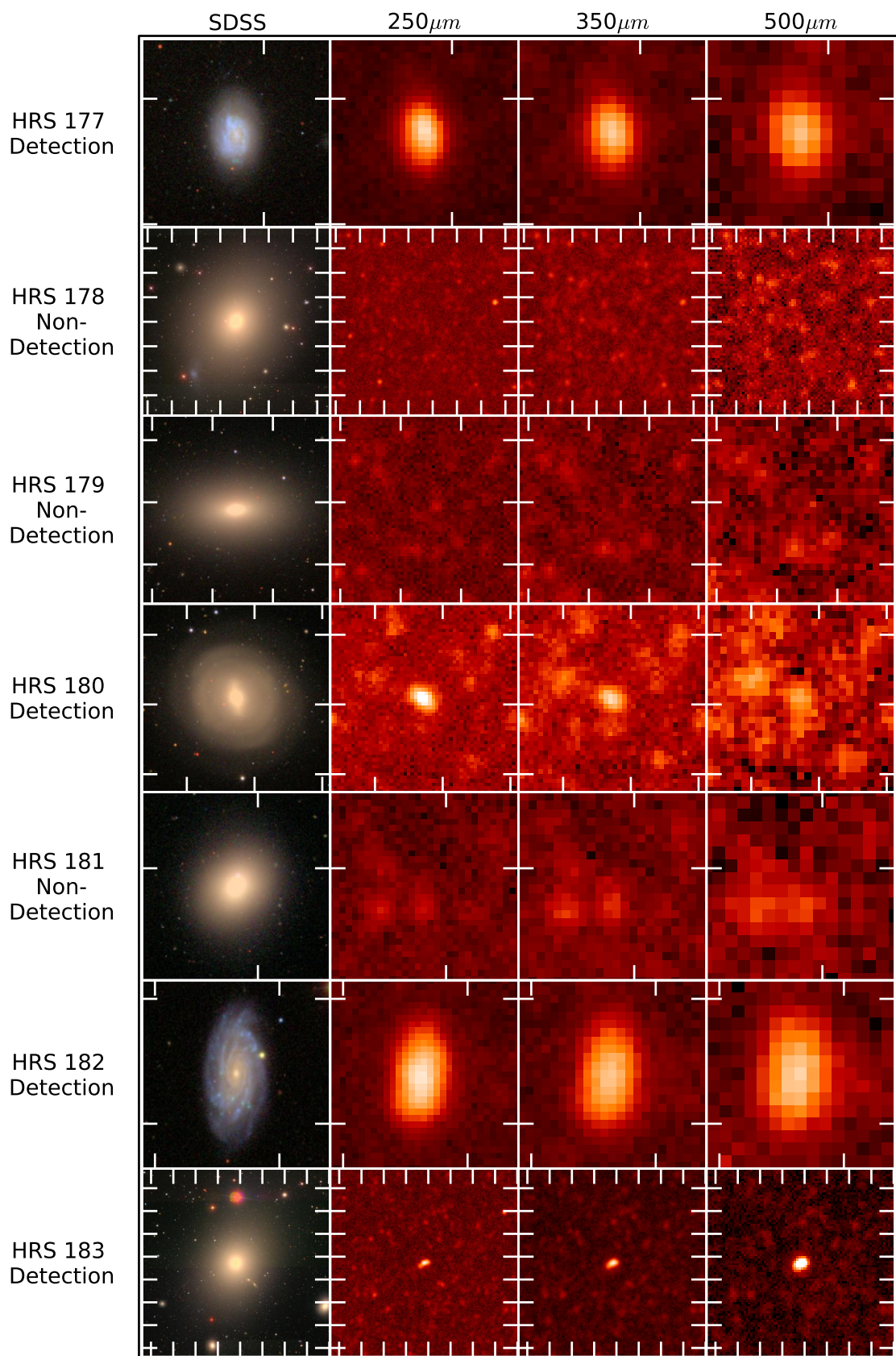


Figure A.1. (*Continued*)

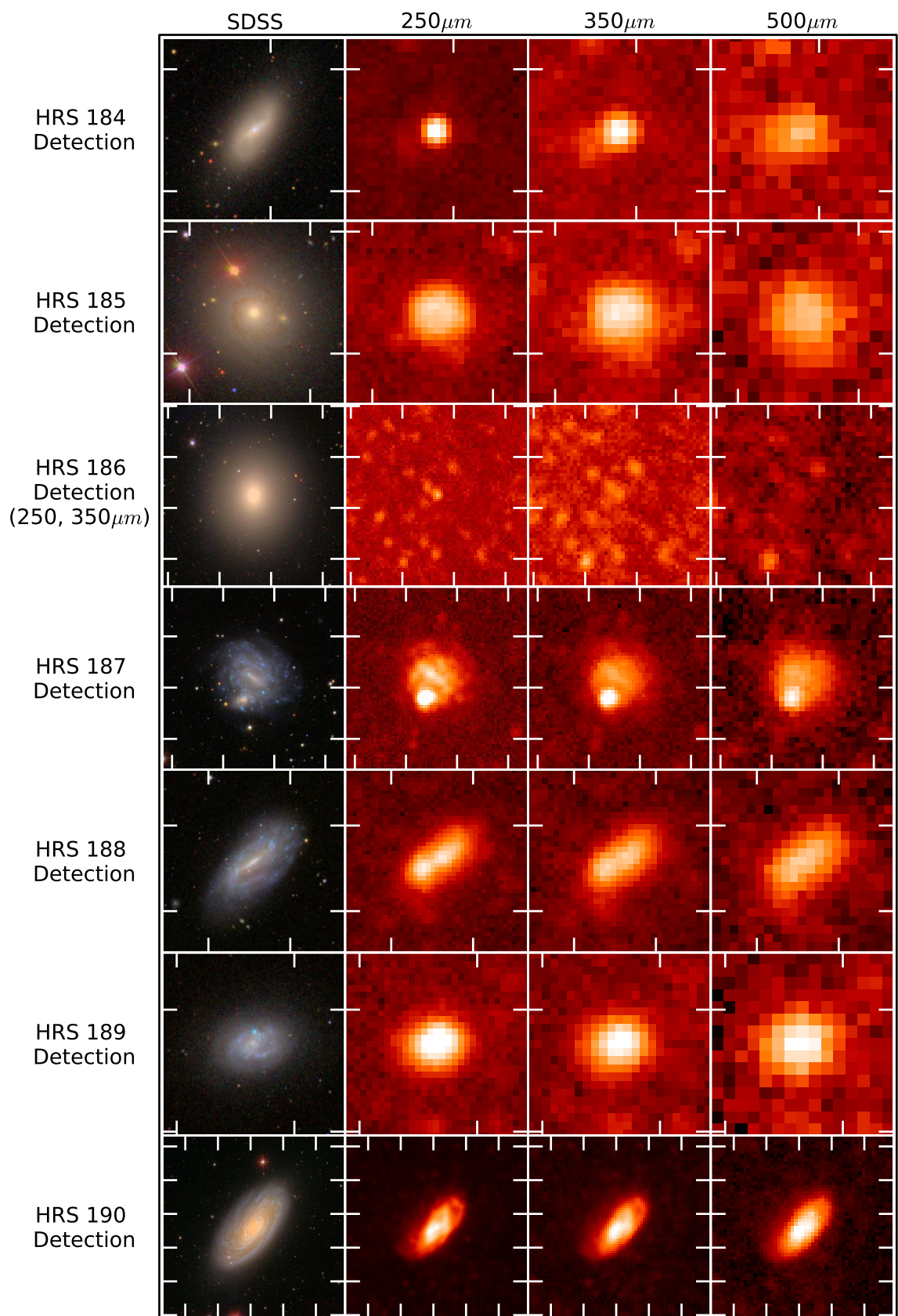


Figure A.1. (*Continued*)

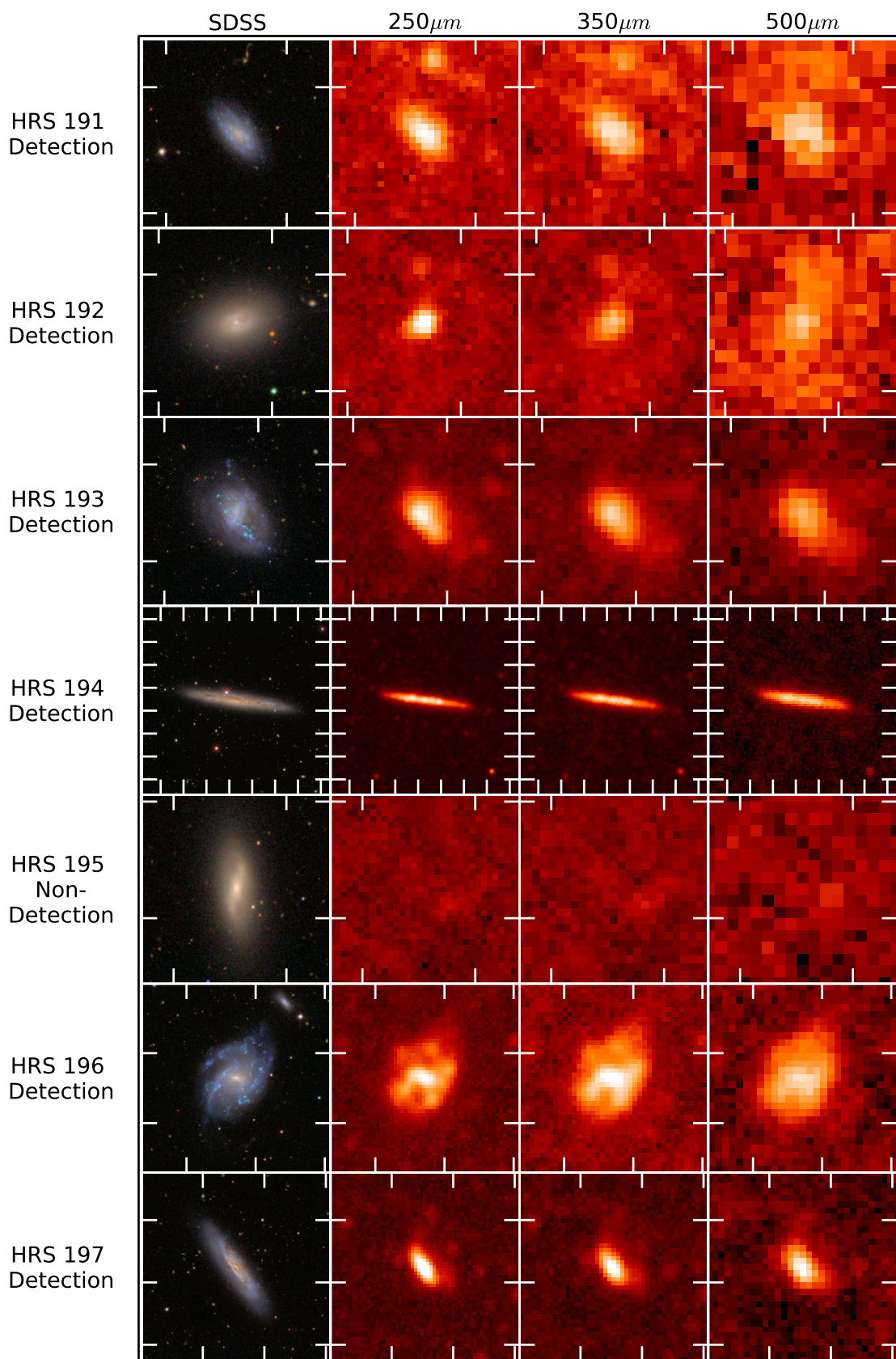


Figure A.1. (*Continued*)

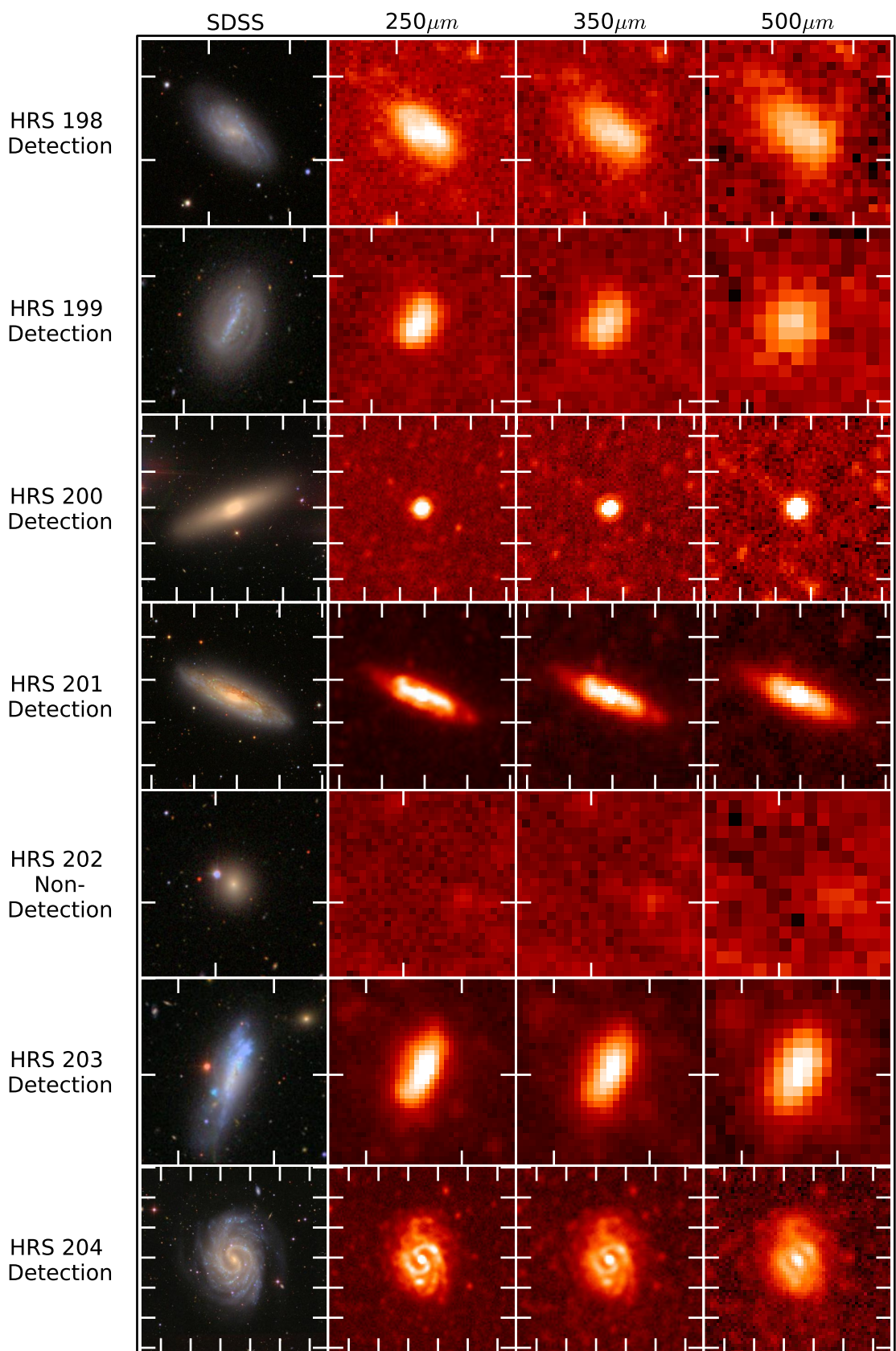


Figure A.1. (*Continued*)

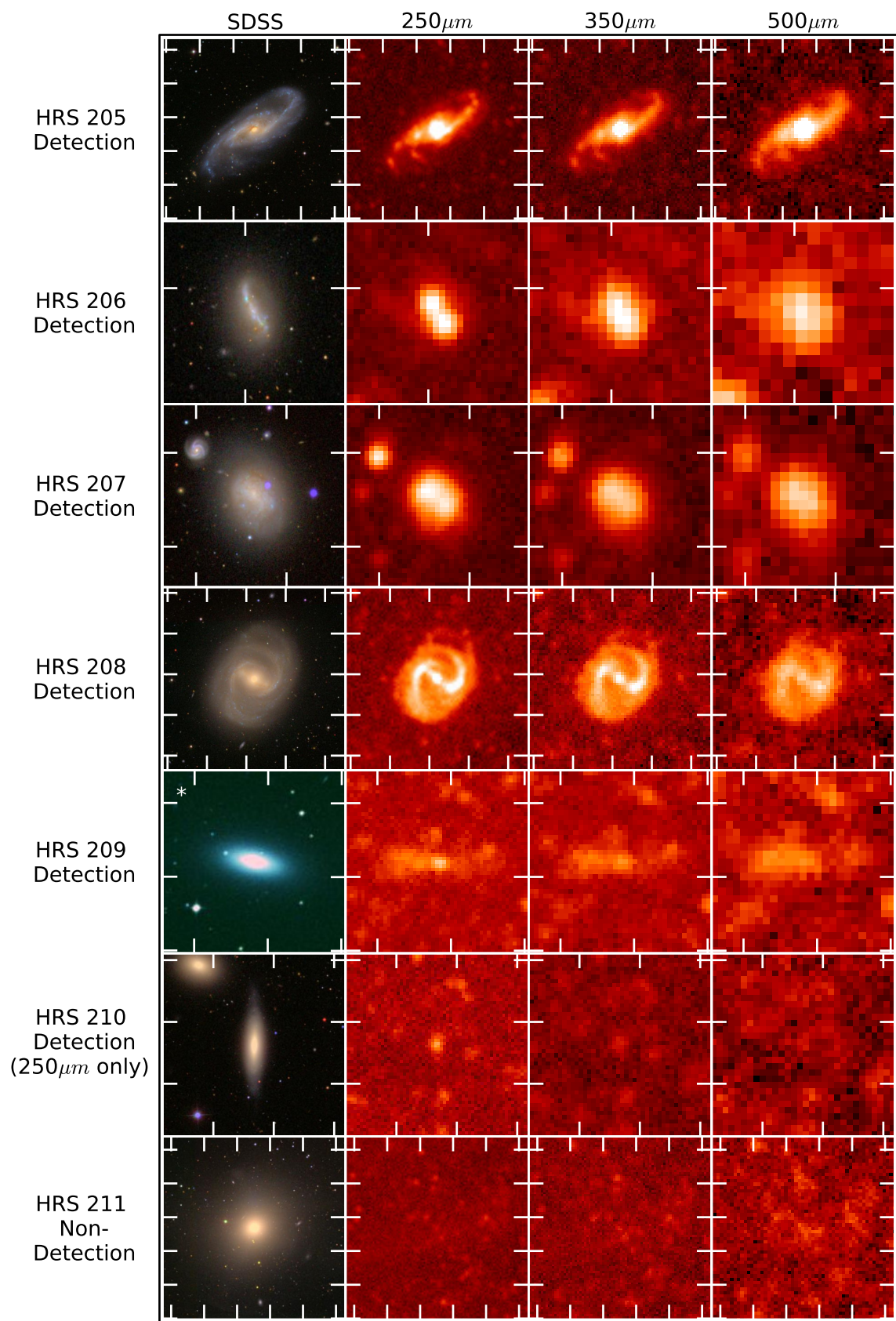


Figure A.1. (*Continued*)

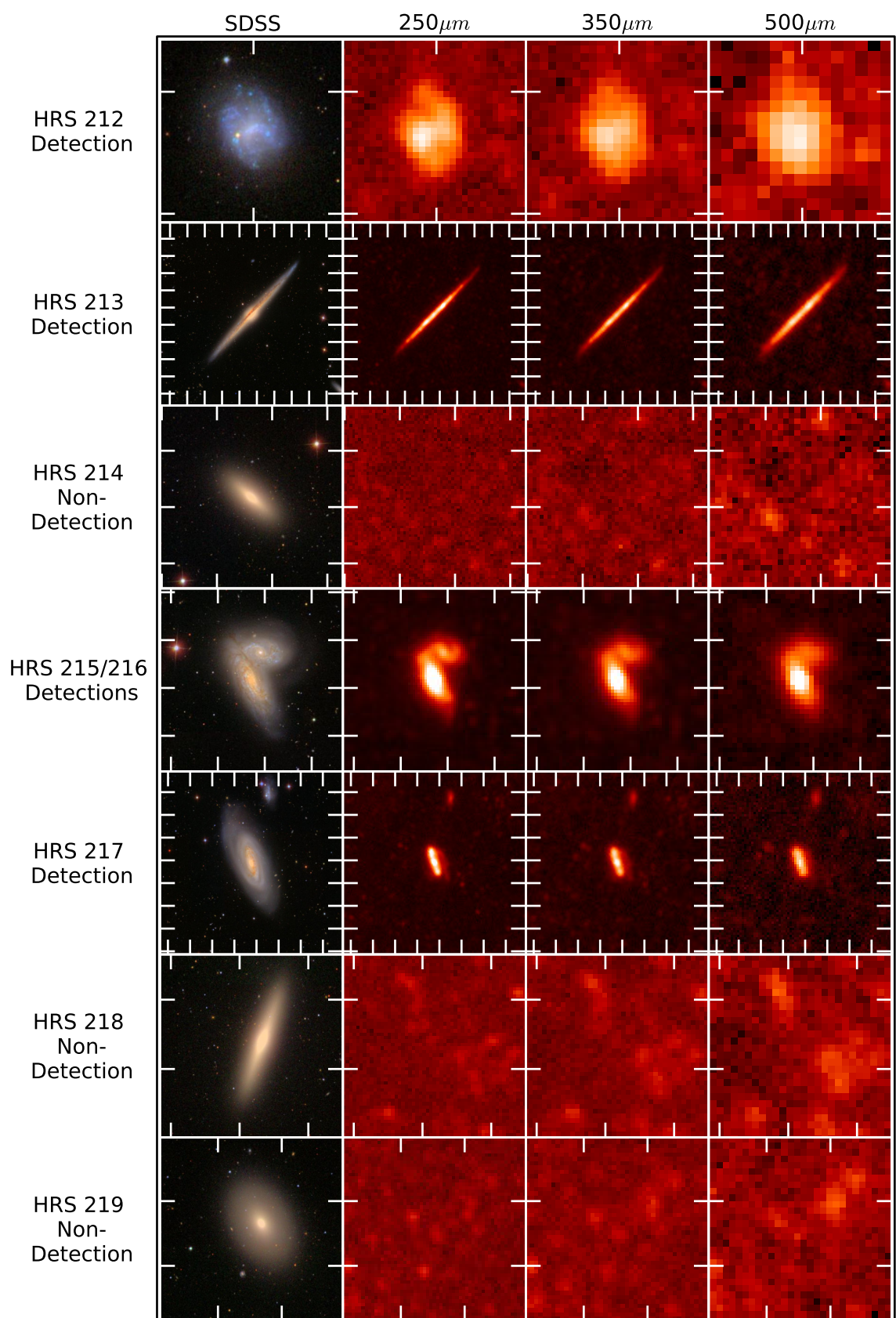


Figure A.1. (Continued)

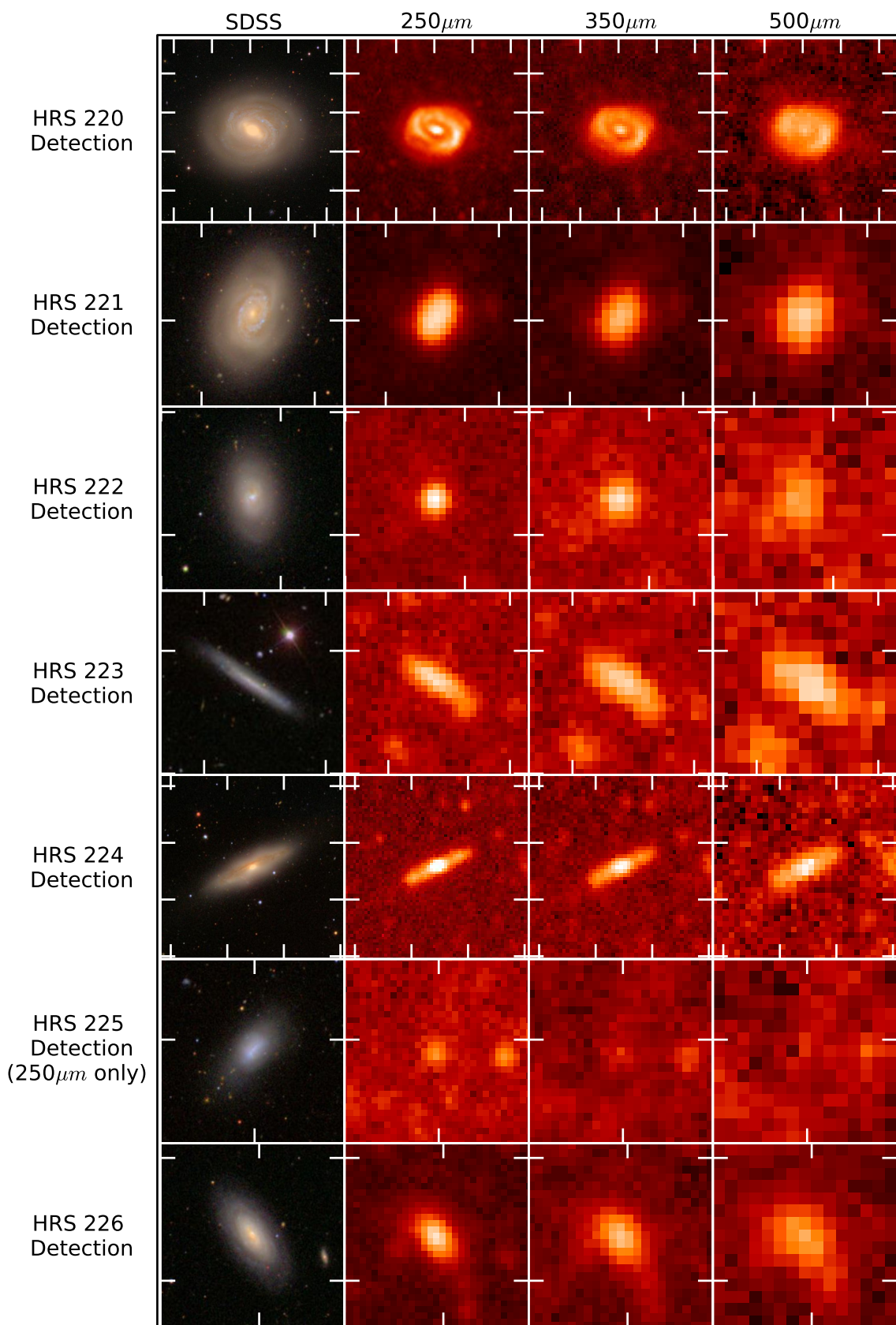


Figure A.1. (*Continued*)

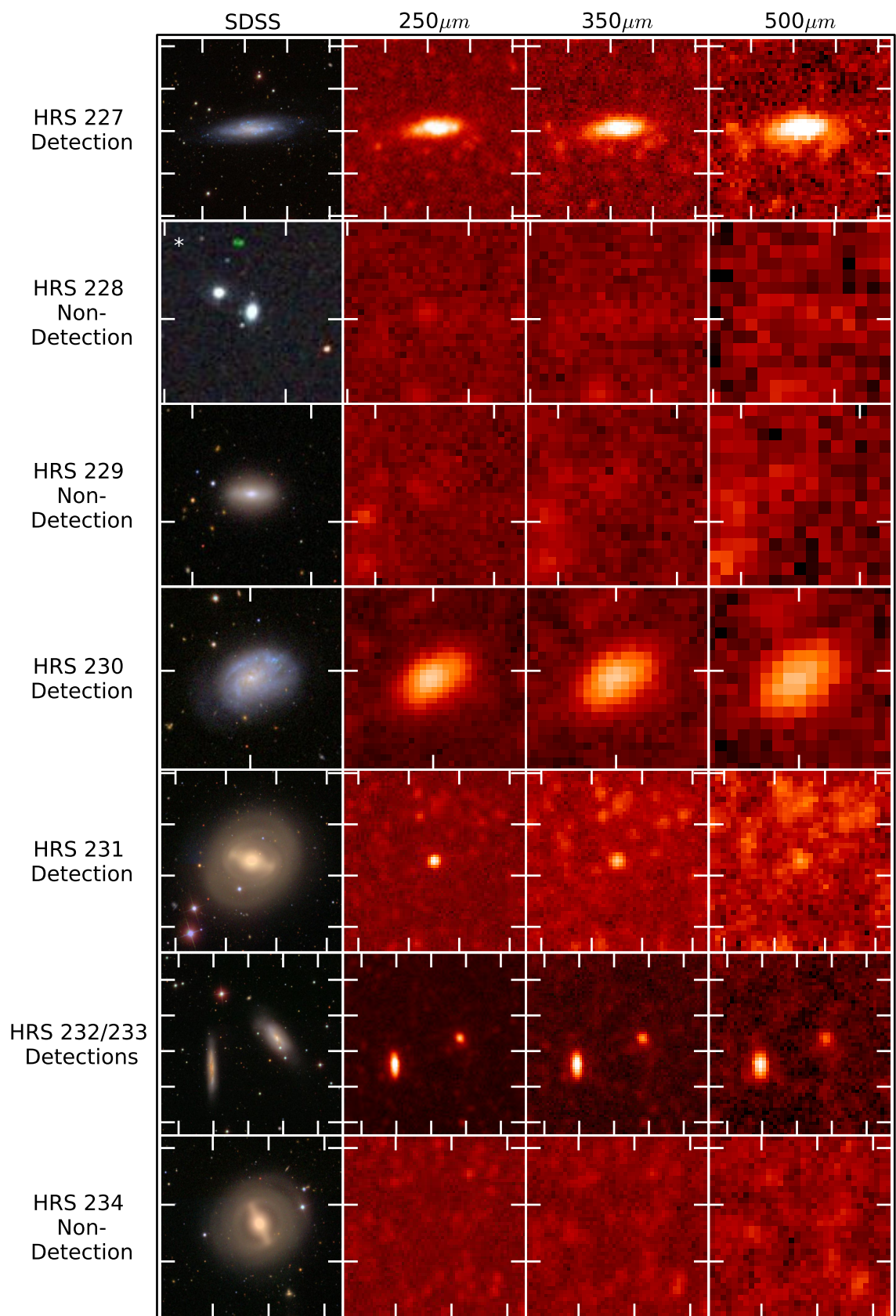


Figure A.1. (Continued)

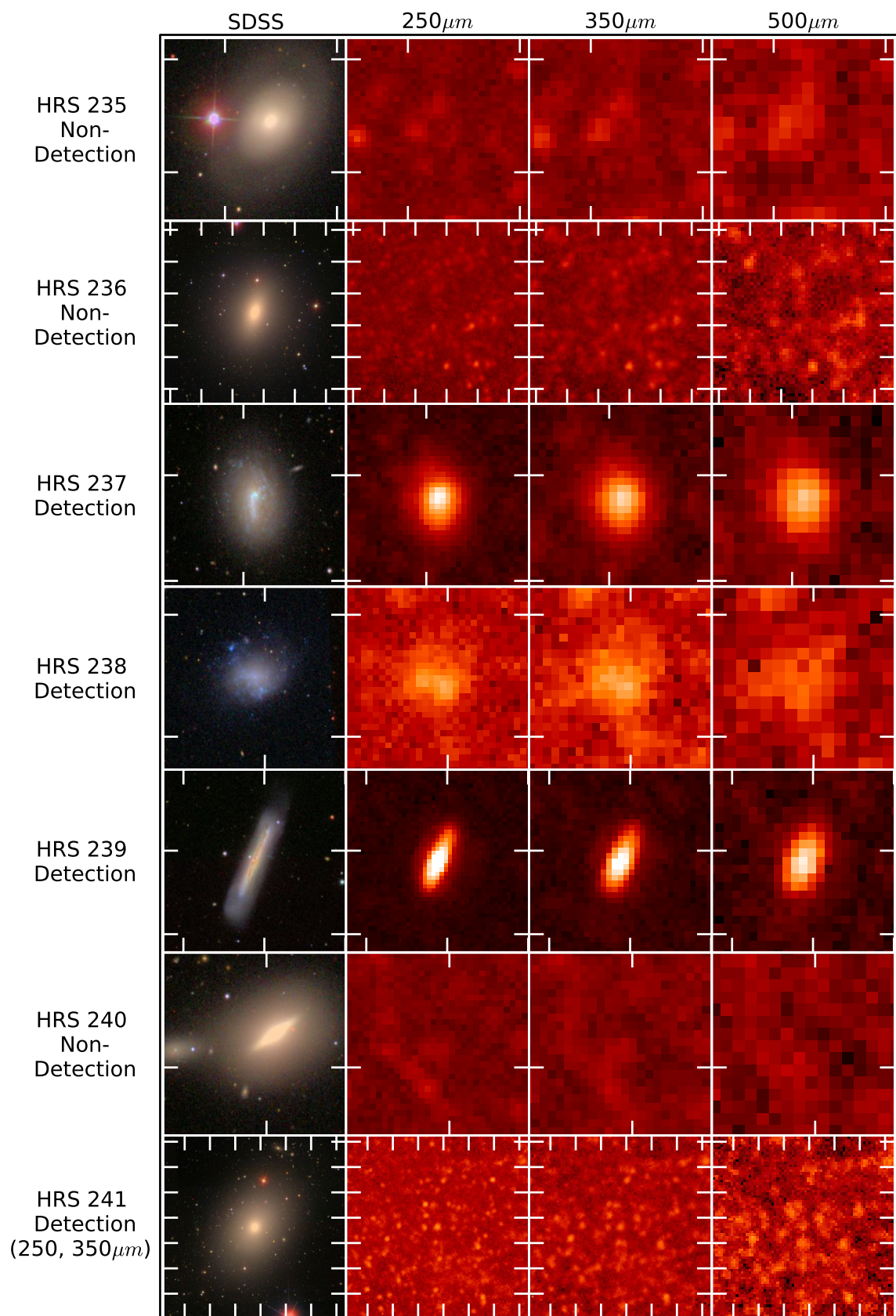


Figure A.1. (*Continued*)

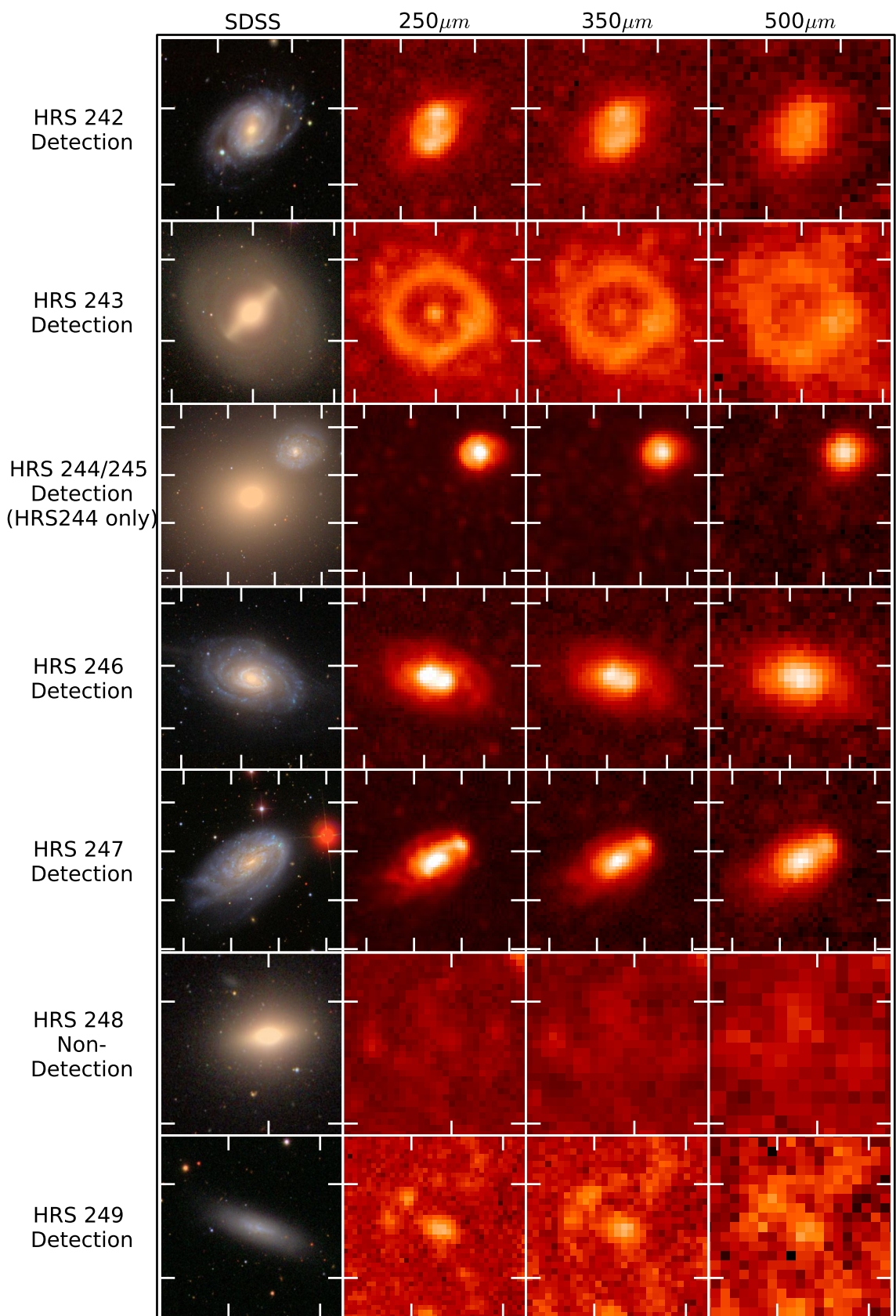


Figure A.1. (Continued)

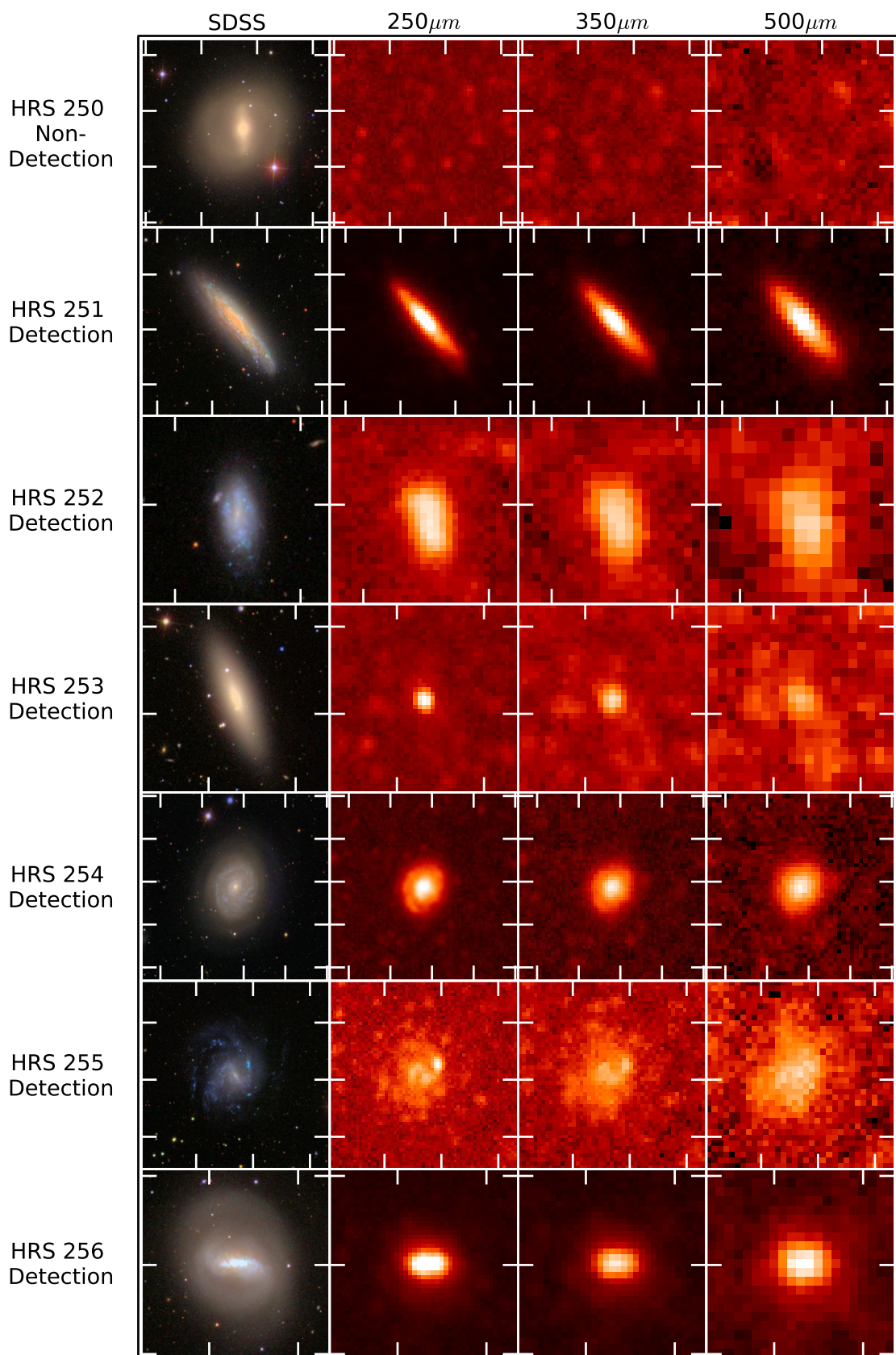


Figure A.1. (*Continued*)

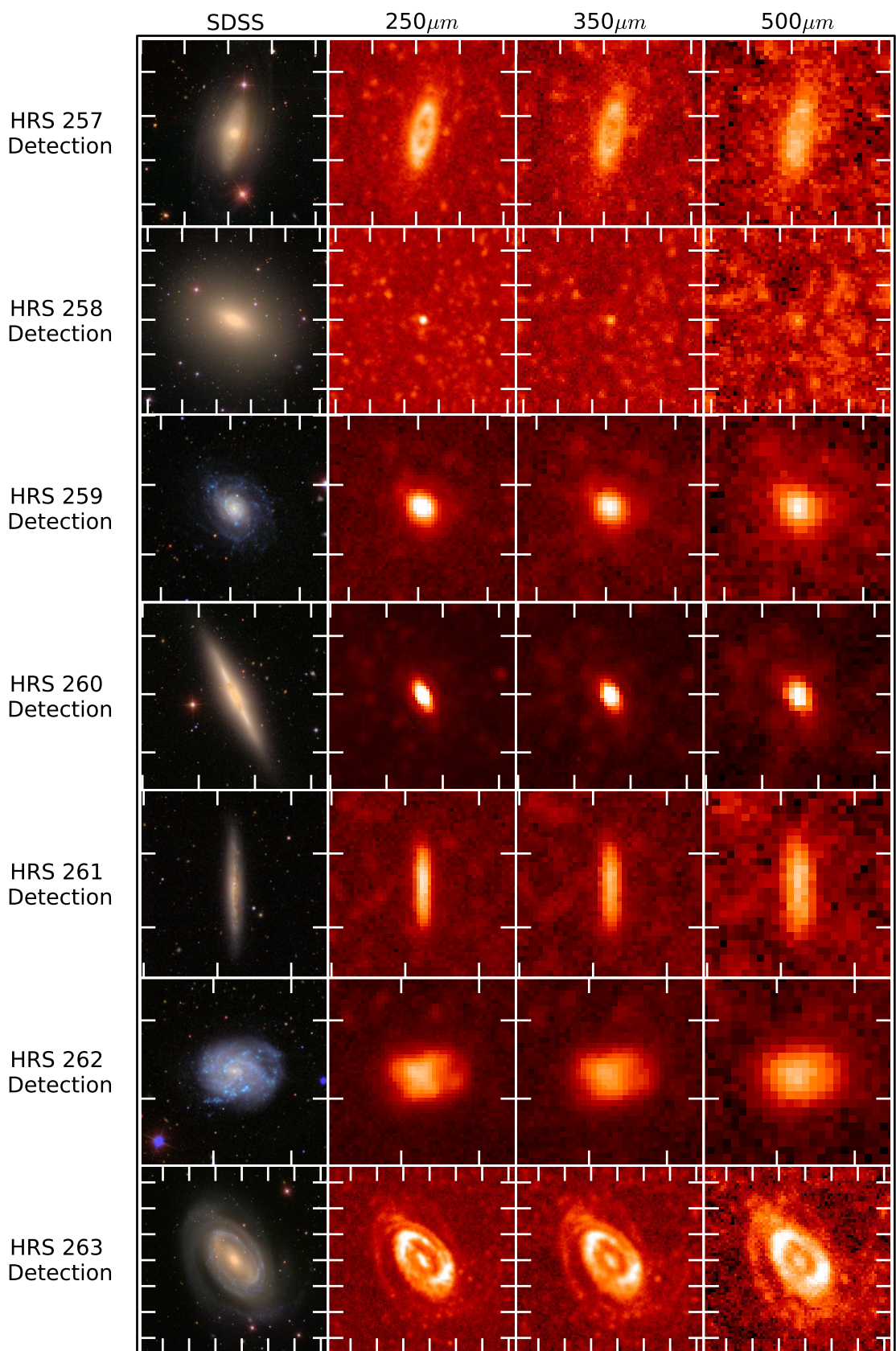


Figure A.1. (*Continued*)

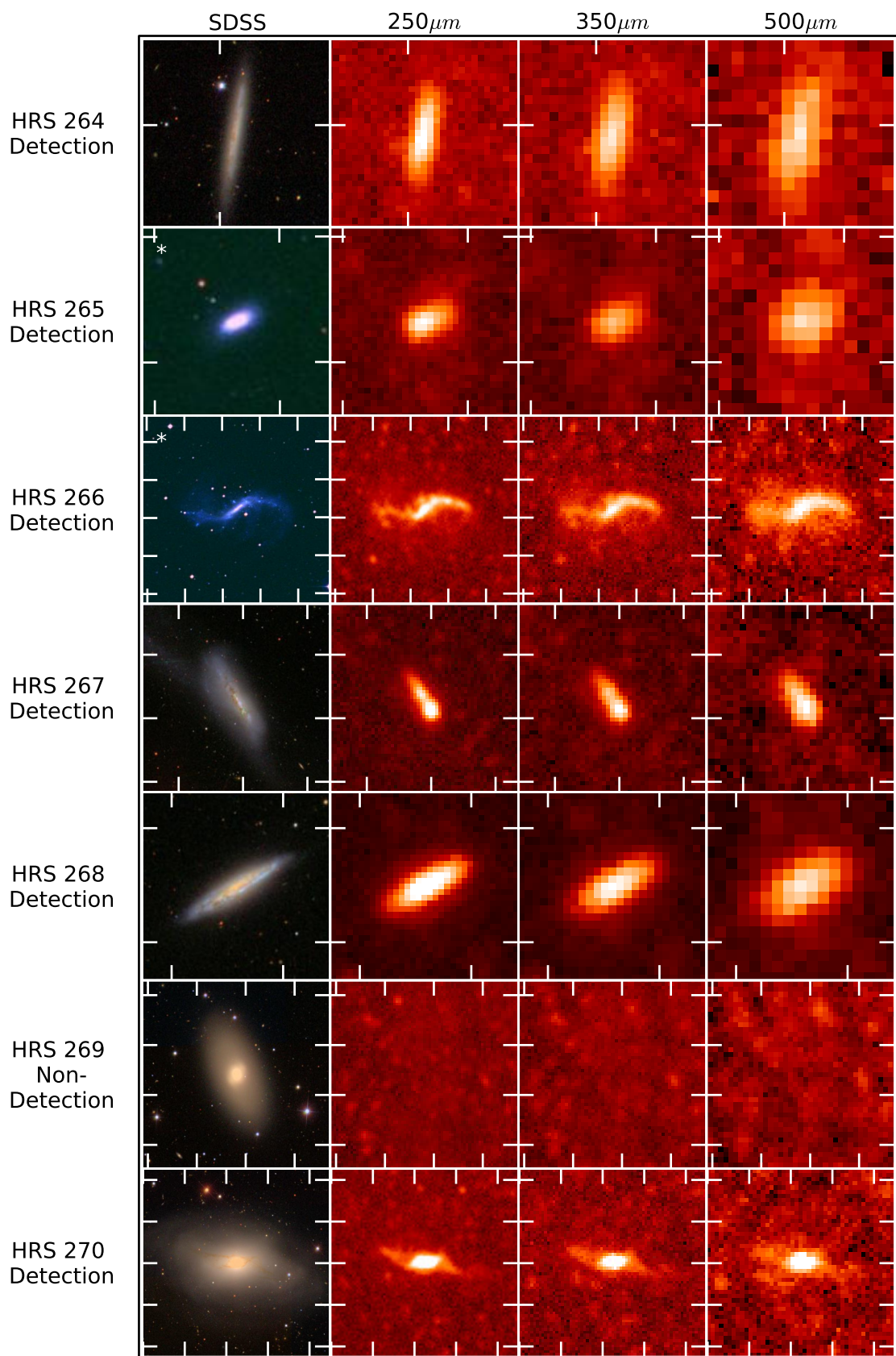


Figure A.1. (*Continued*)

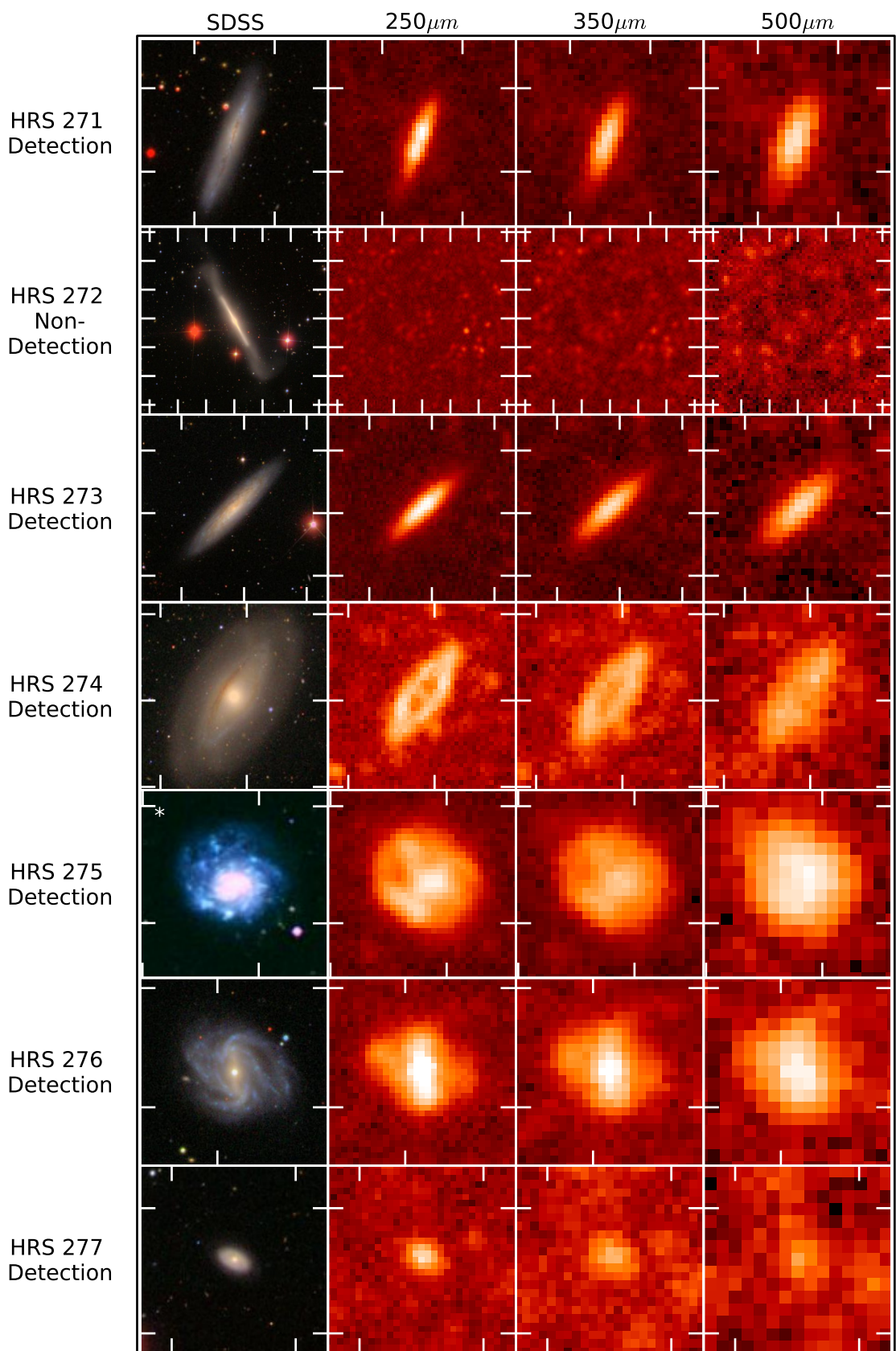


Figure A.1. (*Continued*)

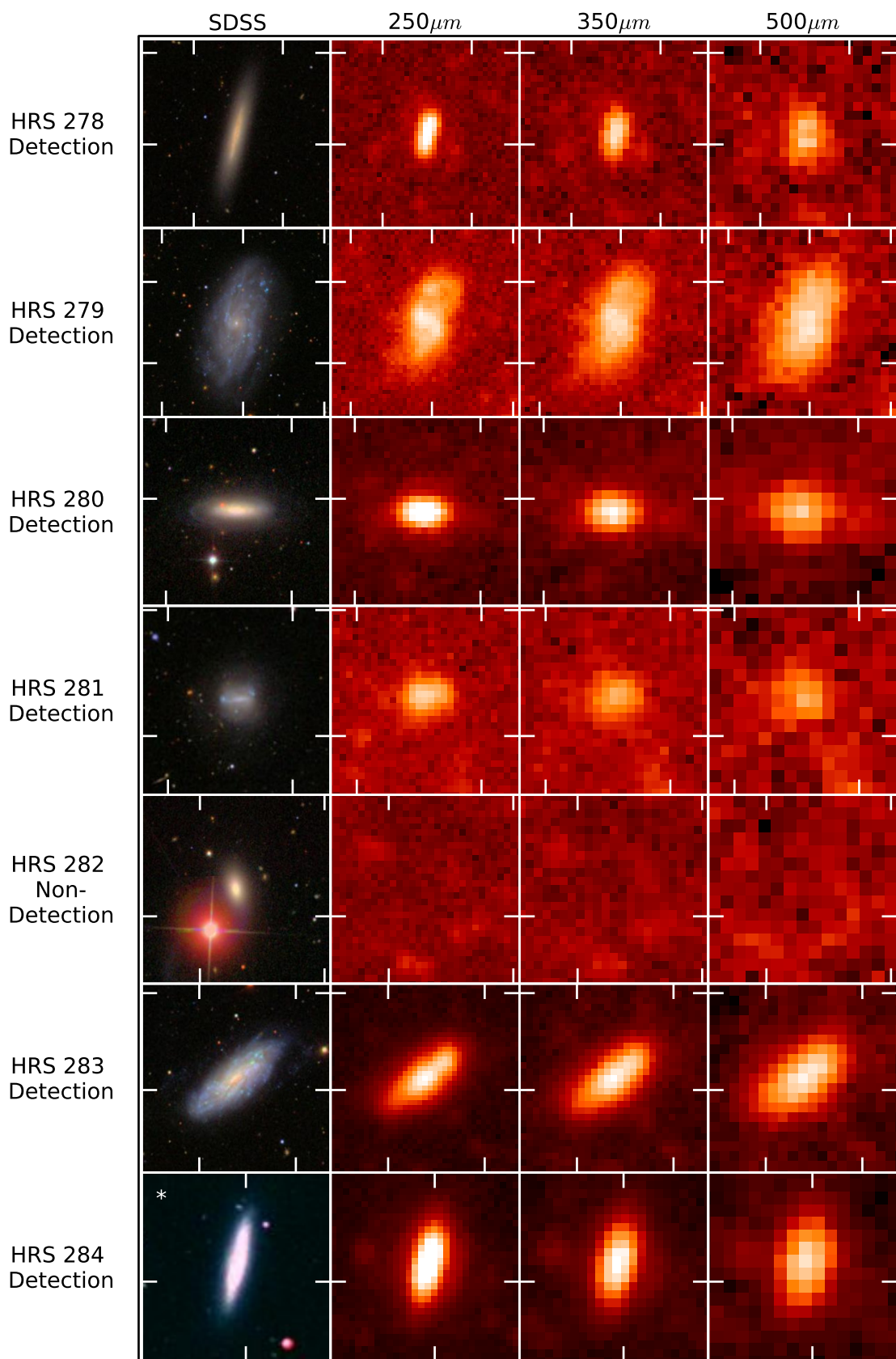


Figure A.1. (*Continued*)

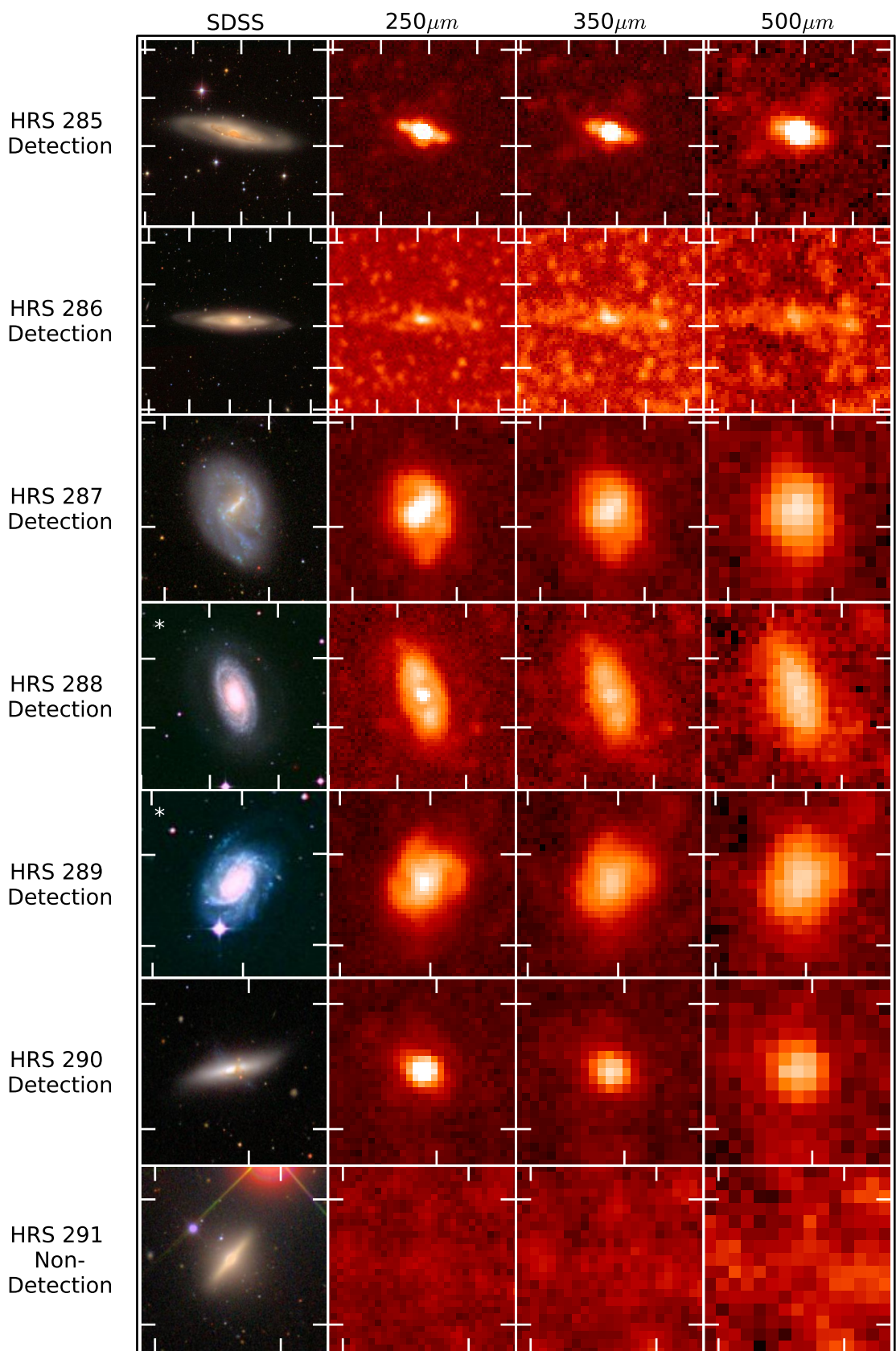


Figure A.1. (Continued)

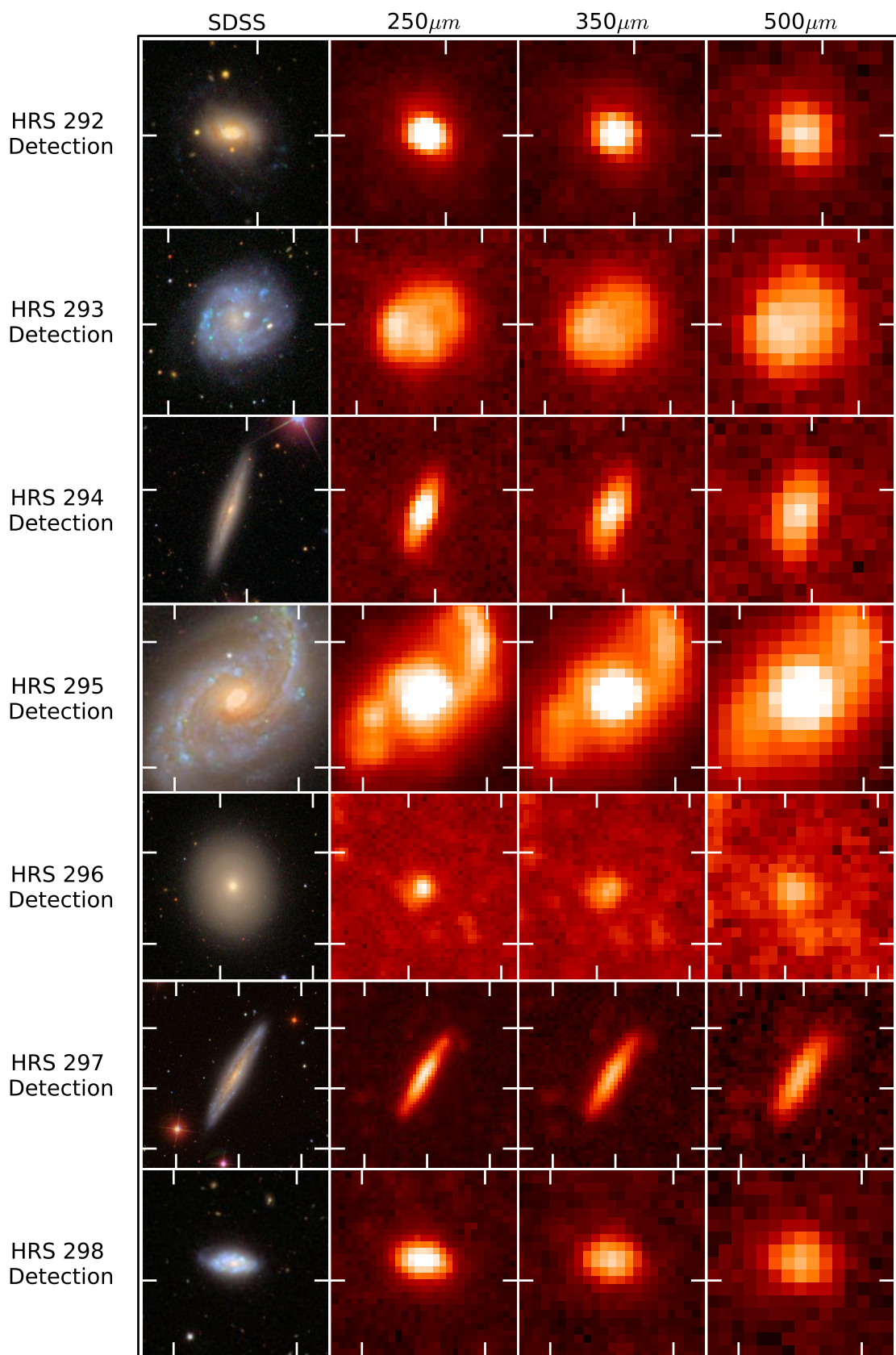


Figure A.1. (*Continued*)

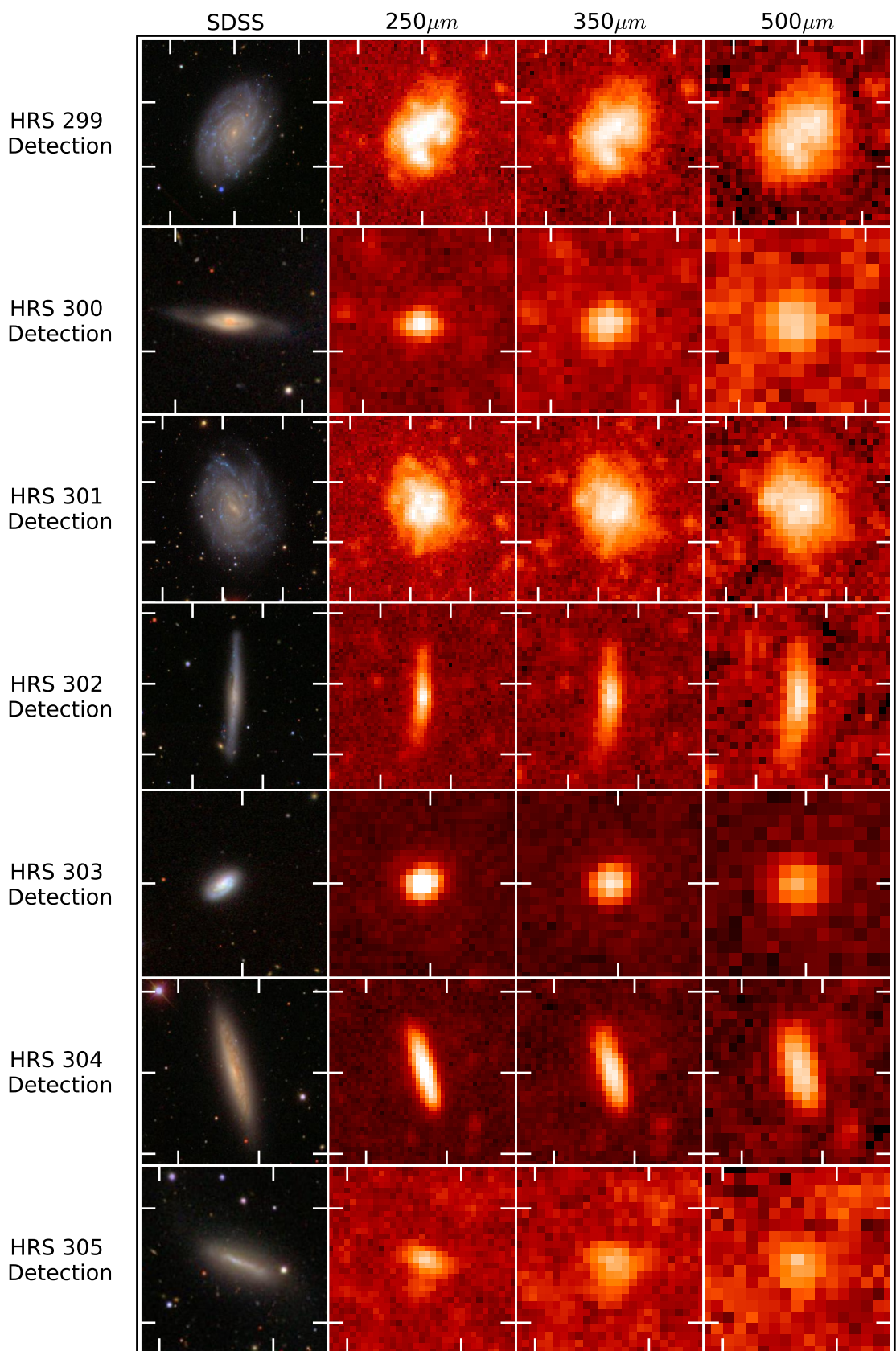


Figure A.1. (Continued)

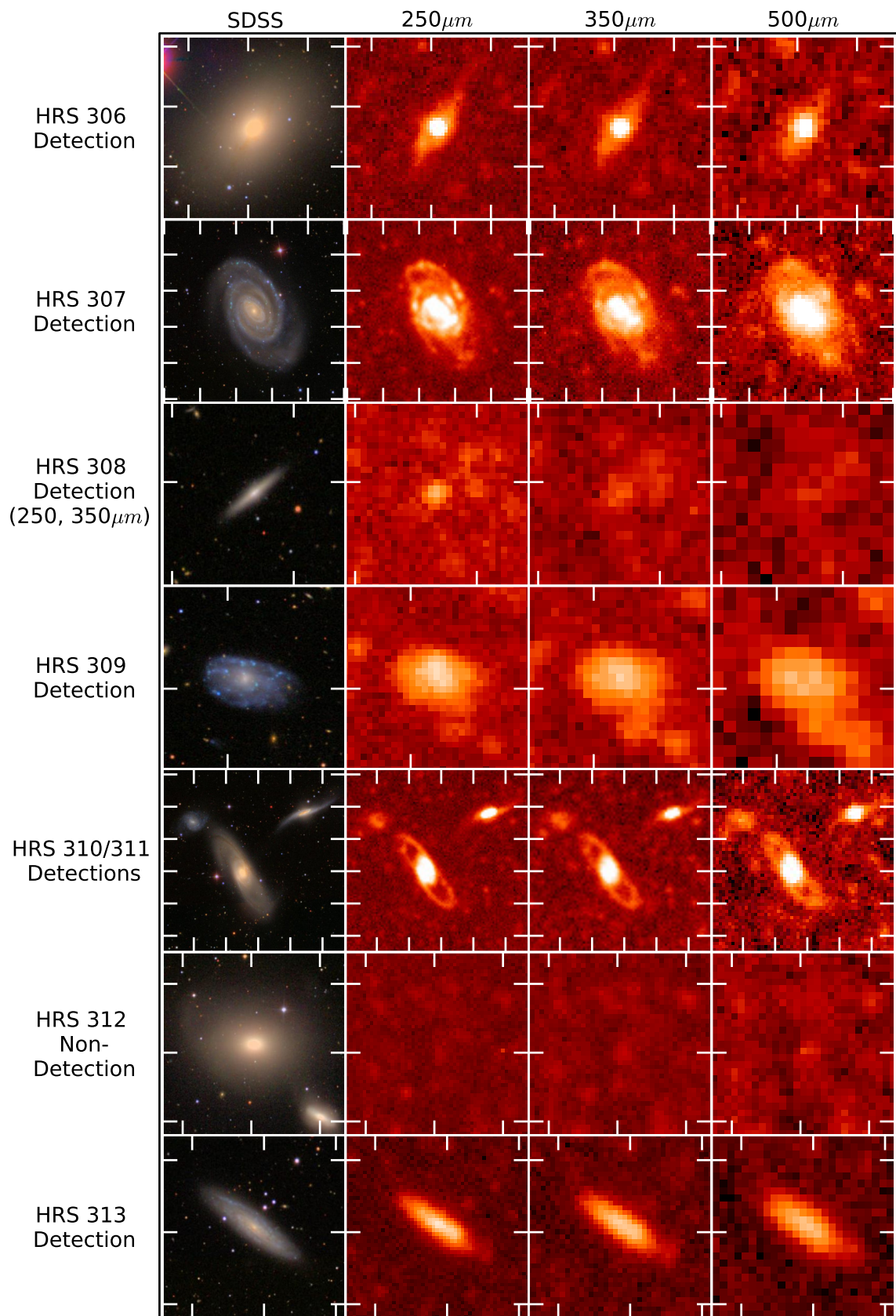


Figure A.1. (Continued)

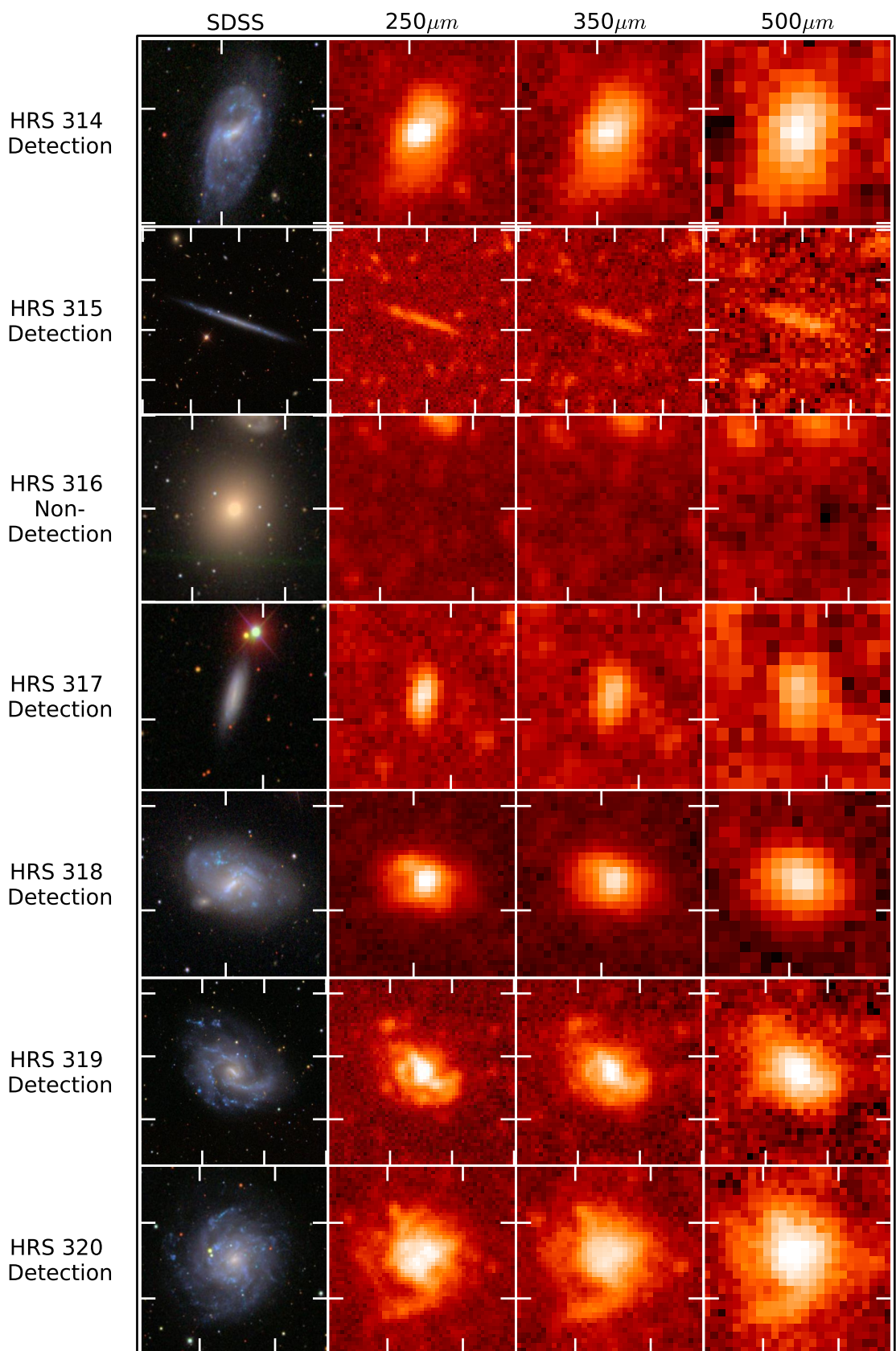


Figure A.1. (*Continued*)

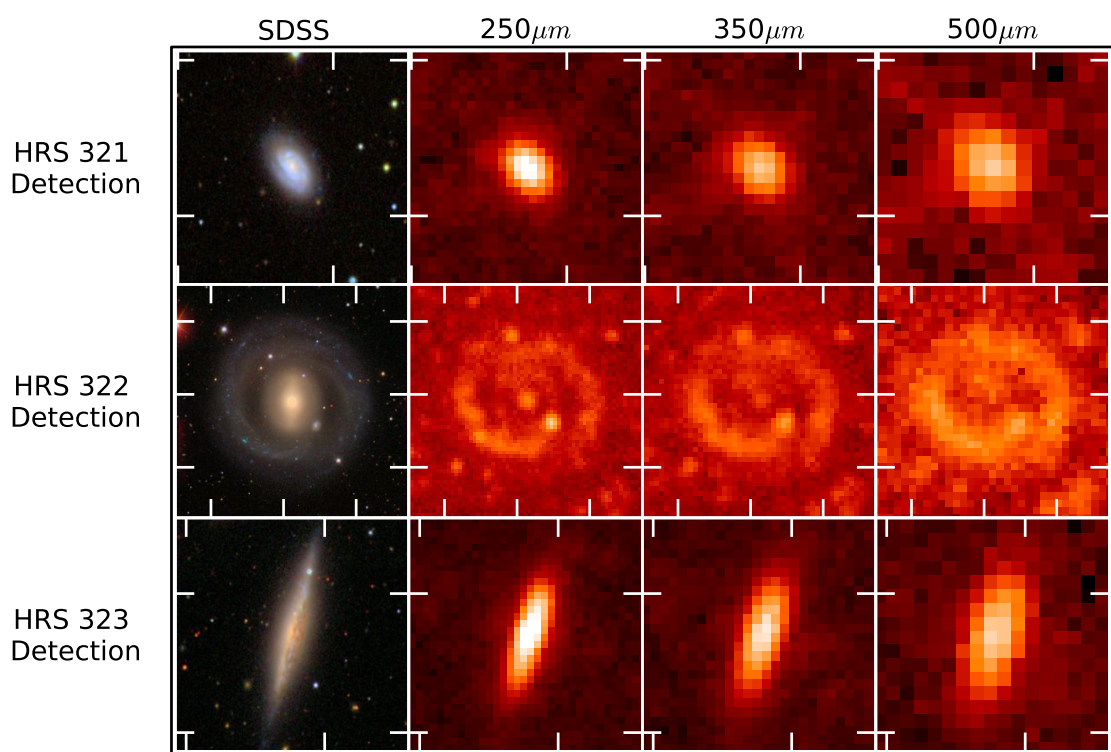


Figure A.1. (*Continued*)

APPENDIX B

BAR GRAPHS COMPARING OBJECT FLUXES FOR TESTED PIPELINES

This appendix contains bar graphs comparing the global flux measured for observations that have been reduced using different pipeline methods in the SAG2 map making review (see Section 2.5.1). The pipeline used is given in the legends on the plots, as explained in Section 2.5.1 and the bars labelled with ‘_mad’ indicate the map was made using MADmap instead of the Naïve mapper. As M100 was accidentally observed twice Figure B.1 shows the percentage difference in the measured flux between the two observations for the different pipelines. Figures B.2 to B.6 show the percentage difference between the global flux and the reference flux from the BRIGADE pipeline (if available with MADmap).

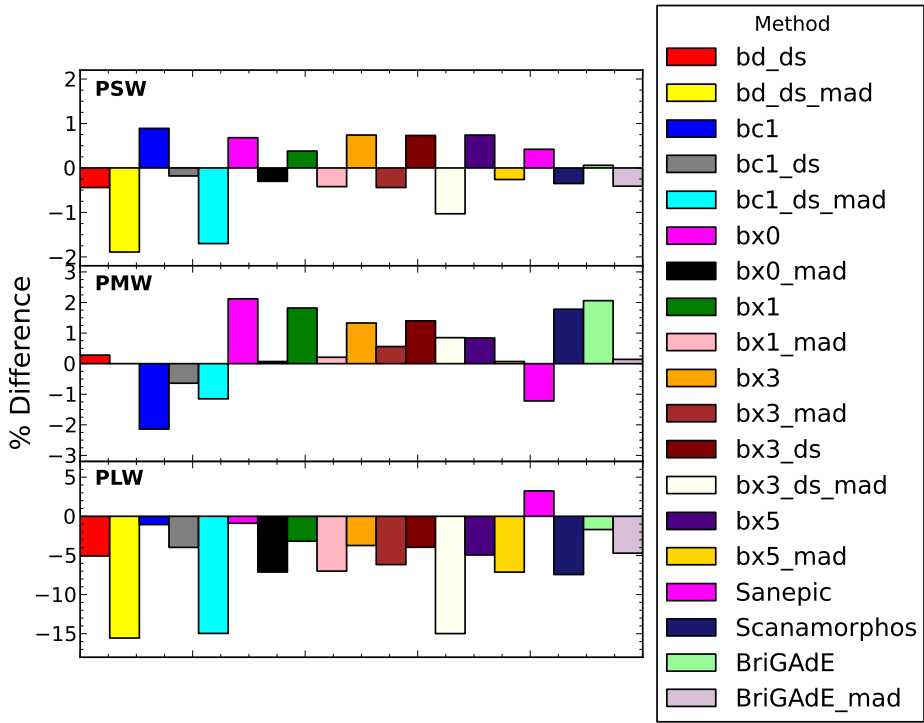


Figure B.1. The percentage difference in the global flux measured for M 100 between observation 0x5000273A and 0x50002CE3. This value is given for each pipeline tested during the SAG2 map making review.

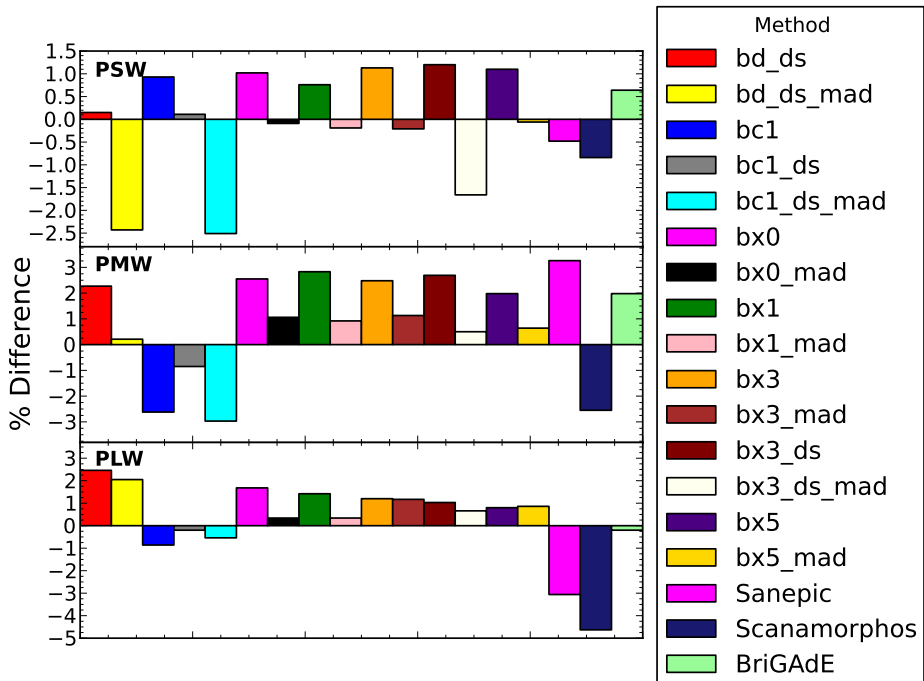


Figure B.2. The percentage difference in the global flux measured for M 100 for observation 0x5000273A using the BRIGADE pipeline using MADmap as the reference flux.

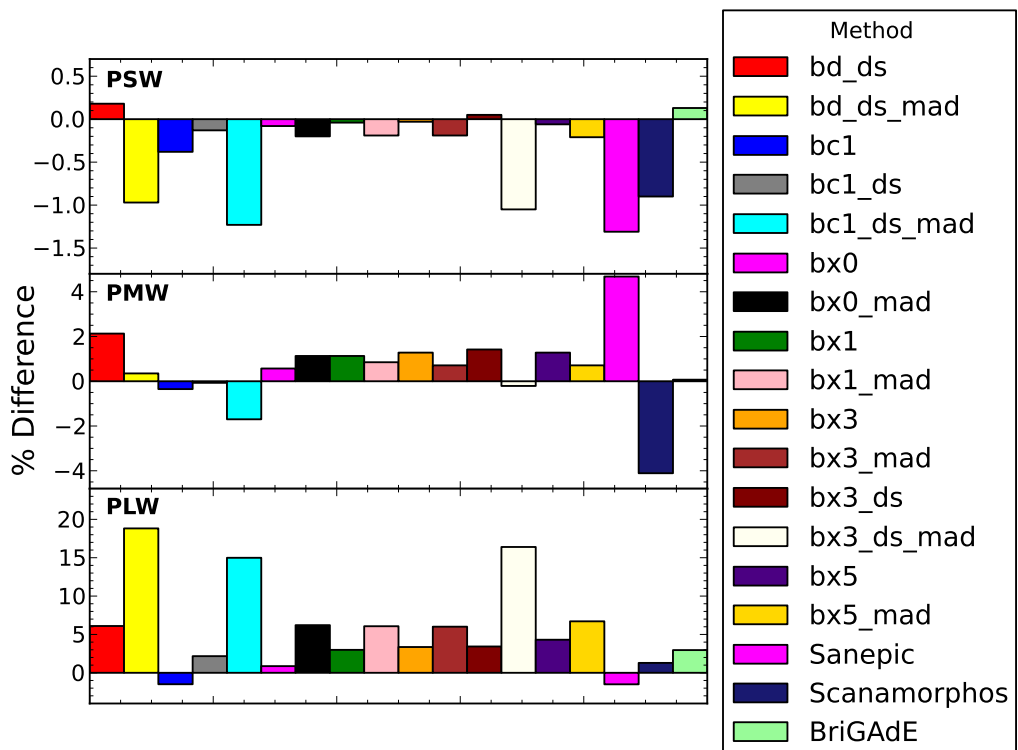


Figure B.3. The percentage difference in the global flux measured for M 100 for observation 0x50002CE3 using the BRIGAdE pipeline using MADmap as the reference flux.

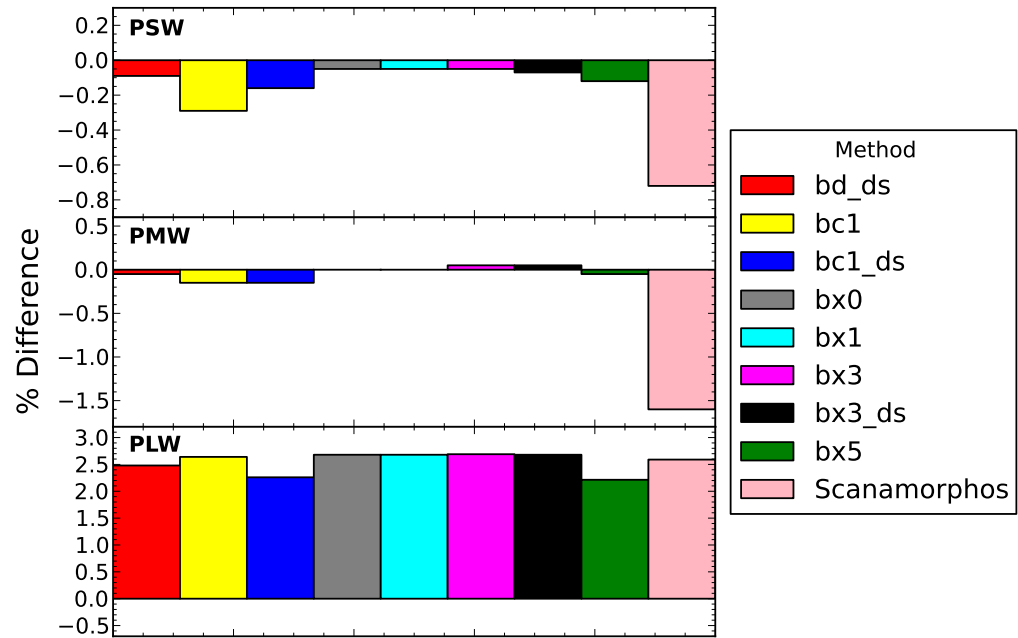


Figure B.4. The percentage difference in the global flux measured for M 82 using the BRIGAdE pipeline as the reference flux.

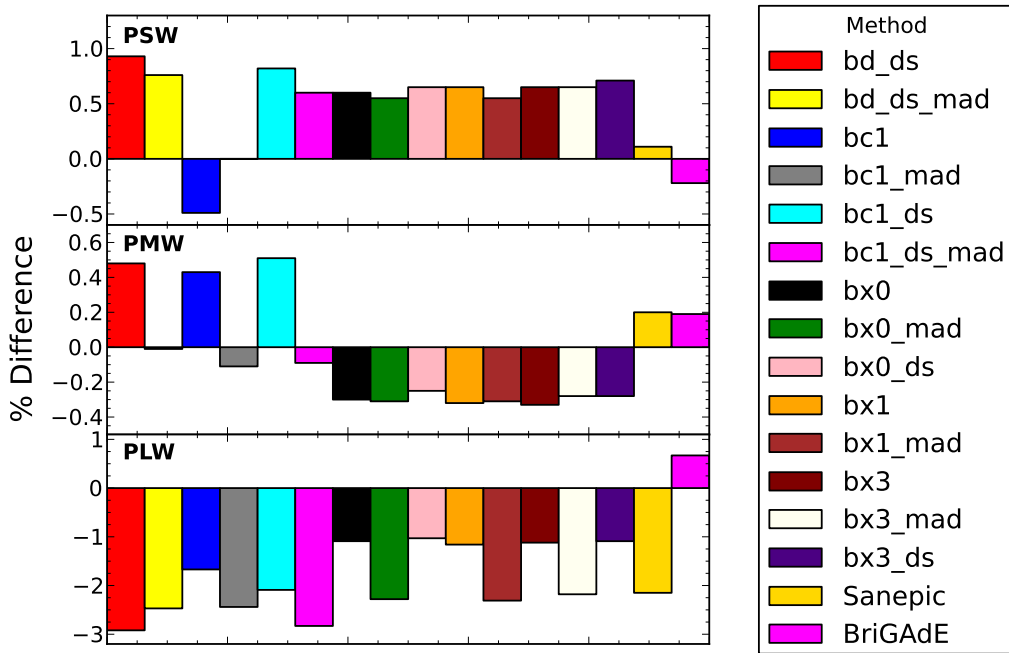


Figure B.5. The percentage difference in the global flux measured for M 91 using the BRIGAdE pipeline using MADmap as the reference flux.

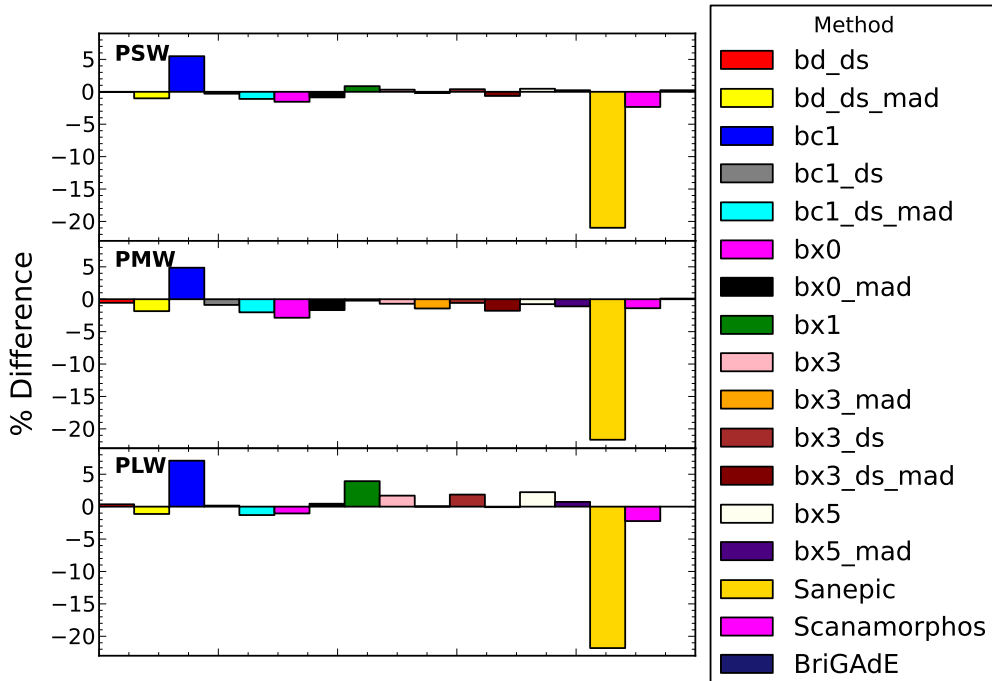


Figure B.6. The percentage difference in the global flux measured for NGC 6822 using the BRIGAdE pipeline using MADmap as the reference flux.

APPENDIX C

PROOF OF MODIFIED BLACKBODY DUST EMISSION MODEL

This appendix provides a proof of the single-temperature modified blackbody model for dust emission which is used throughout this thesis.

When radiation passes through a region of space which contains material three processes can occur: emission, absorption or scattering. The emission and absorption can then be quantified by:

- **Emission**

The energy emitted into a solid angle, per unit time, volume and frequency is given by,

$$dE = j_\nu dV d\Omega dt d\nu \quad (\text{C.1})$$

where j_ν is the emission coefficient and has units of $\text{W m}^{-3} \text{sr}^{-1} \text{Hz}^{-1}$. The emissivity ε_ν is defined as $\varepsilon_\nu = j_\nu(4\pi)$.

- **Absorption**

The absorption coefficient α_ν (also known as the opacity), is the amount of energy removed from radiation as it travels a path s . The change in intensity can therefore be written as

$$dI_\nu = -\alpha_\nu I_\nu ds \quad (\text{C.2})$$

If a ray of light travels a distance ds through a medium the change of intensity is the sum of the absorption and emission that occurs,

$$\frac{dI_\nu}{ds} = -\alpha_\nu I_\nu + j_\nu \quad (\text{C.3})$$

this is often referred to as the radiative transfer equation. The optical depth (τ_ν) is a measure of the quantity of light removed from a beam by scattering or absorption after it has travelled through a given path. The optical depth is defined as:

$$\frac{I}{I_0} = e^{-\tau_\nu} \quad (\text{C.4})$$

The optical depth can therefore be related to the absorption coefficient by $d\tau_\nu = \alpha_\nu ds$ and the source function can be defined by $S_\nu = j_\nu/\alpha_\nu$. Substituting τ_ν and S_ν into the transfer equation becomes,

$$\frac{dI_\nu}{d\tau} = -I_\nu + S_\nu \quad (\text{C.5})$$

which is now solvable. The general solution to Equation C.5 is

$$I_\nu = I_\nu(0)e^{-\tau_\nu} + \int_0^{\tau_\nu} e^{-(\tau_\nu - \tau'_\nu)} S_\nu(\tau'_\nu) d\tau'_\nu \quad (\text{C.6})$$

but, if S_ν is a constant (which we assume is true for dust)

$$I_\nu = S_\nu + e^{-\tau_\nu} (I_\nu(0) - S_\nu) \quad (\text{C.7})$$

The source function for dust held at a temperature (T) is a blackbody (i.e., $S_\nu = B_\nu(T)$), and using the condition that when $T = 0$ that $I_\nu = 0$ equation C.7 can be simplified to

$$I_\nu = B_\nu(T)(1 - e^{-\tau_\nu}) \quad (\text{C.8})$$

As dust emits at much longer wavelengths than the size of a dust grain, the assumption is made that the dust is optically thin so $\tau \ll 1$. For this case the Taylor expansion for exponential can be used where $e^x \approx 1 + x + \frac{x^2}{2!} + \frac{x^3}{3!} \dots$. Equation C.8 then simplifies to

$$I_\nu = \tau_\nu B_\nu(T) \quad (\text{C.9})$$

The absorption coefficient can be written as the product of the dust grain cross-section (σ), the absorption efficiency (Q_{abs}) and the number density (ξ_{dust}) of dust grains,

$$\alpha_\nu = \sigma Q_{abs} \xi_{dust}. \quad (\text{C.10})$$

As τ_ν is the integral of the absorption coefficient along a path, τ_ν can be written as

$$\tau = n_{dust} \sigma Q_{abs} \quad (\text{C.11})$$

where n_{dust} is the column density of dust. The luminosity of the dust is the intensity multiplied by the cross-sectional area of the galaxy (or emitting medium) (A_{dust}) and integrated over the whole solid angle which gives,

$$L_\nu = 4\pi A_{dust} n_{dust} \sigma Q_{abs} B_\nu(T) \quad (\text{C.12})$$

and can be easily converted to an observable flux (F_ν) by using the area of a sphere ($4\pi r^2$) and the distance to the object (D):

$$F_\nu = \frac{A_{dust} n_{dust} \sigma Q_{abs}}{D^2} B_\nu(T) \quad (\text{C.13})$$

A new quantity called the mass-opacity coefficient (κ_ν) can be defined which relates the absorption coefficient (α_ν) and the density of dust (ρ):

$$\kappa_\nu = \frac{\alpha_\nu}{\rho} \quad (\text{C.14})$$

Using equation C.10 and that $\rho = M_{dust}/V$ (where V is the volume of the medium) then equation C.14 can be written as,

$$\kappa_\nu = \frac{\sigma Q_{abs} \xi_{dust}}{\rho} = \frac{\sigma Q_{abs} \xi_{dust} V}{M_{dust}} = \frac{A_{dust} n_{dust} \sigma Q_{abs}}{M_{dust}} \quad (\text{C.15})$$

Using the Mie solution and Maxwell's equations (see Chapter 1), Q_{abs} is proportional to ν^β . In equation C.15 the only quantity which depends on the frequency is Q_{abs} and so κ_ν can be expressed as

$$\kappa_\nu = \kappa_0 \left(\frac{\nu}{\nu_0} \right)^\beta \quad (\text{C.16})$$

where κ_0 is the value of κ_ν at a reference frequency (ν_0). Equations C.13 and C.15 can now be combined to give the final formula:

$$F_\nu = \frac{\kappa_\nu M}{D^2} B_\nu(T) \quad (\text{C.17})$$

APPENDIX D

NOTES ON ELLIPTICALS DETECTED BY HERSCHEL

This Appendix describes the elliptical galaxies detected in the HRS as described in Chapter 6. These notes were written by Haley Gomez.

HRS 3, NGC 3226. A semicircular lane of dust in NGC 3226 is seen as absorption in the optical (Martel et al., 2004) with dusty strands extending north–south. The source is known to be interacting with the nearby spiral NGC 3227 (the bright source to the south of the elliptical—Figure 6.2), which has clear tidal gas trails (Mundell et al., 2004). The elliptical appears slightly extended in the 250 μm image but more compact than in the optical image (Figure 6.2). NGC 3226 is part of the Leo Cloud.

HRS 138, NGC 4374 (M 84). M 84 has a radio bright core and radio jets. *Hubble Space Telescope* (HST) images show dust lanes across the center of the galaxy (Bower et al., 1997), which are approximately perpendicular to the radio jet. The galaxy was detected at 850 μm with SCUBA by Leeuw et al. (2000). They concluded that most of the 850 μm flux was synchrotron emission, but that the emission at shorter wavelengths detected by *IRAS* was produced by $\sim 10^5 M_\odot$ of dust at a temperature of 35 K (see also Boselli et al., 2010a). The 250 μm source is unresolved and is coincident with the radio core (Figure 6.2). NGC 4374 is a member of the Virgo Cluster.

HRS 150, NGC 4406 (M 86). M 86 is a well-known IR-bright giant elliptical. Two dust features were detected with *IRAS* and originally attributed to dust stripped from M 86 due to its motion through the cluster. The discovery of atomic gas offset

from the center of M 86 and decoupled from its stellar disk supports a tidal interaction (Li & van Gorkom, 2001), confirmed when Kenney et al. (2008) detected strong H α features extending from M 86 to the nearby spiral NGC 4438. The distribution and velocity of the ionized gas provide clear evidence for tidal interaction between these two giants. *Herschel* SPIRE observations of M 86 and NGC 4438 showed that the dust emission is spatially correlated with the ionized gas between the two galaxies (Gomez et al., 2010; Cortese et al., 2010a) implying that the dust is material stripped from the nearby spiral. In Figure 6.2, the appearance of the dust emission in M 86 is clearly different to the other ellipticals in our sample, with faint filamentary features seen within $D(25)$. NGC 4406 is a member of the Virgo Cluster.

HRS 183, NGC 4486 (M 87). M 87 is the brightest galaxy in the Virgo Cluster and well known for the jet extending from the nucleus seen at radio, optical, and X-ray wavelengths (Junor et al., 1999). The presence of dust was inferred from *HST* g – z color images (Ferrarese et al., 2006) and the strong FIR emission seen with *Spitzer* (Perlman et al., 2007). The latter result might be explained by synchrotron emission from the central radio source. Although the optical images show dust is present, *Herschel* observations of M 87 with PACS and SPIRE as part of HeViCS (Baes et al., 2010a; Boselli et al., 2010a) found no evidence of a dust component in excess of the synchrotron emission in the FIR and submm. Baes et al. place an upper limit on the dust mass of $10^5 M_{\odot}$. In the *Herschel* image, M 87 is a bright, extended source.

HRS 186, NGC 4494. NGC 4494 is often described as an ‘ordinary elliptical’ (Capaccioli et al., 1992). O’Sullivan & Ponman (2004) found that its X-ray luminosity was two order of magnitudes lower than expected for its optical luminosity and there are signs of a small dust disk in absorption (Tran et al., 2001). X-ray faint galaxies such as NGC 4494 may arise due to losing their hot X-ray gas in outflows. Further evidence of interactions with nearby galaxies or mergers is the low metallicity estimated from the X-ray gas ($< 0.1 Z_{\odot}$, O’Sullivan & Ponman, 2004), and this may indicate dilution of interstellar material via an infall of unenriched (cold) material. The galaxy is slightly extended at 250 μ m. NGC 4494 is a member of the Coma I Cloud.

HRS 241, NGC 4636. NGC 4636 has dust features and an unusual X-ray morphology (Temi et al., 2007b). The origin of this morphology is thought to be recent outbursts from the central AGN (Jones et al., 2002). Temi et al. (2003) used *ISO* observations to show that the dust mass for NGC 4636 is far in excess of that expected from stellar mass loss and proposed that the dust was accreted in a very recent merger with a

dusty, gas-rich galaxy (similar to M86, Gomez et al., 2010). NGC 4636 is part of the Virgo Cluster.

HRS 258, NGC 4697. NGC 4697 is an X-ray-faint galaxy given its optical luminosity, which may be a result of severe loss of interstellar gas via stripping or outflows (Sarazin et al., 2001). As in NGC 4494, the metallicity of the gas is low ($< 0.07Z_{\odot}$), pointing toward dilution of the interstellar medium with unenriched cold gas. The source is slightly extended at $250 \mu\text{m}$. NGC 4697 is in the outer regions of the Virgo Cluster.

APPENDIX E

FIR EMISSION VERSUS OPTICAL AND X-RAY FOR EARLY-TYPE GALAXIES

This Appendix provides a detailed description of the correlation analysis used in Chapter 6. This Appendix was written by Haley Gomez using luminosities that I provided.

We investigated whether there is a correlation between L_X and L_B using the statistics in the ASURV package for dealing with censored data. We find evidence for a correlation for the elliptical galaxies ($P = 99.3\%$ ¹). The relationship between the two parameters for ellipticals² is described by the following relationship with deviation from the regression $\sigma_r = 0.43$:

$$\log L_B = (2.95 \pm 1.03) \log L_X + 10.79 \quad (\text{E.1})$$

This relationship agrees with other IR samples dominated by massive ETGs (see also Brown & Bregman, 1998), whereas X-ray studies indicative of the entire population are described by $L_X \propto L_B^{2.3}$ (O'Sullivan et al., 2001; Temi et al., 2004).

If the dust produced in ETGs is due to stellar mass loss, the dust mass would be roughly proportional to the mass of the stars, and hence to L_B . If the dust is then widely dispersed and heated by the starlight as well as electron collisions in the hot, X-ray emitting gas, the FIR emission will also depend on the density of the gas or on the stellar density, which are both roughly proportional to $L_B^{1/2}$. Therefore, we

¹Using the Kendall τ test, a statistic used to measure the association between X and Y ; this test is appropriate for small samples with upper limits where the underlying distributions of X and Y are not known.

²Using the Buckley-James method, a standard linear regression estimator. This test requires that the censoring distribution about the fitted line is random and does not require the residuals to be Gaussian as other regression methods do.

would expect $L_{\text{FIR}} \propto L_B^{1.4-1.6}$. Bregman et al. (1998) indeed found this relationship was true for *IRAS*-detected ETGs, though Temi et al. (2004) found no correlation for their *ISO*-detected sources. In the *Herschel* sample, we see that the FIR luminosity of S0+S0a galaxies does appear to increase with the optical luminosity, although this is not a statistical correlation, with Spearman rank³ coefficient $r_S = 0.36$ and probability that a correlation is present of $P = 97\%$. The S0+S0a data can be fit by the following equation² with $\sigma_r = 0.39$:

$$\log L_{\text{FIR}}(\text{S0}) = (1.22 \pm 0.42)\log(L_B) - 3.53. \quad (\text{E.2})$$

The FIR luminosity of the elliptical galaxies increases with L_B but again, we find that the correlation is not statistically significant, with L_B ($\tau = 0.36$ and $P = 91\%$ ¹), the results of the regression analysis produces the following relationship (with $\sigma_r = 0.33^2$):

$$\log L_{\text{FIR}}(\text{E}) = (1.00 \pm 0.77)\log(L_B) - 2.44. \quad (\text{E.3})$$

The correlations in Equations (E.2) and (E.3) are plotted in Figure 6.10. The lack of any strong correlation between L_{FIR} and L_B does not provide any evidence for the hypothesis that the dust responsible for the FIR–submm emission is produced by stellar mass loss, although the ETGs do at least fall in roughly the right place in the figure.

In Figure 6.10 (lower panel), we also compare the dust mass with optical and X-ray luminosities but find no evidence for a correlation due to the small numbers in the samples with both *Herschel* detections and X-ray fluxes in the literature.

There is also no evidence for a significant correlation between dust mass and L_B for S0 galaxies ($r_S = 0.27$ and $P = 90\%$), with a best-fit relationship ($\sigma_r = 0.58^3$):

$$\log M_d(\text{S0}) = (1.11 \pm 0.62)\log L_B - 5.08 \quad (\text{E.4})$$

The dust mass and optical luminosity for the ellipticals are also not correlated ($\tau = 0.30$ and $P = 90\%$ ¹), with a best-fit relationship ($\sigma_r = 0.87$)²:

$$\log M_d(\text{E}) = (1.89 \pm 1.99)\log L_B - 14.40 \quad (\text{E.5})$$

³Using the Spearman rho correlation test; this statistic is more appropriate than the Kendall τ used for the ellipticals since the S0s are a larger sample with more detections. The correlation determines how well the relationship between X and Y can be described by a monotonic function. This test is less sensitive to outliers than the similar Pearson correlation test. We tested that the Kendall's τ and Spearman correlation tests give similar values.

The remaining panel in Figure 6.10 shows dust mass rather than FIR luminosity plotted against X-ray luminosity, with both quantities being normalized by L_B ; the correlation is weaker when FIR luminosity is converted into dust mass.

BIBLIOGRAPHY

- Aannestad, P. A. 1975, ApJ, 200, 30
- Aaronson, M., & Olszewski, E. W. 1984, Nature, 309, 414
- Abazajian, K. N., Adelman-McCarthy, J. K., Agüeros, M. A., et al. 2009, ApJS, 182, 543
- Abdo, A. A., Ackermann, M., Ajello, M., et al. 2010, ApJ, 710, 133
- Agladze, N. I., Sievers, A. J., Jones, S. A., Burlitch, J. M., & Beckwith, S. V. W. 1996, ApJ, 462, 1026
- Allamandola, L. J., Tielens, A. G. G. M., & Barker, J. R. 1989, ApJS, 71, 733
- Anderson, L. D., Zavagno, A., Rodón, J. A., et al. 2010, A&A, 518, L99
- Armand, C., Milliard, B., & Deharveng, J. M. 1994, A&A, 284, 12
- Arnouts, S., Schiminovich, D., Ilbert, O., et al. 2005, ApJ, 619, L43
- Athey, A., Bregman, J., Bregman, J., Temi, P., & Sauvage, M. 2002, ApJ, 571, 272
- Auld, R., Smith, M. W. L., Bendo, G., et al. 2012, MNRAS, 420, 1882
- Baes, M., Fritz, J., Gadotti, D. A., et al. 2010a, A&A, 518, L39
- Baes, M., Clemens, M., Xilouris, E. M., et al. 2010b, A&A, 518, L53
- Baldry, I. K., Glazebrook, K., Budavári, T., et al. 2005, MNRAS, 358, 441
- Barlow, M. J. 1978, MNRAS, 183, 367
- Barlow, M. J., Krause, O., Swinyard, B. M., et al. 2010, A&A, 518, L138
- Barmby, P., Ashby, M. L. N., Bianchi, L., et al. 2006, ApJ, 650, L45

- Becker, R. H., White, R. L., & Helfand, D. J. 1995, *ApJ*, 450, 559
- Bekki, K., Couch, W. J., & Shioya, Y. 2002, *ApJ*, 577, 651
- Bell, E. F., Wolf, C., Meisenheimer, K., et al. 2004, *ApJ*, 608, 752
- Bendo, G. J., Galliano, F., & Madden, S. C. 2012a, *MNRAS*, 423, 197
- Bendo, G. J., Joseph, R. D., Wells, M., et al. 2003, *AJ*, 125, 2361
- Bendo, G. J., Buckalew, B. A., Dale, D. A., et al. 2006, *ApJ*, 645, 134
- Bendo, G. J., Calzetti, D., Engelbracht, C. W., et al. 2007, *MNRAS*, 380, 1313
- Bendo, G. J., Wilson, C. D., Pohlen, M., et al. 2010a, *A&A*, 518, L65
- Bendo, G. J., Wilson, C. D., Warren, B. E., et al. 2010b, *MNRAS*, 402, 1409
- Bendo, G. J., Boselli, A., Dariush, A., et al. 2012b, *MNRAS*, 419, 1833
- Berman, S. 2001, *A&A*, 371, 476
- Bernstein, R. A., Freedman, W. L., & Madore, B. F. 2002, *ApJ*, 571, 56
- Bianchi, S., & Ferrara, A. 2005, *MNRAS*, 358, 379
- Bigiel, F., Leroy, A., Seibert, M., et al. 2010, *ApJ*, 720, L31
- Bigiel, F., Leroy, A., Walter, F., et al. 2008, *AJ*, 136, 2846
- Binggeli, B., Sandage, A., & Tammann, G. A. 1985, *AJ*, 90, 1681
- Blain, A. W., Smail, I., Ivison, R. J., & Kneib, J.-P. 1999, *MNRAS*, 302, 632
- Blair, W. P., Kirshner, R. P., & Chevalier, R. A. 1982, *ApJ*, 254, 50
- Block, D. L., Bournaud, F., Combes, F., et al. 2006, *Nature*, 443, 832
- Boissier, S., & Prantzos, N. 1999, *MNRAS*, 307, 857
- Boquien, M., Calzetti, D., Combes, F., et al. 2011, *AJ*, 142, 111
- Boselli, A., & Gavazzi, G. 2006, *PASP*, 118, 517
- Boselli, A., Lequeux, J., & Gavazzi, G. 2002, *Ap&SS*, 281, 127
- . 2004, *A&A*, 428, 409

- Boselli, A., Ciesla, L., Buat, V., et al. 2010a, *A&A*, 518, L61
- Boselli, A., Eales, S., Cortese, L., et al. 2010b, *PASP*, 122, 261
- Boselli, A., Boissier, S., Heinis, S., et al. 2011, *A&A*, 528, A107
- Bournaud, F., Duc, P.-A., Brinks, E., et al. 2007, *Science*, 316, 1166
- Bouwens, R., Broadhurst, T., & Illingworth, G. 2003a, *ApJ*, 593, 640
- Bouwens, R. J., Illingworth, G. D., Blakeslee, J. P., & Franx, M. 2006, *ApJ*, 653, 53
- Bouwens, R. J., Illingworth, G. D., Rosati, P., et al. 2003b, *ApJ*, 595, 589
- Bower, G. A., Heckman, T. M., Wilson, A. S., & Richstone, D. O. 1997, *ApJ*, 483, L33
- Bower, R. G., Benson, A. J., & Crain, R. A. 2012, *MNRAS*, 422, 2816
- Bracco, A., Cooray, A., Veneziani, M., et al. 2011, *MNRAS*, 412, 1151
- Braun, R., Thilker, D. A., Walterbos, R. A. M., & Corbelli, E. 2009, *ApJ*, 695, 937
- Bregman, J. N., Snider, B. A., Grego, L., & Cox, C. V. 1998, *ApJ*, 499, 670
- Bressan, A., Panuzzo, P., Buson, L., et al. 2006, *ApJ*, 639, L55
- Brown, B. A., & Bregman, J. N. 1998, *ApJ*, 495, L75
- Buat, V., Giovannoli, E., Takeuchi, T. T., et al. 2011, *A&A*, 529, A22
- Bunker, A. J., Stanway, E. R., Ellis, R. S., & McMahon, R. G. 2004, *MNRAS*, 355, 374
- Calzetti, D. 2001, *PASP*, 113, 1449
- Calzetti, D., Wu, S.-Y., Hong, S., et al. 2010, *ApJ*, 714, 1256
- Cantalupo, C. M., Borrill, J. D., Jaffe, A. H., Kisner, T. S., & Stompor, R. 2010, *ApJS*, 187, 212
- Capaccioli, M., Caon, N., & D'Onofrio, M. 1992, *MNRAS*, 259, 323
- Cappellari, M., Emsellem, E., Krajnović, D., et al. 2011, *MNRAS*, 413, 813
- Chanal, P. 2003, PhD Thesis (Paris XI University)

- Chapman, S. C., Smail, I., Windhorst, R., Muxlow, T., & Ivison, R. J. 2004, *ApJ*, 611, 732
- Chemin, L., Carignan, C., & Foster, T. 2009, *ApJ*, 705, 1395
- Chung, A., van Gorkom, J. H., Kenney, J. D. P., Crowl, H., & Vollmer, B. 2009, *AJ*, 138, 1741
- Ciesla, L., Boselli, A., Smith, M. W. L., et al. 2012, *A&A*, 543, A161
- Clemens, M. S., Jones, A. P., Bressan, A., et al. 2010, *A&A*, 518, L50
- Cole, S., Lacey, C. G., Baugh, C. M., & Frenk, C. S. 2000, *MNRAS*, 319, 168
- Combes, F., Young, L. M., & Bureau, M. 2007, *MNRAS*, 377, 1795
- Corbelli, E., Bianchi, S., Cortese, L., et al. 2012, *A&A*, 542, A32
- Cortese, L., Catinella, B., Boissier, S., Boselli, A., & Heinis, S. 2011, *MNRAS*, 415, 1797
- Cortese, L., & Hughes, T. M. 2009, *MNRAS*, 400, 1225
- Cortese, L., Bendo, G. J., Boselli, A., et al. 2010a, *A&A*, 518, L63
- Cortese, L., Davies, J. I., Pohlen, M., et al. 2010b, *A&A*, 518, L49
- Cortese, L., Ciesla, L., Boselli, A., et al. 2012a, *A&A*, 540, A52
- Cortese, L., Boissier, S., Boselli, A., et al. 2012b, *A&A*, 544, A101
- Coupeaud, A., Demyk, K., Meny, C., et al. 2011, *A&A*, 535, A124
- Courteau, S., Widrow, L. M., McDonald, M., et al. 2011, *ApJ*, 739, 20
- Crocker, A. F., Bureau, M., Young, L. M., & Combes, F. 2011, *MNRAS*, 410, 1197
- Dale, D. A., Aniano, G., Engelbracht, C. W., et al. 2012, *ApJ*, 745, 95
- Davies, J. 2012, ArXiv e-prints:1204.4649
- Davies, J. I., Alton, P., Trehewella, M., Evans, R., & Bianchi, S. 1999, *MNRAS*, 304, 495
- Davies, J. I., Baes, M., Bendo, G. J., et al. 2010, *A&A*, 518, L48
- Davies, J. I., Bianchi, S., Cortese, L., et al. 2012, *MNRAS*, 419, 3505

- Davis, T. A., Alatalo, K., Sarzi, M., et al. 2011, MNRAS, 417, 882
- de Graauw, T., Helmich, F. P., Phillips, T. G., et al. 2010, A&A, 518, L6
- de Jong, T., Clegg, P. E., Rowan-Robinson, M., et al. 1984, ApJ, 278, L67
- De Lucia, G., Springel, V., White, S. D. M., Croton, D., & Kauffmann, G. 2006, MNRAS, 366, 499
- Deming, D., Seager, S., Richardson, L. J., & Harrington, J. 2005, Nature, 434, 740
- Désert, F.-X., Macías-Pérez, J. F., Mayet, F., et al. 2008, A&A, 481, 411
- Devereux, N. A., & Eales, S. A. 1989, ApJ, 340, 708
- Devereux, N. A., & Young, J. S. 1990, ApJ, 359, 42
- di Serego Alighieri, S., Trinchieri, G., & Brocato, E. 1990, in Astrophysics and Space Science Library, Vol. 160, Windows on Galaxies, ed. G. Fabbiano, J. S. Gallagher, & A. Renzini, 301
- di Serego Alighieri, S., Gavazzi, G., Giovanardi, C., et al. 2007, A&A, 474, 851
- di Serego Alighieri, S., Bianchi, S., Pappalardo, C., et al. 2012, A&A, submitted
- Dowell, C. D., Pohlen, M., Pearson, C., et al. 2010, in Society of Photo-Optical Instrumentation Engineers (SPIE) Conference Series, Vol. 7731, Society of Photo-Optical Instrumentation Engineers (SPIE) Conference Series
- Draine, B. T. 2003, ARA&A, 41, 241
- Draine, B. T., & Li, A. 2007a, ApJ, 657, 810
- . 2007b, ApJ, 657, 810
- Draine, B. T., & Salpeter, E. E. 1979, ApJ, 231, 438
- Draine, B. T., Dale, D. A., Bendo, G., et al. 2007, ApJ, 663, 866
- Dressler, A. 1980, ApJ, 236, 351
- Dunne, L., Eales, S., Edmunds, M., et al. 2000, MNRAS, 315, 115
- Dunne, L., & Eales, S. A. 2001, MNRAS, 327, 697
- Dunne, L., Gomez, H. L., da Cunha, E., et al. 2011, MNRAS, 417, 1510

- Dupac, X., Bernard, J.-P., Boudet, N., et al. 2003, A&A, 404, L11
- Eales, S., Dunne, L., Clements, D., et al. 2010a, PASP, 122, 499
- Eales, S., Smith, M. W. L., Auld, R., et al. 2012, ApJ, 761, 168
- Eales, S. A., Smith, M. W. L., Wilson, C. D., et al. 2010b, A&A, 518, L62+
- Edmunds, M. G. 2001, MNRAS, 328, 223
- Elbaz, D., Cesarsky, C. J., Fadda, D., et al. 1999, A&A, 351, L37
- Emsellem, E., Cappellari, M., Krajnović, D., et al. 2007, MNRAS, 379, 401
- . 2011, MNRAS, 414, 888
- Engel, H., Tacconi, L. J., Davies, R. I., et al. 2010, ApJ, 724, 233
- Engelbracht, C. W., Hunt, L. K., Skibba, R. A., et al. 2010, A&A, 518, L56
- Faber, S. M., & Gallagher, J. S. 1976, ApJ, 204, 365
- Fabian, A. C. 2012, ArXiv e-prints:1204.4114
- Feigelson, E. D., & Nelson, P. I. 1985, ApJ, 293, 192
- Ferrarese, L., Côté, P., Jordán, A., et al. 2006, ApJS, 164, 334
- Ferrari, F., Pastoriza, M. G., Macchetto, F. D., et al. 2002, A&A, 389, 355
- Filho, M. E., Barthel, P. D., & Ho, L. C. 2006, A&A, 451, 71
- Forbes, D. A. 1991, MNRAS, 249, 779
- Ford, G. P., Gear, W. K., Smith, M. W. L., et al. 2012, ApJ, submitted
- Foyle, K., Wilson, C. D., Mentuch, E., et al. 2012, MNRAS, 421, 2917
- Fritz, J., Gentile, G., Smith, M. W. L., et al. 2012, A&A, 546, A34
- Galarza, V. C., Walterbos, R. A. M., & Braun, R. 1999, AJ, 118, 2775
- Gavazzi, G., & Boselli, A. 1999, A&A, 343, 86
- Gavazzi, G., Boselli, A., Donati, A., Franzetti, P., & Scodéglio, M. 2003, A&A, 400, 451
- Giovanelli, R., & Haynes, M. P. 1985, ApJ, 292, 404

- Gomez, H. L., Baes, M., Cortese, L., et al. 2010, A&A, 518, L45
- Gomez, H. L., Clark, C. J. R., Nozawa, T., et al. 2012, MNRAS, 420, 3557
- González-Martín, O., Masegosa, J., Márquez, I., Guainazzi, M., & Jiménez-Bailón, E. 2009, A&A, 506, 1107
- Gordon, K. D., Clayton, G. C., Misselt, K. A., Landolt, A. U., & Wolff, M. J. 2003, ApJ, 594, 279
- Gordon, K. D., Rieke, G. H., Engelbracht, C. W., et al. 2005, PASP, 117, 503
- Gordon, K. D., Bailin, J., Engelbracht, C. W., et al. 2006, ApJ, 638, L87
- Gordon, K. D., Engelbracht, C. W., Fadda, D., et al. 2007, PASP, 119, 1019
- Gorjian, V., Wright, E. L., & Chary, R. R. 2000, ApJ, 536, 550
- Goudfrooij, P., & de Jong, T. 1995, A&A, 298, 784
- Goudfrooij, P., Hansen, L., Jorgensen, H. E., et al. 1994, A&AS, 104, 179
- Graham, A. W., & Worley, C. C. 2008, MNRAS, 388, 1708
- Greggio, L., & Renzini, A. 1990, ApJ, 364, 35
- Grenier, I. A., Casandjian, J.-M., & Terrier, R. 2005, Science, 307, 1292
- Griffin, M., Dowell, C. D., Lim, T., et al. 2008, in Society of Photo-Optical Instrumentation Engineers (SPIE) Conference Series, Vol. 7010, Society of Photo-Optical Instrumentation Engineers (SPIE) Conference Series
- Griffin, M. J., Abergel, A., Abreu, A., et al. 2010, A&A, 518, L3
- Grossi, M., Hunt, L. K., Madden, S., et al. 2010, A&A, 518, L52
- Guelin, M., Zylka, R., Mezger, P. G., et al. 1993, A&A, 279, L37
- Gunn, J. E., & Gott, III, J. R. 1972, ApJ, 176, 1
- Habing, H. J., Miley, G., Young, E., et al. 1984, ApJ, 278, L59
- Hanish, D. J., Meurer, G. R., Ferguson, H. C., et al. 2006, ApJ, 649, 150
- Hauser, M. G., Arendt, R. G., Kelsall, T., et al. 1998, ApJ, 508, 25
- Haynes, M. P., & Giovanelli, R. 1984, AJ, 89, 758

- Haynes, M. P., Giovanelli, R., Martin, A. M., et al. 2011, AJ, 142, 170
- Helou, G., Soifer, B. T., & Rowan-Robinson, M. 1985, ApJ, 298, L7
- Herschel* Observer's Manual. 2012, *Herschel Space Observatory*, <http://hereschel.esac.esac.int/Docs/Herschel/html/observatory.html>
- HIFI Observers' Manual. 2011, *Herschel Space Observatory*, http://hereschel.esac.esac.int/Docs/HIFI/html/hifi_om.html
- Hildebrand, R. H. 1983, QJRAS, 24, 267
- Hinz, J. L., Rieke, M. J., Rieke, G. H., et al. 2007, ApJ, 663, 895
- Ho, L. C., Filippenko, A. V., & Sargent, W. L. W. 1997, ApJS, 112, 315
- Holland, W. S., Cunningham, C. R., Gear, W. K., et al. 1998, in Society of Photo-Optical Instrumentation Engineers (SPIE) Conference Series, Vol. 3357, Society of Photo-Optical Instrumentation Engineers (SPIE) Conference Series, ed. T. G. Phillips, 305–318
- Hoopes, C. G., Heckman, T. M., Strickland, D. K., et al. 2005, ApJ, 619, L99
- Hopkins, A. M. 2004, ApJ, 615, 209
- Hopkins, A. M. 2007, in Astronomical Society of the Pacific Conference Series, Vol. 380, Deepest Astronomical Surveys, ed. J. Afonso, H. C. Ferguson, B. Mobasher, & R. Norris, 423
- Hubble, E. P. 1925, Popular Astronomy, 33, 252
- Hughes, D. H., Serjeant, S., Dunlop, J., et al. 1998, Nature, 394, 241
- Iono, D., Yun, M. S., & Ho, P. T. P. 2005, ApJS, 158, 1
- Israel, F. 2000, in Molecular Hydrogen in Space, ed. F. Combes & G. Pineau Des Forets, 293–+
- Israel, F. P. 2005, A&A, 438, 855
- Jones, C., Forman, W., Vikhlinin, A., et al. 2002, ApJ, 567, L115
- Junor, W., Biretta, J. A., & Livio, M. 1999, Nature, 401, 891
- Kaneda, H., Onaka, T., & Sakon, I. 2005, ApJ, 632, L83

- Kaneda, H., Onaka, T., Sakon, I., et al. 2008, *ApJ*, 684, 270
- Kaviraj, S., Schawinski, K., Devriendt, J. E. G., et al. 2007, *ApJS*, 173, 619
- Kenney, J., Beck, R., Helou, G., et al. 2006, in Spitzer Proposal ID #30945, 30945–+
- Kenney, J. D. P., Tal, T., Crowl, H. H., Feldmeier, J., & Jacoby, G. H. 2008, *ApJ*, 687, L69
- Kennicutt, R. C., & Evans, N. J. 2012, *ARA&A*, 50, 531
- Kennicutt, R. C., Calzetti, D., Aniano, G., et al. 2011, *PASP*, 123, 1347
- Kennicutt, Jr., R. C. 1989, *ApJ*, 344, 685
- . 1998a, *ARA&A*, 36, 189
- . 1998b, *ApJ*, 498, 541
- Kennicutt, Jr., R. C., Armus, L., Bendo, G., et al. 2003, *PASP*, 115, 928
- Kennicutt, Jr., R. C., Hao, C.-N., Calzetti, D., et al. 2009, *ApJ*, 703, 1672
- Kessler, M. F., Steinz, J. A., Anderegg, M. E., et al. 1996, *A&A*, 315, L27
- Knapp, G. R., Guhathakurta, P., Kim, D.-W., & Jura, M. A. 1989, *ApJS*, 70, 329
- Kormendy, J., & Gebhardt, K. 2001, in American Institute of Physics Conference Series, Vol. 586, 20th Texas Symposium on relativistic astrophysics, ed. J. C. Wheeler & H. Martel, 363–381
- Krebs, J., & Hillebrandt, W. 1983, *A&A*, 128, 411
- Kuno, N., Sato, N., Nakanishi, H., et al. 2007, *PASJ*, 59, 117
- Lagache, G., Haffner, L. M., Reynolds, R. J., & Tufte, S. L. 2000, *A&A*, 354, 247
- Lagache, G., Puget, J.-L., & Dole, H. 2005, *ARA&A*, 43, 727
- Larson, R. B., Tinsley, B. M., & Caldwell, C. N. 1980, *ApJ*, 237, 692
- Laurikainen, E., Salo, H., Buta, R., Knapen, J. H., & Comerón, S. 2010, *MNRAS*, 405, 1089
- Le Floc'h, E., Papovich, C., Dole, H., et al. 2005, *ApJ*, 632, 169

- Leeuw, L. L., Hawarden, T. G., Matthews, H. E., Robson, E. I., & Eckart, A. 2002, ApJ, 565, 131
- Leeuw, L. L., Sansom, A. E., & Robson, E. I. 2000, MNRAS, 311, 683
- Leroy, A. K., Bolatto, A., Gordon, K., et al. 2011, ApJ, 737, 12
- Li, A. 2005, in American Institute of Physics Conference Series, Vol. 761, The Spectral Energy Distributions of Gas-Rich Galaxies: Confronting Models with Data, ed. C. C. Popescu & R. J. Tuffs, 123–133
- Li, Y., & van Gorkom, J. H. 2001, in Astronomical Society of the Pacific Conference Series, Vol. 240, Gas and Galaxy Evolution, ed. J. E. Hibbard, M. Rupen, & J. H. van Gorkom, 637
- Lis, D. C., Serabyn, E., Keene, J., et al. 1998, ApJ, 509, 299
- Lisenfeld, U., Verdes-Montenegro, L., Sulentic, J., et al. 2007, A&A, 462, 507
- Lonsdale Persson, C. J., & Helou, G. 1987, ApJ, 314, 513
- Low, J., & Kleinmann, D. E. 1968, AJ, 73, 868
- Lucero, D. M., & Young, L. M. 2007, AJ, 134, 2148
- Madau, P., Ferrara, A., & Rees, M. J. 2001, ApJ, 555, 92
- Maiolino, R., Nagao, T., Grazian, A., et al. 2008, A&A, 488, 463
- Maiolino, R., Mannucci, F., Cresci, G., et al. 2010, The Messenger, 142, 36
- Martel, A. R., Ford, H. C., Bradley, L. D., et al. 2004, AJ, 128, 2758
- Martin, C., & GALEX Team. 2005, in IAU Symposium, Vol. 216, Maps of the Cosmos, ed. M. Colless, L. Staveley-Smith, & R. A. Stathakis, 221
- Martin, D. C., Fanson, J., Schiminovich, D., et al. 2005, ApJ, 619, L1
- Matsumoto, T., Matsuura, S., Murakami, H., et al. 2005, ApJ, 626, 31
- Matsuura, M., Dwek, E., Meixner, M., et al. 2011, Science, 333, 1258
- Mattila, K. 2003, ApJ, 591, 119
- Mauch, T. 2005, PhD Thesis (University of Sydney)

- McConnachie, A. W., Irwin, M. J., Ferguson, A. M. N., et al. 2005, MNRAS, 356, 979
- Mei, S., Blakeslee, J. P., Côté, P., et al. 2007, ApJ, 655, 144
- Ménard, B., Scranton, R., Fukugita, M., & Richards, G. 2010, MNRAS, 405, 1025
- Mennella, V., Brucato, J. R., Colangeli, L., et al. 1998, ApJ, 496, 1058
- Mentuch Cooper, E., Wilson, C. D., Foyle, K., et al. 2012, ApJ, 755, 165
- Meny, C., Gromov, V., Boudet, N., et al. 2007, A&A, 468, 171
- Mie, G. 1908, Annalen der Physik, 3, 377
- Miville-Deschénes, M.-A., Lagache, G., & Puget, J.-L. 2002, A&A, 393, 749
- Montalto, M., Seitz, S., Riffeser, A., et al. 2009, A&A, 507, 283
- Moore, B., Lake, G., Quinn, T., & Stadel, J. 1999, MNRAS, 304, 465
- Morganti, R., de Zeeuw, P. T., Oosterloo, T. A., et al. 2006, MNRAS, 371, 157
- Muñoz-Mateos, J. C., Gil de Paz, A., Boissier, S., et al. 2009, ApJ, 701, 1965
- Mundell, C. G., James, P. A., Loiseau, N., Schinnerer, E., & Forbes, D. A. 2004, ApJ, 614, 648
- Naab, T., & Ostriker, J. P. 2009, ApJ, 690, 1452
- Narayanan, D., Krumholz, M. R., Ostriker, E. C., & Hernquist, L. 2012, MNRAS, 421, 3127
- Neugebauer, G., Habing, H. J., van Duinen, R., et al. 1984, ApJ, 278, L1
- Nguyen, H. T., Schulz, B., Levenson, L., et al. 2010, A&A, 518, L5
- Nieten, C., Neininger, N., Guélin, M., et al. 2006, A&A, 453, 459
- Nilson, P. 1995a, VizieR Online Data Catalog, 7026, 0
- . 1995b, VizieR Online Data Catalog, 7026, 0
- Nolthenius, R. 1993, ApJS, 85, 1
- Noordermeer, E., van der Hulst, J. M., Sancisi, R., Swaters, R. A., & van Albada, T. S. 2005, A&A, 442, 137

- O'Halloran, B., Galametz, M., Madden, S. C., et al. 2010, A&A, 518, L58
- Oliver, S. J., Wang, L., Smith, A. J., et al. 2010, A&A, 518, L21
- Oosterloo, T., Morganti, R., Crocker, A., et al. 2010, MNRAS, 409, 500
- Ordénovic, C., Surace, C., Torrésani, B., & Llébaria, A. 2008, Statistical Methodology, 5, 373
- O'Sullivan, E., Forbes, D. A., & Ponman, T. J. 2001, MNRAS, 328, 461
- O'Sullivan, E., & Ponman, T. J. 2004, MNRAS, 349, 535
- Ott, S. 2010, in Astronomical Society of the Pacific Conference Series, Vol. 434, Astronomical Data Analysis Software and Systems XIX, ed. Y. Mizumoto, K.-I. Morita, & M. Ohishi, 139–+
- Ouchi, M., Shimasaku, K., Okamura, S., et al. 2004, ApJ, 611, 660
- PACS Observers' Manual. 2011, *Herschel Space Observatory*, http://hereschel.esac.esa.int/Docs/PACS/html/pacs_om.html
- PACS Photometer Calibration Document. 2011, *Herschel Space Observatory*, http://hereschel.esac.esa.int/twiki/pub/Public/PacsCalibrationWeb/pacs_bolo_fluxcal_report_v1.pdf
- PACS Photometer Point Spread Function Document. 2010, *Herschel Space Observatory*, <http://hereschel.esac.esa.int/twiki/pub/Public/PacsCalibrationWeb/bolopsfv1.01.pdf>
- . 2012, *Herschel Space Observatory*, http://hereschel.esac.esa.int/twiki/pub/Public/PacsCalibrationWeb/bolopsf_20.pdf
- Pahre, M. A., Ashby, M. L. N., Fazio, G. G., & Willner, S. P. 2004, ApJS, 154, 229
- Panuzzo, P., Rampazzo, R., Bressan, A., et al. 2011, A&A, 528, A10
- Panuzzo, P., Vega, O., Bressan, A., et al. 2007, ApJ, 656, 206
- Papovich, C., & Bell, E. F. 2002, ApJ, 579, L1
- Papovich, C., Dole, H., Egami, E., et al. 2004, ApJS, 154, 70
- Paradis, D., Veneziani, M., Noriega-Crespo, A., et al. 2010, A&A, 520, L8

- Paradis, D., Paladini, R., Noriega-Crespo, A., et al. 2012, *A&A*, 537, A113
- Parkin, T. J., Wilson, C. D., Foyle, K., et al. 2012, *MNRAS*, 422, 2291
- Pascale, E., Auld, R., Dariush, A., et al. 2011, *MNRAS*, 415, 911
- Patanchon, G., Ade, P. A. R., Bock, J. J., et al. 2008, *ApJ*, 681, 708
- Paturel, G., Petit, C., Prugniel, P., et al. 2003, *A&A*, 412, 45
- Peebles, P. J. E., & Nusser, A. 2010, *Nature*, 465, 565
- Pellegrini, S. 2010, *ApJ*, 717, 640
- Pérez-González, P. G., Rieke, G. H., Egami, E., et al. 2005, *ApJ*, 630, 82
- Perlman, E. S., Mason, R. E., Packham, C., et al. 2007, *ApJ*, 663, 808
- Pilbratt, G. L., Riedinger, J. R., Passvogel, T., et al. 2010, *A&A*, 518, L1
- Planck Collaboration. 2011a, *A&A*, 536, A19
- . 2011b, *A&A*, 536, A16
- . 2011c, *A&A*, 536, A21
- . 2011d, *A&A*, 536, A24
- Planck Collaboration, Ade, P. A. R., Aghanim, N., et al. 2011, *A&A*, 536, A23
- Poglitsch, A., Waelkens, C., Geis, N., et al. 2010, *A&A*, 518, L2
- Rangwala, N., Maloney, P. R., Glenn, J., et al. 2011, *ApJ*, 743, 94
- Reach, W. T., Dwek, E., Fixsen, D. J., et al. 1995, *ApJ*, 451, 188
- Renault, C., Barrau, A., Lagache, G., & Puget, J.-L. 2001, *A&A*, 371, 771
- Rieke, G. H., & Low, F. J. 1972, *ApJ*, 176, L95
- Rieke, G. H., Young, E. T., Engelbracht, C. W., et al. 2004, *ApJS*, 154, 25
- Roberts, M. S. 1962, *AJ*, 67, 437
- Roussel, H. 2011, Submitted to *PASP*, available at arXiv:1205.2576
- Rowan-Robinson, M., Roseboom, I. G., Vaccari, M., et al. 2010, *MNRAS*, 409, 2

- Rowlands, K., Dunne, L., Maddox, S., et al. 2012, MNRAS, 419, 2545
- Sage, L. J., Welch, G. A., & Young, L. M. 2007, ApJ, 657, 232
- Saintonge, A., Kauffmann, G., Kramer, C., et al. 2011, MNRAS, 415, 32
- Salpeter, E. E. 1974, ApJ, 193, 579
- Sandage, A. 1961, The Hubble atlas of galaxies (Carnegie Inst of Washington)
- Sanders, J. S., & Fabian, A. C. 2006, MNRAS, 371, 1483
- Sandstrom, K. M., Leroy, A. K., Walter, F., et al. 2012, ArXiv e-prints
- Sarazin, C. L., Irwin, J. A., & Bregman, J. N. 2001, ApJ, 556, 533
- Sargent, B. A., Srinivasan, S., Meixner, M., et al. 2010, ApJ, 716, 878
- Sarzi, M., Shields, J. C., Schawinski, K., et al. 2010, MNRAS, 402, 2187
- Sauvage, M., & Thuan, T. X. 1992, ApJ, 396, L69
- Schawinski, K., Kaviraj, S., Khochfar, S., et al. 2007, ApJS, 173, 512
- Schmidt, M. 1963, ApJ, 137, 758
- Schmitt, H. R. 2001, AJ, 122, 2243
- Schruba, A., Leroy, A. K., Walter, F., et al. 2011, AJ, 142, 37
- Schweizer, F., & Seitzer, P. 1992, AJ, 104, 1039
- Seki, J., & Yamamoto, T. 1980, Ap&SS, 72, 79
- Serra, P., Morganti, R., Oosterloo, T., et al. 2009, in Panoramic Radio Astronomy: Wide-field 1-2 GHz Research on Galaxy Evolution
- Shapiro, K. L., Falcón-Barroso, J., van de Ven, G., et al. 2010, MNRAS, 402, 2140
- Shetty, R., Kauffmann, J., Schnee, S., & Goodman, A. A. 2009a, ApJ, 696, 676
- Shetty, R., Kauffmann, J., Schnee, S., Goodman, A. A., & Ercolano, B. 2009b, ApJ, 696, 2234
- Shirey, R., Soria, R., Borozdin, K., et al. 2001, A&A, 365, L195
- Sil'chenko, O. K., Moiseev, A. V., & Shulga, A. P. 2010, AJ, 140, 1462

- Skibba, R. A., Engelbracht, C. W., Dale, D., et al. 2011, ApJ, 738, 89
- Skrutskie, M. F., Cutri, R. M., Stiening, R., et al. 2006, AJ, 131, 1163
- Smail, I., Ivison, R. J., Blain, A. W., & Kneib, J.-P. 2002, MNRAS, 331, 495
- Smith, M. W. L., Vlahakis, C., Baes, M., et al. 2010, A&A, 518, L51+
- Smith, M. W. L., Eales, S. A., Gomez, H. L., et al. 2012a, ApJ, 756, 40
- Smith, M. W. L., Gomez, H. L., Eales, S. A., et al. 2012b, ApJ, 748, 123
- Soifer, B. T., Rowan-Robinson, M., Houck, J. R., et al. 1984, ApJ, 278, L71
- Sparks, W. B., Macchetto, F., & Golombek, D. 1989, ApJ, 345, 153
- SPIRE Observers' Manual. 2011, *Herschel Space Observatory*, http://hereschel.esac.esa.int/Docs/SPIRE/html/spire_om.html
- SPIRE Photometry Cookbook. 2011, *Herschel Space Observatory*, http://hereschel.esac.esa.int/twiki/pub/Public/SpireCalibrationWeb/SPIREPhotometryCookbook_jul2011_2.pdf
- SPIRE Pipeline Description Document. 2009, *Herschel Space Observatory*, http://hereschel.esac.esa.int/twiki/pub/Public/SpireCalibrationWeb/Pipe%_Description_2.1.pdf
- Springob, C. M., Haynes, M. P., Giovanelli, R., & Kent, B. R. 2005, ApJS, 160, 149
- Stansberry, J. A., Gordon, K. D., Bhattacharya, B., et al. 2007, PASP, 119, 1038
- Stark, A. A., & Binney, J. 1994, ApJ, 426, L31
- Stepnik, B., Abergel, A., Bernard, J.-P., et al. 2003, A&A, 398, 551
- Stickel, M., Klaas, U., Lemke, D., & Mattila, K. 2002, A&A, 383, 367
- Strong, A. W., & Mattox, J. R. 1996, A&A, 308, L21
- Strong, A. W., Moskalenko, I. V., Reimer, O., Digel, S., & Diehl, R. 2004, A&A, 422, L47
- Struck, C., Appleton, P., Charmandaris, V., Reach, W., & Smith, B. 2004, in Spitzer Proposal ID #3247, 3247-+
- Struve, W. 1847, Etudes d'astronomie stellaire.

- Swedenborg, B. 1734, *Principia rerum naturalium; sive novarum tentaminum phenomena mundi elementaris philosophia explicandi*
- Swinyard, B., & Wild, W. 2010, ISSI Scientific Reports Series, 9, 241
- Swinyard, B. M., Ade, P., Baluteau, J.-P., et al. 2010, A&A, 518, L4
- Tabatabaei, F. S., & Berkhuijsen, E. M. 2010, A&A, 517, A77
- Temi, P., Brighenti, F., & Mathews, W. G. 2007a, ApJ, 660, 1215
- . 2007b, ApJ, 666, 222
- Temi, P., Brighenti, F., Mathews, W. G., & Bregman, J. D. 2004, ApJS, 151, 237
- Temi, P., Mathews, W. G., Brighenti, F., & Bregman, J. D. 2003, ApJ, 585, L121
- The SPIRE Analogue Signal Chain and Photometer Detector Data Processing Pipeline. 2009, *Herschel Space Observatory*, http://hereschel.esac.esa.int/twiki/pub/Public/SpireCalibrationWeb/Phot%_Pipeline_Issue7.pdf
- Thilker, D. A., Braun, R., Walterbos, R. A. M., et al. 2004, ApJ, 601, L39
- Thompson, R. I., Eisenstein, D., Fan, X., et al. 2006, ApJ, 647, 787
- Tran, H. D., Tsvetanov, Z., Ford, H. C., et al. 2001, AJ, 121, 2928
- Trundle, C., Dufton, P. L., Lennon, D. J., Smartt, S. J., & Urbaneja, M. A. 2002, A&A, 395, 519
- Tsai, J. C., & Mathews, W. G. 1996, ApJ, 468, 571
- Tully, R. B., & Fisher, J. R. 1988, Catalog of Nearby Galaxies (Cambridge University Press)
- Turner, A. D., Bock, J. J., Beeman, J. W., et al. 2001, Appl. Opt., 40, 4921
- van Dokkum, P. G., & Franx, M. 1995, AJ, 110, 2027
- Veneziani, M., Ade, P. A. R., Bock, J. J., et al. 2010, ApJ, 713, 959
- Véron-Cetty, M.-P., & Véron, P. 2010, A&A, 518, A10
- Verter, F., & Rickard, L. J. 1998, AJ, 115, 745
- Vlahakis, C., Dunne, L., & Eales, S. 2005, MNRAS, 364, 1253

- Vlahakis, C., Eales, S., & Dunne, L. 2007, MNRAS, 379, 1042
- Walter, F., Sandstrom, K., Aniano, G., et al. 2011, ApJ, 726, L11
- Walterbos, R. A. M., & Greenawalt, B. 1996, ApJ, 460, 696
- Weinzirl, T., Jogee, S., Khochfar, S., Burkert, A., & Kormendy, J. 2009, ApJ, 696, 411
- Werner, M. W., Roellig, T. L., Low, F. J., et al. 2004, ApJS, 154, 1
- Werner, N., de Plaa, J., Kaastra, J. S., et al. 2006, A&A, 449, 475
- Whittet, D. C. B. 2003, Dust in the Galactic Environment, 2nd edn. (Bristol, United Kingdom: Institute of Physics Publishing)
- Wiebe, D. V., Ade, P. A. R., Bock, J. J., et al. 2009, ApJ, 707, 1809
- Williams, B. F. 2003, AJ, 126, 1312
- Wilson, C. D. 1995, ApJ, 448, L97
- Wolf, C., Meisenheimer, K., Rix, H.-W., et al. 2003, A&A, 401, 73
- Wolfire, M. G., Hollenbach, D., & McKee, C. F. 2010, ApJ, 716, 1191
- Wright, E. L. 2001, ApJ, 553, 538
- Wright, E. L., Mather, J. C., Bennett, C. L., et al. 1991, ApJ, 381, 200
- Wright, G. S., James, P. A., Joseph, R. D., & McLean, I. S. 1990, Nature, 344, 417
- Wright, T. 1750, An Original Theory or New Hypothesis of the Universe
- Wrobel, J. M. 1991, AJ, 101, 127
- Wrobel, J. M., & Heeschen, D. S. 1988, ApJ, 335, 677
- Wyder, T. K., Martin, D. C., Schiminovich, D., et al. 2007, ApJS, 173, 293
- Xilouris, E. M., Madden, S. C., Galliano, F., Vigroux, L., & Sauvage, M. 2004, A&A, 416, 41
- Yi, S. K., Lee, J., Sheen, Y.-K., et al. 2011, ApJS, 195, 22
- Yi, S. K., Yoon, S.-J., Kaviraj, S., et al. 2005, ApJ, 619, L111

- Yin, J., Hou, J. L., Prantzos, N., et al. 2009, A&A, 505, 497
- York, D. G., Adelman, J., Anderson, Jr., J. E., et al. 2000, AJ, 120, 1579
- Young, J. S., & Scoville, N. 1982, ApJ, 260, L41
- Young, L. M., Bendo, G. J., & Lucero, D. M. 2009, AJ, 137, 3053
- Young, L. M., Bureau, M., Davis, T. A., et al. 2011, MNRAS, 414, 940
- Ysard, N., Juvela, M., Demyk, K., et al. 2012, A&A, 542, A21
- Yun, M. S., Reddy, N. A., & Condon, J. J. 2001, ApJ, 554, 803
- Zhu, M., Papadopoulos, P. P., Xilouris, E. M., Kuno, N., & Lisenfeld, U. 2009, ApJ, 706, 941
- Zibetti, S., Charlot, S., & Rix, H.-W. 2009, MNRAS, 400, 1181
- Zwicky, I. F. 1942, ApJ, 95, 555